Smart Dielectric Elastomer Generators

Enabling technologies for real-world implementation

By

PLINIO RODRIGUES DE OLIVEIRA ZANINI

Department of Engineering Mathematics
UNIVERSITY OF BRISTOL

A dissertation submitted to the University of Bristol in accordance with the requirements of the degree of DOCTOR OF PHILOSOPHY in the Faculty of Engineering.

SEPTEMBER 2018

Word count: 30082

Abstract

Dielectric Elastomer Generators (DEGs) are an emerging technology able to answer the need for cheap and available energy solutions, from energy scavenging at small scale to energy generation in large devices. Consisting of rubbery stretchable capacitors, DEGs can convert mechanical energy into electrical energy when their charges are displaced against the electric field during their relaxing phase. Despite having characteristics such as high energy density, low cost, and easy scalability, there are still significant challenges in their implementation. This includes the need for high voltage priming to enable the energy conversion and the adequate timing to charge/discharge the DEG. This thesis seeks to investigate and propose solutions for smart charge management in DEGs at different scales.

Starting from a model-based analysis of the energy conversion phenomenon during the charging and discharging transients, we describe how undesired electrical-to-mechanical energy conversion, exhibited as an actuator-like effect, can reduce the overall energy generated during a cycle.

Subsequently, we analyse different layouts of Self-Priming Circuits (SPCs), a scheme to passively promote the charge and discharge of DEGs. SPC-DEG systems can receive low voltage priming and then increase the system voltage and the amount of energy generated per cycle, eliminating the need for a high voltage time-controlled charge. Our model is experimentally validated and gives good quantitative accuracy. Using the SPC-DEG model and considering the actuator-like behaviour, we predict that the SPC-DEG systems can undergo a self-stabilising condition, which we then verify experimentally, and propose methods to estimate the emergent steady state.

In addition, we develop the Self-sensing Peak Detection (SSPD) method that self-senses the deformation characteristic of DEGs and uses it as a signal to autonomously promote charge and discharge. The method was successfully implemented experimentally and has potential to optimally control DEG cycles even for unpredictable frequency and amplitude deformations.

This thesis demonstrates possible solutions for charge management of DEGs and their implementation in the future.

Dedication and acknowledgements

Fisrt of all, I would like to express my sincere gratitude to my supervisors Jonathan Rossiter and Martin Homer. Your constant guidance, advice, support and encouragement (as well as the spontaneous silly jokes during the meetings) made my PhD experience amazing and a real period of enrichment. You inspire me as a researcher, both in terms of ambition and professional conduct.

I would like to thanks the support of my colleagues in Bristol, both from BRL and BUNCAER who I shared laughs, lunch breaks (RIP lunch club), some football, movies and provided me with the chance to watch some awesome seminars. I wish I have got to know some of you more. In special Espen, Andy H., Aaron, Martin G., Gabor, Keren, Krishna, Djen, Tim, Majid and Chongjing, for both technical and moral support when things didn't go too well. I hope the SoftLab group grows even stronger.

I would like to thank Prof. Seelecke and the iMSL group from Saarland University, who welcomed and made me feel at home during the 7 weeks I was in Saarbruecken. It was a really rich experience that made me to mature as a researcher. A special thanks to Gianluca, not only for the major contribution towards the self-sensing topic in this thesis but also for the help with basic control related questions and the sincere friendship.

Thanks to Prof. Anderson, who received me and made me feel welcomed at the Biomimetics Lab in the University of Auckland. The knowledge exchange I had with the Biomimetics Lab was fundamental for my research. I would like to thanks all the team I worked with during my time in New Zealand, you made me feel at home and it was an honour to name Plinio Bay (the lab corner with the most dubious sense of humour). In special, I would like to acknowledge Patrin for his support, work-related or not, while I was there, and after.

I would like to also thank my friends in Bristol. Thanks, Felipe, Luana, Olivia and Barbara, for the sharing and supporting environment, helping each other during our PhD difficulties outside of work.

I would like to acknowledge Coni for her support during this past year, especially during the last stressful writing up months.

I not only would like to thank but also dedicate this thesis to my family, my parents Wagner and Claudia, my Grandmother Ruth and my aunt Isabel. You raised me and provided me with all the base education, ambition and courage that allowed me to get here, being always present no matter how far from home I have been in the past 10 years.

AUTHOR'S DECLARATION

I declare that the work in this dissertation was carried out in accordance with the requirements of the University's Regulations and Code of Practice for Research Degree Programmes and that it has not been submitted for any other academic award. Except where indicated by specific reference in the text, the work is the candidate's own work. Work done in collaboration with, or with the assistance of, others, is indicated as such. Any views expressed in the dissertation are those of the author.

SIGNED: ..... DATE: .....

Table of Contents

List of Tables

List of Figures

Figure **Page**

CHAPTER 1

INTRODUCTION

Energy is the foundation of not only our modern society but is also the source of all transformations that led us here, from the control and use of fire, passing by the coal that powered the start of the industrial revolution and the electricity that runs most households across the world nowadays.

Despite all the advances in energy generation, around 1.3 billion people still do not have access to electricity [7]. Accentuating the situation is energy price volatility, both due to the geopolitics that affects oil prices [10] and the intermittent production from renewable sources [88]. It creates extras uncertainty for the population that is subjected to those fluctuations that affect prices and consequently their daily lives. Moreover, the global economy still relies heavily on fossil fuels, which have been pointed out as major causes of global warming, thus accentuating the need to increase the use of renewable resources. Despite their availability, some renewable resources, such as tidal and wave energy are not yet a widespread commercial reality and await development before they can play an important role in the future. Being able to improve power take-off technologies plays an important role to make renewable energies feasible.

On the other hand, the popularisation of electronics and their dependence on batteries also creates technical and environmental issues. While such devices are limited by their energetic autonomy, they also present a challenge in their end-of-life phase since most batteries require specific disposal methods.

Being potentially able to perform in both larger power plants [4, 138] and small-scale energy harvesting devices [66, 77], Dielectric Elastomer Generators (DEGs) represent an emerging

technology that has shown potential to play an important role in future energy generation applications.

1.1 Renewable energy harvesting

The main sources of clean energy are solar, bioenergy (biofuels and biomass), wind, hydropower, geothermal, tidal, human motion, structural vibrations and waves. Apart from solar and biofuels, all the others require, at least at some stage, the conversion from mechanical to electrical energy (turbine rotation, structure oscillation, fluid induced movement). Currently, electromagnetic generators are the reference technology for this conversion.

Electromagnetic generators are typically designed for specific frequencies, where they are able to perform with high efficiency [9, 35, 113, 114]. Thus, they are a good fit for biomass, hydropower and geothermal energy sources, where the generator mechanical exiting frequency is controlled (e.g., fluid flow rate rotating the turbine) and is kept close to the optimal operation point [35]. Wind energy turbines using electromagnetic generators, nowadays a fairly established technology, depend on some combination of gearing mechanisms to improve the mechanical excitation frequency on the generator [132, 146], a high number of poles in their construction [146], or permanent magnet solutions [132, 146, 151], which either reduce efficiency or add significant costs to the final product. Having the energy conversion based on the rate of change of magnetic field, the required excitation frequencies make their application in wave energy devices challenging, since the waves present slow motion; typically of order less than 1Hz [33].

Piezoelectric materials, that are able to develop an electric potential when strained [11], represent another possibility for electromechanical energy conversion. Piezoelectric devices consist of two classes: piezoceramics, such as zirconate titanate (PZT) and lead magnesium niobate-lead titanate (PMN-PT), and piezopolymers, such as polyvinylidene fluoride (PVDF). While the former typically have high electromechanical efficiency [70, 71], they are too stiff for applications that require shape changing; they also contain lead, which has been banned from commercial electronics [70]. The latter, on the other hand, lack the high efficiency of piezoceramics [11]. Hybrid approaches exist, that use piezoelectric fibres in carrier materials [70], but these require complex fabrication processes; scaling up generator size would certainly incur high cost. Additionally, piezoelectric devices, are usually designed to operate closer to resonance, which is far higher than the frequencies expected from renewable energy sources as cited above [115].

Another electromechanical conversion method considers the use of electrostatic harvesters, where a pair of oppositely charged bodies is used to promote the energy conversion [70]. A classic illustrative example is a charged pair of parallel plates: as they are positioned either further apart or displaced in parallel (see Figure 1.1) and their capacitance decreases, the voltage on the

plates, and consequently their electric potential energy increases. To perform energy conversion, they require an initial charging, that, alternatively, could be supplied by a material of constant polarisation, such as an electret, but the voltage range for such materials is usually not enough for efficient use of electrostatic energy harvesters [70]. Overall, their performance is limited by the maximum capacitance and the capacitance change, which requires oscillations in the range of microns while keeping the minimum air gap between the plates of ≈ 0.5mm or less [125]. Despite being a good technology for micro-mechanical systems (MEMS), able to deliver energy harvesting in the scale of milliwatts, [11, 30], scaling electrostatic harvesters up in size, while maintaining the necessary precise design, presents serious practical implementation issues [125]

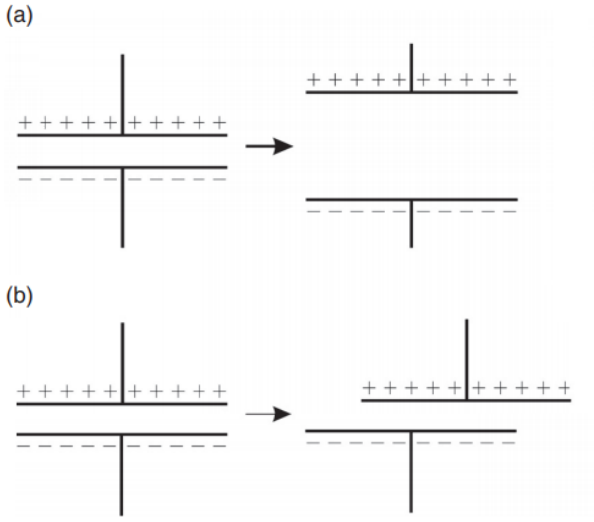

Figure 1.1: Electrostatic transduction with two charged parallel plates: displacement perpendicular to the plates (a), displacement in parallel with the plates (b). Reproduced from [70].

An emerging class of energy harvesting materials, dielectric elastomer generators (DEGs) also show great potential [108]. Consisting of a layer of an elastic dielectric material (elastomer) coated on both sides with flexible electrodes isolated from one another, Dielectric Elastomer (DEs) act as flexible variable capacitors [19]. In generator mode, they can be exploited similarly to the electrostatic devices cited above [108]. Among their advantages over the electrostatic devices are their scalability and consequently lower costs for manufacture [69], and the higher dielectric strength and permittivity the elastomer provides, ensuring higher energy density.

McKay [94] adapted the data from [126] to provide a comparison between the above-cited energy converting classes (including DEGs) in terms of energy density, shown in Table 1.1. The DEG parameters used come from 3M VHB 4905, an acrylic material popularly used for DEG prototypes. Despite studies suggesting a relative dielectric permittivity of 4.7 [74], a conservative

value of 4 was chosen. Koh *et al.* [75] predicted a potential to harvest energy up to four times higher than those obtained in [94]. A DEG energy density about 780mJ/g (DEG density ≈ 1g/cm^3[75]) has been already obtained experimentally [130], reinforcing the potential of DEGs as an emerging energy converting technology. Additionally, [147], following the same procedure as [75], calculated that, theoretically, using natural rubber as the material for the DEG, the energy density could reach 3.5J/g.

Table 1.1: Theoretical energy densities of traditional variable capacitor (electrostatic), dielectric elastomer, and electromagnetic generators. E is the electric field, ϵ_0 vacuum dielectric permittivity, ϵ_r the relative permittivity of the material, B is the magnetic field strength, μ_0 is the magnetic permeability, σ_{yield} is the yield strength of the material, and d is the piezoelectric strain coefficient. Reproduced from McKay [94].

Technology	Governing Equation	Conditions	Energy Density
Electrostatic	$u = \frac{\epsilon_0 E^2}{2}$	$E = 100$MV/m $\epsilon_0 = 8.854$pF/m	44mJ/cm^3
DEG (VHB)	$u = \frac{\epsilon_0 \epsilon_r E^2}{2}$	$E = 150$MV/m $\epsilon_0 = 8.854$pF/m $\epsilon_r = 4$	398mJ/cm^3
Electromagnetic	$u = \frac{B^2}{2\mu_0}$	$B = 1$T $\mu_0 = 1.26\mu$H/m	397mJ/cm^3
Piezoelectric (PZN-PT)	$u = \frac{\sigma_{\text{yield}}^2 d^2}{2\epsilon_0 \epsilon_r}$	$\sigma_{\text{yield}} = 83$MPa $d = 2$nm/V $\epsilon_0 = 8.854$pF/m $\epsilon_r = 4500$	346mJ/cm^3
Piezoelectric (PVDFT)	$u = \frac{\sigma_{\text{yield}}^2 d^2}{2\epsilon_0 \epsilon_r}$	$\sigma_{\text{yield}} = 52$MPa $d = 30$nm/V $\epsilon_0 = 8.854$pF/m $\epsilon_r = 12$	11.5mJ/cm^3

Other advantageous characteristics of DEGs regard the fact that their energy harvesting mechanism is rate-independent, their elastic nature creates shock resilience, they are corrosion resistant and silent in operation [138]. Due to their high potential, in this thesis, we will investigate their behaviour and how to overcome current implementation challenges, described in more detail below.

1.2 Dielectric Elastomers — General overview

In order to talk about energy harvesting through dielectric elastomers, first one needs to comprehend that they are multifunctional materials, able to work as actuators [40, 90, 109, 123], sensors [87, 133, 143, 149] and generators [77]. Dielectric Elastomer Actuators (DEAs) were first

mentioned in [110], where their potential to show high area strain when electrically actuated was highlighted and their working mechanism explained. Later, due to their capacitive nature, their use as sensors has been investigated: it is possible to measure their capacitance and directly relate it to the stretch [87, 136], as exploited in commercially available DE sensors by, for example, StretchSense [5], ElastiSense [2], and Parker [3].

Once charged, the opposing charges on each side of the dielectric yield electrostatic forces (Maxwell stress) that compress the DE in its thickness dimensions, reducing its thickness direction as well as increasing its area, as illustrated in Figure 1.2. Since the energy that is used as input is partially stored in the DEA as electric potential energy, and partially stored as potential elastic energy, with losses caused by the electrodes resistance and the viscoelastic behaviour of the materials, it is possible theoretically to achieve high energy conversion efficiency, but losses in the electrodes and in the viscous behaviour of the elastomer usually limit the efficiency to the range 20-30% [56, 130].

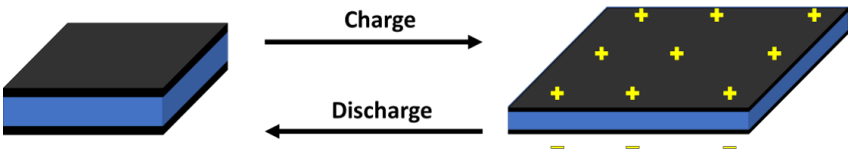

Figure 1.2: DEA actuation mechanism. When charged, DEA presents a reduction in thickness and increase in area due to the electrostatic forces.

As actuators, several applications of DEs have been proposed: pumps [14, 27, 43, 85, 145], tunable lenses [18, 129], valves [50, 91], tactile interactive devices [17, 25] as well of general robotics [26, 28, 29, 78, 111, 112, 124, 128]. To the best of our knowledge, DEAs as a product can be found commercially only through CTsystems, who sells stack actuators [1], but other companies, such as Parker have already provided samples for academic institutions.

The application of DEs as generators will be highlighted further in this chapter.

1.3 Modelling of Dielectric Elastomers

To model DEs, Suo [134] considers a Free Energy approach, describing the DE from a thermodynamic point of view. Considering an equilibrium state, the DE has some force P acting on it and it is connected to a power source with voltage V. As it is deformed by a small amount δl, and charged by a small amount δQ, the Helmholtz free energy, F changes by an amount

$$\delta F = P\delta l + V\delta Q. \tag{1.1}$$

Considering we have a known free energy function F, which has states l and Q, we are able to express the values of P and V as

$$P = \frac{\partial F(l,Q)}{\partial l} \tag{1.2}$$

$$V = \frac{\partial F(l,Q)}{\partial Q}. \tag{1.3}$$

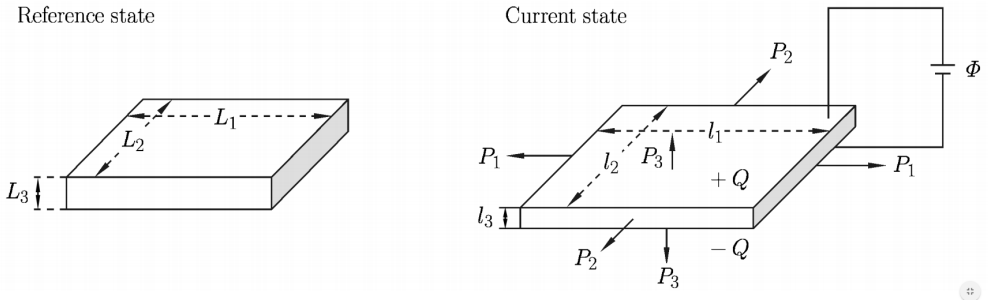

Figure 1.3: A dielectric elastomer in the reference state and in a current state. Reproduced from [134].

Expanding this approach, considering the three spatial dimensions of the DEA with lengths L_1, L_2 and L_3 in resting conditions, as shown in Figure 1.3, we take a state where the DEA is subjected to forces P_1, P_2 and P_3 in the respective coordinate directions. In such a state, the dimensions become l_1, l_2 and l_3. It is also subjected to voltage V which promotes charge Q to be stored in the DEA. If we consider a non-equilibrium situation, the resulting change in free energy satisfies

$$\delta F \leqslant P_1 \delta l_1 + P_2 \delta l_2 + P_3 \delta l_3 + V \delta Q, \tag{1.4}$$

where the equality would hold for an equilibrium state, as in eq. (1.1). Dividing the eq. (1.4) by the volume, to consider true stresses, σ_i, instead of the nominal forces, P_i, which is a more suitable approach for large deformations [116], we obtain

$$\delta(W\lambda_1\lambda_2\lambda_3) \leqslant \sigma_1\lambda_2\lambda_3\delta\lambda_1 + \sigma_2\lambda_1\lambda_3\delta\lambda_2 + \sigma_3\lambda_1\lambda_2\delta\lambda_3 + E\lambda_3\delta(\lambda_1\lambda_2 D), \tag{1.5}$$

where $\lambda_i = l_i/L_i$ is the stretch ratio, $E = V/l_3$ the true electric field, $D = Q/(l_1 l_2)$ the true electrical displacement, and $W = P/(\lambda_1\lambda_2\lambda_3)$ is the density of the free energy function. Considering

$$W = W(\lambda_1, \lambda_2, \lambda_3, D, \epsilon_1, \epsilon_2, ..., \epsilon_M), \tag{1.6}$$

where ϵ_i are the M known internal states, which account for dissipative factors, such as viscoelasticity, we are able to obtain that

$$\left(\frac{\partial W}{\partial \lambda_1} - \frac{\sigma_1 + ED - W}{\lambda_1}\right)\delta\lambda_1 + \left(\frac{\partial W}{\partial \lambda_2} - \frac{\sigma_2 + ED - W}{\lambda_2}\right)\delta\lambda_2 + \left(\frac{\partial W}{\partial \lambda_3} - \frac{\sigma_3 - W}{\lambda_3}\right)\delta\lambda_3 + \left(\frac{\partial W}{\partial D} - E\right)\delta D + \sum_{i=1}^{M} \frac{\partial W}{\partial \epsilon_i}\delta\epsilon_i \leqslant 0, \tag{1.7}$$

which, in equilibrium, becomes

$$\sum_i \frac{\partial W}{\partial \epsilon_i}\delta\epsilon_i \leqslant 0, \tag{1.8}$$

and, further, we obtain that

$$\sigma_1 = \lambda_1 \frac{\partial W}{\partial \lambda_1} - ED - W \tag{1.9}$$

$$\sigma_2 = \lambda_2 \frac{\partial W}{\partial \lambda_2} - ED - W \tag{1.10}$$

$$\sigma_3 = \lambda_3 \frac{\partial W}{\partial \lambda_3} - W \tag{1.11}$$

$$E = \frac{\partial W}{\partial D}. \tag{1.12}$$

While we have four states (λ_1, λ_3, λ_3, and D), the assumption of incompressibility for a DE [73], namely

$$\lambda_1\lambda_2\lambda_3 = 1, \tag{1.13}$$

allows us to reduce eq. (1.7) to three states, such that it becomes

$$\left(\frac{\partial W}{\partial \lambda_1} - \frac{\sigma_1 + \sigma_3 + ED}{\lambda_1}\right)\delta\lambda_1 + \left(\frac{\partial W}{\partial \lambda_2} - \frac{\sigma_2 + \sigma_3 + ED}{\lambda_2}\right)\delta\lambda_2 + \left(\frac{\partial W}{\partial D} - E\right)\delta D + \sum_{i=1}^{M} \frac{\partial W}{\partial \epsilon_i}\delta\epsilon_i \leqslant 0. \tag{1.14}$$

As in [116], we can select

$$\sigma_1 - \sigma_3 = \lambda_1 \frac{\partial W}{\partial \lambda_1} - ED + \sigma_{v1}(\lambda_1, \lambda_2, \dot{\lambda}_1, \dot{\lambda}_2) \tag{1.15}$$

$$\sigma_2 - \sigma_3 = \lambda_2 \frac{\partial W}{\partial \lambda_2} - ED + \sigma_{v2}(\lambda_1, \lambda_2, \dot{\lambda}_1, \dot{\lambda}_2) \tag{1.16}$$

$$E = \frac{\partial W}{\partial D}, \tag{1.17}$$

such that σ_{v1} and σ_{v2} are terms that describe the viscoelastic behaviour of the DE. Inserting eq. (1.15), eq. (1.16) and eq. (1.17) in eq. (1.14), we obtain that

$$-\frac{\sigma_{v1}}{\lambda_1}\delta\lambda_1 - \frac{\sigma_{v2}}{\lambda_2}\delta\lambda_2 + \sum_{i=1}^{M}\frac{\partial W}{\partial \epsilon_i}\delta\epsilon_i \leqslant 0, \tag{1.18}$$

and, consequently, that

$$-\frac{\sigma_{v1}}{\lambda_1}\dot{\lambda}_1 - \frac{\sigma_{v2}}{\lambda_2}\dot{\lambda}_2 + \sum_{i=1}^{M}\frac{\partial W}{\partial \epsilon_i}\dot{\epsilon}_i \leqslant 0. \tag{1.19}$$

The above procedure allows us to describe a DE model by prescribing W, σ_{v1}, σ_{v2}, and the internal variables ϵ_i and their rate variation, such that eq. (1.19) is always satisfied. This approach has the assumption that material deformations are homogeneous, thus avoiding the treatment of stress and strain fields, using instead average stress and strain to represent the DE states.

Similarly to the incompressibility constraint, some symmetric conditions allow us to reduce the system even further [73, 147]:

Uniaxial tension: Considering conditions where the membrane is mechanically loaded and deformed only in direction 1, we have that $\sigma_2 = \sigma_3 = 0$. We approximate that the same constraint can be extended to the stretch ratios, so that

$$\lambda_2 = \lambda_3 = \frac{1}{\sqrt{\lambda_1}}. \tag{1.20}$$

Biaxial tension: Considering conditions where the membrane is equally loaded in directions 1 and 2, we have that $\sigma_1 = \sigma_2$, and we approximate that the same constraint is valid for the stretch ratios, so that

$$\lambda_3 = \frac{1}{\lambda_1} = \frac{1}{\lambda_2}. \tag{1.21}$$

Pure shear: Consisting of a special case of uniaxial tension in direction 1, where direction 2 is either constrained or has its stiffness orders of magnitude higher than the other directions, we can approximate that

$$\lambda_3 = \frac{1}{\lambda_1}, \lambda_2 = 1. \tag{1.22}$$

Those are some of the possibilities of design constraints that allow a model simplification so that we can describe the system as a function of the stretch ratio in only one direction. In such a case, without loss of generality, we choose direction 1, and the material model, given by eq. (1.15), eq. (1.16) and eq. (1.17) can be simplified to

$$\sigma_1 = \lambda_1 \frac{\partial W}{\partial \lambda_1} - ED + \sigma_{v1}(\lambda_1, \dot{\lambda}_1) \tag{1.23}$$

$$E = \frac{\partial W}{\partial D}, \tag{1.24}$$

since we have $\lambda_2 = f(\lambda_1)$ and $\dot{\lambda}_2 = f(\dot{\lambda}_1)$, implying $W(\lambda_1, \lambda_2, D) = W(\lambda_1, f(\lambda_1), D)$.

As in [116], we define

$$W = W_m + W_e + W_v, \tag{1.25}$$

where $W_m(\lambda_1)$ is the strain energy function, representing the elastic portion and typically used in hyperelastic materials [107], $W_e(\lambda_1, D)$ is an electrical energy term that provides the electromechanical coupling in the model, and $W_v(\lambda_1, \dot{\lambda}_1, \epsilon_1, ..., \epsilon_M)$ accounts for the viscoelastic energy dissipation processes. We can rewrite eq. (1.23) as

$$\sigma_1 = \sigma_m(\lambda_1) + \sigma_e(\lambda_1, E) + \sigma_v(\lambda_1, \dot{\lambda}_1, \epsilon_1, ..., \epsilon_M) \tag{1.26}$$

where

$$\sigma_m = \lambda_1 \frac{\partial W_m}{\partial \lambda_1}, \tag{1.27}$$

$$\sigma_e = \lambda_1 \frac{\partial W_e}{\partial \lambda_1} - ED, \tag{1.28}$$

$$\sigma_v = \lambda_1 \frac{\partial W_v}{\partial \lambda_1} + \sigma_{v1}. \tag{1.29}$$

and, similarly, eq. (1.24) becomes

$$E = \frac{\partial W_e}{\partial D}. \tag{1.30}$$

We must then select adequate mathematical functions to represent the components W_m, W_e, W_v. Strain energy functions, W_m, have been a study topic for decades, since they are used to model rubber-like material behaviour [107]. Some commonly used model of strain energy are:

Neo-Hookean [107] :

$$W_{m,NH} = C_{10}(I_1 - 3); \tag{1.31}$$

Mooney-Rivlin [107] :

$$W_{m,MR} = C_{10}(I_1 - 3) + C_{01}(I_2 - 3); \tag{1.32}$$

Ogden [106] :

$$W_{m,\text{Ogden}} = \sum_{i=1}^{N} \frac{\mu_i}{\alpha_i}(\lambda_1^{\alpha_i} + \lambda_2^{\alpha_i} + \lambda_3^{\alpha_i} - 3); \tag{1.33}$$

Yeoh [150] :

$$W_{m,\text{Yeoh}} = \sum_{i=1}^{3} C_{i0}(I_1 - 3)^i; \tag{1.34}$$

Gent [39] :

$$W_{m,\text{Gent}} = -\frac{J_{lim}}{2} \ln\left(1 - \frac{I_1 - 3}{J_{lim}}\right); \tag{1.35}$$

Arruda-Boyce [49] :

$$W_{m,AB} = C_1 \sum_{i=1}^{5} \alpha_i \beta^{i-1} [I_1^i - 3^i]^i \tag{1.36}$$

where $\beta = \frac{1}{\lambda_m^2}, \alpha_1 = \frac{1}{2}, \alpha_2 = \frac{1}{20}, \alpha_1 = \frac{11}{1050}, \alpha_1 = \frac{19}{7000}, \alpha_1 = \frac{519}{673750}$.

In the expressions above, I_1 and I_2 are, respectively, the first and second invariant of the right Cauchy - Green deformation tensor and can be described by

$$I_1 = \lambda_1^2 + \lambda_2^2 + \lambda_3^2. \tag{1.37}$$

and

$$I_2 = \lambda_1^2\lambda_2^2 + \lambda_1^2\lambda_3^2 + \lambda_2^2\lambda_3^2. \tag{1.38}$$

The remaining parameters in the strain energy functions described above represent parameters that are calibrated for the selected material, which can be found, for example, through a uniaxial tension test [147]. Further examples of how to obtain these parameters and their use in modelling can be found in [72, 148].

For the part of the free energy function used for the electromechanical coupling, W_e, one could choose it based on the phenomenon it requires to be considered. For an ideal dielectric elastomer, without electrostriction or polarisation saturation, [134], we have that

$$W_e = \frac{D^2}{2\epsilon_0\epsilon_r}. \tag{1.39}$$

In case one decides to include electrostriction or polarisation saturation, [134] also presents options that consider such effects.

Regarding the function W_s, few works present candidate functions and use this kind of formulation to model the viscoelastic behaviour. Rizzello [116] presents a candidate function to describe an arrangement of linear spring-dashpots, shown in Figure 1.4. Another noteworthy study that obtained thermodynamically consistent models that reproduce the viscoelastic behaviour of DEs is [20], considering non-linear springs and a linear dashpot arrangement, as shown in Figure 1.5.

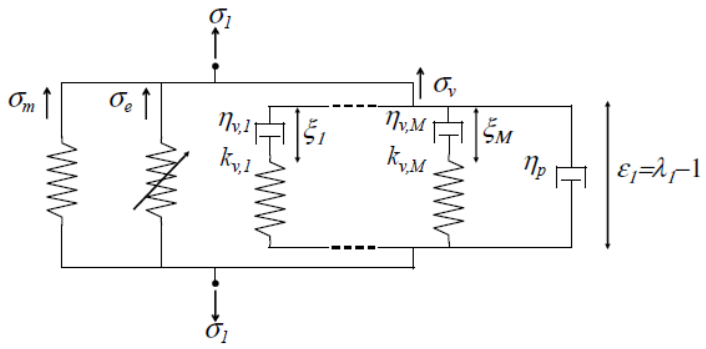

Figure 1.4: Possible spring-dashpot representation for viscoelastic behaviour of DEs. Reproduced from [116].

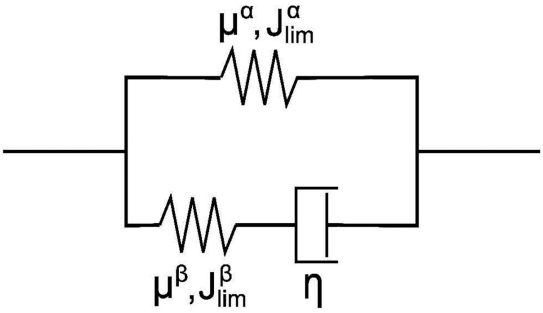

Figure 1.5: Viscoelastic relaxation is modelled using two parallel units. One unit consists of non-linear spring α, and the other unit consists of non-linear spring β and a dashpot η. Reproduced from [20].

A simplified method to model DEs, which takes a tensorial approach, was demonstrated by [44], starting from the Cauchy Stress relationship for hyperelastic materials

$$\sigma_i = \lambda_i \frac{\partial W_m}{\partial \lambda_i} - p, \tag{1.40}$$

where p is the hydrostatic pressure, accounting for the material boundary conditions. Considering the Neo-Hookean function for W_m and pure-shear conditions (as described above), we have:

$$\sigma_1 - \sigma_3 = 2C_{10}\left(\lambda_1^2 - \lambda_3^2\right) = C_{10}\left(\frac{\lambda_1^4 - 1}{\lambda_1^2}\right). \tag{1.41}$$

As a boundary condition, we have that the stress in direction 3 is caused by the electrostatic forces [12], thus

$$\sigma_3 = -\sigma_{\text{Maxwell}} = -\epsilon_0\epsilon_r\frac{V^2}{(\lambda_3 l_3)^2}. \tag{1.42}$$

Considering a constant damping to represent the viscous part of the DE behaviour, d_v, and that the system dynamics can be represented by a lumped mass of $m/2$, where m is the total mass of the polymer, [44] represents the system dynamics by

$$\frac{m}{2}\ddot{l_1} = F_1 - d_v\dot{l_1} - l_2 l_3\left[2C_{10}\left(\frac{\lambda_1^4 - 1}{\lambda_1^2}\right) - \sigma_{\text{Maxwell}}\right], \tag{1.43}$$

where F_1 is an external force that acts on the system in direction 1. We can rewrite eq. (1.43) so that λ_1 and its derivatives eliminate the need to display the other variables that describe the deformed state (l_1,l_2,l_3,$\dot{l}_1$,$\ddot{l}_1$):

$$\frac{m}{2}L_1\ddot{\lambda_1} = F_1 - d_v L_1\dot{\lambda_1} - \frac{L_2 L_3}{\lambda_1}\left[2C_{10}\left(\frac{\lambda_1^4 - 1}{\lambda_1^2}\right) - \epsilon_0\epsilon_r\frac{V^2}{L_3^2}\lambda_1^2\right]. \tag{1.44}$$

If we were to analyse eq. (1.44) according to the free energy approach, we would have

$$\sigma_m = 2C_{10}\left(\frac{\lambda_1^4 - 1}{\lambda_1^2}\right), \tag{1.45}$$

$$\sigma_e = -\epsilon_0\epsilon_r\frac{V^2}{L_3^2}\lambda_1^2, \tag{1.46}$$

$$\sigma_v = \frac{\lambda_1}{L_2 L_3}d_v L_1\dot{\lambda_1}, \tag{1.47}$$

which could be achieved by choosing W_m as the Neo-Hookean model, eq. (1.31), W_e as the ideal model, eq. (1.39), $W_v = 0$, and $\sigma_{v1}(\lambda_1, \dot{\lambda}_1) = \frac{\lambda_1}{L_2 L_3}d_v L_1\dot{\lambda_1}$.

In [44], the model was only validated for stretch ratios up to 20% strain and no dynamic tests were reported. Nonetheless, it presents all the basic characteristic for a generic DE and could support qualitative behaviour analysis for DEGs. Considering a static state, the external force, F_1 must balance the internal forces from the DE, thus

$$F_1 = \frac{L_2 L_3}{\lambda_1}\left[2C_{10}\left(\frac{\lambda_1^4 - 1}{\lambda_1^2}\right) - \epsilon_0\epsilon_r\frac{V^2}{L_3^2}\lambda_1^2\right]. \tag{1.48}$$

Although limited in accuracy, eq. (1.48) provides us with a model to determine equilibrium states on a DE and also analyse how deformation, λ_1, external force, F_1, and applied voltage, V, relate to each other, while providing a simple way to quantify the related energy values to each of these states.

1.4 Dielectric Elastomers Generators — Energy harvesting cycles

The electromechanical conversion for DEGs occurs when the material, from a charged and stretched state, relaxes. During this process, like-charges stored on the electrodes are forced into a smaller area, while opposite-charges, that were initially closer are set apart. On a more fundamental point of view, the mechanic forces restoring DEG's shape act on the charges stored on the DEG's surface by moving then against the electric field of the capacitor-like structure, thus increasing the electric potential energy stored in the DEG [108]. Due to this mechanism, we require the DEG to operate regularly in stretch-relax cycles, as well as in a coordinated manner to guarantee charges are available in it by the start of the relaxing phase, thereby enabling the energy conversion, while collecting the electrical energy output from each cycle. The coordination between the charge/discharge phases and stretch/relax of the DEG we denote as the energy harvesting cycle.

Since the amount of charge in a DEG affects directly its capability to convert energy, and the way a DEG is charged directly affects the losses involved, energy harvesting cycles have been an important topic of research and optimisation in the study of DEGs. Regarding the mode of charge control during the relaxing phase, [47] separates them into three categories: constant charge, constant voltage and constant electric field, as can be seen in Figure 1.6. The constant charge cycle, for example, can be described by the following stages (numbered as they appear in Figure 1.6):

- 1→2: From an initially relaxed phase, the DEG is stretched by a mechanical load and increases its capacitance.
- 2→3: Once stretched, the DEG is polarised through an electrical energy input.
- 3→4: From stretched and polarised, in an open circuit configuration, the mechanical load is released letting the material relax, so reducing the DEG's capacitance. As the capacitance reduces and the charge stored is maintained constant, there is a voltage rise.
- 4→1: Finally, the DEG is discharged from its more energetic state, back to its initial state.

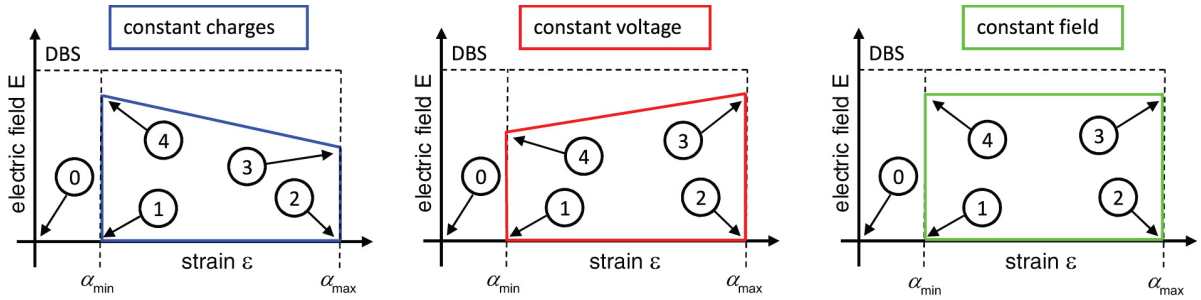

Figure 1.6: Different energy harvesting cycles and the location of intermediary modelled states as described by Graf *et al.* [47]. States are described as 0 for the DEG in its natural state, 1 for the DEG pre-stretched and ready for the cycle, 2 for the stretched material without electrical load, 3 for the DEG electrically charged before the relaxing phase and 4 for it relaxed with the remaining charge from the relaxing phase before discharge. Reproduced from [47]

The other two remaining cycles are variations: in the constant voltage cycle, the DEG discharges in a charge reservoir (kept at constant voltage) while relaxes and discharges the remaining charges by the end of the cycle. In the constant field, part of the discharge of the DEG happens during the relaxing phase as a controlled process, so that the electric field is kept at a constant maximum throughout. All three circuits have associated implementation issues, however, while the constant charge requires an open-circuit condition during the discharge, and the constant voltage could be implemented using a capacitor with capacitance orders of magnitude higher than the DEG, the electric field cycle requires the calculation of the electric field (could be estimated if the material displacement and voltage are known) and careful control of the discharge while the DEG relaxes.

In [47], it was considered that the DEG is charged always up to the maximum voltage possible such that the electric field in the cycle does not exceed a maximum value that could provoke dielectric breakdown failure (dashed DBS line in Figure 1.6). Considering dielectric breakdown as the limitation for how much energy the DEG could harvest for a given deformation, it was calculated in [47] the maximum energy that could be used as input, U_{in}, and the energy harvested for those conditions, $U_{\text{harvested}}$. Such values were calculated based on the ratio between the minimum and maximum capacitance, a^2, and a parametric energy value, U_0, which is based on volume, maximum electric field and material dielectric permittivity. Figures of merit for each of the cycle types are shown in Figure 1.7. We can see that for a given amount of energy charged, the constant charge represents the highest output. That can be explained by the fact there is no discharge during the relaxing phase, thus, there are more charges being displaced, and more electric energy is obtained. The highest amount of energy is harvested by the constant electric field. It presents the same amount of energy being discharged by the end of the relaxing phase as the constant charge (since they present the same electric field at this stage), but also discharges

partially during the relaxing phase, thus providing a higher energy output.

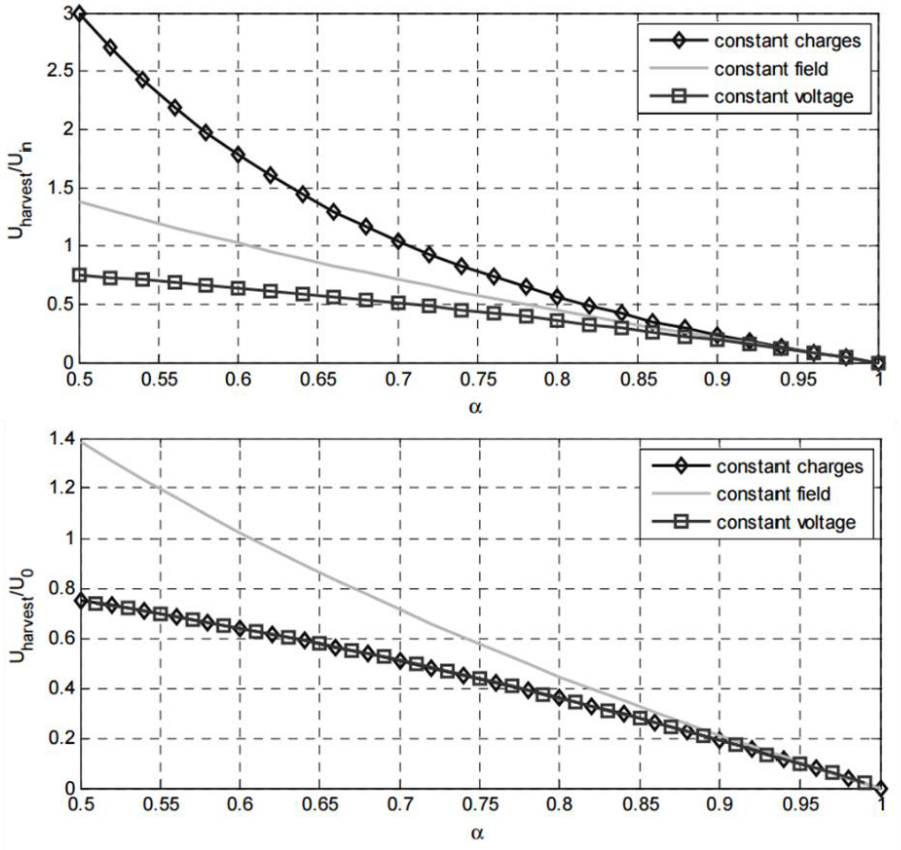

Figure 1.7: Relative electric energy gain (top) and amount of energy harvested per cycle. Reproduced from [47].

An experimental investigation of the cycles styles above was performed in [32], which highlighted the difficulty in controlling the constant electric field cycle, the need for cautious design of the constant charge cycle to avoid exceeding dielectric breakdown during the relaxing phase, and commented on the practical advantage of the constant voltage cycle that allows for better circuit design as the voltages the system will be subject to are already constrained. Although the energy was not computed in [32], another study provided some insights [15]. It was confirmed experimentally in [15] that the constant charges cycle provides the highest relative energy gain, $U_{\text{harvested}}/U_{\text{in}}$, but it was also found that $U_{\text{harvested}}$ from the constant charge cycle was higher than that of the constant voltage cycle by 12%, contrasting with the theoretical conclusions from [47].

A combination of the constant charges and constant electric field cycles was proposed in [51]. Based on a study of the electrical losses [48], a scheme consisting of an alternation between

the two aforementioned cycles was proposed and the ideal charging and discharging are found through an optimisation routine, such that the final cycle is able to deliver higher energy output than the cycles it is based on. Such cycle combination was reproduced by [15], but, since the losses were not discussed, it is hypothesised the optimal cycle described in [51] was not obtained, explaining why the resulting cycle showed an intermediary performance between the constant charges and constant field cycles. Another optimisation study was performed in [137], where the losses during the charging phase and discharging phase were analysed, and the charging and the discharging intervals for a constant electric field cycle were optimised for maximal energy output through current control. In [13], the failure mechanisms of DEGs were modelled and used as boundary parameters for the design of an optimal constant charges cycle, demonstrating that different failure modes, such as dielectric breakdown, loss of tension, mechanical rupture and electromechanical instability, could bound the maximal performance, not only the dielectric breakdown as simplified in [47] that propose they should be equal.

A variation of the above-presented cycles was proposed in [130]. Considering also the practical implementation, it proposes the use of a capacitor in parallel with the DEG during its relaxing phase (which can be achieved through a diode, see Figure 1.8b). Through this design, the DEG is able to harvest a higher amount of energy by exploring its allowed states (where it does not reach any of the failure modes, see Figure 1.8a). Such a cycle was able to achieve energy and power densities of 780mJ/g, and 170mW/g, among the highest ever recorded for energy conversion systems.

1.5 Dielectric Elastomer Generators — Applications

Since DEGs need a cyclic process to convert mechanical to electrical energy, their application to renewable energies has, for a long time, been motivated by wave energy converters. DEGs appear as a suitable candidate to make wave energy converters a reality. Different wave energy devices have been designed, including buoys to extract energy from heaving motion [21, 24, 89, 100, 127], flaps to harvest the surge motion [103], and oscillating water column generators [139, 140]. It was estimated in [23] that the buoy design proposed could yield an energy cost of US$0.18/kWh, with potential to reach US$0.05-US$0.07/kWh, an optimistic scenario, given that wave energy was estimated to cost between £0.12-£0.44/kWh [64]. Additionally, it has been proposed that the use of natural rubber for the manufacture of DEGs could also deliver energy with a small carbon footprint, with prices ranging between $.05-$0.12/kWh [147].

In the work of Chiba *et al.* [21], the energy conversion unit consisted of tubular shaped DEGs, as illustrated in the device seen in Figure 1.9. Another buoy design was proposed by [127], consisting of a semi-submerged floating round buoy attached to a mooring device in such a way that, as it moves, it compresses a DEG stack (see figure 1.10a). This type of design was further

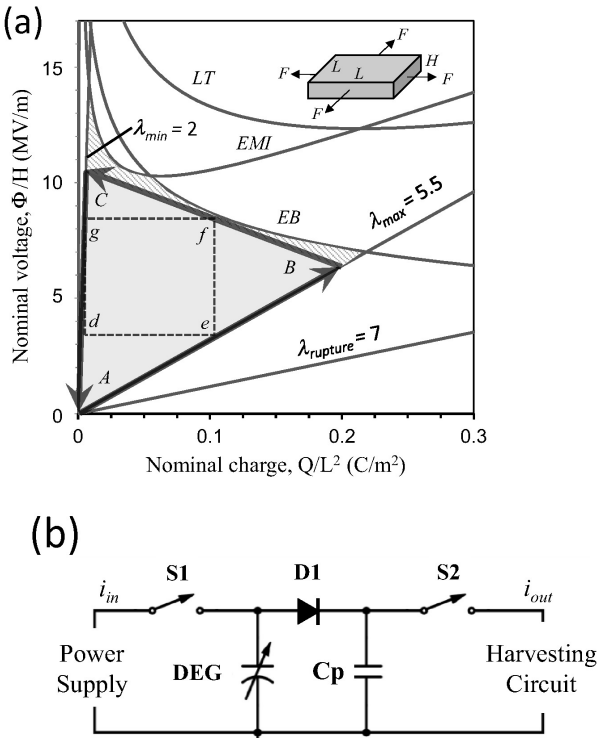

Figure 1.8: (a) The proposed electromechanical harvesting scheme is shown by the triangle A-B-C-A on the voltage-charge work-conjugate plane. Also, shown are the loci of the possible failure modes by electrical breakdown (EB), electromechanical instability (EMI), loss of tension (LT), and rupture stretch (λ rupture). The diagram is constructed for equibiaxial loading (inset) and for acrylic materials (VHB 4900 series, 3M), and is based on the work by Koh et al. [8] For comparison, the constant-voltage electromechanical harvesting cycle d-e-f-g is also shown. (b) Circuit diagram used to control the electromechanical cycle showing a power supply, the elastomer (DEG), a transfer capacitor (Cp), a diode (D1), a charging switch (S1), harvesting switch (S2), and harvesting circuits block that collects the electrical energy. Reproduced from [130].

modelled in [100], where a dual DEG stack was also proposed, such that it operates in both compression and tension; it was reported that such a device could yield an energy density up to 100mJ/cm^3.

In [103], poly-surge, a flapping mechanism to extract energy from surge motion was proposed (design shown in Figure 1.11). It was evaluated against the possibility of using linear conventional electromagnetic generators, but demonstrated performance around 30% inferior. Nonetheless, it is highlighted in [103] that such conventional devices suffer from power/torque limits that might stop energy production on severe sea conditions, an efficiency that varies with speed and power output, and might require further mechanisms for speed reduction. An evolution of the poly-surge concept was later developed, and consisted in using two antagonistic membranes, which was able

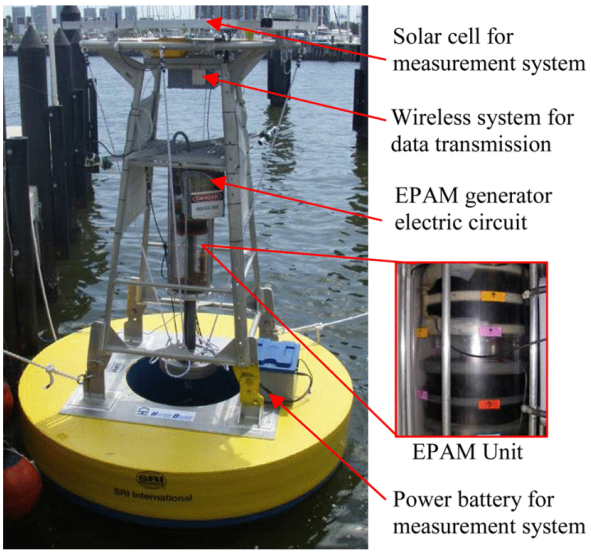

Figure 1.9: Energy harvesting buoy equipped with a DEG unit (Electroactive Polymer Artificial Muscle: EPAM) for energy conversion. Reproduced from [23].

to increase its energy productivity by 55% while decreasing the required amount of DEG by 65% [101]. SBM Offshore has been investing in wave energy through DEG by developing the S3 WEC device [8, 65], shown in Figure 1.12. It will consist of a 400m tube made out of DEGs submerged close to the surface. It is claimed to have several resonance modes, with natural periods between 0 and 15s, enabling the device to harvest energy efficiently from poly-chromatic waves. Since the DEG used is longitudinally constrained by fibres on its design, the deformations due to the wave motion are entirely converted into radial deformations across its structure.

A promising wave energy harvester device is the DEG oscillating water column (DEG-OWC) [104, 139, 141], developed as part of the PolyWEC consortium (from which the concepts from [100] and [103] belong as well). The design of its latest version, which include a duct to provide added mass and tune the membrane resonance, is shown in Figure 1.13. Using the cycle proposed by [130], the DEG-OWC was able to achieve energy density of 145mJ/g and convert up to 18% of the wave energy into electricity. It was shown that the prototype was able to deliver up to 870mW, which, on a real-scale device, could correspond to a device able to deliver hundreds of kW. Since the material used for the prototype (for the sake of stiffness scaling) was the acrylic 3M VHB 4905, a different material could provide an even better result: some materials, such as natural rubber, have shown better potential results for energy harvesting [147].

Another popular source of energy for DEG application is human motion. Since the heel-strike energy harvester created by SRI International [77, 108], it has been a recurrent topic in DEG applications. With regards to the shoe experiment, in this case, the heel-strike generator cell

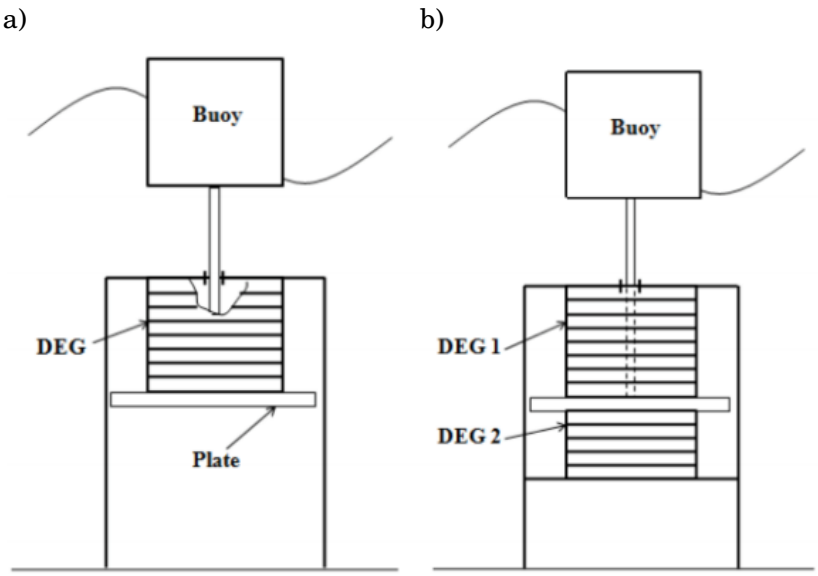

Figure 1.10: Energy harvesting buoyancy device for energy generation through DEGs. Single DEG stack operating in compression only (a). Dual DEG stack operating in compression and tension(b). Reproduced from [100].

was composed of a flat DEG on top of a chamber filled with gel, while constrained by a grid with holes on top, as shown in Figure 1.14. Every heel strike, the compression would increase chamber pressure and the DEG would balloon through the orifices of the grid. The heel-strike generator was reported to be able to power night vision goggles, yielding as much as 1W of electrical power, a maximum energy density of 300mJ/g, and approximately 33% efficiency [77], being made of 20 layers of 3M VHB 4910.

Jean-Mistral *et al.* [66], acknowledging that a shoe generator could be located too far from possible devices that would use its power, designed instead a structure to be attached behind the knee so that it would stretch at every step. Due to safety concerns, the device used lower voltages, 170V, at which 1mW was generated. An important issue when developing human motion energy harvesters, which has not been properly verified on reported studies, is user comfort, especially if scaling up the design for a multilayer stack, when elastic forces could disturb user motion, for example.

In order to harvest wind energy, experiments using a crank-slider mechanism to convert a turbine rotational movement to a uniaxial stretch of the DEG have been conducted [82, 83]. In [82], a variation of the crank radius was performed, obtaining the result that higher deformations would allow greater energy harvesting, in accordance with what is common knowledge in the area. The lack of data about wind speed, turbine parameters and overall system efficiency does not

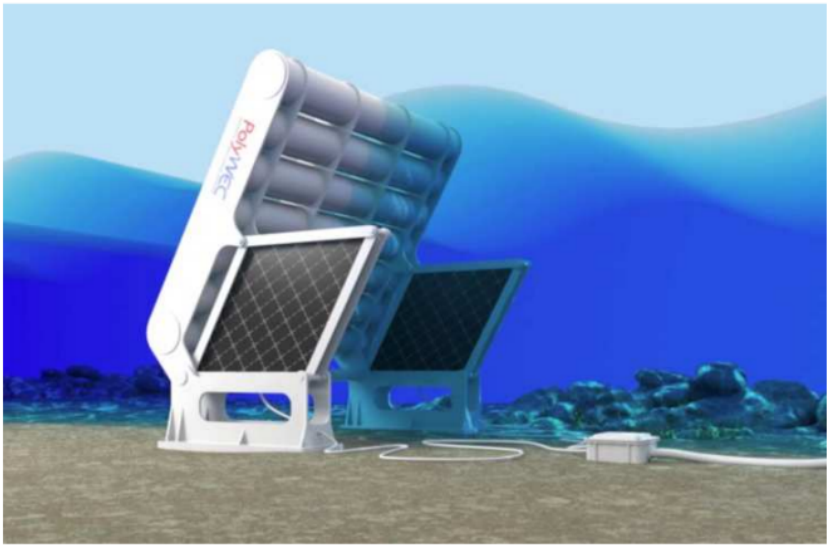

Figure 1.11: Illustration of poly-surge final design. Reproduced from [103].

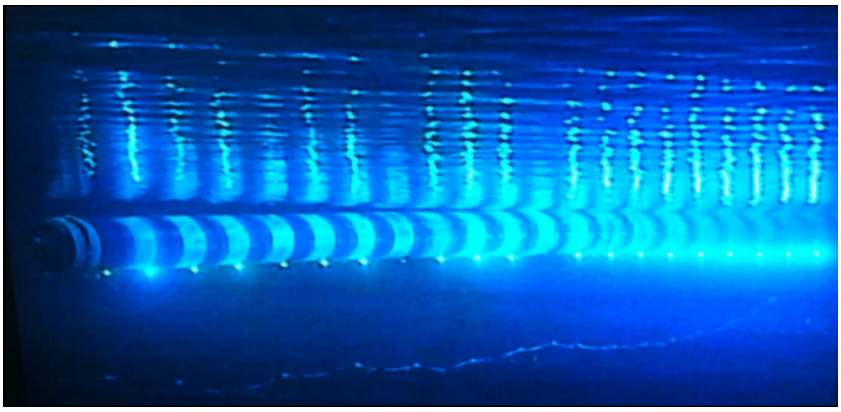

Figure 1.12: The S3 WEC protytpe from SBM Offshore during a submerged test. Reproduced from [65].

allow a proper evaluation of DEGs suitability for this kind of application. Another important point is that commercially available electromagnetic energy generators achieve very high efficiency, thus, it is hard to evaluate if the solution proposed using a DEG coupled through a mechanism is a suitable one to exploit such type of energy source.

Generating energy using DEGs as transducers for fluidic flow has been an issue since the nature of DEGs demands cyclic behaviour. Devices using crank-slider mechanisms have been reported for both wind (as shown above) and hydropower. For example, Chiba *et al.* [22] showed a waterwheel of 30cm diameter that could harvest 35mJ per revolution, but also did not report

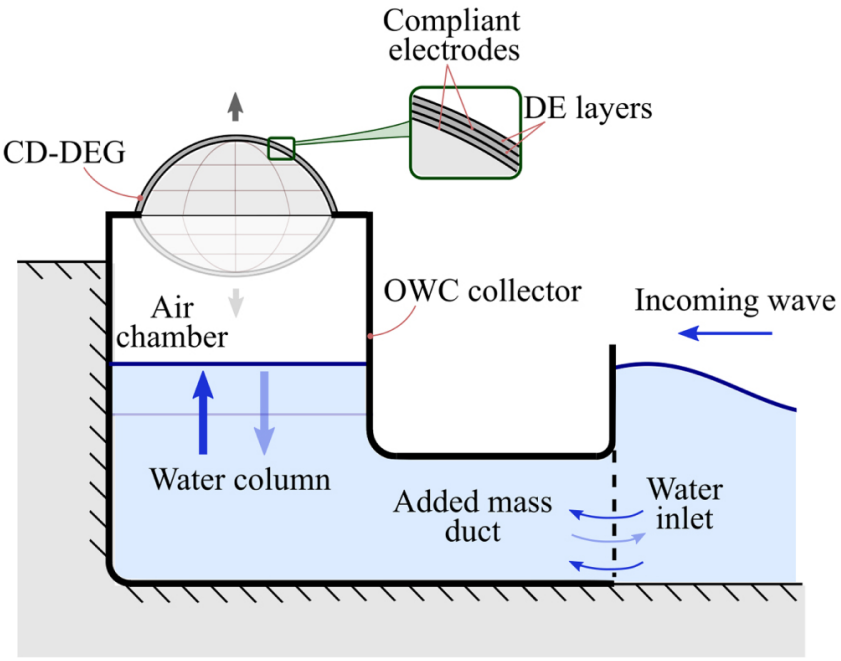

Figure 1.13: Schematic drawing of the DEG-OWC, including a fixed-structure collector and a circular diaphragm DEG. Water column displacement provides pressure changes in the air chamber causing the CD-DEG to expand upward or downward. Reproduced from [104].

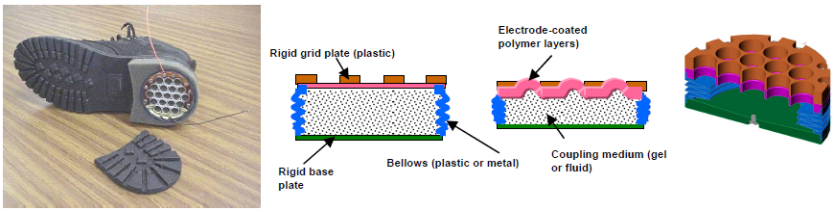

Figure 1.14: Heel-strike generator developed at SRI International; adapted boot with the device installed (left), cross section of device (right). Reproduced from [77].

enough data to allow efficiency and scalability evaluations. Maas and Graf [86] reported a concept of flow energy converter that would use a valve actively opening and closing fast enough to create the action of a shock wave to be explored. A schematic explanation of the process used is shown in Figure 1.15. It is definitely a new concept, but there is no experimental data reported to allow conclusions, and some issues remain to be verified, such as the ratio between harvested energy and that spent to actuate the valve. Another possibility for flow harvesting is exploring the energy from induced vortexes. Hoffstadt *et al.* [53] studied a concept of cylinder attached to a rigid structure by DEGs, which, through wind-induced turbulence, would vibrate and stretch the DEGs. Figure 1.16 shows the design of the vortex generator device. The experimental device was unable to generate the desired extension on the DEG, but the concept remains to be further

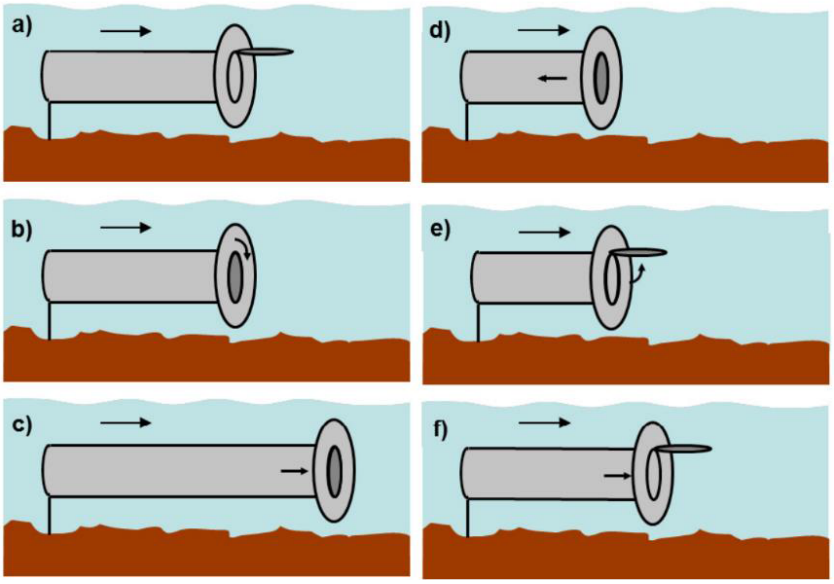

Figure 1.15: The flow energy converter cycle concept proposed by Graf and Maas (2012). a) Outer rigid ring close to flowing output, the tube is pre-stretched even with vale opened. b) The valve closes quickly. c) Due to a shock wave created by the fast closure, the tube is stretched to its maximum length and at this state charged. d) As the shock wave is reflected, a negative pressure inside the tube arises and induces a contraction to a stretch level smaller than initial pre-stretch. At this point, the discharge happens. e) The valve opens to allow the return to the initial state. f) The cycle is ready to start once again. Reproduced from [86].

explored.

Since DEGs work on cycles, another possibility of application is thermal machines, where cyclic processes are used to convert heat to mechanical energy. Thus, DEGs could be incorporated to directly transduce the mechanical movement, usually linear, to electrical energy. Studies using DEGs as chambers for internal combustion engines showed interesting concepts and apparently promising results [77], but no paper was published with details; this, therefore remains an interesting concept to be investigated. McKay *et al.* [98] experimented to substitute the power piston of a Stirling engine by a DEG and used a voice coil actuator to move the displacer piston. Figure 19 illustrates the design used. Through testing different temperatures and different DEG dimensions, they investigated the electrical energy output, being able to harvest energy from temperature differences as low as 19.5K, which are promising results for low-grade heat applications. On the other hand, the energy input required by the voice coil actuator was not measured and it was probably higher than the DEG output, showing the design would require another solution to be implemented.

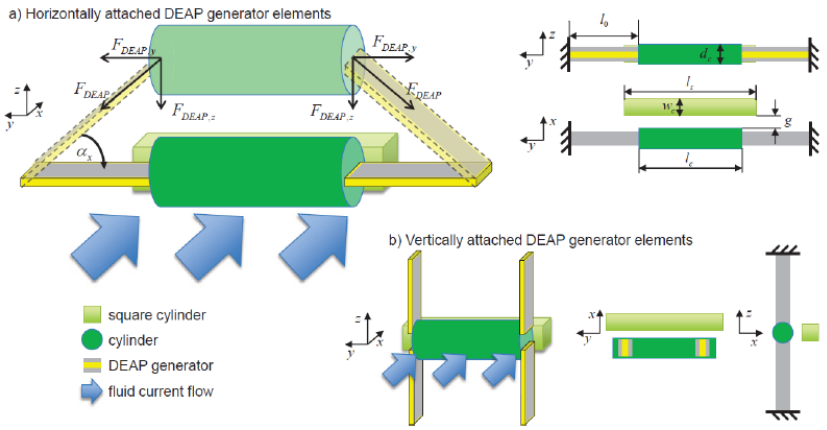

Figure 1.16: a) Vortex induced vibration energy harvesting concept by Hoffstadt *et al.*. Horizontal layout. b) Vertical layout variation. Reproduced from [53].

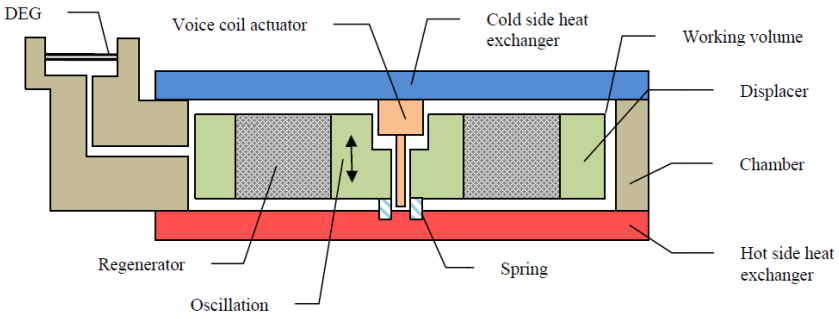

Figure 1.17: Section view of the Stirling engine coupled with a DEG. Reproduced from [98].

1.6 Thesis goals

While DEGs have a good potential for a range of real-world applications, presenting high energy density and low cost as major advantages for DEGs to perform both in small energy scavenging devices (e.g. human-motion applications) and in bigger power plants (e.g. wave energy conversion), they still have significant limitations, such as the requirement for priming at each cycle in order to enable their energy transducing capabilities. Additionally, DEs are multifunctional materials, thus, investigating their generator behaviour without considering their other working modes (sensing and actuation) is both a simplification and a negligence of their capabilities.

Moreover, for practical implementations, challenging conditions such as unpredictable loads, with varying amplitudes and frequencies present difficulties for the coordinate charge and discharge of DEGs, that must be aligned with them.

In this thesis, we will investigate the behaviour of DEGs to further understand when they might present more than one working mode, evaluating whether such behaviours are beneficial or not. Furthermore, we aim at exploiting this multimodal behaviour of DEs, in conjunction with other techniques and technologies associated with DEs, to design smart DEGs, able to self-regulate and self-manage.

1.7 Thesis structure

This thesis consists of 6 chapters organised as follows:

In Chapter 1, we explain the motivation for DEG study, how they are modelled, introduce the concept of energy harvesting cycle for DEGs and demonstrates some of their applications.

In Chapter 2, we will investigate the charging phase of a constant charges energy harvesting cycle, considering that the DE is subjected to an oscillating force/pressure instead of being constrained by a determined maximum/minimum stretch during the cycle. In this situation, we will show how the DEG acts in an actuator-like manner, having its deformation states affected not only by the external force but also by the electric field stored in it, an issue that is continued throughout the remainder of the thesis. We perform a novel investigation, analysing such effect, quantifying the energy conversion in a dissipative DEG during the charging phase.

In Chapter 3, we explore the concept of Self-Priming DEGs, a concept first developed by McKay *et al.* [92, 93] to promote the charging and discharging of DEGs autonomously and eliminate the need for a high-voltage priming source. We will discuss further this concept, extending previous work by developing, for the first time, the necessary models to analyse and design such systems from an electric circuit point of view, as well as presenting the experimental validation of those models.

In Chapter 4, we study the behaviour of Self-Priming DEGs through a novel approach, evaluating not only the electric characteristics, but also how their electromechanical coupling can affect their performance. We predict and verify experimentally that, under certain circumstances, the DEG might exhibit a self-stabilising behaviour, where its voltage, after some cycles, is bound to converge as an oscillation that is a steady limit cycle, for a designated mechanical excitation. We propose a methodology to predict such behaviour by modelling, demonstrate it for a simplified model, and propose a method to predict this behaviour in real-working systems.

In Chapter 5, we demonstrate an original method to integrate the sensing capabilities of DEs to DEGs, so that the latter are able to self-manage, detecting its ideal charging and discharging moments, as well as providing a tool for diagnostics that could be used to avoid failure modes.

In chapter 6, we conclude this thesis by detailing its achievements and providing guidelines for future work

1.8 Related publications

- P. ZANINI, G. RIZZELLO, S. SEELECKE, M. HOMER, AND J. ROSSITER, *Self-sensing for robust automatic charge management of dielectric elastomer generators*, in Proc. SPIE, Y. Bar-Cohen, ed., vol. 10594 (2018), p. 105941J.
- P. ZANINI, J. ROSSITER, AND M. HOMER, *Modelling the effect of actuator-like behavior in dielectric elastomer generators*, Applied Physics Letters, 107 (2015).
- P. ZANINI, J. ROSSITER, AND M. HOMER , *Modeling self-priming circuits for dielectric elastomer generators towards optimum voltage boost*, Proc. SPIE, 9798 (2016), p. 97980W.
- P. ZANINI, J. ROSSITER, AND M. HOMER , *Frequency-domain trade-offs for dielectric elastomer generators*, Proc. SPIE, 10163 (2017), p. 101631C.
- P. ZANINI, J. ROSSITER, AND M. HOMER , *Self-stabilizing dielectric elastomer generators*, Smart Materials and Structures, 26 (2017), p. 35037.

1.9 Summary

DEGs are an emerging technology for electromechanical energy conversion, with the potential to impact positively the way we generate electricity. As multimodal materials, we intend to explore their different modes to develop methods such that DEGs can be explored in a more reliable way in real-world scenarios.

CHAPTER 2

ACTUATOR-LIKE BEHAVIOUR IN DIELECTRIC ELASTOMER GENERATORS

In order to design applications for dielectric elastomer generators, a first step is to fully understand their behaviour. In this chapter, we seek to describe the influence of the electromechanical coupling in the charging and discharging phases, relating the electrical states (charge and voltage) to the mechanical ones (stretch and force). We initially describe a possible modelling approach that is able to display the dynamics we are interested in, and the energy harvesting cycle we use as a case study. Following that, we analyse how the manifestation of the electromechanical coupling can be seen, and quantify its influence regarding energy conversion during the charging phase. We conclude by analysing the effect on the discharging phase and comparing the overall impact of the actuation-like behaviour for the different charge schemes used. This chapter is based on the paper "Modelling the effect of actuator-like behavior in dielectric elastomer generators" [153]

2.1 Introduction

In contrast to more traditional capacitive energy harvesting methods, that use mechanisms such as parallel plates varying in distance or sliding in plane to promote capacitance change [11], DEGs are composite materials with embedded electrodes and an intrinsic mechanism for position restoring, not needing spring-like elements to be added to promote the return to its initial state. In addition, the compliance of DEs makes them non-linear capacitors: as charges are stored, electrostatic forces are generated, deforming the material and increasing its capacitance, thus allowing further charges to flow into the DE. Such non-linear behaviour resulting from the electromechanical coupling can have particular influence over the charging, and discharging

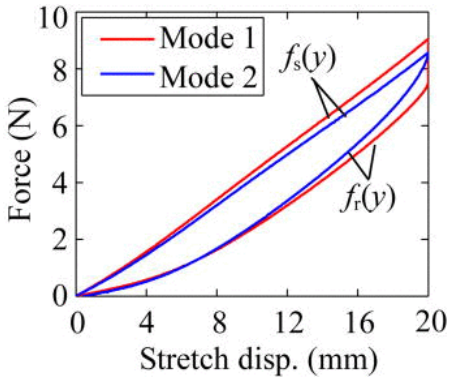

Figure 2.1: Force as a function of displacement for a DEG under two different charging modes in a position based cycle. Reproduced from [144].

of DEs, directly affecting their performance and affecting their efficiency, thus the need to investigate it further.

Designing DEAs, one typically maximises the change in either force or deformation as a consequence of electrically charging the elastomer. When using DEs as generators, on the other hand, one does not seek a force change or additional deformation due to the electrical state, but such effects still manifest themselves due to the nature of the material. The aforementioned effect can be designated as the actuation-like effect of DEGs [153]. The actuation-like effect can be visualised in different manners depending on the mechanical system layout, and how charging or discharging is performed in the chosen energy harvesting cycle.

When designing and modelling DEGs, we split the mechanical system layout into two categories: position-based or force-based cycling. Position-based cycling corresponds to mechanical systems such as cranked mechanisms, where the strain cycle is fixed [45]. Force-based cycling more accurately emulates natural phenomena such as waves and wind gusts, from which we may wish to harvest renewable energy. In these phenomena, a pressure or force variation acts against the material and strain is not mechanically constrained.

Regarding position-based cycles, an increase in the electric field (due to charging) in the DEG will lead to a decrease in the force necessary to keep that fixed stretch state since the electrostatic force acting normally on the membrane will contribute towards the DE's planar expansion. Several examples can be found in literature, since a simple crank-slide mechanism or servomotors can be used to stretch the elastomer and perform experiments: in [144], two different energy harvesting scenarios are compared, one consisting of charging the DEG briefly after it reaches its maximum deformation (mode 1) and another that charges the DEG with constant voltage while it stretches (mode 2). Analysing the results presented in [144], illustrated

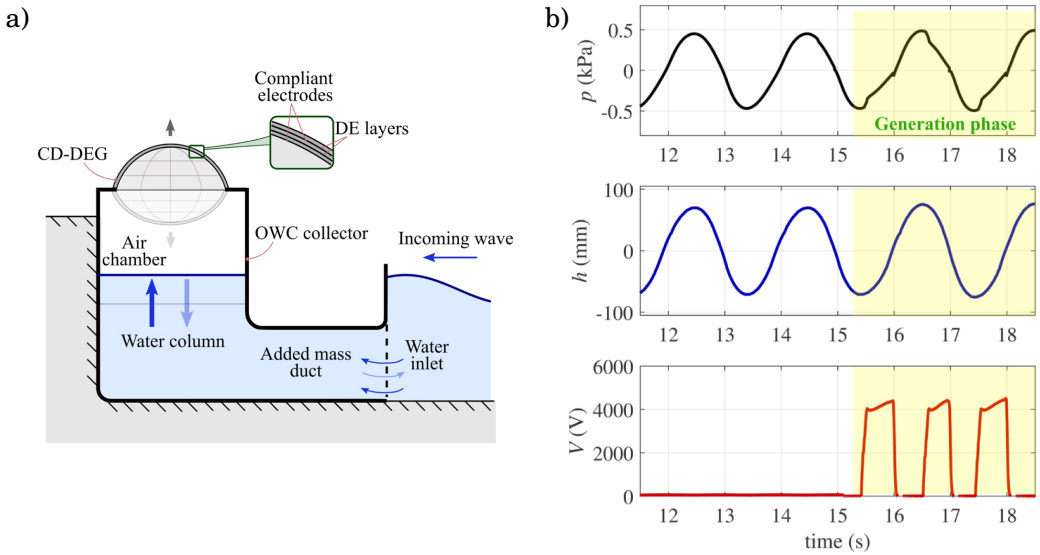

Figure 2.2: DEG based wave generator scheme(a). Pressure inside the air chamber (black), height of the deformed DEG (blue) and voltage applied to the DEG (red) (b) . Adapted from [104].

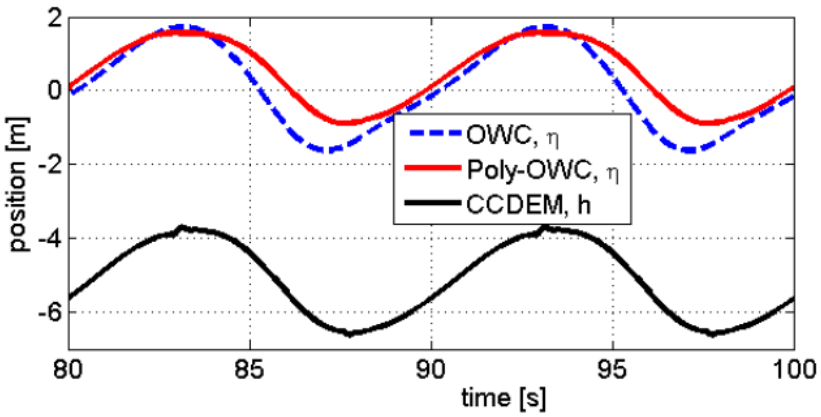

Figure 2.3: Force as a function of displacement for a DEG under two different charging modes in a position based cycle. Reproduced from [140].

in Figure 2.1, one can notice that the force necessary to deform the DEG to its maximal stretch in mode 1 is higher (since the electrostatic forces are already present in the charge-while-stretching mode 2), and drops when the DEG reaches its maximum stretch, when it is supposedly charged. Another example [104] presents experimental results from a proposed design of a wave energy generator, as shown in Figure 2.2. It can be noticed that while keeping a controlled (sinusoidal) displacement of the elastomer, the pressure that acts towards that deformation would decrease in modulus when the material is charged. Similarly, when we consider a force-based scenario, an increase in the electrostatic forces due to charging will sum with the fixed force and increase the stretch. The literature also contains other examples of the actuator-like effect: considering a force-based cycle represented by a controlled oscillating pressure from waves (sinusoidal pressure input) acting on a DEG wave energy generator [140], the simulation results present an increase in deformation (displacement of the tip of the inflating membrane) when the DEG is charged, as shown in Figure 2.3.

Many studies have previously investigated energy harvesting cycles [51, 57, 130, 140, 144] but the actuation-like effect is either neglected in the modelling work [51], or is present in the results but little discussed [57, 130, 140, 144]. In [130], an optimised cycle is proposed and its experimental results show that, after charge, the force in the DEG is reduced (as expected for position-based cycles), which is pointed out to be a consequence of the charges in the membrane and the viscoelastic relaxation. In [140] the sharp stress variations for the membrane of the simulated DE are pointed as a result of the activation and deactivation of the electric field for the proposed cycle. Using the results reported in [144], shown in Figure 2.1 one can see that when the cycle contains a fast charging process (rise in voltage due to a connection being made, e.g. using a switch), it leads to a quick decrease in the elastic force on the membrane, as in mode 1. When the material is stretched under a constant voltage condition, as in mode 2, its stiffness reduces and the necessary force to perform the stretching process decreases. Similarly [57] uses a cycle alternating between a lower voltage power supply for the stretch phase and a higher voltage capacitor, as shown in Figure 2.4, which acts as a constant high voltage charge reservoir. Since charge and discharge are performed in such constant voltage conditions, we can see in Figure 2.4 that the DE becomes softer than when it is disconnected from the voltage sources, as expected.

Since energy harvested is (at least initially) proportional to the electrical energy input bias during charging, energy harvesting capabilities are thought to increase with the use of higher electric fields [47]. On the other hand, as the electric field is increased towards material limits, the charge-induced actuation will be an increasingly important issue, which must be taken into account in any realistic energy harvesting cycle. In particular, the actuation-like effect will be more pronounced in soft materials, such as the ones sought for actuators [16, 34, 110], which are commonly used for DEGs.

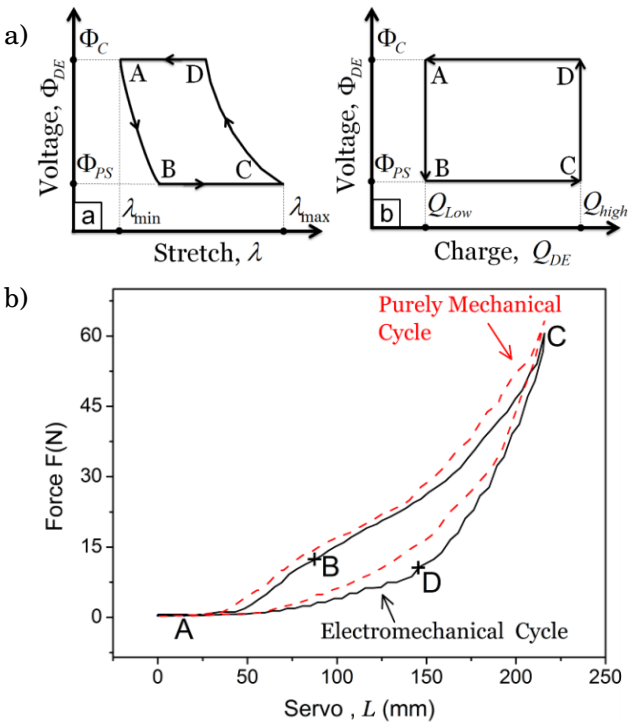

Figure 2.4: (a) Energy harvesting cycle charging DEG while stretching under constant voltage and discharging in reservoir capacitor at a higher voltage. From [57]. (b) Force as a function of servo displacement L for the DEG cycle (solid black curve), the DEG cycle with another DE sample without connecting to the power supply (dashed red curve). Adapted from [57].

This chapter seeks both to report the phenomenon of charge-induced actuation, focusing on force-based scenarios, and to understand how to deal with it, through comparisons of energy input, conversion and losses. The Section 2.2 will describe and explain the model and cycle chosen to illustrate the phenomenon, as well as the simulation techniques used. Following that, in Section 2.3, we will describe and analyse the results obtained in the simulations performed, comparing two different scenarios and quantifying the energy conversions from the electrical and mechanical points of view, in the processes of charging and discharging the DEG. Finally, Section 2.4 concludes the chapter by summarising the results discussed in the previous sections and analysing how they impact DEG applications.

2.2 Methods

First, in order to investigate the actuation-like effect in DEGs, we chose as a case study a classical constant charge energy harvesting cycle [47], which has been widely used [32, 67, 81, 82, 102] due to its simplicity to illustrate the energy conversion process in DEGs. To evaluate the actuation during the charging phase, we compare two different methods to move from the

stretched and uncharged state to the stretched and charged state. Both are illustrated in Figure 2.5, and involve the transition from quasi-equilibrium state 2 (stretched and uncharged) to a quasi-equilibrium at state 3 (stretched and charged with bias voltage) via different intermediate states. Note that we denote those states as quasi-equilibrium since they are still dependent on dynamical effects, such as creep and stress relaxation. Thus, a stationary load state and infinite time would both be necessary to reach a true equilibrium when viscoelastic effects settle.

The first method (mode A), instantaneously injects sufficient charge at state 2 to elevate the bias electric field to state 2.5'. The electrical supply is then disconnected. The DEG then undergoes actuation due the reduction in stiffness resulting of this induced electric field while planar stress, moving it to state 3, with decreasing electric field and voltage as capacitance increases in open-circuit conditions. Such a method emulates an instantaneous charge when the DEG is receiving its maximal deforming pressure and close to its maximal capacitance, as prescribed for a constant charge cycle [47]. In the second method (mode B), a voltage, equal to the one achieved during state 3 for mode A, is instantaneously applied at state 2, which raises the electric field to state 2.5''. The DEG then undergoes a similar actuation process, as a result of the charges, but this time constrained to the constant voltage supplied. Electric field and strain both increase, as charges from the power supply flow to the DEG as its capacitance increases, until state 3 is reached. Mode B was chosen such that it has a similar implementation to mode A, using the same circuit, only differing by the voltage level on the priming source and time interval the DEG is exposed to its priming voltage. In order to compare the different modes, the applied voltage in Mode B is chosen such that the equilibrium in state 3 exactly matches that for mode A. Having the same state 3 for both methods guarantees that all remaining characteristics of the cycle are identical.

The charging/discharging circuit is shown in Figure 2.6. At the start of the cycle, both S1 and S2 are open. At the end of the stretching phase, S1 is closed and the material is allowed to charge. For mode A, S1 is reopened as soon as state 2.5' is reached. For mode B, S1 is reopened when equilibrium (state 3) is reached. At the end of the relaxing phase (state 4), S2 is closed to allow the discharge of the energy output.

The resulting voltage versus charge plot can be visualised in Figure 2.7. The electrical energy input that is stored in the DEG is computed as the area under the curve from state 2 to state 3, while the electrical energy output is computed by the area under the curve from state 4 to state 1. Note that the total energy used as input, when keeping the power supply at constant voltage V, to charge a capacitor from 0V to V is still VQ, while, on the other hand, only $VQ/2$ will be stored. Such mechanism is the main source of losses for the charging process here utilised. The area inside the plots shown in Figure 2.7 represents the energy output of a cycle.

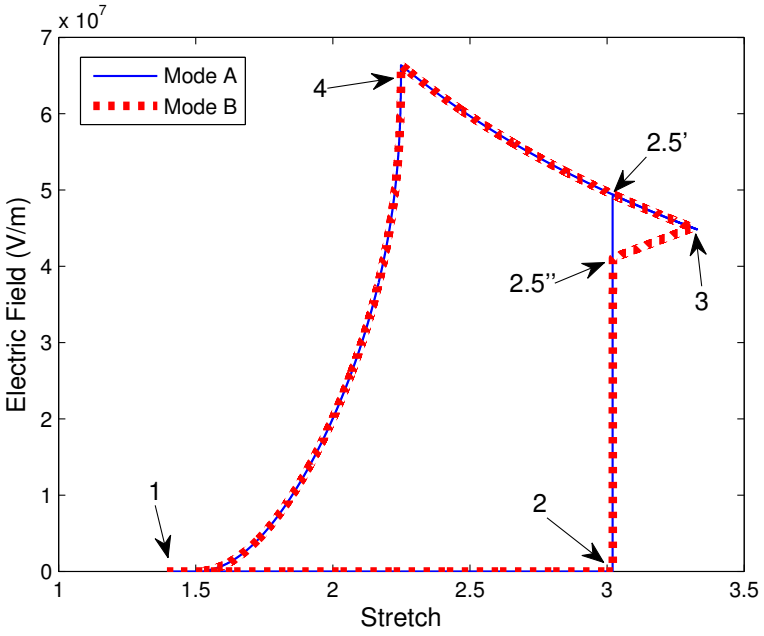

Figure 2.5: Electric field versus stretch ratio of the DEG, for both charging modes.

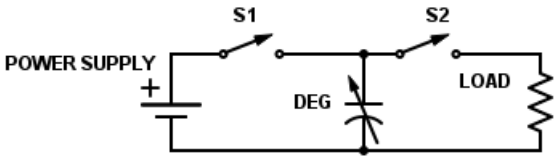

Figure 2.6: DEG circuit: S1 allows the DEG to charge under constant voltage, while S2 discharges the DEG through a constant load.

In order to couple the charging modes with the electromechanical model of a DEG, a common method is to consider equilibrium states of a harvesting cycle [44, 130, 135]. Here we developed a simulation model based on Graf et al [44], applied to a uniaxially deformed material under pure-shear conditions, as shown in Figure 2.8. To be able to visualise the desired phenomenon, we consider a model able to express the viscous and hyperelastic behaviour of DEGs. Following the approach of [44], we consider a Neo-Hookean hyperelastic material model and a linear damper with a constant damping coefficient d_v, as in eq. (1.44). The pure shear configuration, an approximation of a uniaxial stretch with either constrained width or where the dimensions of the DE being stretched satisfied $y \gg x$, means we will consider

$$\lambda_y = \lambda_{y_0}, \tag{2.1}$$

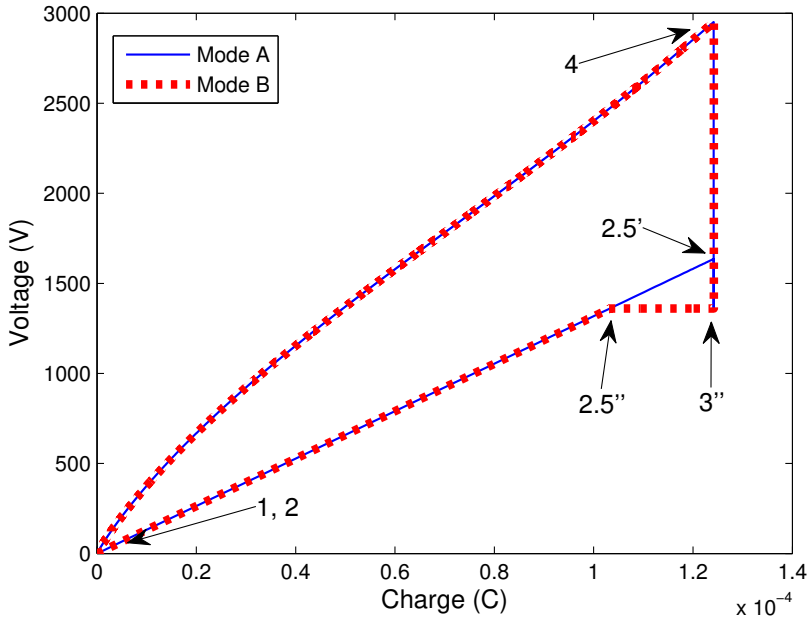

Figure 2.7: Voltage versus charge plot for the DEG. Area demarcated by the triangle 2.5'-2.5''-3 indicates the extra electrical work done by the mode A over mode B

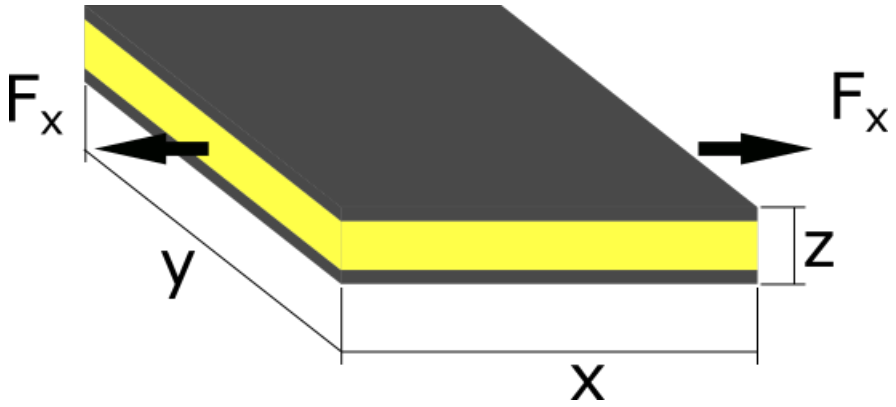

Figure 2.8: Scheme of the DEG under uni-axial stretch and its coordinated axis for the implemented model

where $\lambda = l/l_0$ is the stretch ratio, defined as the ratio between the length of the deformed body, l and its undeformed length l_0. Since the material incompressibility states that

$$\lambda_x \lambda_y \lambda_z = 1, \tag{2.2}$$

and the deformation is bounded in the y-direction eq. (2.1), in another dimension, the model is reduced to one degree of freedom, directly linking the stretch in the x-direction, to the change in

material thickness, λ_x. If we consider an initial state with no deformation, $\lambda_{x_0} = \lambda_{y_0} = \lambda_{z_0} = 1$, we can state that

$$\lambda_z = {\lambda_x}^{-1}. \tag{2.3}$$

Thus, following the approach described in [44], for a Neo-Hookean model, we can calculate the material stress due to the elastic forces in the direction of the uniaxial force applied, σ_x, as

$$\sigma_x = G\frac{\lambda_x^4 - 1}{\lambda_x^2} + \sigma_z, \tag{2.4}$$

where G is the shear modulus and σ_z the stress in the z direction.

Applying Newton's 2nd law of motion, we have that

$$F_x - F_v - F_{el} = m\ddot{x}, \tag{2.5}$$

where m is the equivalent mass, F_x is the force being directly applied to the material in order to deform it (in the x-direction by model definitions above), x the length of the deformed material in the pull direction. The equivalent force caused by the viscous damping of the material is defined as

$$F_v = d_v\dot{x}, \tag{2.6}$$

and F_{el} the elastic restoring force, is defined as

$$F_{el} = \frac{B}{x}\sigma_x, \tag{2.7}$$

a function of the ratio between the normal area to the x direction (defined by B/x, where B is the material volume) and the material stress from eq. (2.4)

The applied stress normal to the dielectric elastomer electrode area due to the electrostatic forces, σ_z, is given by

$$\sigma_z = -e_r e_0\left(\frac{V}{z}\right)^2 = -e_r e_0\left(\frac{V}{z_0}\right)^2\lambda_x^2 \tag{2.8}$$

where e_r is the material relative permittivity, $e_0 = 8.85 \times 10^{-12}$ the vacuum permittivity, V the applied voltage, and z_0 the initial thickness. The charge stored, Q, and the capacitance, C, are included via the standard relationship

$$V = Q/C \tag{2.9}$$

To find equilibria, we consider $\ddot{x} = \dot{x} = 0$, and combine eq. (2.4), eq. (2.7) and eq. (2.8) into eq. (2.5), yielding

$$F_x = \frac{B}{x_0^2}\left(G - e_r e_0 \left(\frac{V}{z_0}\right)^2\right)x - BG\frac{x_0^2}{x^3} \tag{2.10}$$

which, with eq. (2.9), allows us to prescribe independently any two of the four states (x,V,Q,F_x) and determine the remaining ones if a steady state exists.

In order to evaluate the electrical and viscous losses for both charging modes, we impose a sinusoidal mechanical forcing at 1Hz. This simulates the DEG deformation in a device applied to a real scenario such as wave energy harvesting or a human walking. The shear modulus used was 73 kPa, based on a reduction to order 1 of the Ogden model parameters derived by Wissler and Mazza [148] for 3M VHB 4910, which is consistent with data obtained in a similar approach from [111]. The DEG sample we considered had an initial area of 0.02m^2 and was 0.1mm thick, with an initial capacitance of 8.3nF. The damping coefficient d_v, proposed in the model [43], was chosen as d_v = 0.8Ns/m such that it matches the step response timescale shown for VHB 4910 in [20]. The DEG electric model considers a variable capacitor with no leakage and a 500Ω series resistance, to emulate the electrodes, matching a thick (1-2mm range) hand-painted carbon grease electrode with 100Ωcm resistivity [6] or a 100nm single-walled carbon nanotube electrode with 0.5kΩ/□ [122]. Electrical dissipation is then calculated as the dissipated energy through the electrode, which is assumed as the series resistance specified, during the charging/discharging processes. We estimated the electric energy input in the simulations by

$$\int_{Q_1}^{Q_2} V dq. \tag{2.11}$$

The dissipated electric energy was estimated by

$$\int_{t_1}^{t_2} R_e I dt, \tag{2.12}$$

where I is current through the electrodes, R_e is the series resistance and t is the time. The external mechanical work was calculated by

$$\int_{x_1}^{x_2} F dx, \tag{2.13}$$

where F is the external loading force and x is the length of the DEG. The damped mechanical energy is calculated by

$$\int_{x_1}^{x_2} d_v \dot{x} dx, \tag{2.14}$$

where $\dot{x}$ is the rate of change in length of the DEG, thus $d_v\dot{x}$ is the viscoelastic force in the proposed model. The strain energy is calculated using the Neo-Hookean model formulation

proposed in eq. (1.31), and its variation calculated by a simple difference. Additionally, we compute the actuation energy, the electromechanical energy converted, by considering the work performed by the electrostatic forces, σ_z as shown in eq. (2.8):

$$\int_{z_1}^{z_2} \sigma_z A dz, \tag{2.15}$$

where z is the DEG thickness and A the DEG normal area.

2.3 Results and discussion

2.3.1 Charging — Electrical point of view

Considering the viscous nature of most DEs, it is reasonable to assume that the charging and discharging processes occur much faster than the mechanical deformations due to the electrostatic forces, especially since in its manufacture, low resistance electrodes are an important aspect. This can be visualised in Figure 2.9, particularly when comparing Figure 2.9a with Figure 2.9b and Figure 2.9c. We can see that the charging happening at $t = 0.5$s, correspondent to phase 2–2.5'or 2–2.5'', can be considered instantaneous compared to the corresponding deformation process that follows, between 2.5'/2.5''and 3. The consequence of such behaviour is shown in Figure 2.7, which allows us to visualise mode A (blue continuous line): after state 2, charging occurs instantaneously under constant capacitance, leading to the unstable state 2.5', which then relaxes and approaches equilibrium at stage 3 again.

In Figure 2.9b, we show the evolution of voltage as a function of time, for both charging modes, as the DEG undergoes a 1 Hz sinusoidal forcing between 1.5N and 4.5N, shown in Figure 2.9d. As can be also seen on Figure 2.9c, state 2 occurs just before the bias voltage is applied, while state 3 takes place when the charging phase on mode B (dotted red line) ends, corresponding to a close match in the amount of charge and approximately the same voltage (at around $t = 0.58$s).

Note that although the curves approximately converge to the quasi-equilibrium state 3, they do not match perfectly at this point, since the model used is dynamic, and it is not possible to reach an equilibrium (in a smooth system) in a finite time; a step forcing with the maximum force being constant during an infinite time would be required to achieve the equilibrium state. However, the two trajectories do converge quickly during the transition 3–4, since the charges in the DEG are designed to be the same at the start of stage 3, and then proceed to the same state 4, of maximum voltage when the force is minimum, prior to discharge, outputting the same amount of energy. Notice that time taken for the trajectories to converge at state 3 depends on the material viscosity and the magnitude and frequency of the electrical and mechanical loads applied; the values here chosen mean that the differences in independent variables in state 4 are essentially zero.

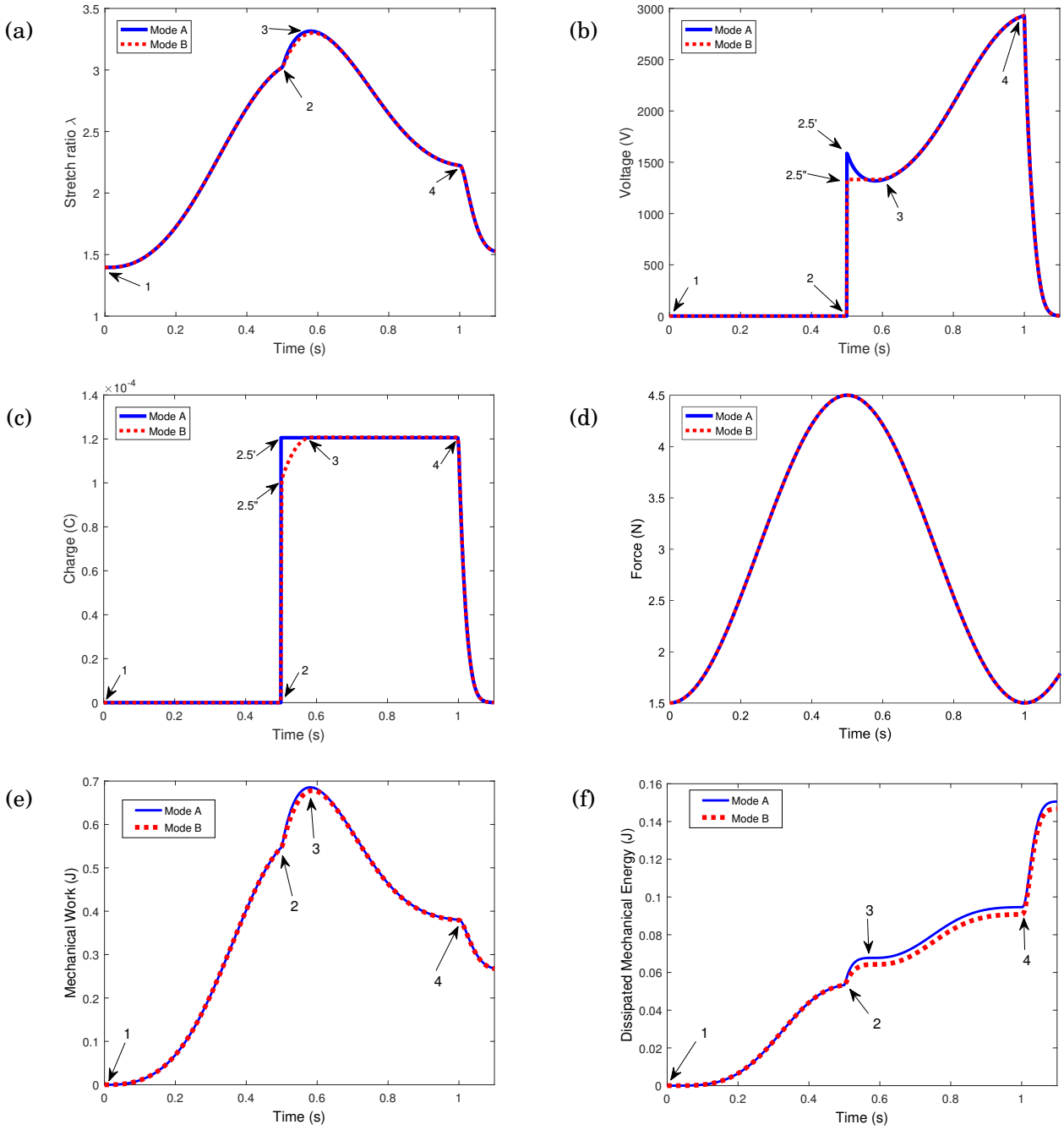

Figure 2.9: (a) Stretch ratio versus time plot for the DEG. (b) Voltage versus time plot for the DEG. (c) Charge ratio versus time plot for the DEG. (d) Mechanical force applied versus time plot for the DEG. (e) External mechanical work versus time plot for the DEG. (f) Dissipated mechanical energy through viscoelasticity versus time plot for the DEG. In all cases, mode A is shown as a solid blue line, mode B as a dashed red line.

When charging a capacitor, with constant capacitance, to a voltage V, in order to store a charge Q it is necessary to expend an amount of energy VQ, although only $VQ/2$ is stored [144]. Hence, when charging with constant capacitance, there is an implicit loss of 50% of the electric energy input. Wang *et al*. [144] suggest that to guarantee that energy will be harvested in a cycle, it is necessary that the capacitance of the charging state should be at least twice the capacitance of the discharging state. On the other hand, when charging with constant voltage, we have a change in energy U_e of

$$U_e = \int_{Q_1}^{Q_2} V\,dq = V(Q_2 - Q_1) \tag{2.16}$$

Since half this energy is stored, as before, the other half is converted to mechanical work, as described for actuator behaviour by Carpi *et al*. [19].

From Figure 2.7 it is easy to see how high the losses can be while charging in mode A compared to mode B. In mode B, the charging can be divided into two phases: the first, from uncharged to voltage $V_{2.5"}$ and charge $Q_{2.5"}$, followed by the second, under constant voltage, to voltage $V_3 = V_{2.5"}$ and charge Q_3. The area below the curves in Figure 2.7 shows the amount of energy expended in charging. In particular, the triangle between the points 2.5', 2.5"and 3 corresponds to the extra electrical work done – energy spent for charging – in mode A.

We compare both charging energies, calculated by direct simulation, in table 2.1. In order to have 85mJ electric energy stored in state 3, it is necessary to input 190 mJ electric energy using mode A, but only 160mJ using mode B (for the same stored energy). The electric energy dissipated in this process corresponds to the 50% lost during capacitor charging, together with losses in the resistive elements (e.g. electrodes).

Table 2.1: Electrical energy balance during process 2-3 comparing charging modes A and B.

		Mode A	Mode B
a	Electric Energy Input at 2.5'/2.5"	0.190 J	0.131 J
b	Electric Energy Input 2.5'/2.5"-3	0 J	0.029 J
c	Total Electric Energy input 2-3 (a+b)	0.190 J	0.160 J
d	Electric Energy Dissipated 2-3	(0.088) J	(0.061) J
e	Actuation Energy (electrical to mechanical conversion) 2-3	(0.017) J	(0.014) J
f	Electric Energy Stored at 3 (c+d+e)	0.085 J	0.085 J

Table 2.2: Mechanical energy balance during process 2-3 comparing charging modes A and B.

		Mode A	Mode B
g	External Mechanical Work 2-3	0.138 J	0.130J
h	Mechanical Energy Damped 2-3	(0.014) J	(0.011) J
i	Actuation Energy (electrical to mechanical conversion) 2-3	0.017 J	0.014 J
j	Strain Energy change 2-3 (g+h+i)	0.141 J	0.133 J

2.3.2 Charging — Mechanical point of view

Given the electromechanical coupling in the material, it is necessary also to analyse the energy conversion and the losses from a mechanical point of view. It is important to notice that, to create a comparable scenario, the mechanical input is the same for both, as shown in Figure 2.9d. The slight difference in state 3 stretch ratio between modes A and B (λ_x = 3.33 and λ_x = 3.31 respectively), which can be seen in Figure 2.9a, is due to the fact that the model is dynamic, and equilibrium is not achieved in a finite time, as described above. This causes slightly different interactions between the two states 2.5'and 2.5''and the sinusoidal forcing. The actuation force on mode A is stronger (since it has 100% of the charges loaded at state 2.5') and closer to the peak of the external forcing, thus slightly increasing actuation strain. However, the material is still charged to the same level as mode B at state 3 and, past this point, mechanical parameters converge to the same state 4 in advance of the discharge phase.

As the DEG is charged under external forcing, this external force will also act on part of the deformation, therefore generating mechanical work. We term this External Mechanical Work during process 2-3, shown in Table 2.2 (row g). Thus, the slightly higher external work applied in mode A is a consequence of the higher stretch. On the other hand, this higher external work is recovered when the material is relaxed, as can be seen in Figure 2.9e, when the curves diverge at approximately 0.55s but converge after a further approximately t = 0.05s. This is because the extra work done, as a consequence of the larger displacement, is stored as elastic energy. Thus the difference in strain energy and external work, 3mJ, is equal for both modes.

In contrast, the difference between the total work done, necessary to store strain energy and overcome viscous losses, corresponds to the actuation energy shown in Table 2.1 (row e) and Table 2.2 (row i). For mode B, the actuation energy corresponds to 14 mJ, half of the electrical energy input under constant voltage, matching previous studies [19]. The difference in actuation between mode A and mode B comes from the higher actuation forces imposed in mode A, when the charging is quicker and Maxwell stresses are applied more abruptly. Hence, the material

imposes higher damping in mode A (seen on Figure 2.9f), which is translated into the difference of about 30% in viscous losses, with the same magnitude of actuation force.

2.3.2.1 Parameter variation - viscous behaviour

To access the effect of the viscous behaviour of the material in the actuator-like effect, using the same conditions, we simulated the scenario increasing d_v by 50%. Calling the previous results scenario 1, the results of scenario 2, with higher viscous behaviour, can be seen in Table 2.3 and 2.4. Note that, different from scenario 1, mode A and B, in this case, do not reach the same states 3 and 4 in scenario 2, which have the input voltage designed to match based on the actuation level in scenario 1. Consequently, the correct comparison for the data shown in scenario 2 is with the same mode in scenario 1.

As a result of the higher viscous force, the stretch ratio obtained for modes A and B was inferior, 3.24 and 3.22 respectively. Thus, having inferior capacitance, the amount of energy stored and the amount of energy used as input was smaller than previously. The actuation energy reduced as well, in line with the smaller input of electric energy. While in scenario 1, state 3 was reached about 0.08s from the middle of the forcing cycle, in scenario 2, it happens in 0.10s. This higher interval of time, explains the higher external mechanical work for mode B in scenario 2 when compared to scenario 1, since it provides a longer integration interval in the computation.

Table 2.3: Electrical energy balance during process 2-3 comparing charging modes A and B for $d_v = 1.2 Ns/m$.

		Mode A	Mode B
a	Electric Energy Input at 2.5'/2.5"	0.178 J	0.125 J
b	Electric Energy Input 2.5'/2.5"-3	0 J	0.027 J
c	Total Electric Energy input 2-3 (a+b)	0.178 J	0.152 J
d	Electric Energy Dissipated 2-3	(0.089) J	(0.062) J
e	Actuation Energy (electrical to mechanical conversion) 2-3	(0.016) J	(0.013) J
f	Electric Energy Stored at 3 (c+d+e)	0.073 J	0.077 J

2.3.2.2 Parameter variation - series resistance

In scenario 3, we kept the same original value of d_v and increase the value of the series resistance to 5kΩ. Note that it strongly affects the charging speed, but, to analyse the issues that such a change could represent, which could be due to a damaged electrode, the switch timings were kept the same as in scenario 1.

Table 2.4: Mechanical energy balance during process 2-3 comparing charging modes A and B for $d_v = 1.2Ns/m$.

		Mode A	Mode B
g	External Mechanical Work 2-3	0.135 J	0.131J
h	Mechanical Energy Damped 2-3	(0.016) J	(0.013) J
i	Actuation Energy (electrical to mechanical conversion) 2-3	0.016 J	0.013 J
j	Strain Energy change 2-3 (g+h+i)	0.135 J	0.131 J

Table 2.5: Electrical energy balance during process 2-3 comparing charging modes A and B for series resistance of 5kΩ.

		Mode A	Mode B
a	Electric Energy Input at 2.5'/2.5"	0.140 J	0.135 J
b	Electric Energy Input 2.5'/2.5"-3	0 J	0.026 J
c	Total Electric Energy input 2-3 (a+b)	0.140 J	0.161 J
d	Electric Energy Dissipated 2-3	(0.089) J	(0.067) J
e	Actuation Energy (electrical to mechanical conversion) 2-3	(0.006) J	(0.013) J
f	Electric Energy Stored at 3 (c+d+e)	0.045 J	0.081 J

Table 2.6: Mechanical energy balance during process 2-3 comparing charging modes A and B for series resistance of 5kΩ.

		Mode A	Mode B
g	External Mechanical Work 2-3	0.082 J	0.124J
h	Mechanical Energy Damped 2-3	(0.005) J	(0.010) J
i	Actuation Energy (electrical to mechanical conversion) 2-3	0.006 J	0.013 J
j	Strain Energy change 2-3 (g+h+i)	0.083 J	0.127 J

Since the charging interval was kept the same as in scenario 1, and, due to higher series resistance, current levels are smaller, charge is incomplete for mode A, the DEG does not achieve the same voltage as the power supply that charges it. As such, in mode A, we have a higher losses to input ratio in the electrical energy side, since the highest current, when losses are higher, happens mostly in the beginning of the charging. Such issue highlight the need for an adequate method to adjust charging time in DEGs.

In mode B, charge during phase 2-2.5"represents a higher portion of the whole charging interval, since it happens slower. Consequently, we have higher electrical losses, since this is the charging phase with higher losses.

2.3.3 Discharging and overall cycle analysis

Such effect of the electromechanical coupling can be also visualised clearly in the discharge phase. Comparing Figures 2.9a and 2.9d, it is clear that, for the same minimum force 1.5N, state 1 has a lower stretch ratio than state 4 ($\lambda = 1.39$ and $\lambda = 2.24$ respectively). Such a difference, again, can be accounted by the electrostatic pressure from the charges in the material, as suggested by Figure 2.5. Since the electric field in the DEG rises during the relaxing phase (between states 3 and 4), the electrostatic forces also increase, thus explaining why the difference in stretch with the material charged and discharged (respectively states 4 and 1) is higher than that seen during the charging phase (between states 2 and 3). Once the material is discharged, stretch levels return to those caused solely by the mechanical forcing. This process presents a number of variables, from the electromechanical coupling as analysed for the charging effect, to more complex ones, as the type of load into which the DEG is discharged. Moreover, clever design techniques, such as the one shown in Figure 2.2, using the right pre-stretch level in the membrane and no movement bias direction can reduce this effect in the discharge phase, ensuring the DEG returns to its resting geometry.

For our current example, seeking to highlight solely the electromechanical coupling, the discharge is made through a 500kΩ resistance. Since the output through a resistance can be seen as a resistive voltage divider configuration, the use of resistance 1000 times higher than the associated series resistance from the DEG (500Ω), limits the current and guarantees most of the energy output will be dissipated through the resistor, instead of the electrodes. As a consequence, discharge happens as a slower process; it can be seen in Figure 2.7 that there is not a straight line between states 4 and 1, since the capacitance changes significantly during the process. This also means that more energy can be harvested through this process, as the capacitance decreases along with the reduction of the electrostatic pressure due to the discharge process. The timescale is dependent on both the viscous behaviour of the DEG and the type of load chosen, as discussed in [37] for a different cycle scheme.

It is interesting to notice that, as the actuation-like behaviour becomes more evident (either using materials that are softer and have higher dielectric permittivity or using higher electric field), the stretch ratio in state 4 will be higher, meaning the DEG will relax less. Thus, the useful capacitance swing, that between the charge and discharge phase, would then be reduced, and could create a potential limit for the energy harvesting capabilities of the material. Here the electrical energy output was 197 mJ for the total cycle (whether in mode A or B), compared with a

total energy input of 190 mJ for mode A and 160 mJ for mode B (shown in table 2.1 (row c)). Thus, for mode A, only 7 mJ of energy was harvested, while mode B harvested 37 mJ. The difference arises entirely in process 2-3, principally due to smaller electrical losses (90% of the difference), but also as a result of reduced viscous losses (10% of the difference).

2.4 Conclusion

In conclusion, we have demonstrated that the implicit actuation behaviour of DEGs can significantly affect the energy harvesting cycle, and this effect should be taken into account as part of any generator design process. One method to reduce these detrimental effects is to charge under constant voltage during this actuation phase, as shown, but, ideally, one would want to control the charging to achieve a smoother curve between states 2 and 3, instead of discontinuity points such as states 2.5'and 2.5'', used here for conceptual demonstration of the ideas. This controlled charging process could potentially be achieved through current limitation and more complex charging control, which are not trivial. The actuation-like behaviour reported can be also seen in, and impact on, the discharge phase, but will be highly dependent on the type of circuit used to extract the energy from the DEG. Theoretically, it might create a limitation for the amount of energy that can be harvested, which will be further discussed in Chapter 4 of this thesis, where we investigate the effects of the electromechanical coupling in DEGs associated with self-priming circuits. Bearing in mind the special attention that the charging and discharging phases of DEGs require, in the following chapters of this thesis, we will investigate further how to control such phases in real-world implementations.

CHAPTER 3

MODELLING SELF-PRIMING DIELECTRIC ELASTOMER GENERATORS

As stated in the previous chapter, the charging process represents a major issue for Dielectric Elastomer Generators (DEGs), since it has a significant potential to provide losses for the system. Furthermore, the charging of DEGs is also challenging from a practical point of view, requiring high voltage to promote high energy output, and proper timing coordination to exploit the maximum capacitance swing. In order to simplify the implementation of DEGs high-voltage priming and the need to accurately time the charging and discharging, the implementation of self-priming circuits (SPCs) for DEGs has been proposed [93]. Such circuits allow for passive management of the charging and discharging of DEGs and only require a low voltage priming to start the system. Despite the various contributions and developments made to improve such SPCs, until 2016 the only proposed method to simulate it was through the use of electronic circuit simulators that apply numerical methods (e.g., LTSpice) [94], and their design rules have been obtained from intuitive observation of simulation results and lack a solid theoretical foundation [96].

Instead, this chapter reports the development of a new analytical mathematical model that allows the description of basic DEG-SPC systems, and the clear deduction of their design rules from a physics-based model. This chapter also presents the expansion of this model to the Integrated Self-Priming Circuit (ISPC), a different SPC-DEG layout, including the modelling of charge leakage, so that their performance can be analysed in a non-ideal situation, as found in the experimental setup used for the model validation. The ISPC modelling here presented is part of an ongoing collaboration with the University of Auckland, as described in detail in this chapter body. This chapter is partially based on our paper “Modeling self-priming circuits for dielectric

elastomer generators towards optimum voltage boost" [154].

3.1 Introduction

As demonstrated in Chapter 2, the way one charges and discharges a DEG will affect the cycle energy gain. Particularly, when looking at how to perform the charging in practice, the issue seems even more relevant. The charging phase timing is usually linked to the maximum capacitance of a DEG in a cycle, either marking its theoretical ideal moment [47], the reference for the charging window [46, 51, 130] or when charging should end [144, 155]. Similarly, the same timing issue can be expanded to the discharge phase and the moment the DEG achieves its minimum capacitance in a cycle. In addition, in DEG energy harvesting cycles, the electrical energy output is generally proportional to the electrical energy input used to prime it during a cycle, since the energy conversion happens when the restoring forces from the stretched material displace these charges, as explained in section 1.4. As a consequence, one seeks to prime the DEG with high voltages in each cycle in order to maximise its output. On the other hand, such charging typically relies on the use of bulky boost converters [84] and an active control system to manage the timing of charging and discharging has to be implemented. If we consider applications where we intend to make the energy harvesting system more compact, the increasing level of complexity these additional accessories provide might jeopardise real-world implementation of DEGs.

To promote passive energy harvesting through DEGs, a common circuit configuration relies on the use of capacitors and diodes, such as the one used by Koh *et al.* [147], shown in Figure 3.1. As the DEG expands, and its voltage decreases to the level Φ_L, from the low voltage capacitor C_{in}, C_{in} starts charging the DEG as its capacitance increases. Conversely, as the DEG relaxes, its voltage rises; once it reaches and exceeds the voltage from C_{out}, Φ_H, it starts discharging into C_{out}. This configuration presents the disadvantage that C_{in} is required to have capacitance far higher than the DEG so that the charges flowing to the DEG will not yield a significant change in Φ_L. As Φ_H will tend to increase (due to the current flowing towards C_{out} from the DEG) and Φ_L tends to decrease with time (due to the current flowing from C_{in} to the DEG), the boost produced by the DEG capacitance change might become insufficient and the energy harvesting process will stop. A similar design, used by Huang *et al.* [56], consists of a high voltage power supply in place of the capacitor C_{in}, and a Zener diode connects the DEG to C_{out}, in which case the DEG will discharge once its voltage is higher than the Zener voltage, and C_{out} can start fully discharged. Such circuits present some problems, since they still rely on high voltage sources to prime the DEG, and can only be operated during a limited amount of time (the capacitor that receives the DEG output will reach a voltage level that will disable the DEG discharge). Furthermore, from a cycle point of view, they combine the constant charges and constant voltage output, the latter having the worst performance regarding energy output and relative energy gain per cycle according to [47].

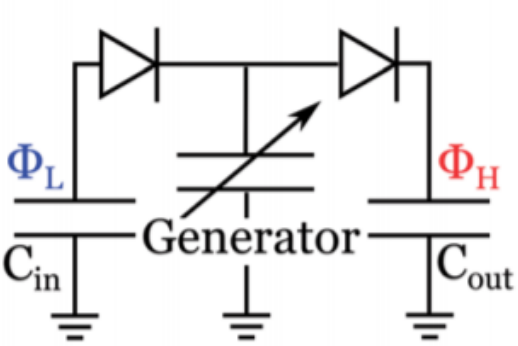

Figure 3.1: Circuit for passive energy harvesting through a DEG. A capacitor C_{in} charged with voltage Φ_L acts as low voltage reservoir, while a capacitor C_{out} charged with voltage $\Phi_H > \Phi_L$ is used as high voltage reservoir. In the figure, "Generator" indicates the variable capacitor that symbolises the DEG. Reproduced from [147].

Another possibility to promote passive energy harvesting in DEGs, avoiding the need for either high voltage power supplies or active charge control is the use of electrets [68, 142]. Electrets are solid dielectric materials able to hold static charges for a long period of time, in a quasi-permanent manner. When there is a small gap between the DEG and the electret, the latter induces an electric field and thus polarises the DEG. However, alternatives using electrets have demonstrated low power; predicting theoretical energy density for electrets of -2000V potential to be around 4.17mJ/g [79]. Furthermore, the priming mechanism, dependent on the gap between the DEG and the electret, and the fact that electrets are rigid materials, impose limiting design constraints, such as an extra mechanism to move the electret closer to an specific position (e.g. a system with hinges that bring the electret closer to the DEG when the DEG is stretched has been used [142]) leaving a gap to the DE and the impossibility of exploiting higher deformations than what the cited mechanism is designed for. Alternatively, piezoelectric materials [31, 80] have been employed as a way to charge DEGs. While piezoelectric energy harvesters do not require a specific position regarding the DEG membrane, which provides higher design flexibility, they still restrict the amount of energy that would be available for charging the DEG, e.g. the amount of charge that could be used to perform the energy conversion. Moreover, while such approaches promote passive charging of the DEG, one still needs to use one of the solutions highlighted above with diodes and capacitors to collect the energy stored in the DEG at every cycle, or be able to coordinate switches to discharge the correct time, thus requiring extra electronic hardware.

An alternative solution to provide the high voltage input for DEGs while coordinating charging and discharging in a passive manner is the use of Self-priming Circuits (SPCs), as proposed by McKay *et al.* [93]. An SPC consists of an inverse charge pump, toggling between high and low

capacitance states, depending on its polarisation. The circuit is composed of diodes and capacitors, as illustrated in Figure 3.2. An SPC can be polarised in a High Voltage (HV) form, which will only allow current to charge the capacitors, or in a High Charge (HC) state, which will only allow current to flow from the SPC (considering the SPC, as illustrated in Figure 3.2, is connected such that $V_A > V_B$). The HV configuration, or series configuration, presents fewer branches and more capacitors in series, while the HC configuration, or parallel, presents more branches and fewer capacitors in series, as shown in Figure 3.3. Such forms will be toggled by the charges they hold (determining the SPC voltage in either polarisation state) and the voltage in its terminals induced by the circuit they are inserted: if voltage induced by the circuit in the SPC terminals is higher than the voltage of the SPC in its HV configuration, current will flow towards it; if voltage induced by the circuit in the SPC terminals is lower than the voltage of the SPC in its HC configuration, current will flow from the SPC.

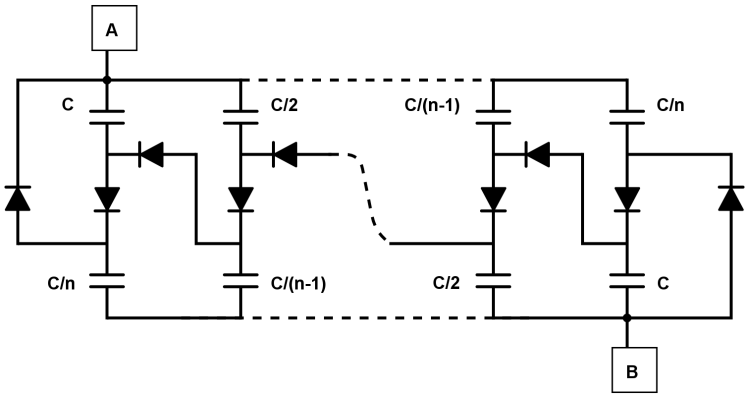

Figure 3.2: Basic n-stage SPC general scheme. Adapted from McKay *et al.* [96].

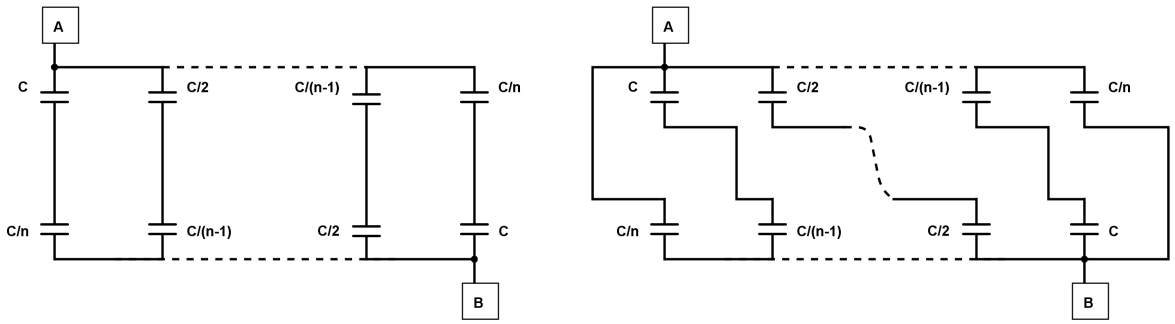

Figure 3.3: SPC effective configuration with (a) HV polarization, and (b) HC polarization. Adapted from McKay *et al.* [96].

The advantage of using an SPC is that it allows part of the energy output in a DEG cycle to be passively stored and used as an input in the following one, thus solving the issue of determining the timing for charging and discharging, as well as avoiding the need of a constant priming source. Through the use of an SPC, it is possible to initially prime the DEG-SPC system with low voltage and, by cycles of stretching-relaxing the DEG, to bring the system to high voltage and increase its energy output. Among its limitations, there is the need for a minimum capacitance swing for the boost to occur, which depends on the number of stages or SPC "order" n [96]: the higher the order, the lower the necessary capacitance change, but also the smaller the effective boost, and the higher the design complexity.

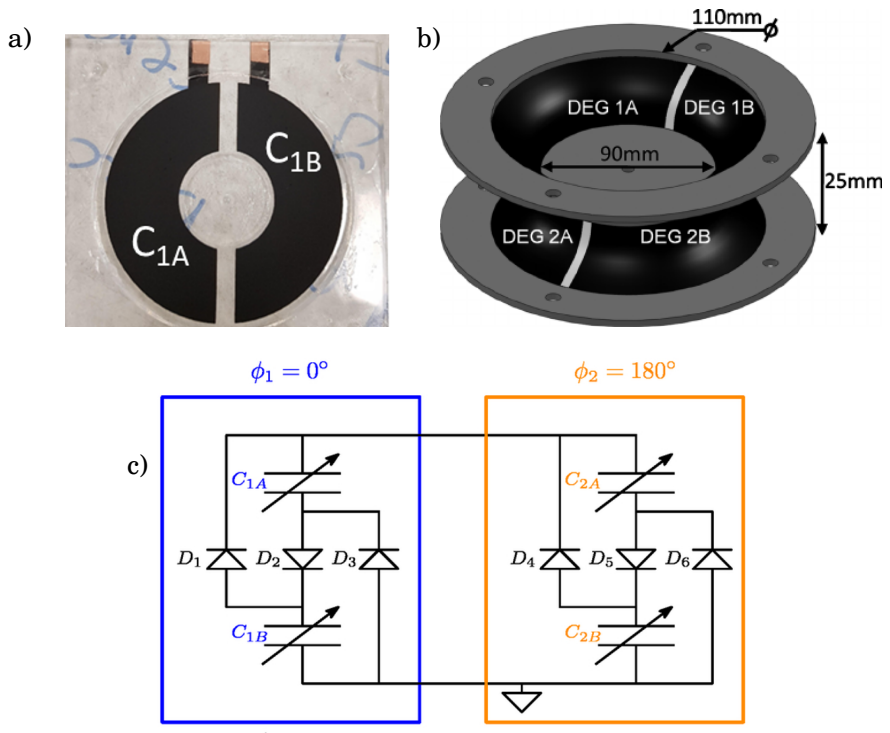

Figure 3.4: (a,b) ISPC is composed of 2 membranes to be moved in an antagonistic way. Each membrane is partitioned in at least two DEGs (parts A and B in the panels (a) and (b)). (a) One membrane of 1st order ISPC. We denote C_1 the DEG composed by parts C_{1A} and C_{1B}. Adapted from [63]. (b) 1st order ISPC 3D assemble. Reproduced from [92]. (c) ISPC 1st order circuit configuration: two antagonistic DE membranes (C_1 and C_2), partitioned into two DEGs (parts A and B), connected through a SPC-like diode-scheme. Reproduced from [63].

SPCs have been a promising topic of research, and upgrades have been made to their layout, such as using antagonistic DEG membranes to replace the capacitors normally used (called Integrated Self-Priming Circuits — ISPC) [92], illustrated in Figure 3.4. The ISPC design increases the energy density of dielectric elastomer devices, substituting the bulky/rigid charge-

storing capacitors by active DE elements, which act as both charge reservoirs, as in the basic SPC, and active energy converters. The main disadvantage of the ISPC design is the need of an antagonistic design for the membranes, imposing extra complexity for the energy harvesting layout choice. Another further development of SPCs is the use of Dielectric Elastomer Switches (DES) [105], flexible resistive elements incorporated in the membrane, which are able to toggle between high and low resistance depending on their stretch levels, replacing the diodes in the ISPC [97], thus creating a completely flexible generator independent of rigid electronic components. The ISPC design using DES presented a higher energy density, by avoiding stiff electronics, nonetheless, it still requires a convenient application where the softness can actually be a true advantageous characteristic, since a stiff energy storing solution might still be required, and the antagonistic design can be indeed exploited while avoiding the limitation of minimum capacitance swing necessary for the SPC induced boost to happen [96].

Further studies that highlight the use of SPCs regard the extraction of the harvested energy from such systems. For example, Ikegame *et.al* [60] used a Zener diode to limit the voltage and activate a wireless radio-transmitter, demonstrating the use of SPC-DEG systems to independently power an electronic device, transmitting ambient temperature data despite the efficiency of the step-down conversion from the SPC-DEG system to the capacitor reported as being 0.66%. Later, a passively-switched flyback converter was used for the same experiment [59], showing that efficiency in the order of 75% could be achieved; this demonstrated a more complete version of an energy harvesting device, with not only the energy conversion unit but an application to use the harvested energy.

In this chapter, we will focus on the electrical behaviour of the SPC-DEG system, neglecting the actuator-like effect described in the previous chapter (though we will return to this coupling in later chapter). Section 3.2 explains how SPC-DEG systems work, describing each phase the SPC-DEG system undergoes during a stretch-relax cycle and introduces some of the modelling considerations. Section 3.3 introduces the model obtained from the SPC-DEG system. Section 3.4, through the use of the model obtained, proposes a simplified model for an ideal SPC-DEG system and obtains the model that describes the exponential voltage increase at each cycle. Section 3.5 uses the simplified model from Section 3.4 to define and explore the design rules for this system. Section 3.6 provides a model for the ISPC layout. Section 3.7, based on the experimental results reported in [62], validates the model proposed in Section 3.6. Finally, Section 3.8 concludes the chapter by highlighting the key findings and explaining how the studies of SPC-DEG system will progress in this thesis across the following chapter.

3.2 Self-priming circuits — basic setup

As described previously for the DEG energy harvesting cycle, the DEG-SPC system also passes through different phases during the DEG stretch-relax cycle. These cycle phases and main model assumptions for the basic SPC design are detailed below, and the resulting voltage and capacitance during the cycle are shown in Figure 3.5. Since the SPC is composed of fixed capacitances, having its total capacitance depending on the configuration, for a same amount of charges in it, its voltage will depend on the state that is active.

3.2.1 Cycle phases

Using an SPC connected in parallel with the DEG, we can increase the voltage every time the DEG is cycled, as shown in Figure 3.6. The SPC provides a way to promote a cumulative effect to the voltage boost a DEG can provide when its capacitance is reduced. Note that the voltages represented in Figure 3.5 for the HV and HC forms reflect the voltage if the SPC was simply a capacitor with constant capacitance with a certain amount of charge stored. However, given the arrangement of the diodes, charge only flows into the SPC in its HV form, and from it in its HC form. If we consider a DEG stretch-relax cycle between fixed maximum and minimum stretch, we can describe the DEG-SPC cycle in four phases (see Figure 3.7).

Phase 1 Starting from the DEG stretched and in its maximum capacitance state, $C_{\mathrm{DEG}_{\mathrm{max}}}$, the DEG capacitance starts decreasing as it relaxes. Since the DEG voltage (blue curve in Figure 3.5a) is lower than that the SPC in HV form (red dashed curve in Figure 3.5a), the charge will not flow to the SPC. At the same time, the DEG voltage is higher than the SPC voltage in its HC form (green dashed curve in Figure 3.5a), thus, there is no charge flow from the SPC into the DEG. Consequently, the amount of charge in the DEG is constant and we have a voltage increase in the DEG similar to the constant charge cycle [47].

Phase 2 As the voltage on the DEG achieves the same level of that in the SPC in its HV form at time t_{12}, the DEG starts discharging into the SPC. The DEG voltage keeps rising due to its capacitance decrease, and the SPC voltage rises as charges from the DEG charge its capacitors.

Phase 3 Once the DEG stops relaxing and starts being stretched again, at time t_{23}, its capacitance starts to rise. As a consequence, the voltage starts dropping in the DEG. In a similar situation to Phase 1, there is no charge flow between the SPC and the DEG: the DEG voltage is lower than the SPC voltage in its HV form and higher than the SPC in its HC form, preventing the flow of charge to or from the SPC.

Phase 4 When the voltage in the DEG reaches that of the SPC in its HC form at time t_{34}, a charging current starts to flow from the SPC. As the DEG has a capacitance decrease, its voltage

keeps dropping. The SPC also loses charge due to drain into the DEG. At the moment the DEG's capacitance stops rising and starts decreasing again at time t_{41}, the cycle restarts, going back to Phase 1.

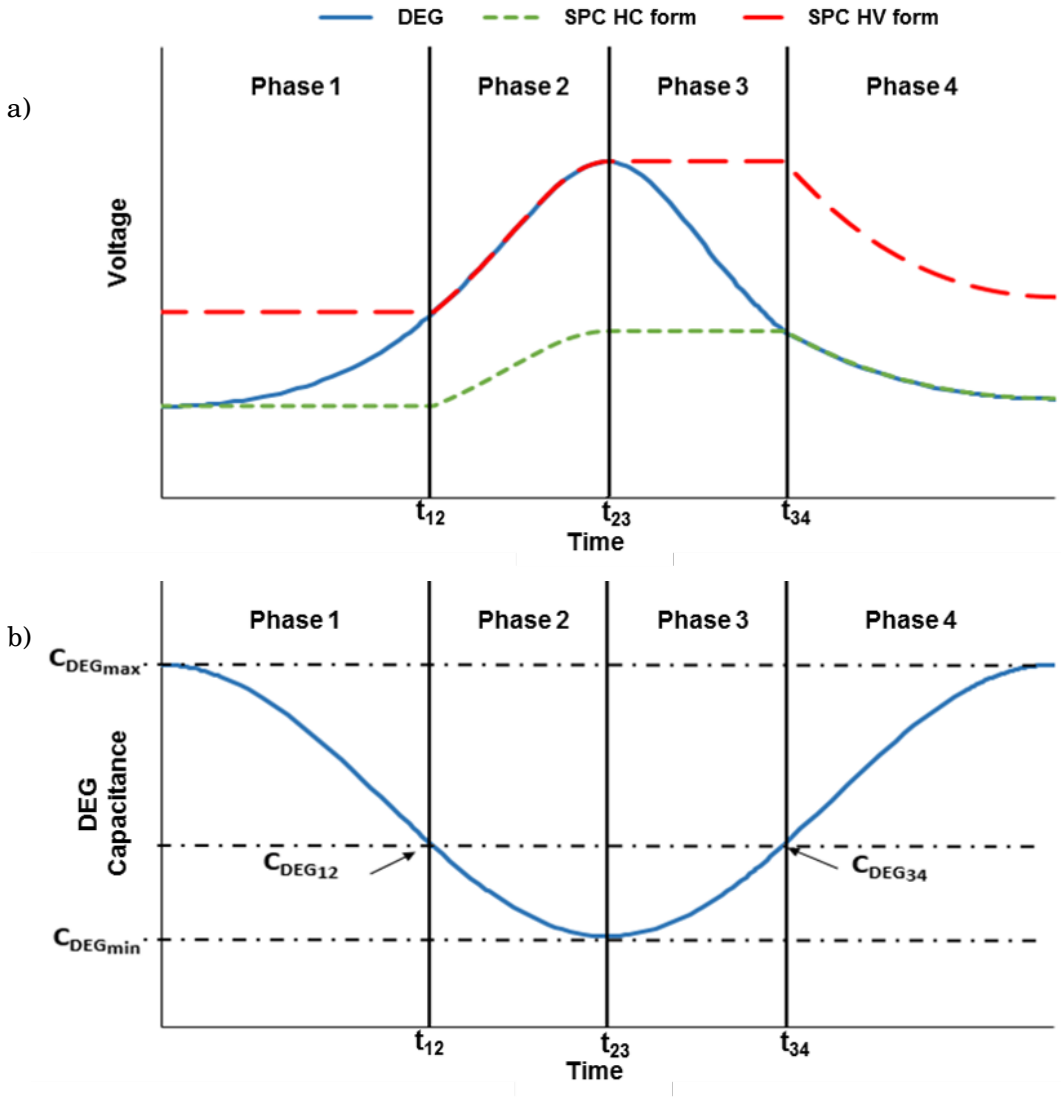

Figure 3.5: Voltage curves for a SPC-DEG system: DEG (solid blue line); SPC in HC form (dotted green line); SPC in HV form (dashed red line) (a). DEG capacitance (b).

Later in this chapter, we will discuss how the mechanism just described is able to boost the DEG voltage between cycles, so that the overall system voltage by the end of a cycle is higher at by the end of it, as shown in Figure 3.6.

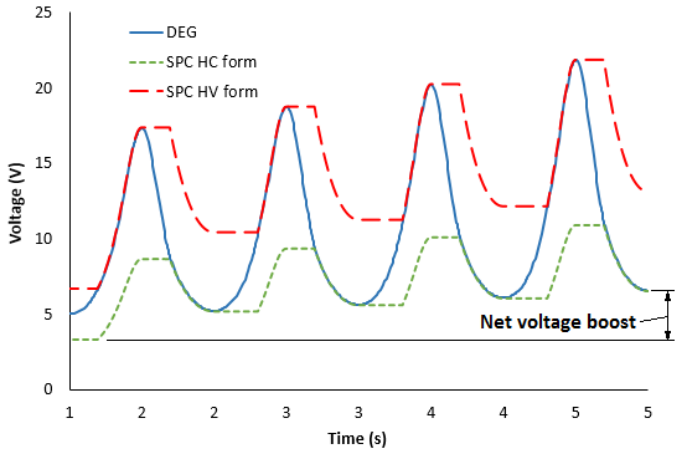

Figure 3.6: Voltage as a function of time for the DEG and the SPC, in both its HC and HV form.

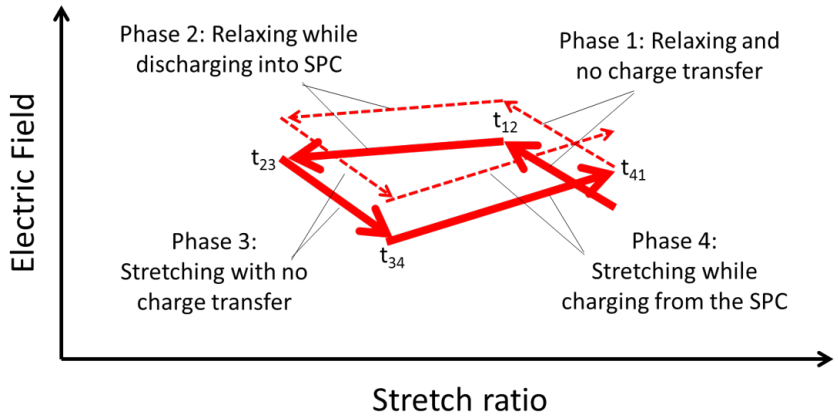

Figure 3.7: The DEG-SPC cycle, shown as electric field as a function of stretch. Two cycles shown: first cycle shown as solid line.

3.2.2 SPC model considerations

The design of the SPC, as shown in Figure 3.2, has the result that, in the HV form of the SPC, there are n branches in parallel, each with capacitance $\frac{C}{(n+1)}$, and, in the HC form, there are $n+1$ stages with capacitance $\frac{C}{n}$. Thus, the equivalent capacitance of the circuit can be written in each form as

$$C_{\mathrm{SPC_{HV}}} = C\left(\frac{n}{n+1}\right), \tag{3.1}$$

$$C_{\mathrm{SPC_{HC}}} = C\left(\frac{n+1}{n}\right). \tag{3.2}$$

Regarding the model initial states, considering the starting scenario when the circuit is primed with a voltage V_p, in an equilibrium condition (no current flow and stationary membrane), the SPC will be receiving charges, meaning it will be in its HV configuration. Thus, we can calculate that each capacitor with capacitance C has a voltage drop of

$$V_{C_0} = \frac{V_p}{(n+1)}. \tag{3.3}$$

This implies that the initial voltage of the SPC in which the HC form will be active is

$$V_{\mathrm{SPC_{HC}}} = nV_{C_0}. \tag{3.4}$$

Similar reasoning can be applied when toggling to HV form; the voltage at which it will be triggered is

$$V_{\mathrm{SPC_{HV}}} = \frac{n+1}{n} V_{\mathrm{SPC_{HC}}}. \tag{3.5}$$

3.3 Modelling the boost cycle phases

In this section, we introduce a mathematical model of each phase of the DEG-SPC voltage boosting cycle. Figure 3.8 illustrates the high-level circuit scheme of the DEG-SPC system, attached to a resistive load, Z, which could either represent a non-ideal voltage monitoring system or a resistor-like method for energy extraction. The source V_0 is used only to supply an initial charge for the DEG-SPC system, and the diode prevents charge to flow back through it when the voltage boost occurs. For this model, we consider that the DEG stretches and relaxes sinusoidally between two fixed positions, creating maximum and minimum area configurations, thus corresponding to a simple variable capacitor oscillating sinusoidally between $C_{\mathrm{DEG_{min}}}$ and $C_{\mathrm{DEG_{max}}}$. In particular, for the models presented in this chapter, the DEG is considered to be simply a variable capacitor with no interference from the electromechanical behaviour (we considered the latter effect in a later chapter).

3.3.1 Phase 1

We consider the cycle starting at a time $t = t_0$ from a charged state in the local voltage minimum for a cycle, $V_0 < V_{\mathrm{SPC_{HC}}}$, and with the DEG beginning to relax from a stretched position with local maximum capacitance $C_{\mathrm{DEG_{max}}}$.

As explained previously, while the DEG relaxes, its capacitance is reduced and the voltage increases. No charge exchange happens between the SPC and the DEG, since the voltage is not

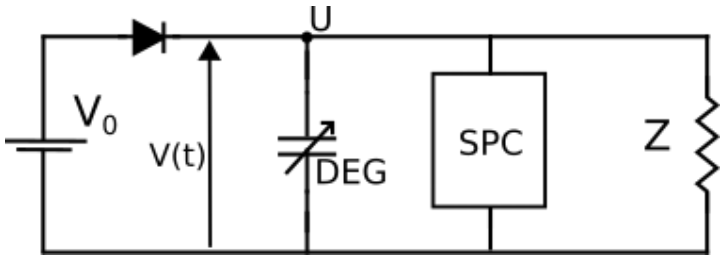

Figure 3.8: Circuit scheme of DEG-SPC system attached to a load.

large enough to trigger the HV form of the SPC. Meanwhile, some of the charge leaks through the load (which represents either an energy harvesting impedance or simple losses/leakage in the system), resulting in

$$C_{\mathrm{DEG}}(t)V(t) = Q(t) = Q_0 - \frac{V(t)}{Z} = V_0 C_{\mathrm{DEG}_{\max}} - \frac{V(t)t}{Z}, \tag{3.6}$$

where $Q(t)$ is the charge in the DEG and Q_0 is the charge level in the DEG provided by the voltage source V_0. The voltage in Phase 1, $V_1(t)$, can be found solving eq. (3.6) to give

$$V_1(t) = V_0\left(\frac{C_{\mathrm{DEG}_{\max}}}{C_{\mathrm{DEG}}(t) + t/Z}\right). \tag{3.7}$$

As the voltage increases, it reaches the level held by the SPC in its high voltage form, $V_{\mathrm{SPC_{HV}}}$. At this point we transition to the next phase, in which the DEG starts discharging into the SPC. The transition occurs at a time t_{12}, which can be found as the first positive solution of $V_1(t_{12}) = V_{\mathrm{SPC_{HV}}}$. From Equation 3.7 this is equivalent to

$$V_{\mathrm{SPC_{HV}}} = V_0\left(\frac{C_{\mathrm{DEG}_0}}{C_{\mathrm{DEG}}(t_{12}) + t_{12}/Z}\right), \tag{3.8}$$

an implicit equation for t_{12}, which depends on $C_{\mathrm{DEG}}(t)$.

3.3.2 Phase 2

During Phase 2, the DEG voltage increases and not only supplies current to the load but also discharges into the SPC in its HV form. To describe the voltage behaviour, we start by writing Kirchhoff's current law for the node U (see Figure 3.8) in a general case:

$$\frac{V(t)}{Z} + C_{\mathrm{SPC}}\frac{dV(t)}{dt} + C_{\mathrm{DEG}}(t)\frac{dV(t)}{dt} + V(t)\frac{dC_{\mathrm{DEG}}(t)}{dt} = 0. \tag{3.9}$$

Given that $C_{\mathrm{SPC}} = C_{\mathrm{SPC_{HV}}}$ in this phase, and considering the initial conditions of this phase $C_{\mathrm{DEG}}(t_{12}) = C_{\mathrm{DEG}_{12}}$ and $V(t_{12}) = V_{\mathrm{SPC_{HV}}}$, Equation 3.9 can be solved to give us the voltage in Phase 2, $V_2(t)$, as

$$V_2(t) = V_{\mathrm{SPC_{HV}}}\left(\frac{C_{\mathrm{SPC_{HV}}} + C_{\mathrm{DEG}_{12}}}{C_{\mathrm{SPC_{HV}}} + C_{\mathrm{DEG}}(t)}\right)e^{\beta_2(t)}, \tag{3.10}$$

where

$$\frac{d\beta_2}{dt} = -\frac{1}{Z(C_{\mathrm{SPC_{HV}}} + C_{\mathrm{DEG}}(t))}. \tag{3.11}$$

For $Z >> 1$, the peak voltage can then be found when the DEG capacitance reaches its minimum value, by using $C_{\mathrm{DEG}}(t_{23}) = C_{\mathrm{DEG_{min}}}$, noting that t_{23} marks the transition time to Phase 3.

3.3.3 Phase 3

After reaching its minimum capacitance, the DEG starts being stretched again and its capacitance increases, leading to a voltage drop. The current through the SPC ceases, since its voltage in the HC form is higher than that of the DEG. Thus, there is only current from the DEG to the attached load, as in Phase 1. Now, the voltage drops from the peak voltage, V_{max}, achieved when the DEG reaches its minimal capacitance, $C_{\mathrm{DEG_{min}}}$. Using the same approach as before, we obtain

$$V_3(t) = V_{\mathrm{max}}\left(\frac{C_{\mathrm{DEG_{min}}}}{C_{\mathrm{DEG}}(t) + t/Z}\right). \tag{3.12}$$

As the voltage drops, it will reach the potential of the SPC in its HC state, $V_{\mathrm{SPC_{HC}}}$, at time $t = t_{34}$, and, at this point, we have a transition to the next phase. We can find the DEG state based on its capacitance when the DEG will start charging up using the energy stored in the SPC, $C_{\mathrm{DEG_{34}}} = C_{\mathrm{DEG}}(t_{34})$. Substituting into Equation 3.12, we have

$$V_{\mathrm{SPC_{HC}}} = V_{\mathrm{max}}\left(\frac{C_{\mathrm{DEG_{min}}}}{C_{\mathrm{DEG_{34}}} + t_{34}/Z}\right), \tag{3.13}$$

again, an implicit equation for t_{34}, dependent on the $C(t)$.

3.3.4 Phase 4

During Phase 4, the DEG voltage reaches the SPC voltage in its HC form and starts charging up from it. As this phase uses the same circuit analyzed in Phase 2, we use again the generalized Equation 3.9 as a starting point. We apply the initial conditions for the phase transition at t_{34}, and obtain that

$$V_4(t) = V_{\mathrm{SPC_{HC}}}\left(\frac{C_{\mathrm{SPC_{HC}}} + C_{\mathrm{DEG_{34}}}}{C_{\mathrm{SPC_{HC}}} + C_{\mathrm{DEG}}(t)}\right)e^{\beta_4(t)}, \tag{3.14}$$

with

$$\frac{d\beta_4}{dt} = -\frac{1}{Z(C_{\mathrm{SPC_{HC}}} + C_{\mathrm{DEG}}(t))}. \tag{3.15}$$

3.3.5 Following cycle

From Equation 3.14, we can see clearly that a local minimum will be approximately obtained using the maximum value of $C_{\mathrm{DEG}}(t)$. As the voltage curve reaches this local minimum, we return to phase 1 of the cycle, but this time using the DEG's maximum capacitance and the minimum voltage from the previous cycle as initial conditions.

3.4 Modelling voltage boost

Given the model described above, we study a case focused on boosting the voltage, without concerns regarding energy output through external loads and neglecting the effects of non-ideal elements. Thus, we obtain a simplified version of the model by neglecting the attached impedance, Z, considering it infinite and ignoring the current drained through it, in order to obtain analytic results.

3.4.1 Simplified model

Through Equations eq. (3.7), eq. (3.10), eq. (3.12) and eq. (3.14) we have described the DEG-SPC system cycle considering current drained through a load with impedance Z. If we consider $Z \to \infty$ and that it is not the first cycle to run, we can define the voltage behaviour as a function, $V^{\star}(t)$, which is given in each phase described previously,

$$V_1^{\star}(t) = V_{\min}\left(\frac{C_{\mathrm{DEG}_{\max}}}{C_{\mathrm{DEG}}(t)}\right), \tag{3.16}$$

$$V_2^{\star}(t) = V_{\mathrm{SPC}_{\mathrm{HV}}}\left(\frac{C_{\mathrm{SPC}_{\mathrm{HV}}} + C_{\mathrm{DEG}_{12}}}{C_{\mathrm{SPC}_{\mathrm{HV}}} + C_{\mathrm{DEG}}(t)}\right), \tag{3.17}$$

$$V_3^{\star}(t) = V_{\max}\left(\frac{C_{\mathrm{DEG}_{\min}}}{C_{\mathrm{DEG}}(t)}\right), \tag{3.18}$$

$$V_4^{\star}(t) = V_{\mathrm{SPC}_{\mathrm{HC}}}\left(\frac{C_{\mathrm{SPC}_{\mathrm{HC}}} + C_{\mathrm{DEG}_{34}}}{C_{\mathrm{SPC}_{\mathrm{HC}}} + C_{\mathrm{DEG}}(t)}\right), \tag{3.19}$$

where $V_{\min}$ corresponds to the local minimum in the DEG voltage curve achieved at the end of Phase 4 and $V_{\max}$ the local maximum voltage obtained at the end of Phase 2.

Following the same approach and neglecting the current through the impedance, we can also describe the capacitances in the DEG at the transition between phases:

$$C_{\mathrm{DEG}_{12}} = \frac{V_{\min} C_{\mathrm{DEG}_{\max}}}{V_{\mathrm{SPC}_{\mathrm{HV}}}}, \tag{3.20}$$

$$C_{\mathrm{DEG}_{34}} = \frac{V_{\max} C_{\mathrm{DEG}_{\min}}}{V_{\mathrm{SPC}_{\mathrm{HC}}}}, \tag{3.21}$$

where, in this scenario,

$$V_{\mathrm{SPC_{HV}}} = \frac{n+1}{n} V_{\min}, \tag{3.22}$$

$$V_{\mathrm{SPC_{HC}}} = \frac{n}{n+1} V_{\max}., \tag{3.23}$$

as described above.

3.4.2 Voltage boost model

We say that there has been a voltage boost if the peak voltage in a cycle is higher than the peak in the previous one. We evaluate the boost through the parameter B, defined as the ratio between the maximum voltage in a cycle and that of the previous one. The set of equations described in Section 3.4.1 allows us to determine the relation between a local maximum in the voltage curve for the j^{th} cycle, V_{max_j}; the process can be extended to define the next local maximum, $V_{\mathrm{max}_{j+1}}$, located in the following cycle. Combining eq. (3.16), eq. (3.17), eq. (3.18), and eq. (3.19) and breaking them down into the basic parameters C and n, we obtain that the boost , B, can be described by

$$B = \frac{V_{\mathrm{max}_{j+1}}}{V_{\mathrm{max}_j}} = \frac{C^2 + (C_{\mathrm{DEG_{min}}} + C_{\mathrm{DEG_{max}}})C + C_{\mathrm{DEG_{min}}} C_{\mathrm{DEG_{max}}}}{C^2 + \left(\dfrac{n^2 C_{\mathrm{DEG_{max}}} + (n+1)^2 C_{\mathrm{DEG_{min}}}}{n(n+1)} \right) C + C_{\mathrm{DEG_{min}}} C_{\mathrm{DEG_{max}}}}. \tag{3.24}$$

Equation 3.24 provides insights about several aspects of system design and behaviour. First, it allows us to verify the minimum requirements for the boost to exist, namely when $B > 1$. It can also be seen that the boost stays constant if both the SPC characteristics (n and C) and the DEG capacitance swing ($C_{\mathrm{DEG_{max}}}/C_{\mathrm{DEG_{min}}}$) are maintained. Another possibility is verifying the design parameters that lead to a maximum boost, which can be achieved easily by differentiation of eq. (3.24) with respect to the appropriate parameter(s). We can search for the value of C that maximises the boost and also determine how increasing the number of stages, n, affects the SPC.

3.4.2.1 Condition for boost to exist

To obtain boost, we must have $B > 1$, which leads us straightforwardly to the condition

$$n > \frac{1}{C_{\mathrm{DEG_{max}}}/C_{\mathrm{DEG_{min}}} - 1}. \tag{3.25}$$

3.4.2.2 Maximum boost

In order to choose the value C which will provide the maximum boost, $C = C_{\mathrm{ideal}}$, we seek solutions of $dB/dC = 0$, which gives

$$C_{\mathrm{ideal}} = \sqrt{C_{\mathrm{DEG_{min}}} C_{\mathrm{DEG_{max}}}}. \tag{3.26}$$

We can see in Figure 3.9 a plot of B (eq. (3.24)) as a function of design parameters C, $C_{\mathrm{DEG}_{\mathrm{max}}}$ and $C_{\mathrm{DEG}_{\mathrm{min}}}$, demonstrating the importance of selecting the right value of C, as the voltage could even decrease at each cycle ($B < 1$) if inappropriately chosen. If the capacitance of the SPC is too high ($C \to \infty$ implying that $C_{\mathrm{SPC}_{\mathrm{HV}}} \to \infty$ and $C_{\mathrm{SPC}_{\mathrm{HC}}} \to \infty$), the capacitance swing from the DEG would be negligible when compared to the SPC's capacitance; the Phase 2 voltage rise would stop as all the charges would flow from the DEG to the SPC instead of promoting the rise of the SPC-DEG system voltage. On the other hand, if the SPC capacitance is too low ($C \to 0$ so both $C_{\mathrm{SPC}_{\mathrm{HV}}} \to 0$ and $C_{\mathrm{SPC}_{\mathrm{HC}}} \to 0$), it would not be able to accommodate enough charge to keep the boosting process going. In this case, we would have a voltage swing due exclusively to a DEG capacitance change when it holds constant charge, having only Phases 1 and 3 of the cycle (eq. (3.17) and eq. (3.19) would converge to eq. (3.16) and eq. (3.18)). It is also possible to verify how relevant the capacitance change, evaluated here as $C_{\mathrm{DEG}_{\mathrm{max}}}/C_{\mathrm{DEG}_{\mathrm{min}}}$ is, as its effect on the voltage boost is clearly visible in Figure 3.9. The higher the capacitance change, the higher the maximum voltage boost possible.

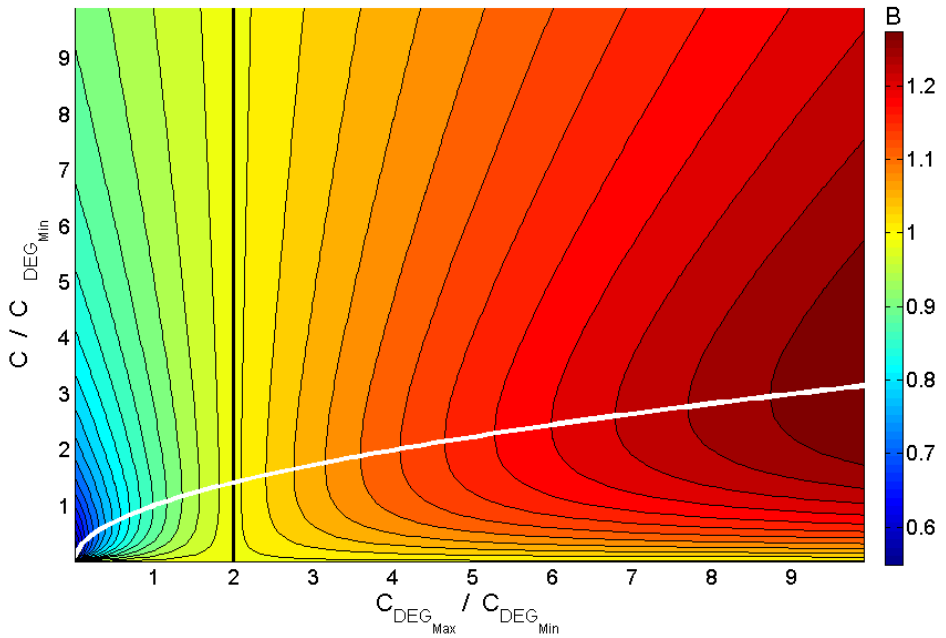

Figure 3.9: Voltage boost, B, shown as a function of DEG capacitance change, $C_{\mathrm{DEG}_{\mathrm{max}}}/C_{\mathrm{DEG}_{\mathrm{min}}}$, for different SPC base capacitance, C, for a one stage SPC ($n = 1$). The white line indicates the peak boost as suggested by Equation 3.26. The thick black line corresponds to $B = 1$ and separates the region with boost (right) from that where the condition in Equation 3.25 is not fulfilled and $B < 1$ (left)

3.4.2.3 Effect of the number of stages

The number of stages, n, in the SPC will influence the denominator of Equation 3.24, specifically the coefficient A of the linear term in C,

$$A = \frac{n^2 C_{\mathrm{DEG}_{\max}} + (n+1)^2 C_{\mathrm{DEG}_{\min}}}{n(n+1)}. \tag{3.27}$$

It is trivial to observe that if $n \to \infty$, $A \to C_{\mathrm{DEG}_{\max}} + C_{\mathrm{DEG}_{\min}}$, hence, the denominator of Equation 3.24 becomes the same as the numerator and there is no boost. We can find the number of stages that maximises the boost by solving $dB/dn = 0$ for n, and comparing the values of B for the two integers either side of the turning point. E.g. for $C_{\mathrm{DEG}_{\max}}/C_{\mathrm{DEG}_{\min}} > 3$, we can also verify that the maximum boost is obtained for $n = 1$. On the other hand, Figure 3.10 illustrates how increasing the number of stages allows the boost to exist in a broader range of situations when the capacitance swing is reduced, though it also shows a reduction in the voltage boost. This can be explained by the decrease in the difference of the SPC capacitance when toggled between its HV and HC forms, decreasing its effectiveness. Looking back at Equations 3.1 and 3.2, the more stages are used, the closer the ratio $(n+1)/n$ is to 1, and the closer the SPC effect becomes of that of a simple capacitor with capacitance C, and the boosting is reduced.

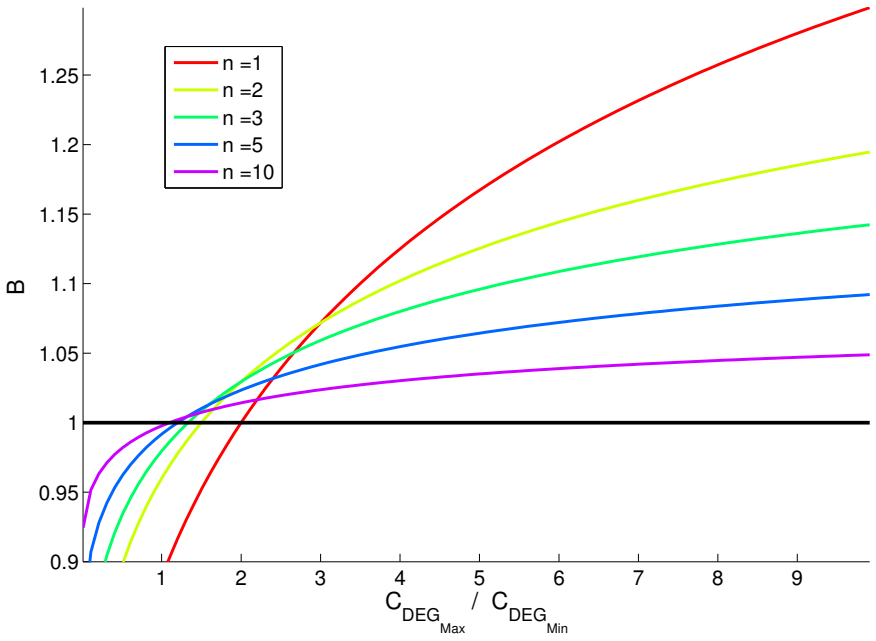

Figure 3.10: Voltage boost, B, versus the DEG's capacitance swing, $\frac{C_{\mathrm{DEG}_{\max}}}{C_{\mathrm{DEG}_{\min}}}$, for different numbers of stages, n. The black line corresponds to $B = 1$, and separates the region with boost (above) from that without (below).

3.5 Design rules

An important point that validates the current analysis is the correspondence with the rules proposed in McKay *et al.* [96]. There, it was suggested that C and n should be chosen such that

$$C_{SPC_{HC}} = C_{\mathrm{DEG}_{\max}}, \tag{3.28}$$

and

$$\frac{(n+1)}{n} = \sqrt{\frac{C_{\mathrm{DEG}_{\max}}}{C_{\mathrm{DEG}_{\min}}}}. \tag{3.29}$$

Uniting both of these conditions, we get to the same choice of C expressed in eq. (3.26). In addition, n is chosen in a way that will necessarily obey the condition expressed in Equation eq. (3.25). In contrast, using eq. (3.26) and observing the condition in eq. (3.25), we are able to choose the parameters C and n independently.

3.6 Integrated Self-Priming Circuit — loss modelling

In this section, we report the modelling of an ISPC following a similar approach to section 3.3, and use experimental results obtained at the University of Auckland to validate the model. As mentioned previously, an ISPC system consists, in its most basic form (order $n = 1$), of two pairs of DEGs, assembled in an antagonistic fashion, such that when one relaxes, the other stretches, as illustrated in Figure 3.4b. When we take that to the SPC scenario, it means that when one of the DEGs is discharging, it charges the other, not only substituting the need for the external capacitors but also promoting two boost phases for a single cycle. furthermore, ISPCs have higher energy density than SPC-DEG systems, since they do not require the use of external capacitors, using instead DEGs connected through diodes. ISPCs can also be arranged in a higher order manner, where DEGs that deform in phase are arranged in one side (components inside blue rectangle in Figure 3.4c is a first order, $n = 1$, example) while the other side has DEGs that will deform 180^o out of phase from the other side. These DEGs could be either manufactured on the same membrane or in different membranes, provided they obey the capacitance ratios suggested in the scheme shown in Figure 3.11.

Figure 3.11 shows the design of a general nth order scheme, in terms of the wiring of one of the sides of an ISPC. Note that it consists essentially of the replacement of the capacitors in the SPC, shown in Figure 3.2, for DEG segments, such that their capacitances are a fraction of that of the biggest one, $C(t)$. The electrical system as a whole can be seen in Figure 3.12, consisting of two ISPC sides (ISPC DEG1 and ISPC DEG2), which can have branches arranged as shown in Figure 3.11, together with a proposed leakage load, with equivalent resistance R_L. Since the system is assembled in an antagonistic fashion, while the side ISPC DEG1 has the capacitance of the DEGs on its branches increasing, the side ISPC DEG2 has it decreasing, and vice versa.

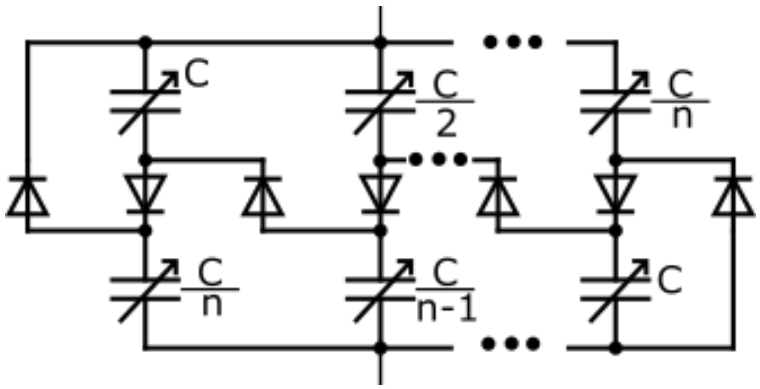

Figure 3.11: General scheme of a single side of an n^{th} order ISPC: C indicates the value of the biggest DEG in the scheme, while C/j, for $j = 1,2,...,n$ are DEGs that have a fraction $(1/j)$ of the capacitance of the biggest element C,with capacitances changing proportionally to that of C.

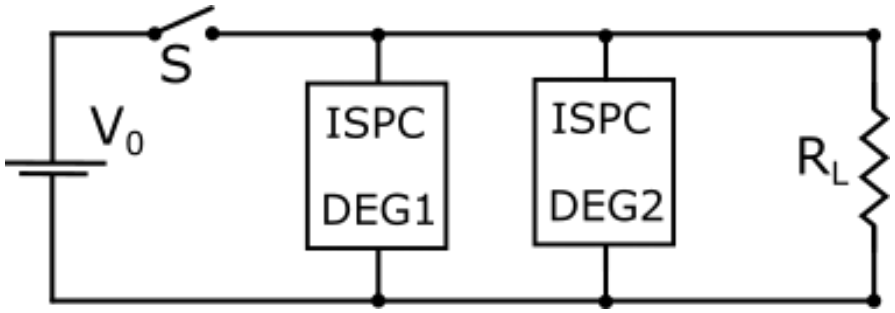

Figure 3.12: Circuit used for the model approach proposed. boxes ISPC DEG1 and ISPC DEG2 denote a circuit arrangement of DEGs as shown in Figure 3.11, but such that the DEGs in ISPC DEG1 have their voltage increasing while the ones in ISPC DEG2 decrease and vise versa.

In order to model the ISPC, we consider the equivalent capacitance of each side (ISPC DEG1 and ISPC DEG2) for each of the configurations possible. When the ISPC side with maximum member capacitance C is in a configuration able to receive charges (DEGs connected in series), the capacitance of each ISPC side is given by

$$C_{par}(t) = \frac{nC(t)}{n+1}, \tag{3.30}$$

while, in a configuration where charges flow from the ISPC side (DEGs in parallel), the capacitance is given by

$$C_{ser}(t) = \frac{(n+1)C(t)}{n}. \tag{3.31}$$

Considering just the toggling between series and parallel configurations of a side of a stationary ISPC, since the charge stored in each of the DEGs remains the same, we can relate the voltage in

each configuration as

$$V_{par} = \frac{nV_{ser}}{n+1}, \tag{3.32}$$

where V_{par} is the voltage of the referred side in the parallel configuration and V_{ser} in the series configuration.

The reader might note that we use different notation from that in Section 3.2.2 for the basic SPC-DEG system. While the notation of HV and HC form reminds the reader that those are the SPC forms active in a cycle, when the SPC-DEG system is closer to maximum voltage or having the SPC charged, we opt to use the notation of parallel and series in this section since we do not have a single DEG charging or close to peak voltage in a cycle, as we will see in the results that follow.

For the present study, we will denote C_1 and C_2 the maximum capacitance DEG in each of the sides of the ISPC, as illustrated by the parameter C in Figure 3.11. As a visual aid, we will illustrate the phases, indicating features such as current direction and reverse biased and forward biased diodes, using a first order (n = 1) ISPC circuit, where each side has only two DEGs of the same capacitance, shown in Figure 3.13, although the model is constructed in full generality, considering a n^{th} order system. Furthermore, we will illustrate the voltage curves for the ISPC phases considering $C_1(t)$ and $C_2(t)$ as sinusoidal functions with opposite phases, but generic functions $C_1(t)$ and $C_2(t)$ are considered for the modelling approach here demonstrated.

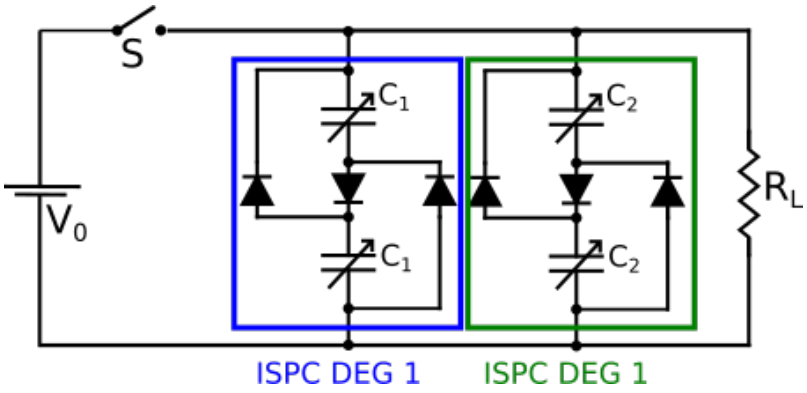

Figure 3.13: Example of circuit using a first order ISPC: circuit containing the variable capacitors of capacitance $C_1(t)$ represent ISPC DEG1 from Figure 3.12, and the circuit with the variable capacitors of capacitance $C_2(t)$ represent ISPC DEG2.

The approach taken in Section 3.3, analysing the final boost per cycle and design rules is not considered here, as it is part of ongoing collaborative work. Instead we will focus on deriving

the mathematical model that describes the dynamics of the system during each phase and the transition conditions between them, and validating the model with experimental data.

3.6.1 Initial system prime

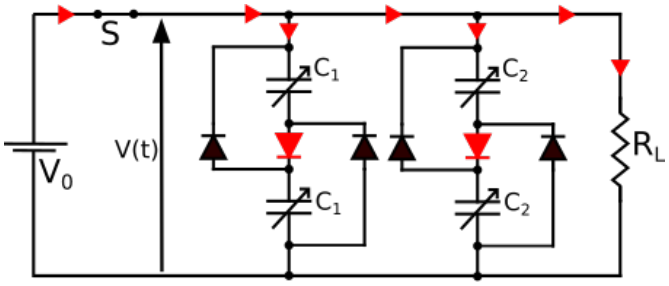

Figure 3.14: ISPC initial priming. S closes and charges flow to the DEGs into each branch of the ISPC.

To start the system, the ISPC still requires a low voltage priming, V_0, which is provided by closing the switch S, as shown in Figure 3.14. Since both ISPC sides will be receiving charges, they are both in their series configuration. Supposing that they are in a stationary situation, once switch S is opened, at time t_0, both the sides of the ISPC will be in their parallel configuration, due to the absence of external voltage sources. The system voltage, measured on the node where the switch S connects with the ISPC (see Figure 3.14), becomes

$$V(t_0) = \frac{nV_0}{(n+1)}, \tag{3.33}$$

as indicated by eq. (3.32).

Note that in all subsequent phases, the low voltage source V_0 is disconnected and the switch S remains open for all $t > t_0$, and so will not be plotted in the circuit diagrams that follow.

3.6.2 Phase 1

Considering we start from a condition with side ISPC DEG1 (max capacitance C_1) in its maximum capacitance state and side ISPC DEG2 (maximum capacitance C_2) in its minimum, when the system starts being mechanically deformed, such that the capacitance C_1 reduces and the capacitance C_2 increases, the side 1 voltage will maintain its parallel configuration and part of its charges will leak through R_L, as shown in Figure 3.15. Therefore the system voltage $V(t)$ (measured exactly as above) evolves according to

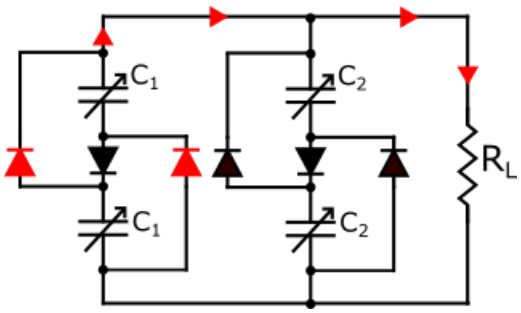

Figure 3.15: During phase 1, the branch of C_1 determines the system voltage, and also is the one charge leaks from to R_L.

$$0 = C_{1,\text{par}}\frac{dV}{dt} + V\frac{dC_{1,\text{par}}}{dt} + \frac{V}{R_L}. \tag{3.34}$$

Meanwhile, side ISPC DEG2 is unable to receive charge, due to its capacitance rise and the fact that its series configuration presents a higher voltage than the system voltage, and so no current flows. Nonetheless, as the capacitance C_2 changes (in a prescribed way, due to the mechanical deformation), the voltage in side 2, $V_{C_{2,\text{ser}}}$, also changes, according to

$$0 = C_{2,\text{ser}}\frac{dV_{C_{2,\text{ser}}}}{dt} + V_{C_{2,\text{ser}}}\frac{dC_{2,\text{ser}}}{dt}. \tag{3.35}$$

We can determine the time at which side 2 can start to receive charge, when $V_{C_{2,\text{ser}}} = V$, by solving eq. (3.34) and eq. (3.35).

The system evolution in this phase is shown schematically in Figure 3.16. As the system voltage rises (due to the decrease of capacitance C_1), it will reach the voltage of C_2 branch in its series configuration, which is decreasing as C_2 increases. Thus, we have a transition point at time t_{12} and voltage $V(t_{12})$, found as described above. Since eq. (3.34) and eq. (3.35) are dependent on $C_1(t)$ and $C_2(t)$, and we look for a general scenario, we cannot provide analytic solutions for this system of equations and determine t_{12} in closed form. However, for design and experimental scenarios, where $C_1(t)$ and $C_2(t)$ are known, the procedures here described can be applied to identify t_{12} and the subsequent transition times.

3.6.3 Phase 2

After the transition at time t_{12}, the current from side 1, in its parallel form, not only flows to the leakage resistor R_L, but also to side 2 in its series form, as shown in Figure 3.17. The voltage in the system is then determined by the equation

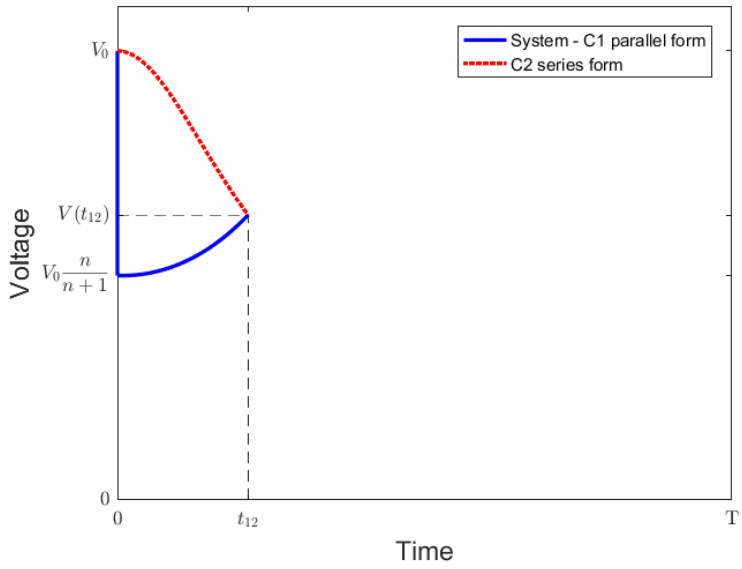

Figure 3.16: Voltage curves during phase 1 of a ISPC cycle: System voltage dependent on side 1 in its parallel form (solid blue line) and voltage level that triggers current flowing into side 2 in series form (red dashed line).

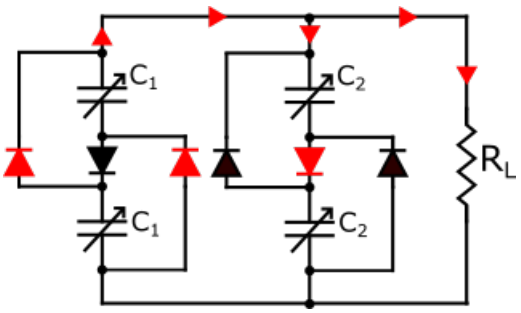

Figure 3.17: During phase 2, side 1 supplies current to side 2.

$$0 = (C_{1,\text{par}} + C_{2,\text{ser}})\frac{dV}{dt} + V\left(\frac{dC_{1,\text{par}}}{dt} + \frac{dC_{2,\text{ser}}}{dt} + \frac{1}{R_L}\right). \tag{3.36}$$

This phase will last for as long as there is current flowing towards C_2, given be the condition

$$i_{C_{2,\text{ser}},2} = -\left(V\frac{dC_{2,\text{ser}}}{dt} + C_{2,\text{ser}}\frac{dV}{dt}\right) > 0, \tag{3.37}$$

and visualised in Figure 3.18. The transition should happen close to half of the cycle if the DEGs follow a regular and non-hysteretic stretch profile (e.g.: sinusoidal), as shown in Figure 3.19. For an ideal case, with no leakage, such transition would happen simultaneously with the maximum

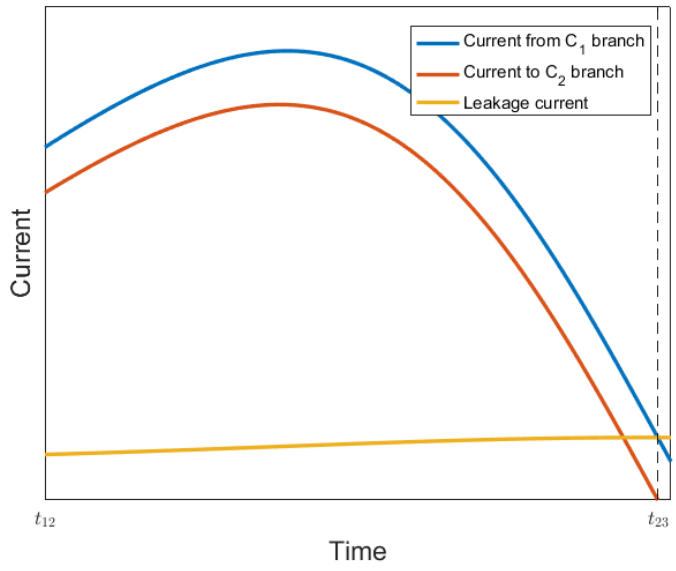

Figure 3.18: Current as a function of time during phase 2 of a ISPC cycle.

capacitance of C_2 and the minimum of C_1. For the present case, solving the system determined by eq. (3.36) and eq. (3.37), the transition time t_{23} happens before the turning points in C_1 and C_2, due to the leakage.

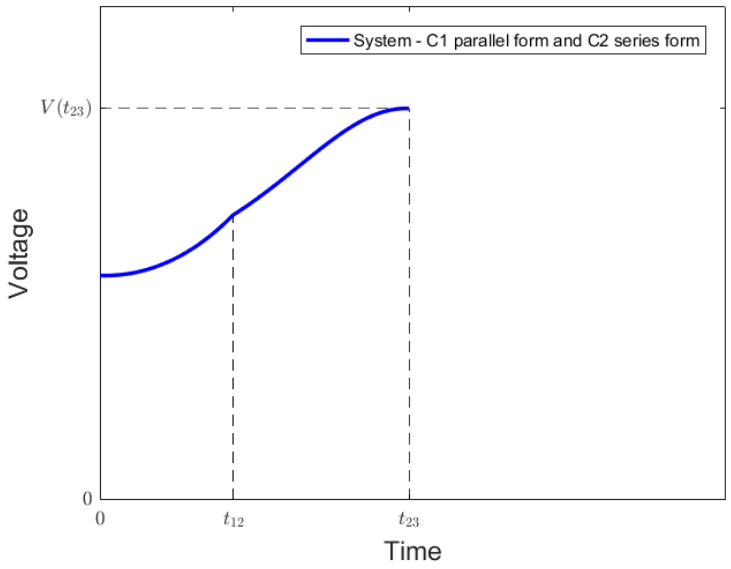

Figure 3.19: Voltage as a function of time during phase 2 of a ISPC cycle.

To visualise in a more intuitive manner the reason the transition happens earlier for non-ideal systems, take the example that capacitances C_1 and C_2 vary in a sinusoidal manner. The deformation rate, that leads to $\frac{dC_i}{dt}$, reduces as the deformation approaches its maximum/minimum point. Since the voltage rise is produced by the corresponding change in capacitance, as $\frac{dC_i}{dt} \to 0$ the rate of voltage rise also tends to zero, and the charge leakage through the membrane becomes more significant, so that the moment when $\frac{dV}{dt} = 0$ will happen before $\frac{dC_i}{dt} = 0$. Thus, the boost in voltage provided by the reduction in capacitance C_1 stops after it can no longer supply current to increase the voltage in side 2 while also overcoming the leakage, thus producing the local maximum V_M. As $\frac{dC_1}{dt}$ reduces further, it can no longer supply current to keep side 2 at the same voltage, and all the power generated by the capacitance reduction is dissipated through R_L.

3.6.4 Phase 3

As the voltage of side 2 in series form is now higher than side 1 in its parallel, but the voltage in side 2 in parallel form is still lower than of that of side 1 series form, side 1 in its parallel form is still dominant in the system. This results in a system voltage governed by equation eq. (3.34). In this phase, however, the voltage is falling, either by the effects that lead to the earlier peak in a non-ideal system or by the increase in capacitance C_1 after it reached its minimum.

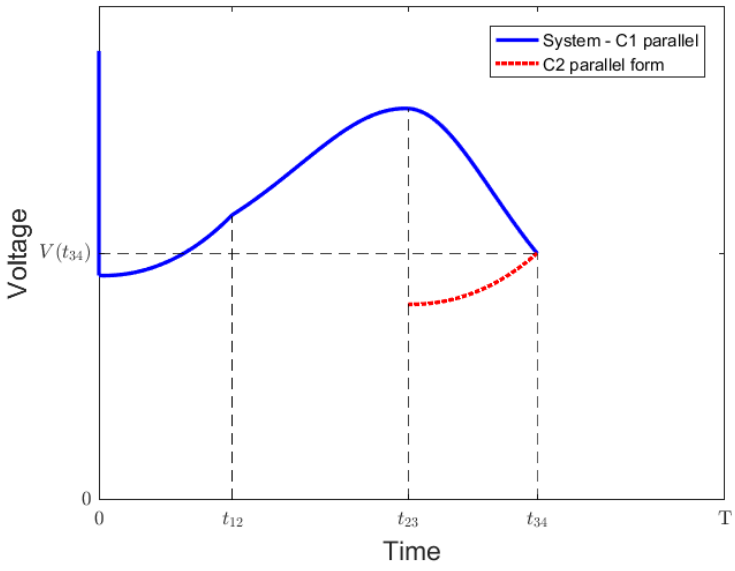

Figure 3.20: Voltage as a function of time during phase 3 of a ISPC cycle.

Meanwhile, the capacitance of side 2 reaches a maximum and starts decreasing, which leads to the increase of its voltage. Phase 4 ends at time t_{34}, when the voltage on side 2 (in parallel form) reaches the decreasing voltage of the system, governed by side 1, and there is an inversion of

control of the system voltage: unable to receive current in its parallel form, current no longer flows through side 1. Instead, side 2, in its parallel form, will control the system voltage.

3.6.5 Phase 4

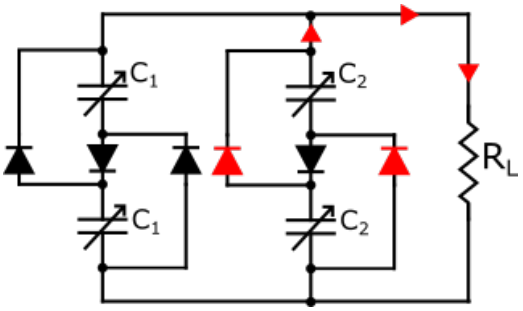

Figure 3.21: During phase 4, side 2 controls the system voltage in its parallel form.

Now, side 2,in its parallel form, controls the system voltage, similar to phase 1 scenario. By solving

$$0 = C_{2,\text{par}}\frac{dV}{dt} + V\frac{dC_{2,\text{par}}}{dt} + \frac{V}{R_L}, \tag{3.38}$$

for the system voltage, V,we are able to obtain the system voltage for the phase. Simultaneously, as the capacitance C_1 reduces, the voltage of side 1 reduces. Thus, the next transition point will happen when the voltage in side 1, given by,

$$0 = C_{1,\text{ser}}\frac{dV_{C_{1,\text{ser}}}}{dt} + V_{C_{1,\text{ser}}}\frac{dC_{1,\text{ser}}}{dt}, \tag{3.39}$$

reaches the system voltage, as time t_{45}. Such a transition point is graphically visualised in Figure 3.22.

3.6.6 Phase 5

In Phase 5, we have an analogous scenario to Phase 2, but with sides 1 and 2 in opposite situations, due to the 180° phase difference, as shown in Figure 3.23. As the capacitance C_2 reduces, it charges side 1 in its series form, while boosting the system voltage, as can be seen in Figure 3.24.

Phase 5 will end when side 2 is no longer able to supply charges to side 1, thus having its charges only drained by the leakage. As in Phase 2, the system voltage, $V(t)$, can be found by solving the equation

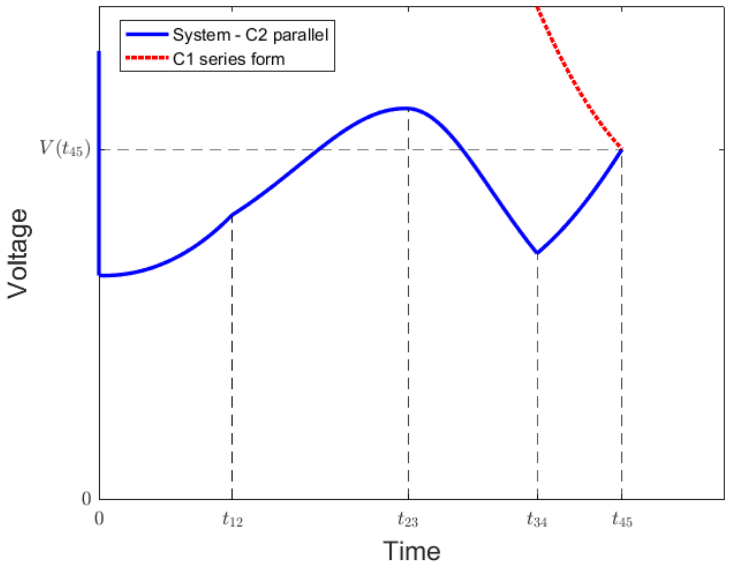

Figure 3.22: Voltage as a function of time during phase 4 of a ISPC cycle.

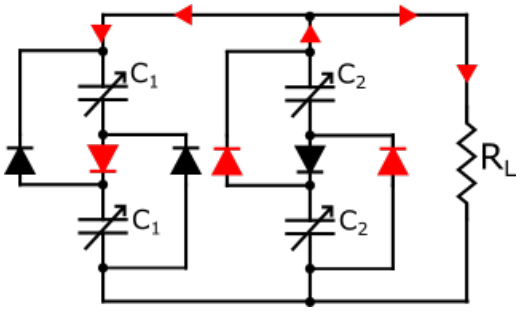

Figure 3.23: During phase 5, side 2, in its parallel form, delivers charge to the side 1.

$$0 = (C_{2,\text{par}} + C_{1,\text{ser}})\frac{dV}{dt} + V\left(\frac{dC_{2,\text{par}}}{dt} + \frac{dC_{1,\text{ser}}}{dt} + \frac{1}{R_L}\right), \tag{3.40}$$

while the current in side 1 is found through

$$i_{C_{1,\text{ser}}} = -\left(V\frac{dC_{1,\text{ser}}}{dt} + C_{1,\text{ser}}\frac{dV}{dt}\right). \tag{3.41}$$

When $i_{C_{1,\text{ser}}} = 0$, we then transition to the next phase. Table 3.1 summarises the cycles described, showing what is the active form for each phase and which side controls the system voltage.

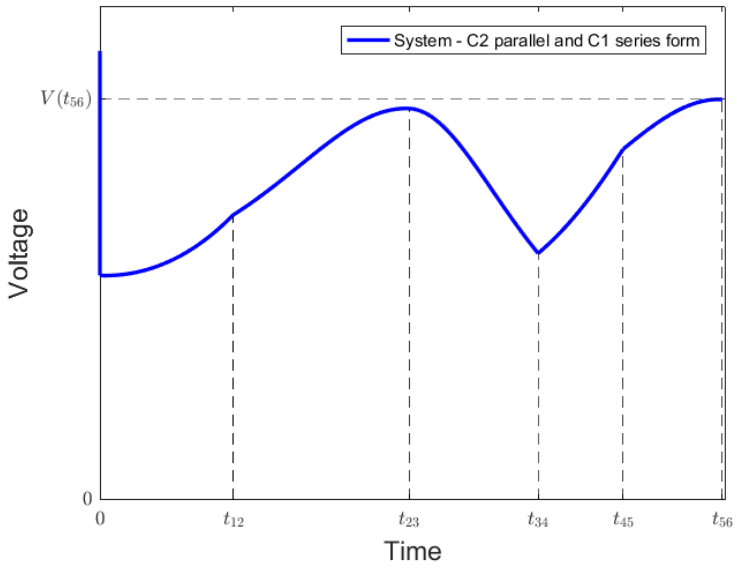

Figure 3.24: Voltage as a function of time during phase 5 of a ISPC cycle.

Table 3.1: ISPC Phases summary

Phase	Side 1 form	Side 2 form	Side controlling System
1	Parallel	Series	1
2	Parallel	Series	1 / 2
3	Parallel	Parallel	1
4	Series	Parallel	2
5	Series	Parallel	1 / 2

3.6.7 Next phases

As the cycle goes on, the following phase has the same dynamic as Phase 3 with the sides 1 and 2 in inverse positions. Therefore, as the systems cycles, it will repeat in sequence phases 2 to 4, with the alternation of position of sides 1 and 2, as described above.

3.7 Experimental validation

In order to validate our model, we compare it with results obtained through experiments. We use here data presented in [62], provided as part of the collaborative effort with the University of Auckland. The device used to deform the DEGs is shown in Figure 3.25; it consists of a reciprocating machine, driven by a geared electric motor, which, attached to a linear encoder, provides closed-loop control to ensure stable cycling behaviour. As shown in Figure 3.25, the

system consists of a 1st order ISPC ($n = 1$), containing two pairs of two DEGs each. The pairs are connected using GP02-40 diodes as an ISPC branch. The DEGs were made using a VHB4905 sheet (prestrained 374%) on which the electrodes were painted using a carbon doped silicone mix.

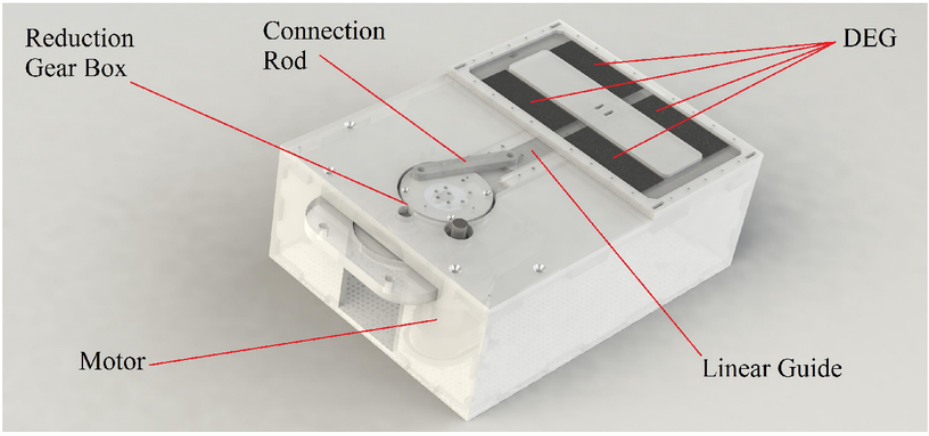

Figure 3.25: Reciprocating machine used for the ISPC experiments. A crank slider mechanism, moved by a motor, the linear guide attaches under the panel attached to the membrane with the DEGs and slides in a reciprocating movement. Reproduced from [62].

The capacitance of each of the DEGs in the system was measured using a Hioki IM3523 LCR meter, example results are shown in Figure 3.27. The target was to have a capacitance swing between 1.4nF and 3nF, given by

$$C(t) = [0.8\sin(2\pi f t) + 2.2]\text{nF}, \tag{3.42}$$

for a frequency $f = 1.01$Hz for the case investigated. Since the electrodes are hand painted, there is a clear mismatch in the capacitance values obtained for the experiment.

In order to determine appropriate parameters values for our proposed model, the method used in [61] to find the equivalent leaking resistance was used: allowing the SPC-DEG to discharge, the system voltage will eventually fall below that of the SPC's HC form (see point A in Figure 3.28a) and the system will be discharging from all its capacitive elements into the leakage element (as in Figure 3.28b), thus a simple regression based on a discharging RC circuit can be achieved using only two points (points B and C in Figure 3.28). Illustrating this method with the presented experiment, we consider the points with voltage $V_B = 679.079$V and $V_C = 607.063$V with the interval $\Delta t = t_C - t_B = 3.05$s. Since the discharge started from a peak, in voltage, it means that one of the ISPC sides was in its maximum deformation state, while the other in its minimum (or

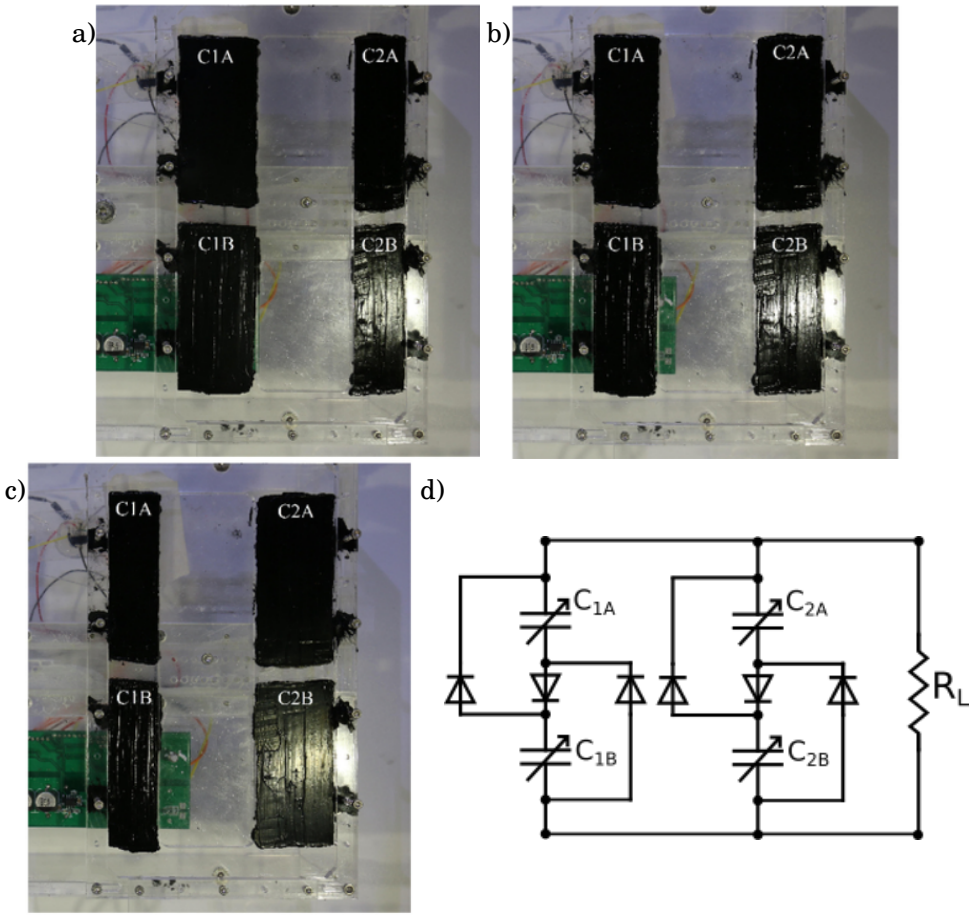

Figure 3.26: Positions of the DEG membranes in the reciprocating machine from Figure 3.25: a) DEG pair 1 in its maximum deformation, while DEG pair 2 is in its minimum configuration; b) both DEG pairs in their middle positions; c) DEG pair 2 in its maximum deformation, while DEG pair 1 is in its minimum configuration. d) Schematic showing circuit connections; R_L represents the leaking element in the circuit (high impedance voltage monitor).

close to), so we can approximate that the total capacitance discharge will be, generally,

$$C_{\text{eq,discharge}} = \frac{n+1}{n} C_{DEG_{max}} + \frac{n+1}{n} C_{DEG_{min}}, \tag{3.43}$$

in the present case providing an equivalent capacitance of $C_{\text{eq,discharge}} = 8.8\text{nF}$. As the discharge process can be described by

$$V_C = V_B e^{\frac{-\Delta t}{R_L C_{\text{eq,discharge}}}}, \tag{3.44}$$

thus the leakage resistance R_L can be easily found by rearranging to give

$$R_L = \frac{\Delta t}{C_{\text{eq,discharge}} \ln \frac{V_B}{V_C}}, \tag{3.45}$$

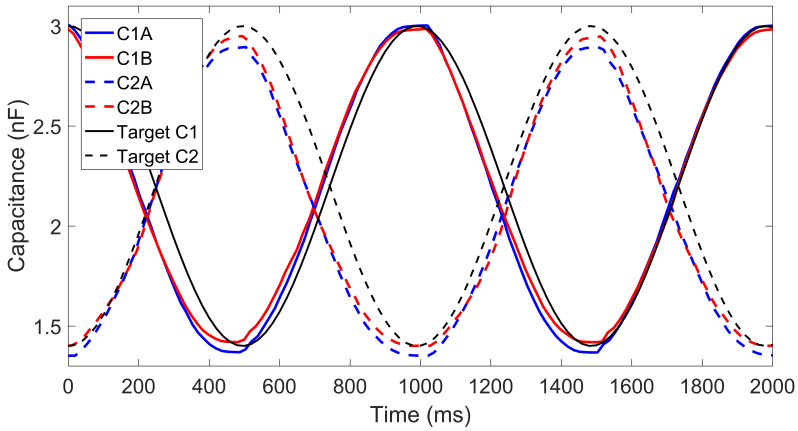

Figure 3.27: Capacitance measurements for the ISPC DEG membranes from the experimental setup

which provides an approximate value of $R_L = 3.1G\Omega$.

Inputting the expected capacitance change (1.4nF to 3nF) and the leakage resistance calculated above into the proposed model (section 3.6), implemented in MATLAB to perform the simulation (code can be found in Appendix A), the model provides a good fit, as shown in Figure 3.29. The differences between the cycles can be explained by the deviation in the capacitance swing from the experimental set up to the parameters used in the model. It can be illustrated by an analysis of the experimental voltage curve in Figure 3.29: not all the cycles boost in the same manner and the maximums and minimums found are not always evenly spaced. It demonstrates the need for adequate manufacture of ISPCs, as the imbalance reduces, and can even eliminate boosting for some cycles.

3.8 Conclusion

In this chapter, we explored the concept of self-priming circuits, introducing their development history and why they are a promising enabling technology for dielectric elastomer generators. We described the functioning of its most basic form, and also an integrated self-priming circuit design.

We have developed an analytical model that describes the physics behind each phase of the cycle of a SPC-DEG system with a load attached to it. To further understand the system, we explored the ideal scenario where no leakage exists on the system, promoting a simple closed-form analytic expression that describes the boost per cycle of the SPC-DEG system. These simplifications allowed us to derive the condition for the boost to exist assuming no losses, the

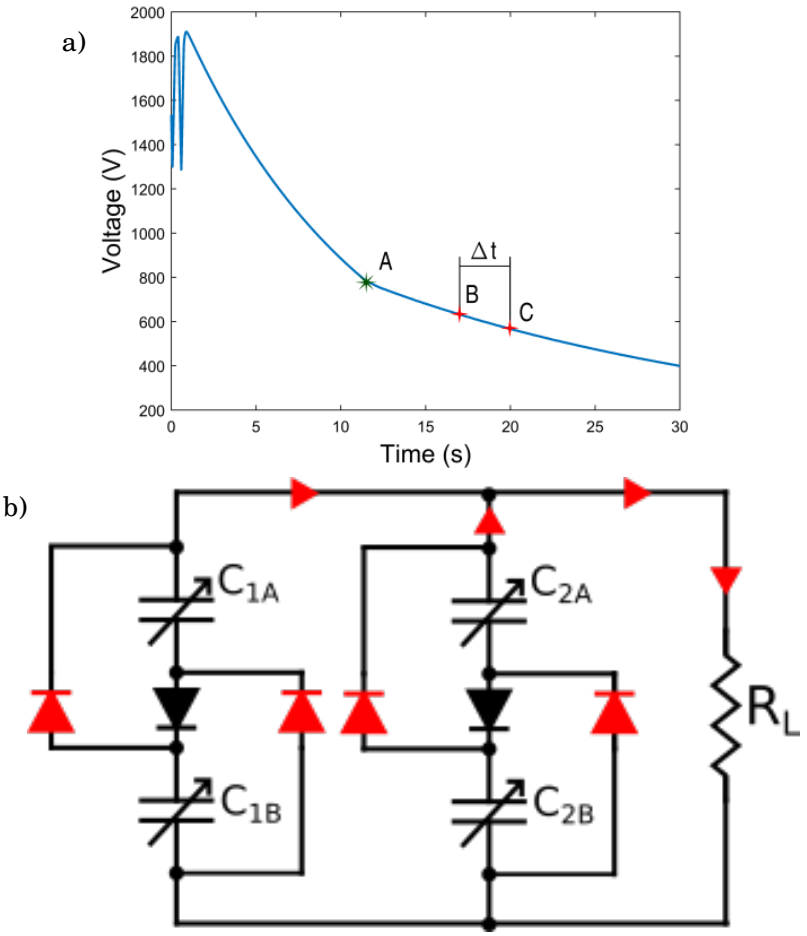

Figure 3.28: a) Voltage as a function of time for the ISPC discharging after a boosting cycle. b) Modelled circuit for the discharge scenario.

ideal parameters for the SPC design; we also demonstrated how their variation affects the final voltage boost. Using the same approach, we proposed a model for a general order ISPC and used it to successfully validate the modelling approach against experiments.

Being straightforward to implement, requiring a simple circuit attachment, SPCs are an ideal solution to implement DEGs in real-world energy harvesting systems, where active charge control is not a suitable option. ISPCs present better performance metrics, such as energy density and efficiency [92], but are limited by the possibilities of implementation of an antagonistic design, as well as requiring more careful manufacture to assure the DEGs have the adequate capacitance and swing.

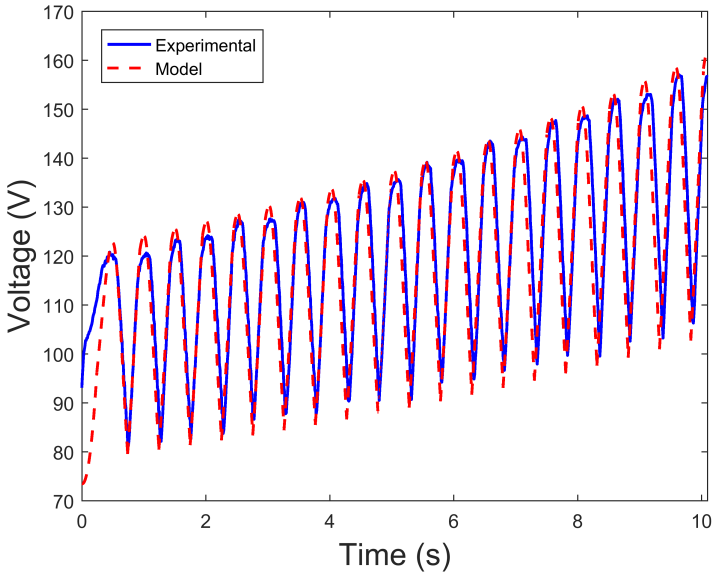

Figure 3.29: Voltage as a function of time for the model proposed compared to the experimental data.

Nonetheless, the present chapter analysed SPC/ISPCs under the hypothesis that DEGs can be represented as a simple variable capacitor, which Chapter 2 already showed does not hold for some situations, in particular, force-based scenarios. Such situations will be studied further in the next chapter.

CHAPTER 4

SELF-PRIMING DIELECTRIC ELASTOMER GENERATORS: ELECTROMECHANICAL COUPLING

In the previous chapter we investigated systems Dielectric Elastomer Generators attached to Self-Priming Circuits (SPC-DEG systems), ignoring the fact that their electrical state affects their mechanical behaviour through the actuator-like behaviour, which potentially affects the outcomes from the system. This approach is commonly followed in the SPC-DEG systems' literature, see, e.g. [61, 93, 96]. In contrast, in this chapter, we seek to investigate the effect of the actuator-like behaviour in SPC-DEG systems, both from a modelling point of view and also experimentally. More generally, we aim at complementing the current state of the art knowledge of SPC-DEG systems by taking into account their mechanical characteristics. We report how the actuator-like effect enables a previously unreported behaviour in SPC-DEG systems, in which the voltage level from such systems, expected to rise naturally as the material cycles unless part of the energy is extracted, is able to self-stabilise in a steady state voltage oscillation. We also demonstrate how modelling of SPC-DEG systems can predict such behaviour, how it can be explored to avoid failure modes and, through an experimental investigation performed by the author during his time at the University of Auckland, we demonstrate a practical method to predict the self-stabilisation before it occurs on systems already built. This chapter is partially based on the paper "Self-stabilizing Dielectric Elastomer Generators" [156].

4.1 Introduction

While SPC-DEGs have been considered as a component in a range of studies, such as different layouts [63, 92, 97], modelling approaches [61, 154] and energy extraction mechanisms [59], most approaches in literature consider DEGs solely as variable capacitors undergoing a cyclic

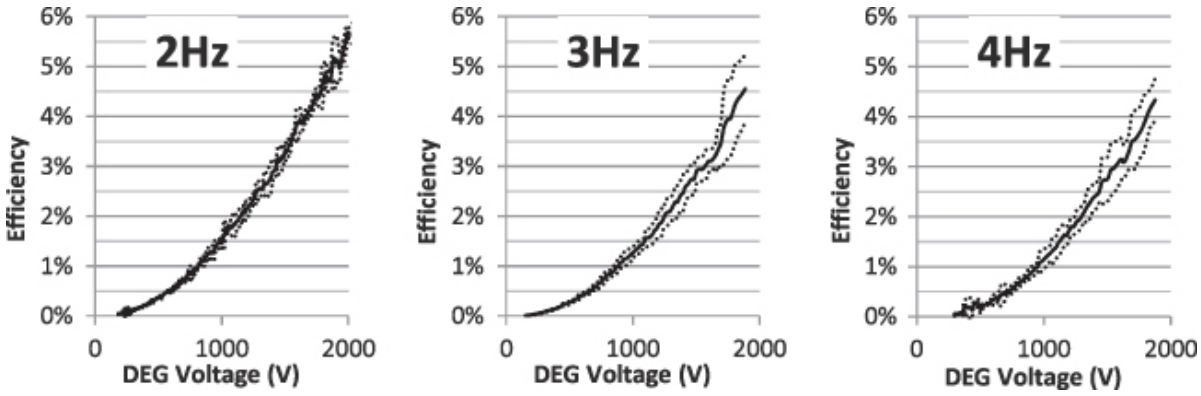

Figure 4.1: Efficiency of a first order SPC-DEG system at different voltages for experiments [93] performed by mechanically displacing the DEG at 2Hz, 3Hz and 4Hz. Seven point moving average (Solid line) and plus/minus one moving average (dotted lines). Reproduced from [93]

capacitance variation between fixed maximum and minimum values. Nonetheless, as shown in Chapter 2, the electrical state of a DEG does affect its mechanical behaviour and, consequently, the system as a whole. A starting point to investigate the electromechanical behaviour of SPC-DEG systems is the analysis of the mechanical-to-electrical energy conversion efficiency: the ratio between electrical energy surplus in the system and mechanical work done at each cycle, from now on designated only as efficiency. In [93], as shown in Figure 4.1, the efficiency was computed for different excitation frequencies and shown to increase as DEG voltage rises, and decrease as the mechanical excitation of the DEG increases. Due to the capacitive nature of SPCs, the increase in voltage from the DEG means more charges are being displaced when the DEG relaxes, thus increasing the electromechanical energy conversion and the efficiency as a consequence. However, due to the viscoelastic nature of DEGs, the higher the frequency – i.e. the faster the membrane displacement – the higher the viscoelastic losses, thus more mechanical work has to be performed to provide the same range of displacement. Consequently, the higher frequency ends up providing higher mechanical losses and decreasing the energy efficiency. Still regarding parameters that affect efficiency, although not included in the analysis performed in [93], low-frequency excitation might also decrease the DEG performance, as the dielectric membrane might present significant leakage for low-frequency excitation [155].

In [97], the performance of Integrated Self-Priming Circuits (ISPCs) using Dielectric Elastomer Switches (DES) [105], and ISPCs using diodes were compared. Such results, illustrated in Figure 4.2, show us a different trend regarding the relation between frequency and efficiency, where efficiency increases when excitation frequency increases. Although the study claims higher frequency provides higher power, it contradicts the previous study [93] and other investigations regarding DEG behaviour [36, 155] claiming the losses remain constant. As the efficiency remains constant for the “soft” ISPC-DEG between excitation frequencies of 1Hz and 2Hz, the author does

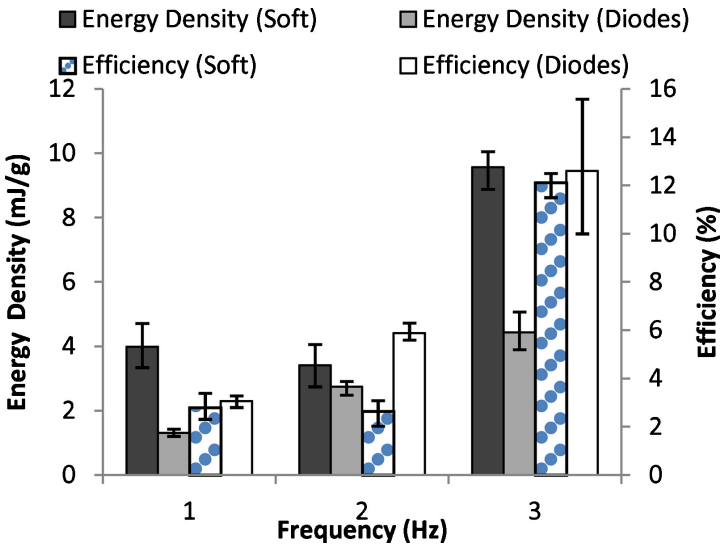

Figure 4.2: Energy density and efficiency for ISPC systems using DES (soft) and diodes. Reproduced from [97]

point to the need of further studies to better understand these systems.

The point of view that deals with DEGs as variable capacitors, mostly based on the position-based cycle approach explained in Chapter 2, contrasts with the fact there is a lack of studies investigating SPC-DEG systems in force-based scenarios. Since the boost behaviour induced by SPCs is dependent on the capacitance swing the DEG undergoes, it is expected that the actuator-like behaviour described in Chapter 2, by provoking further deformation, might affect such boost. As the voltage of the DEG increases, the actuator-like behaviour becomes more evident and we have further deformations of the membrane, leading to a change of the maximum and minimum values of capacitance swing of the DEG.

In this chapter, we investigate the DEG-SPC systems, taking into consideration the actuator-like behaviour. As such, we are able to verify how the actuation-like behaviour of the DEG interferes with the boosting effect of the SPC. To do so, in section 4.2, we start from a quasi-static analytical model and compare with simulations of an integrated fully dynamic numerical model. We evaluate, using the numerical model, the trends in the frequency response analysis of the observed behaviour. Section 4.3 discusses the simulation results and how it provides tools to better understand and predict such stabilisation behaviour in order to allow safer SPC-DEG system design. In section 4.4, we report a series of experiments in SPC-DEG systems where we analyse the consequences of the electromechanical coupling on its outcomes, analysing the energy conversion efficiency and how the self-stabilising behaviour is manifested. Finally, in section 4.5, we use the data obtained from the experiments to demonstrate a method to predict the self-stabilising behaviour.

4.2 Model approach

In contrast to conventional actuator behaviour, in a DEG, the maximum electric field will occur during the minimum stretch in a cycle for a constant charge cycle [47]. As the major boost in a SPC-DEG system (Phase 1 of SPC cycle described in section 3.3.1) happens when no charge is flowing between the SPC and DEG system, a consequence is that the electric field — and the electrostatic stress normal to the membrane — is higher when the DEG is in its minimal stretch state. Thus, we hypothesise an increased effect of the actuation behaviour in the minimum stretch position compared to that in the maximum, and so the capacitance swing, $C_{\mathrm{DEG}_{\mathrm{max}}}/C_{\mathrm{DEG}_{\mathrm{min}}}$, will change cycle-by-cycle, since we expect $C_{\mathrm{DEG}_{\mathrm{min}}}$ to increase more than $C_{\mathrm{DEG}_{\mathrm{max}}}$.

To investigate such behaviour, we start from the model that predicts the boost at the end of a cycle, provided by eq. (3.24), to represent the behaviour of an ideal DEG-SPC system without electric load attached: the energy harvested in one cycle is completely used to prime the following one, thus using eq. (3.24) to describe the voltage gain at each cycle. Although it was obtained on a pure electrical analysis, it provides us with the means to start to analyse when the voltage boost is affected. Rewriting eq. (3.25) to simplify the present analysis, we have that boost will only happen in the system if:

$$C_{\mathrm{DEG}_{\mathrm{max}}} > \omega^2 C_{\mathrm{DEG}_{\mathrm{min}}}, \tag{4.1}$$

where

$$\omega^2 = \frac{n+1}{n}. \tag{4.2}$$

Considering a system with a fixed number of stages, n, if the capacitance swing is reduced, it will certainly affect the boost and will ultimately limit it, in view of the condition expressed in eq. (3.25) and demonstrated in Figure 3.10. In this case, we have that, in the limit where no boost happens,

$$\frac{C_{\mathrm{DEG}_{\mathrm{max}}}}{C_{\mathrm{DEG}_{\mathrm{min}}}} = \omega^2, \tag{4.3}$$

leading to

$$\frac{\lambda_{\mathrm{max}}}{\lambda_{\mathrm{min}}} = f(\omega), \tag{4.4}$$

where λ_{min} and λ_{max} are, respectively, the minimum and maximum stretch ratios the material experiences in the cycle. The function f will depend on the geometry and type of stretch the material is subjected to (pure-shear, equibiaxial, etc.).

Analysing further the model described in Chapter 3, we can compute the ratio between the maximum and minimum voltage inside of a cycle using eq. (3.17), eq. (3.20) and eq. (3.22), yielding

$$\frac{V_{\max}}{V_{\min}} = \omega^2 \left(\frac{C_{\mathrm{SPC_{HV}}} + \omega^{-2} C_{\mathrm{DEG_{max}}}}{C_{\mathrm{SPC_{HV}}} + C_{\mathrm{DEG_{min}}}} \right). \tag{4.5}$$

Inserting eq. (4.3) into eq. (4.5) leads to the relation between maximum ($V_{\max}$) and minimum voltage ($V_{\min}$) oscillation in that hypothesised limit situation to be

$$\frac{V_{\max}}{V_{\min}} = \omega^2. \tag{4.6}$$

In a force-based scenario, as explained in section 2.1, where the movement is bounded by the maximum force, F^+, and minimum force, F^-, we look for a stable periodic solution where there is no voltage boost between cycles, due to the change in the capacitance swing given by the increase in voltage levels. To do so, we use the relation between force, F, stretch ratio, λ, and voltage, V, described by the function $F = h(\lambda, V)$, dependent on the electromechanical model chosen. At the known boundaries of minimum and maximum force, this gives

$$F^- = h(\lambda_{\min}, V_{\max}) \tag{4.7}$$

$$F^+ = h(\lambda_{\max}, V_{\min}), \tag{4.8}$$

which together with eq. (4.3) and eq. (4.4) gives a closed system for $\lambda_{\min}$, $\lambda_{\max}$, $V_{\min}$ and $V_{\max}$. Although this requires a numerical solver for most realistic examples, we are able to provide an analytical solution for a small set of cases. For example, considering a Neo-Hookean model in pure shear conditions with quasi-static forcing (hence neglecting dynamic effects), we can use the model proposed in Chapter 2,

$$F_x = \frac{Vol}{x_0} \left(G - e_r e_0 \left(\frac{V}{z_0} \right)^2 \right) \lambda_x - \frac{VolG}{x_0 \lambda_x^3}, \tag{4.9}$$

where F_x is the applied force, G is the shear modulus, λ_x is the stretch ratio in the forcing direction, e_r is the material relative permittivity, e_0 is the vacuum dielectric permittivity, V the applied voltage, Vol the material volume, z_0 the initial thickness and x_0 is the material initial length in the forcing direction. Note that the (ideal) quasi-static forcing means this is independent of frequency. For this specific case, we can define the ratio

$$\beta = F^+ / F^-. \tag{4.10}$$

In addition, in the case of pure shear configuration, as the capacitance can be described by

$$C_{\mathrm{DEG}} = C_0 \lambda_x^2, \tag{4.11}$$

where C_0 denotes the capacitance in the reference state where $\lambda_x = 1$, we can write for any cycle, using eq. (4.4),

$$\lambda_{\max}/\lambda_{\min} = \omega. \tag{4.12}$$

Solving the system composed by eq. (4.9), eq. (4.10) and eq. (4.12), with boundary conditions as described in eq. (4.7) and eq. (4.8), we find

$$\lambda_{\min} = \frac{x_0 F^-}{VolG\hat{\omega}} \tag{4.13}$$

where $\hat{\omega} = (\omega^4 - 1)/(\beta\omega^3 - 1)$, and

$$V_{\max} = z_0 \sqrt{\frac{G}{e_0 e_r}} \left(1 - \hat{\omega} - \left(\frac{VolG\omega}{x_0 F^-}\right)^4\right)^{1/2} \tag{4.14}$$

is the maximum voltage we can obtain from such a DEG-SPC system in its stable condition. Values of $\lambda_{\max}$ and $V_{\min}$ can be found through eq. (4.6) and eq. (4.12) in a straightforward manner.

To validate the analytical model proposed above, we used a Simulink model, as described in Chapter 2, adapted with SimElectronics components, to build the SPC in a SPICE-like manner. This model is fully time-dependent and, thus, explicitly includes the effects of forcing frequency. To compare with the analytical model, we considered a 0.2 Hz (not static, but slow enough to minimise the effects of viscosity, leakage and inertia) sinusoidal forcing between $F^- = 1$ N and $F^+ = 3$ N. The material dimensions are $x_0 = 5$ cm, $z_0 = 50$ μm, $\frac{Vol}{x_0 z_0} = 15$ cm, and the shear modulus $G = 138$ kPa, obtained from the Yeoh model used by Wissler and Mazza [147] for 3M VHB 4910 dielectric adhesive tape, with the corresponding dielectric relative permittivity $e_r = 4.7$ reported in the same work. The viscoelastic behaviour was simulated using the same damping model and parameters from Chapter 2 simulations. The SPC has a single stage, $n = 1$, and maximal capacitance $C = 25$ nF (optimal for the initial capacitance swing as computed by eq. (3.26)). The resulting dynamics, for the first 120 cycles, are shown in Figure 4.3.

To investigate further how the dynamics would affect the reported self-stabilising effect, we also performed, using the numerical model, a frequency sweep between 0.2 Hz and 3 Hz. In this model we consider effects such as viscoelasticity, using the same viscoelastic model and parameter described in Chapter 2, and current leakage through the DEG membrane, modelled through a resistor (>1TΩ) parallel to the variable capacitor in the DEG model, although we still consider the SPC to be ideal. As resonant frequencies would be dependent on application/design, we do not consider inertial effects in the numerical simulations, setting the model mass to 3g, yielding resonant peaks at frequencies much higher than the ones explored in this investigation.

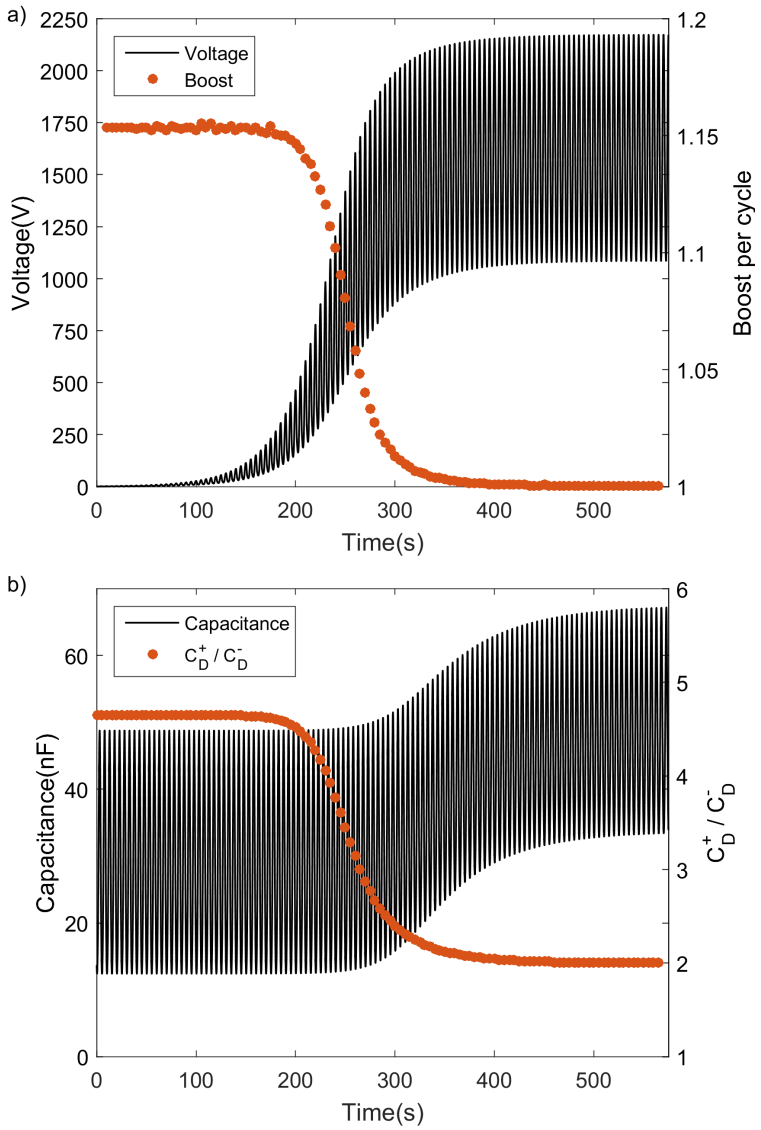

Figure 4.3: Time-domain dynamics of the Simulink model DEG-SPC system with force based cycling: voltage and boost per cycle (a), capacitance and capacitance swing per cycle (b).

4.3 Results and discussion from model analysis

As seen in Figure 4.3a, obtained from the numerical model, the DEG experiences an exponential increase in the voltage levels for the first few cycles, but as the voltages increases and the capacitance swing reduces (Figure 4.3b), the voltage gain between cycles starts to decrease until it reaches a steady state. According to the proposed analytical model we expect to have, in the steady state, a voltage oscillation between 1087 V and 2174 V, close to that obtained from the simulation, between 1085 V and 2173 V, justifying the quasi-static approach. The difference (<0.2%) can be explained by the dynamics (such as current leakage through the membrane and viscosity) which are taken into account in the Simulink model but not in the ideal analytic model. The corresponding capacitance change over time is shown in Figure 4.3b. In the first 40 cycles, the capacitance swing is almost constant, between 11.6 nF and 53.8 nF. As voltage increases, the minimum capacitance increases to 36.2 nF and the maximum to 72.4 nF, thus changing the ratio C_D^+/C_D^- from 4.64 to 2 and equilibrating there as the DEG-SPC system stabilizes. Inserting these values into (1), we have a decrease in boost, B, from 1.17 in the first cycle, to 1, i.e. no further gain.

Regarding the dynamic response, a higher frequency forcing yields higher viscoelastic forces and, therefore, reduced capacitance swing, as seen in Figure 4.4a. Consequently, the boost in the initial cycles is also smaller. Figure 4.4b shows the consequences of the reduced boost: since the boost per cycle is smaller, it takes more cycles for the system to achieve the steady state. In addition, the frequency increase will reduce the final maximum voltage achieved, as seen in Figure 4.4b, since the viscoelastic forces reduce the maximum stretch achieved. It is important to note that such results do not take into account other limiting practical factors such as a charge leaking between the voltage terminal and ground, which could be either due to a monitoring system, a continuous energy extraction circuitry, or even poor manufacture. Such leaking would drain part of the charge in the DEG that promotes the energy conversion each cycle, thus reducing the boost for a given capacitance swing. Thus, the boost per cycle, as shown in Figure 4.3, would be reduced, delaying the effect of the self-stabilisation effect (shown as a boost drop in Figure 4.3), and also the number of cycles that would be required, after the boost starts to decrease, for it to reach 1. Consequently, we would expect a flattening or trend inversion at some point for the curves shown in fig. 4.4b, lowering the maximum voltage and increasing the number of cycles for the steady state for low frequencies.

More fundamentally, the analytical model allows us to investigate and better design DEG-SPC systems by, for example, using the stabilisation to avoid failure modes. Figure 4.5 shows the maximum voltage at steady state, according to the analytical model as a function of the force swing, β and number of SPC stages, n, for $F^- = 1$ N. We can use these results to impose desired maximum electric field and maximum stretch ratio, and then design the number of stages according to the forcing (or vice-versa). In this way, the system will stabilise before failure,

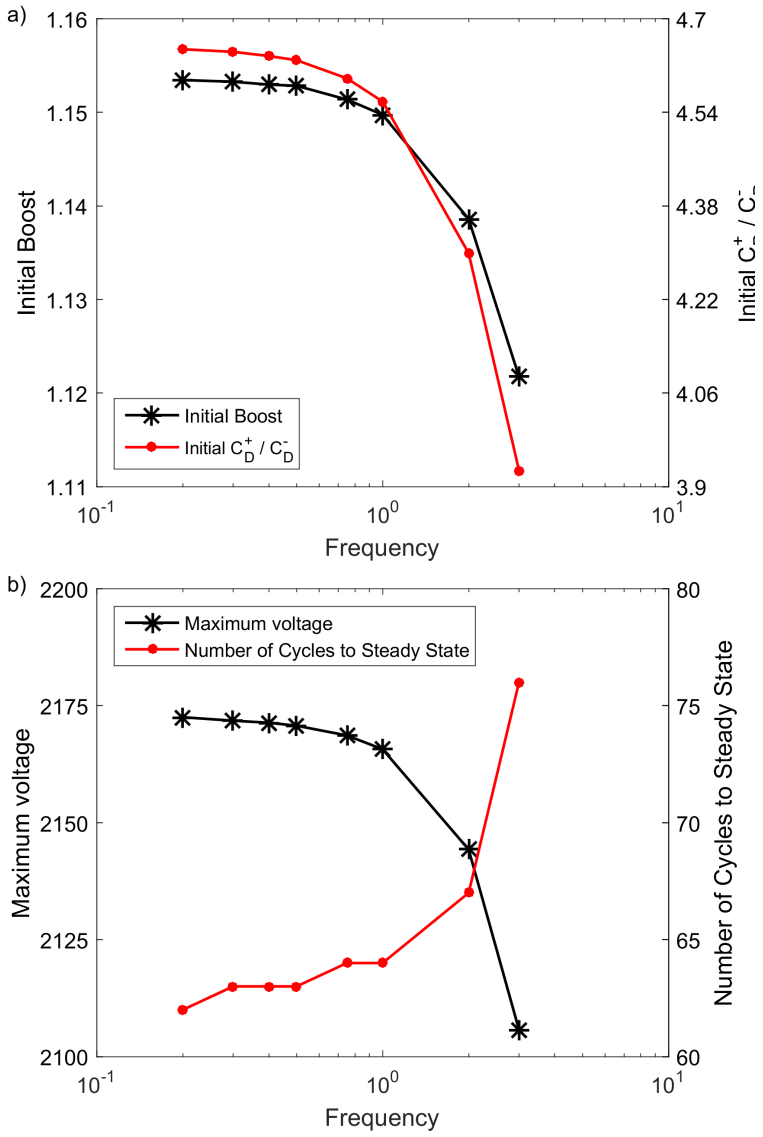

Figure 4.4: Self-stabilisation metrics shown for different excitation frequencies: initial boost and capacitance swing (a), maximum voltage achieved in the steady state and number of cycles before stabilising (b).

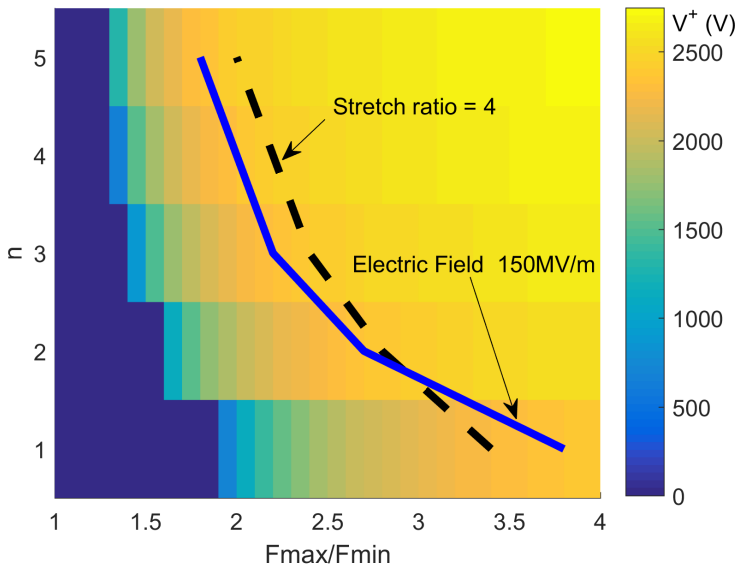

Figure 4.5: Maximum voltage in a stabilised state of the DEG-SPC system for different number of stages and forcing amplitudes. Solid blue line indicates the state for each number of stages and force swing that corresponds to 150MV/m, while dashed black line indicates a stretch ratio of 4.

exploiting the inherent nonlinear dynamics of the system as a passive controller. In case we increase F^-, more force will be needed to obtain a higher force ratio F^+/F^-, thus leading to a higher stretch ratio, bringing the material closer to failure. Note that the material stiffness change resulting from its stretch will play an important role; if the DEG operates in a softer region of its stress-strain curve, a bigger capacitance swing can be obtained for the same force ratio, as in the first cycles, thus leading to a faster approach to the steady-state and higher voltage. Moreover, as seen in Figure 4.4b, the quasi-static case leads to an overestimation of the final steady-state maximum voltage, implying there is an additional safety factor in this method for the maximum voltage/electric field achieved.

4.4 Experimental work

4.4.1 Setup

To further investigate the electromechanical characteristics of SPC-DEG systems, experimental work was performed using a simple SPC design of 1st order ($n = 1$) and main capacitance value, C_{SPC}, of 1.886nF. The system used the load cell SM-50, manufactured by Interface, attached to the reciprocating machine used in the experiments reported in Chapter 3, as seen in Figure 4.6a. The displacement was measured using a laser displacement sensor model ILD 1302-200, manufactured by Micro-Epsilon, the SPC-DEG system voltage was measured through a 5GΩ

(a)

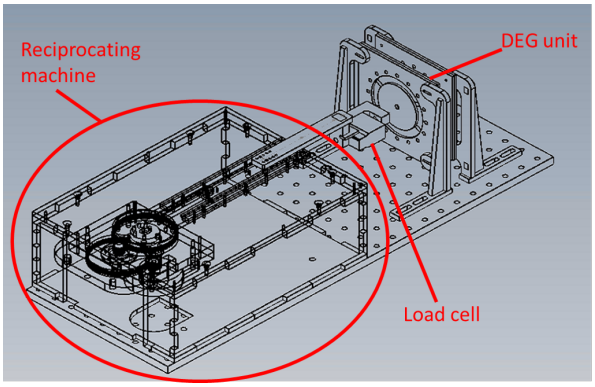

(b)

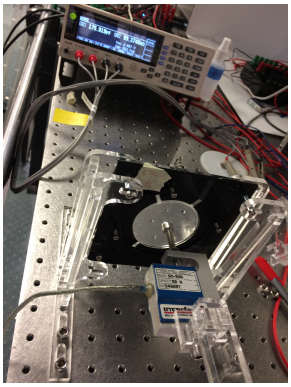

Figure 4.6: Scheme of the experimental setup used (a). DEG membrane assembled in the test rig: as the reciprocating machine cycles, it is pushed out of plane to be deformed.

impedance voltage divider (1000:1), and the data recording was made using National Instruments software LabVIEW.

With the system fully discharged, the DEG capacitance swing was measured in a no charge scenario using a Hioki IM3523 LCR meter, profile shown in Figure 4.7. The dielectric elastomers were made using Wacker ELASTOSIL Film 100μm equibiaxially pre-stretched by 23% and coated with a carbon doped silicone mix – 0.4g of Vulcan XG72R carbon black, 4g of Elastosil LR3162 (2g part A, 2g part B), 12g isooctane and 12g isopropyl – through spray coating to make the electrodes. The elastomers were stuck to the frames creating a cone design, as shown in Figure 4.6b, with an internal diameter of 6cm, and an external diameter of 8cm.

Although the setup used provides a displacement-based, rather than a force-based cycle, as used in the models earlier in this chapter, it still allows further deformation of the DEG as its voltage increases. This is due to the membrane pre-stretch; when the DEG is deformed out of plane, it can deform further, providing some relaxing in the membrane, if the electrostatic forces actuate over it, as indicated in Figure 4.8.

4.4.2 Results

Figure 4.9 shows the force versus displacement curves for the DEG deformation cycle for four different frequencies tested. It is possible to visualise the viscoelastic behaviour of the dielectric elastomer by the increasing hysteresis in the curves for higher oscillation frequencies. This data was then used to estimate the amount of mechanical energy damped at each cycle. It would be expected that higher voltages would allow for higher energy conversion, therefore damping more mechanical energy and increasing the area enclosed by the curves shown. Since the majority of damping happens due to the viscoelasticity and signal logging was subjected to noise, such effect

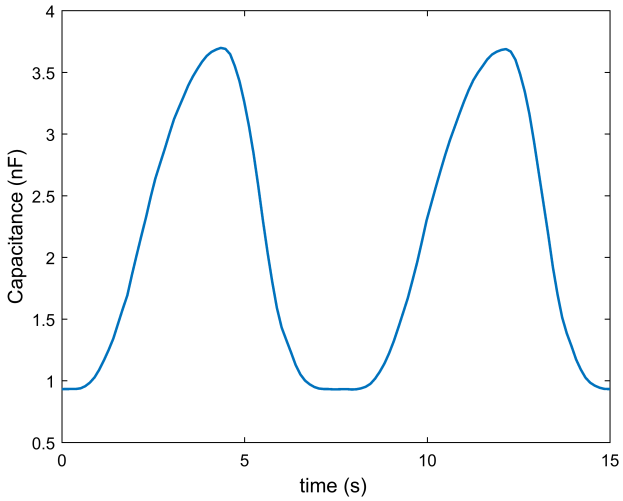

Figure 4.7: Capacitance curve measured for the DEG used while deformed through the reciprocating machine.

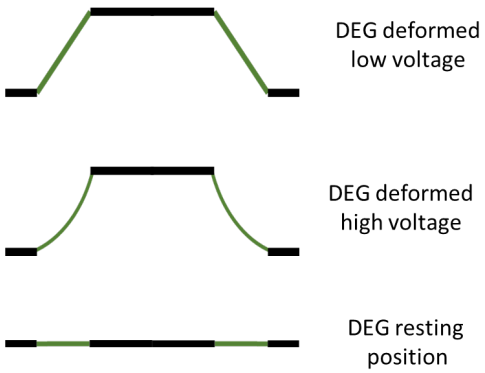

Figure 4.8: Indication of the degree of freedom available for further DEG deformation under high voltage conditions.

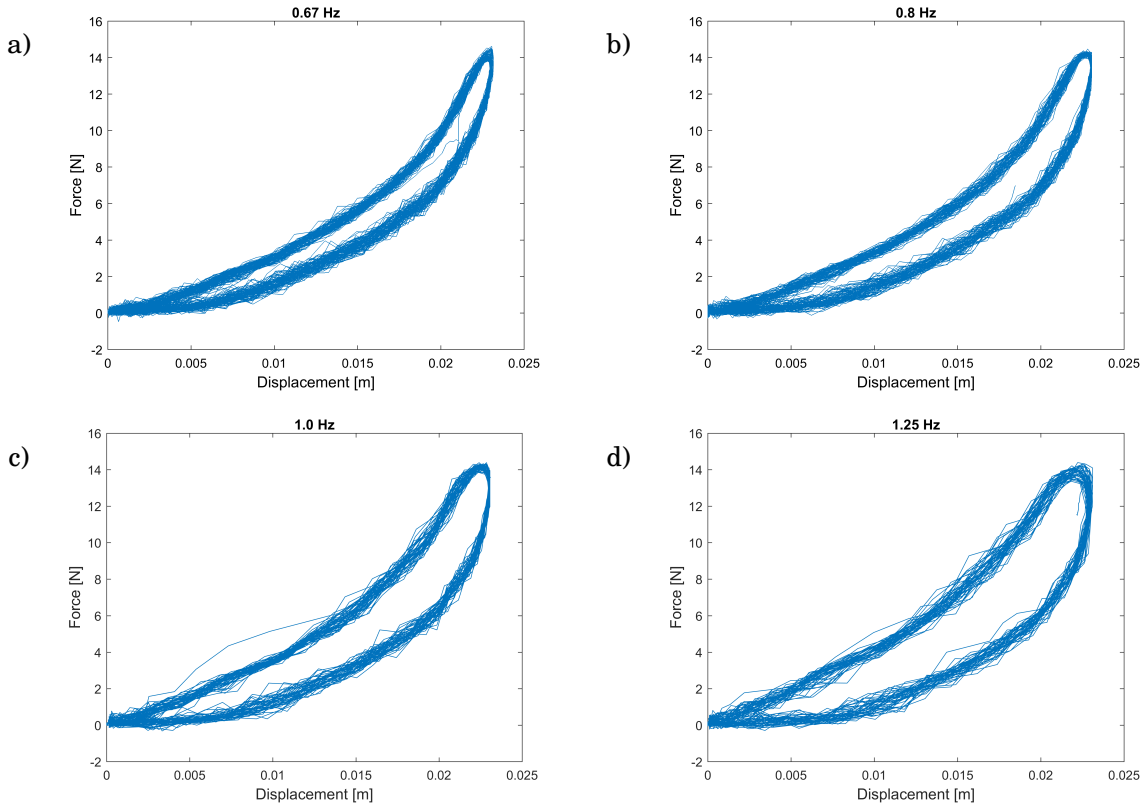

Figure 4.9: Force as a function of displacement for different frequencies: 0.67Hz (a), 0.8Hz (b), 1Hz (c), and 1.25Hz (d).

is not visible in the data obtained. Filtering the data would distort the signal as the digital load cell amplifier, together with the LabVIEW live interface, limited the sampling rate to 50Hz.

Figure 4.11 shows the voltage as a function of time for each cycle. The experiments were stopped as soon as the voltages approximated 2500V to avoid the dielectric breakdown of the sample. As the voltage measurement device presents an impedance of 5GΩ and the DEG sample used has a capacitance in the order of nF, the leakage has a significant impact on the results seen. Low frequencies, in this case, means a bigger interval between each energy harvesting cycle during which part of the electrical energy stored would be dissipated through the leakage element. Thus the higher the frequency, the higher is the voltage boost, since there is less time for the charges to leak from the SPC-DEG system between cycles.

Regarding the existence of the self-stabilising effect, when boost ceases, further evidence can be seen in the results of boost per cycle, shown in Figure 4.10. Here, even for the higher frequencies, such as 1Hz and 1.25 Hz, where the stabilising trend cannot be seen in Figure 4.11, we observe a progressive boost reduction from the first cycles to the later ones. It can be seen that as the

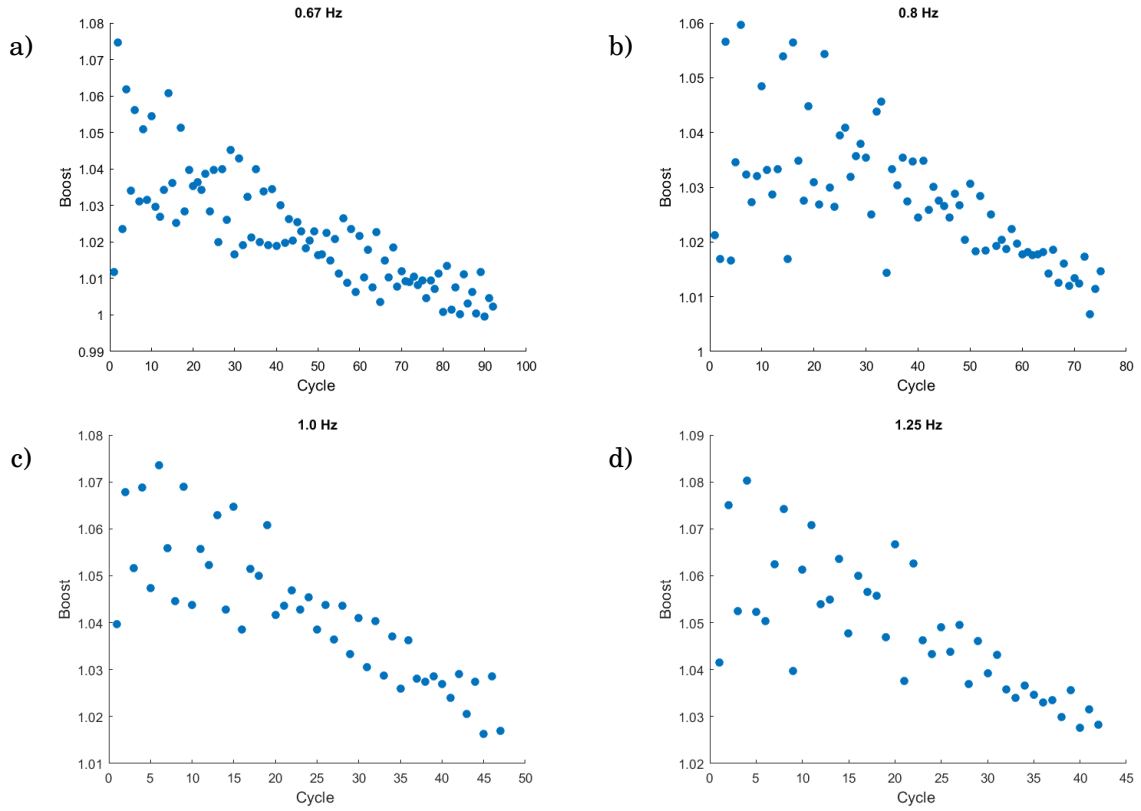

Figure 4.10: Boost per cycle at different frequencies: 0.67Hz (a), 0.8Hz (b), 1Hz (c), and 1.25Hz (d). Boost is computed as the ratio between maximum voltage in a cycle and that of the previous cycle.

system cycles, the boost presents a decreasing trend. Note that the higher variability in the first cycles is due to the noise in the measurement system: as voltage increases, the signal-to-noise ratio increases and the voltage boost calculation becomes more accurate.

On closer inspection, we see a clear stabilising behaviour in Figure 4.11 for lower frequencies, as the models derived earlier in the chapter predicted, which does not appear so clear for the higher frequencies. Such behaviour can be explained by both the electromechanical coupling, as explained earlier in the chapter, and the leakage. The actuator-like behaviour induced by the increasing voltage in the system reduces the capacitance swing, which further reduces the voltage boost. On the other hand, such behaviour is not enough to stop the boosting for the higher frequencies, meaning by itself it cannot explain the stabilisation. In addition, if we had no charge leakage, it would be expected that cycles that start with a boost, would either have their voltage rising indefinitely until failure, as described in the no losses models from Chapter 3 or that the self-stabilisation would happen earlier for higher frequencies, as analysed in Figure 4.4. In contrast, as we include losses, the voltage boost per cycle is then reduced. However, if

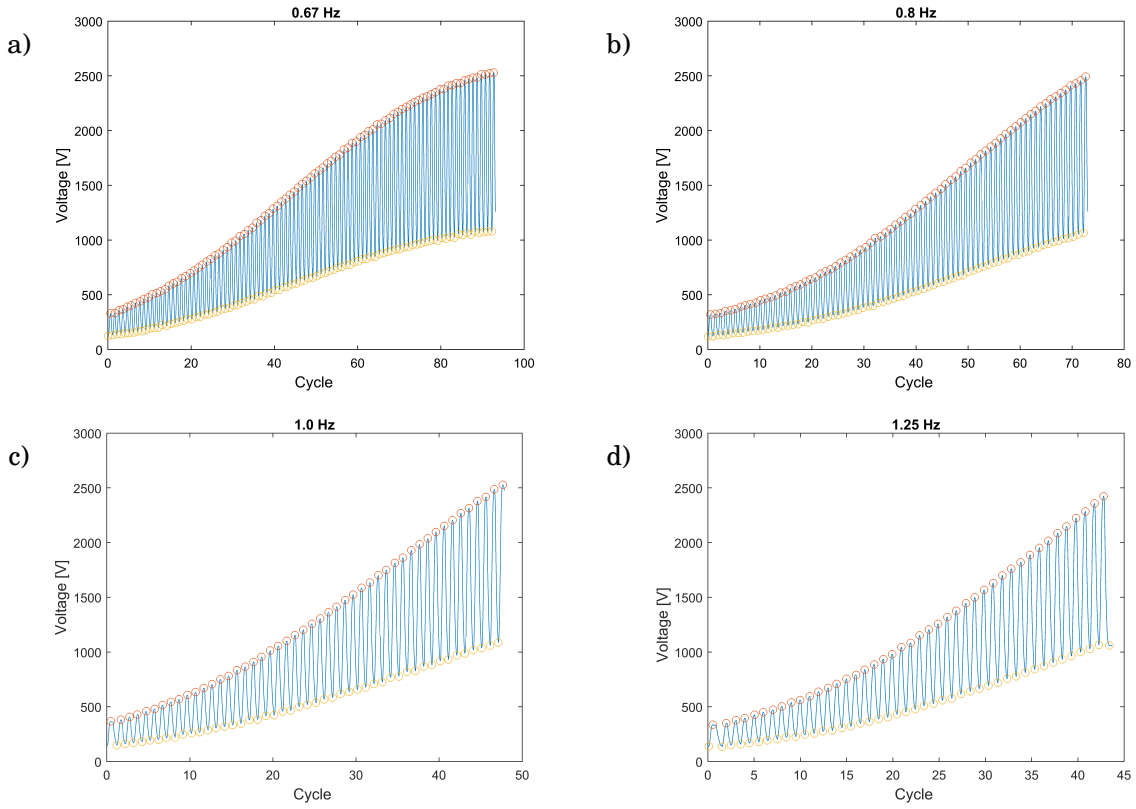

Figure 4.11: Voltage as a function of time (normalised by cycle period): 0.67Hz (a), 0.8Hz (b), 1Hz (c), and 1.25Hz (d).

charge leakage was enough to stop boost, one would expect that the voltage boost would have been inhibited from the first cycles at low voltage, which is not the case. When putting both these factors together, we are able to explain the behaviour seen in the experimental results satisfactorily.

Extra evidence of actuator-like behaviour in the DEG can be seen in Figure 4.12, which shows force (measured by the load cell) as a function of time. As time increases, the voltage increases and the force peak is attenuated, as the negative slope in the maximum force per cycle (orange circles) in all four panels of Figure 4.12 indicates. Note that the small difference between the forcing at different frequencies as shown in Figure 4.12 is an indication of the low viscous damping presented by the silicone membrane used.

Another important factor to analyse, as highlighted in the introduction of the present chapter is the energy harvesting efficiency, as shown in Figure 4.13. In Figure 4.13a, we plot the efficiency, η, with calculation method described in [93], where the efficiency η_i is defined per cycle according to

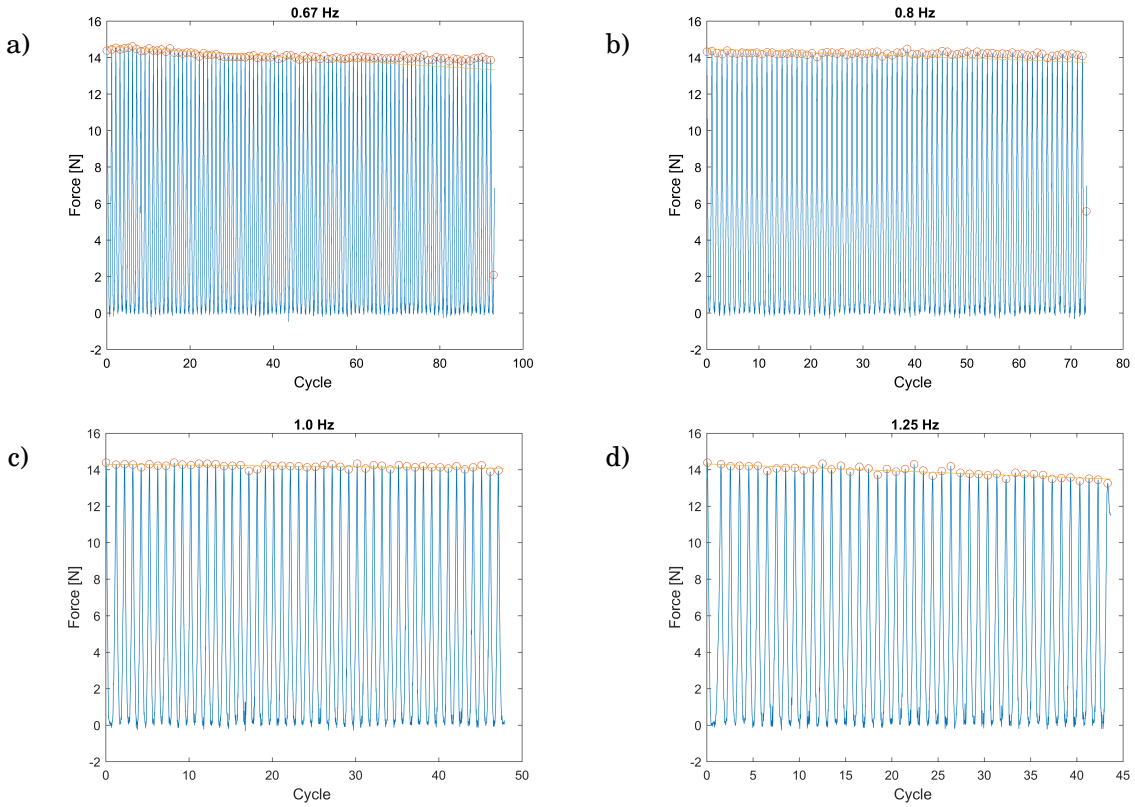

Figure 4.12: Force as a function of time (normalised by cycle period): 0.67Hz (a), 0.8Hz (b), 1Hz (c), and 1.25Hz (d).

$$\eta_i = \frac{\Delta U_{\text{stored},i} + U_{\text{loss},i}}{U_{\text{mech\_damp},i}}, \tag{4.15}$$

where $U_{\text{mech\_damp},i}$ is the mechanical energy damped in a cycle, $\Delta U_{\text{stored},i}$ is the change in energy stored in the system (SPC + DEG) resting capacitance, C_{system}, and $U_{\text{loss},i}$ is the energy dissipated through the leakage in a cycle i. The mechanical energy damped, $U_{\text{mech\_damp},i}$, is calculated through the integration of the force signal F along the displacement, x, between the start, T_i, and end of a cycle, T_{i+1}, as

$$U_{\text{mech\_damp},i} = \sum_{j|t_j \in [T_i, T_{i+1}]} F_j (x_j - x_{j-1}). \tag{4.16}$$

The variation of energy stored in the system is calculated by

$$\Delta U_{\text{stored},i} = \frac{1}{2} C_{\text{system}} (V_i^2 - V_{i-1}^2), \tag{4.17}$$

where V_i is the peak voltage during a cycle, and $C_{\text{system}} = C_{\text{SPC}} + C_{\text{DEG}}$, which was calculated taking C_{DEG} as the minimum of the function displayed in Figure 4.7. The electrical energy dissipated, $U_{\text{loss},i}$ is calculated by integrating the power dissipated in the leakage resistance R_L over a cycle, as described by

$$U_{\text{loss},i} = \sum_{j|t_j \in [T_i, T_{i+1}]} \frac{V_j^2}{R_L}(t_j - t_{j-1}). \tag{4.18}$$

When comparing the efficiency measurements obtained from the above calculations for the experiments performed, shown in Figure 4.13a, we first note that the order of magnitude is similar, 0–5%, to those found in [93]. Secondly, we note that we have a trend similar to that obtained in [93]: as frequency increases, the efficiency decreases for a given voltage and as voltage increases, the efficiency also increases. The first effect could be explained by two different factors: 1) higher frequency implies higher viscoelastic damping, which therefore increases the denominator of the fraction that defines η; 2) $U_{\text{loss},i}$ is continuously increasing through time as the charges leak through the measurement device, and slower cycles tend to increase this effect. It should be noticed, however, that efficiency will likely depend on a series of design factors, such as dimensions, material and even the electrode fabrication, thus not being directly comparable.

When we consider the stored energy conversion metric, $\eta_{\text{stored},i} = \frac{\Delta U_{\text{stored},i}}{U_{\text{mech\_damp},i}}$, which does not account for the energy dissipated through the leakage, U_{loss}, and only that stored, as shown in Figure 4.13b, we notice that most of the frequency effect disappears at least for low voltages, showing that the amount of energy dissipated by the damping actually compensates the increase in energy dissipated electrically, $U_{\text{loss},i}$, which also increases for lower frequencies. The fact that both quantities compensate each other, and eliminate the frequency trend in the data analysed for lower voltages, as shown in Figure 4.13b, might be a particularity of the chosen design, as a more viscous material with the same capacitance would probably not affect $U_{\text{loss},i}$ as much, while still increasing $U_{\text{mech\_damp},i}$. For higher voltages, where the actuator-effect might induce the voltage stabilisation, we notice a decrease in $\eta_{\text{stored},i}$ if we do not account for continuous charge leakage. It can be noticed as a consequence of the start of the self-stabilisation: since the stored energy is the same by the end of a cycle when stabilisation occurs, we have $\Delta U_{\text{stored},i} \longrightarrow 0$ and $\eta_{\text{stored},i} \longrightarrow 0$ as the self-stabilisation trend starts. As we analysed above, the voltage for stabilisation should be lower for lower frequencies, and that is also seen by the decrease in $\eta_{\text{stored},i}$ for lower frequencies in Figure 4.13b.

Note that the efficiency figures reported for SPC-DEG systems are limited due to the methodology used to monitor the system, consisting of a voltage divider circuit in parallel, which drains part of the charges in the SPC-DEG system. Although we include this drained energy in the calculation of η, such charges do not take part in the energy conversion process in the DEG. If

such voltage divider was not connected in the system, one would expect the metric η and η_{stored} to be equal and also present higher values, since more charges would be displaced during the relaxing phase of the DEG where the mechanical-to-electrical energy conversion happens.

As the results of voltage as a function of time above show, reducing frequency makes the effect of the self-stabilisation more apparent. Thus we analyse separately the case of 0.6Hz mechanical excitation, as shown in Figure 4.14. Figure 4.14a shows the boost, where we can clearly see a supplementation of the trend seen in the previous examples: as the DEG cycles, the boost reduces until it stabilises around 1, indicating the stabilisation of the maximum voltage for the cycles to follow. Figure 4.14b, which shows DEG voltage as a function of time, demonstrates self-stabilisation effect clearly so that no boost happens after the expected initial exponential rise on SPC-DEG voltage. In this experiment, a perturbation, as a higher voltage input, was also introduced around the 250^{th} cycle (marked as a dashed line in the figure) to demonstrate that the stabilisation occurs independently of the initial voltage being higher, or lower than the stabilisation point after the perturbation is applied. Additionally, Figure 4.15 shows how the stabilisation occurs in a limit cycle: the voltage versus its first derivative plot expands from the low voltage oscillations increasing in diameter until it self-stabilises in a final shape.

Figure 4.14c shows the maximum force applied to maintain the maximum stretch level for each cycle. It not only shows the same decrease in force as the DEG cycles as the previous examples but also that when the voltage rise stops, the maximum force stabilises. Similarly, when analysing the efficiency, η, in Figure 4.14d, we see the rise, as expected from the previous examples, but also the stabilisation that follows. We can state that if we use the efficiency η_{stored} defined above, it would lead to $\eta_{stored,i} = 0$ once the stabilisation phase is achieved, since the stored energy is a direct function of the voltage, thus, if this is kept constant for following cycles, there is no variation in the stored energy, i. e. $\Delta U_{\text{stored},i} \longrightarrow 0$.

4.5 Self-stabilisation prediction

The experimental results showed how a set of different factors might influence the self-stabilising behaviour and, as was the case for the first experiments performed at higher frequencies, exposing the DEG to high voltages in a test scenario might risk dielectric breakdown failure and jeopardise further use of the device. In face of such scenario, we report a method based on interpolation to predict the self-stabilising behaviour, based on data extracted from lower voltages. Although one could seek to make this kind of prediction through modelling, it would require a well-validated model as well as the knowledge of all the parameters involved, e.g. material model, leakage, geometry, etc. The present approach allows a simple verification for working systems that can be easily implemented based on data obtained, without exposing the DEG to high voltages that could damage it.

a)

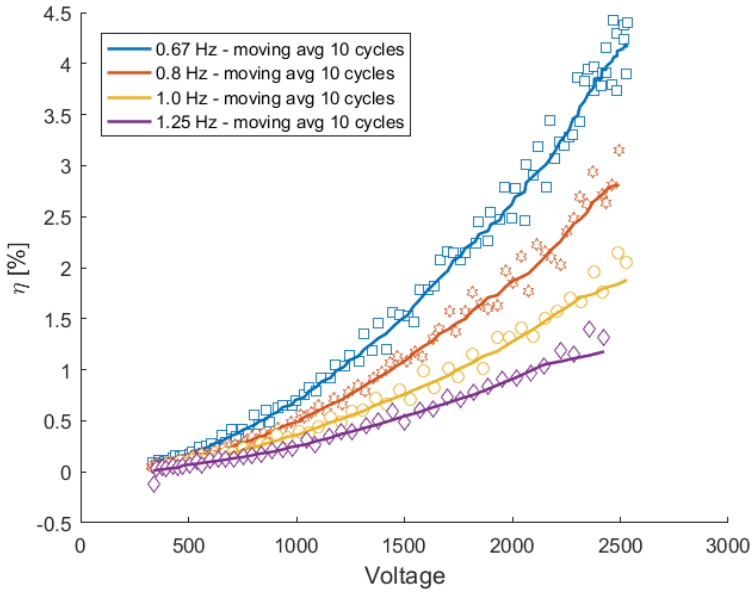

b)

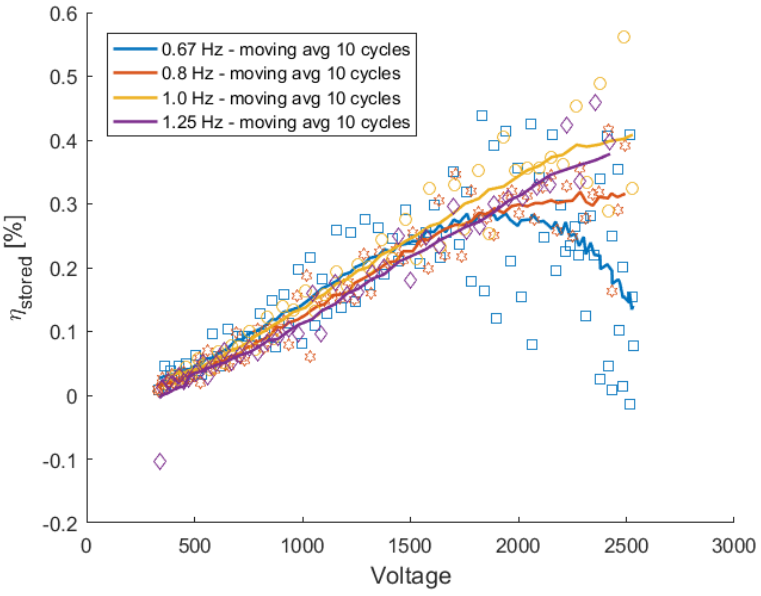

Figure 4.13: Efficiency per cycle as a function of the maximum voltage of that cycle at different oscillation frequencies, accounting for electrical energy dissipate through leakage and surplus in stored energy, η, (a) and the efficiency per cycle accounting the for the surplus in energy stored only, η_{stored}, (b) as a function of cycle maximum voltage

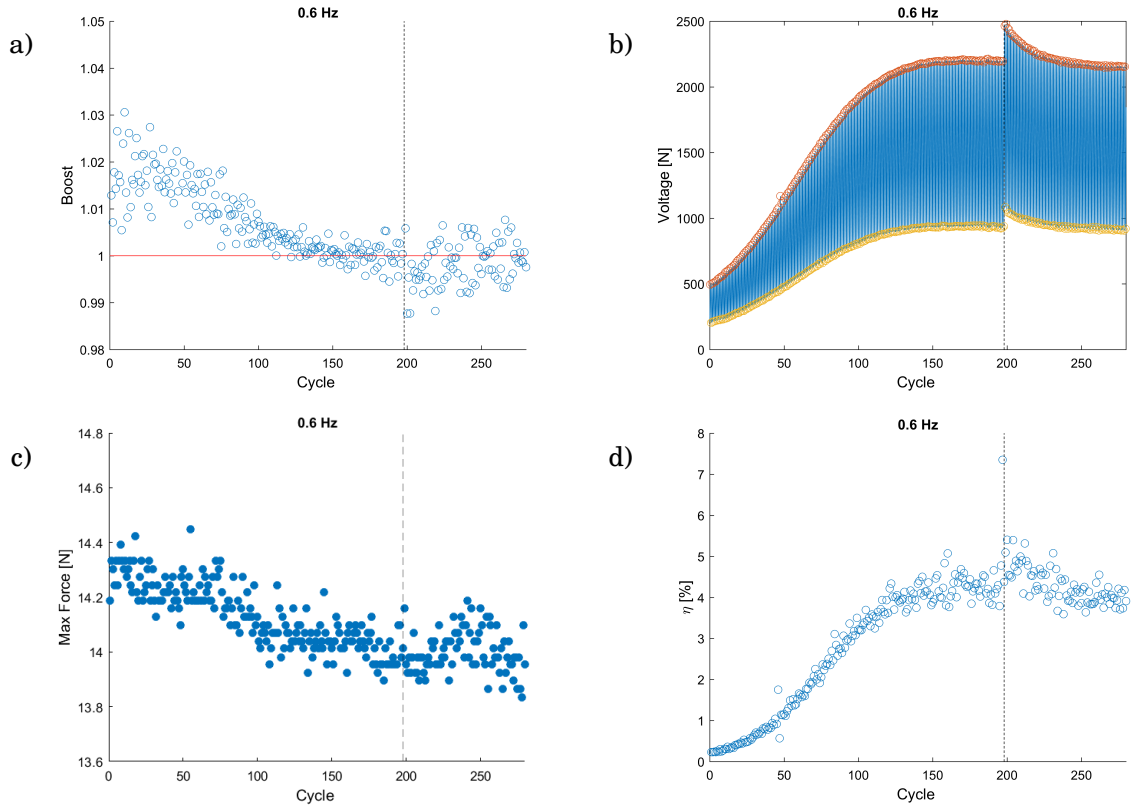

Figure 4.14: Self-stabilisation visualised experimentally. Boost per cycle (a), voltage as a function of time (b), maximum force at each cycle (c), and cycle efficiency, η (d). Black dashed line marks the perturbation moment,

When analysing SPC-DEG systems that present, or might present, a self-stabilisation, we note that we have an initial exponential increase in the maximum voltage for following cycles, with the slope of the derivative of the maximum voltage curve gradually increasing, until an inflection point is reached. This inflection point is highlighted for the data from Figure 4.14b in fig. 4.16a, but can also be identified in the data presented in Figure 4.11. After the inflection point, the trend towards stabilisation becomes clearer and can also be visualised from the variation of boost per cycle, as seen in Figure 4.16b. If we consider the data subsequent to the cycle where the inflection point happens, the decreasing trend of the boost data is clearer. Thus, we propose a method to predict the maximum voltage achieved by the self-stabilising SPC-DEG system consisting of the following steps:

Step 1 Once a data set of maximum voltage per cycle with M points has been obtained, we choose a window size $W < M$. For the example shown in Figure 4.16, $M = 80$ and $W = 30$.

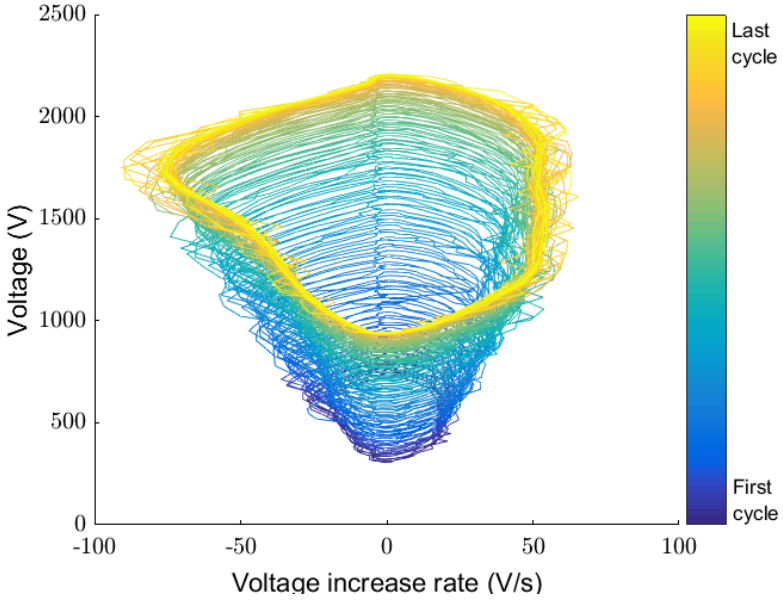

Figure 4.15: Limit cycle representation of the voltage for the SPC-DEG system experiment using 0.6Hz of mechanical excitation. Voltage versus voltage rate plot. Line in deep blue represent the first cycles and line in yellow the last ones.

Step 2 We look for the inflection point of the voltage data by trying to fit a straight line over the data between points j and $j+W$, for $j \in [1, M-W]$ and recording the resultant correlation coefficient R^2 for each fit.

Step 3 We then fit a curve $f_B(k)$ to the boost data (linear fit shown in Figure 4.16b) on the interval starting on $j = j_{\max(\mathrm{R}^2)}$, the element that provided the maximum R^2 from Step 2, and finishing on the last data point we have available, as described by the fitting interval shown in Figure 4.16b. Note that we explore the consequence of the fitting function f_B later in this section.

Step 4 Using the curve obtained by the interpolation of the boost data, we estimate the last cycle the voltage will increase before the stabilisation, j_{SS}, by solving $f_B(j_{\mathrm{SS}}) = 1$. In the example in Figure 4.16, this gives $j = j_{\mathrm{SS}} = 122$.

Step 5 We predict the estimated voltage for each cycle, V_{est_k}, by

$$V_{\mathrm{est}_k} = V_{\mathrm{est}_{k-1}} f_B(k) \tag{4.19}$$

for $k \in [j_{\max(\mathrm{R}^2)}, j_{\mathrm{SS}}]$. For the case above, this results in the red curve in Figure 4.16a, and a final maximum voltage of 1924V, underestimating the real final voltage of 2200V by around 10%.

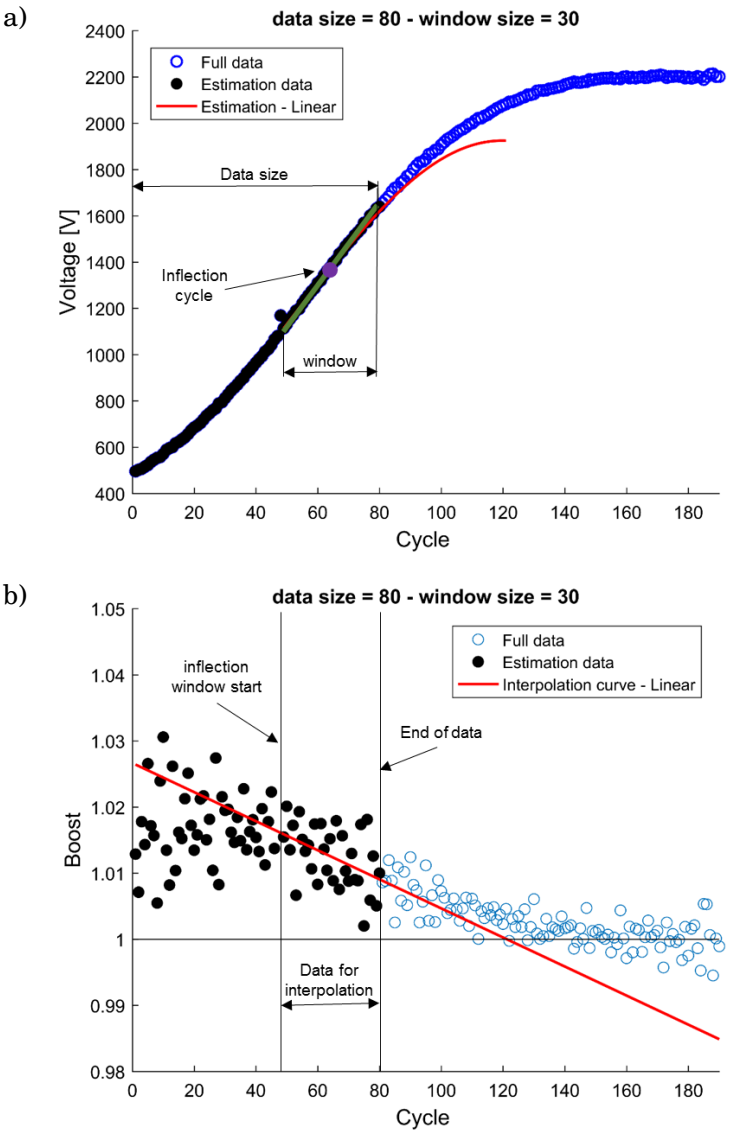

Figure 4.16: Graphical explanation of the method to predict self-stabilising behaviour, using a linear interpolation of the boost data. Maximum voltage at each cycle: sample data (black), validation data (blue) and predicted values for maximum voltage at each cycle (red line) (a). Boost at each cycle: sample data (black), validation data (blue) and interpolating curve (red line) (b)

One could also pick $f_B = a \exp bk + c$, which matches more adequately the exponential decay seen in the plot of boost per cycle as a function of time. A variation tested was interpolating an exponential curve so that $f_B = a \exp bk + .99$. The .99 factor was used to simplify the implementation through the *fit* function from MATLAB, which has the option *exp1* which interpolates a function $y(x) = ae^{bx}$. Technically, choosing 1, instead of .99, which should be the final boost value, creates a situation where $\nexists k | f_B(k) <= 1$. The results for such an approach can be seen in Figure 4.17; The final voltage was found to be 2102V, less then 5% error.

Since the choice of window size, W, might affect the outcome of the present method, we investigated the best way to predict the results based on the described method and how the sample data size, M, influences it. The results from this investigation are shown in Figure 4.18. It is evident that a bigger sample data size (more cycles) provides higher accuracy in the predictions since the end of the available data is closer to the self-stabilisation. On the other hand, big windows in this scenario might include in the regression data the points from the beginning of the cycle with the same weight as the final points, not necessarily improving the accuracy, since earlier points are more influenced by noise. The recommended approach is, given a sample data set with M points, to perform an investigation with different window sizes, equivalent to selecting the results from a vertical line in Figure 4.18 and use an average of the values obtained to estimate the final voltage in the system and in which cycle it is likely to happen.

4.6 Conclusion

Although the analysis of SPC-DEG systems, considering them as purely variable capacitors, has provided us with a series of insights about their behaviour, including design rules and valuable models, it is important to consider that the mechanical design of the system will affect the electrical properties and vice-versa. In this chapter, we discussed modelling approaches for the self-stabilising behaviour that SPC-DEG systems might exhibit, as well as how the data from such models can be used to estimate the stabilisation limit, and to design devices less prone to failure.

In a more robust approach, from the experimental data where the self-stabilising behaviour was seen, we proposed a method to predict the self-stabilisation maximum voltage and timing. Such an approach provides a systematic way of designing SPC-DEG systems. Since the boost is a function of the capacitance values used in the SPC, by adjusting such values, the system could potentially be taken to the stabilisation regime and avoid dielectric breakdown, for example.

While the simulated and tested scenarios represented specific cases, scenarios where the actuator-like behaviour, described in Chapter 2, are due to be significant are more likely to express the self-stabilising behaviour described in this chapter, due to the capacitance swing

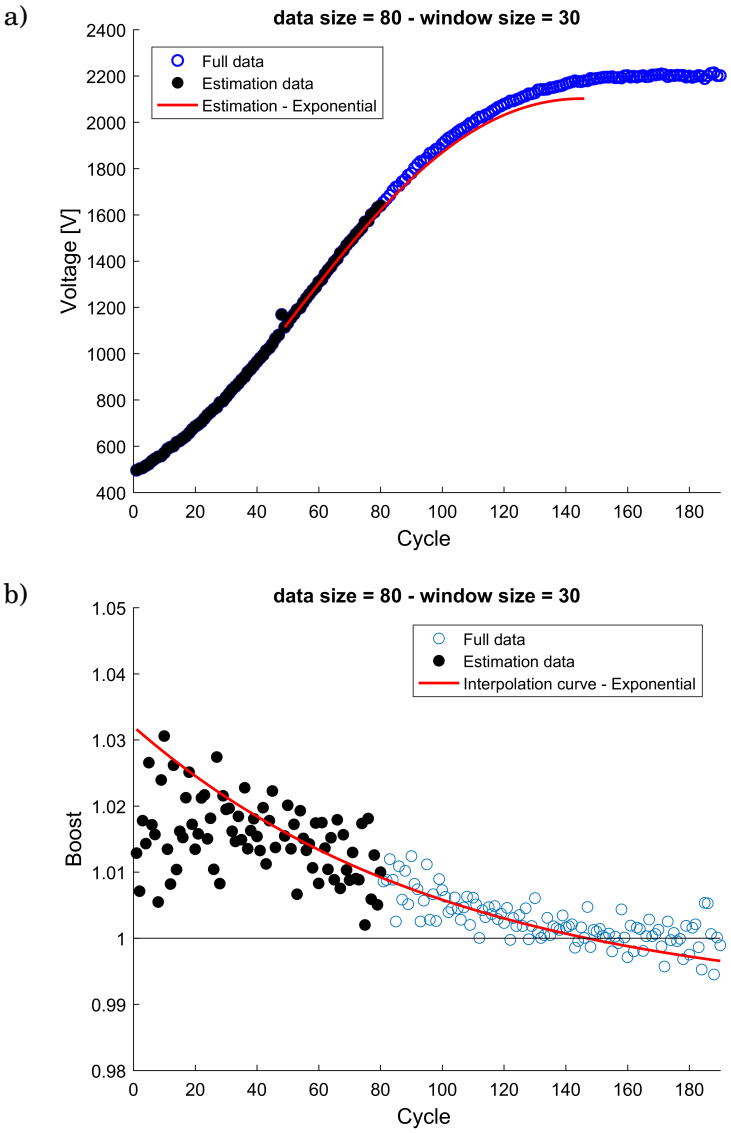

Figure 4.17: Predicted self-stabilising behaviour using a exponential function to interpolate the boost data according to the method developed. Maximum voltage at each cycle: sample data (black), validation data (blue) and predicted values for maximum voltage at each cycle (red line) (a). Boost at each cycle: sample data (black), validation data (blue) and interpolating curve (red line) (b)

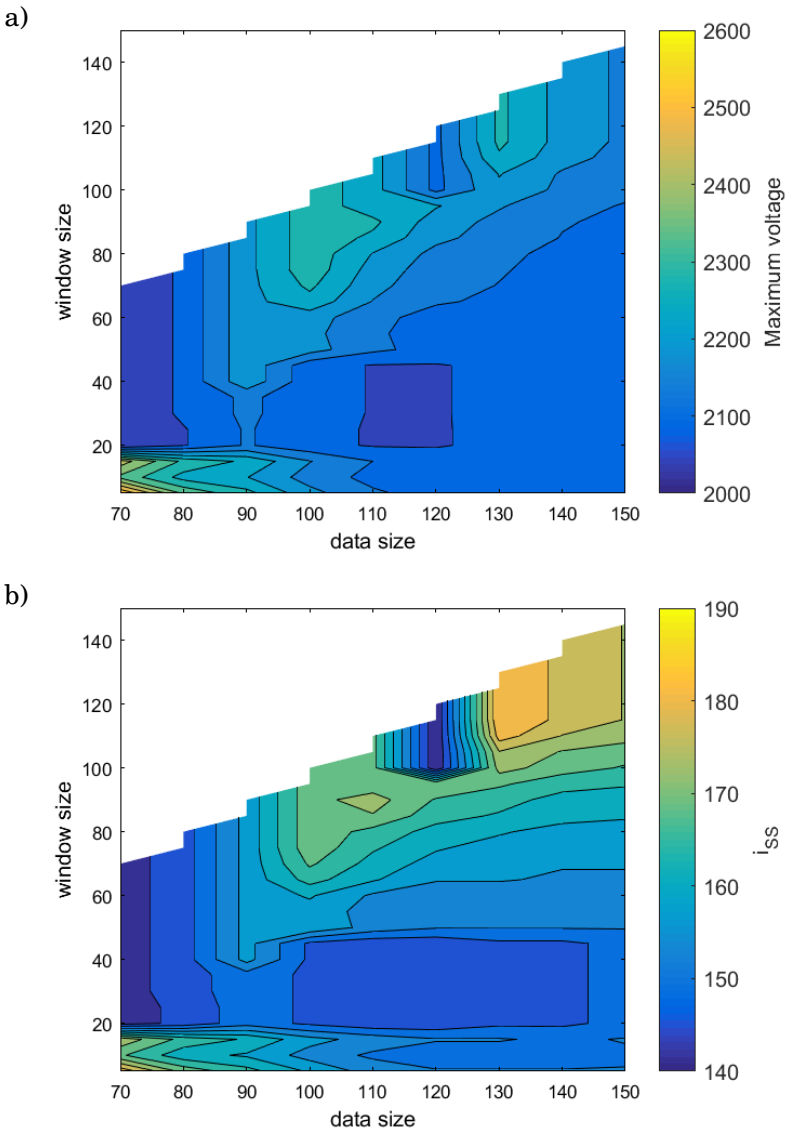

Figure 4.18: Analysis of the influence of sample data size, M, and windows size, W, in the predictions for stabilising voltage (a), and the self-stabilisation cycle, j_{SS} (b). The actual self-stabilisation voltage is 2200V, achieved at around $j_{SS} = 150$

alteration. In case of designs such as the one shown in Figure 2.2, the oscillating water column DEG, for example, this is less likely to be visualised, once the increase in the value of the DEG capacitance for no biasing pressure would depend on the loss of tension, prevent by the pre-stretch of the membrane.

Considering a more general case, we observed that, in a dynamic environment, more factors will affect the self-stabilisation behaviour than just the change in capacitance swing, as the model suggested. In the experimental setup, we noticed that the leakage played an important role in the steady-state behaviour. Higher frequencies, where the effect of leakage was smaller over a single cycle, the self-stabilisation would occur on higher voltage levels. Further studies, where the effect of the leakage and the capacitance swing change could be decoupled would be necessary to more clearly quantify the influence of each of them in the self-stabilising behaviour.

This chapter concluded our analysis of self-priming dielectric elastomer generators, showing how the electromechanical coupling of dielectric elastomers enables different regimes, such as the self-stabilising behaviour. The simplicity of the SPC implementation, passive and requiring no active circuit interference, even to stabilise the voltage, demonstrates that SPCs are an ideal technology to enable energy harvesting scenarios when we seek to harvest energy otherwise lost, such as in wearable applications, and normally associated to low power. Since SPCs do not allow cycles that explore the capacitance change in full for the electromechanical conversion and are unable to output higher power, as would be expected in a power plant such as the wave generator designs proposed for DEGs [104, 127], they might not be the best solution for these cases. An alternative for autonomous systems to automatically manage charge in DEGs while fully exploiting its capacitance change will be investigated in Chapter 5.

CHAPTER 5

SELF-SENSING BASED CONTROL OF DIELECTRIC ELASTOMER GENERATORS

As highlighted in previous chapters, one of the main issues with the implementation of Dielectric Elastomer Generators (DEGs) is the need for pre-charging to perform mechanical-to-electrical energy conversion. In cases when energy harvesting has to be performed in an environment with unpredictable characteristics (e.g., wind, waves, human walking), defining the best times for charge injection and energy extraction in a cycle is a non-trivial problem. This chapter investigates the implementation of self-sensing capabilities for DEGs, and the use of the generated signal to control the cycle. We present a novel Self-Sensing with Peak Detection (SSPD) method to autonomously control the charges on the material, which seeks to fully exploit the relaxing phase for energy conversion thus generating as much energy as possible for a given capacitance change. Importantly, the method requires no previous knowledge of the amplitude or frequency the DEG will be deformed. This chapter is partially based on the conference paper "Self-sensing for robust automatic charge management of dielectric elastomer generators" [152]. Its content is part of collaborative work, partially with Saarland University, where the author visited between July 2017 to August 2017 and obtained training in the self-sensing technique for DEAs that was adapted for the present study. During this period, part of the methods here described and the results provided by the simulation were developed.

5.1 Introduction

As detailed in section 1.4, DEGs perform the conversion from the elastic potential energy they have stored to electrostatic potential energy while the charges on the surface are displaced during the relaxation phase. If we want to maximise the outcome of this energy harvesting cycle,

we must maximise the use of the relaxing phase, through well-timed charge and discharge of the DEG. SPCs, the theme of the previous chapters, are unable to fully exploit the capacitance change since they start discharging while the DEG is still relaxing, thus reducing the charge the mechanical restoration forces perform work against during the relaxing phase, and reducing the cycle output. Ideally, to guarantee maximum energy output, a DEG should finish charging before it reaches its maximum capacitance, and cease discharging at minimum capacitance [76]. Furthermore, as shown in Chapter 3, SPC-DEG systems require a minimum capacitance swing in order to generate energy; due to their passive nature, they would not be able to be turned off in a situation where the DEG is not being deformed enough.

When looking for devices in a larger scale, such as the proposed wave energy power plants [65, 138], to optimise energy generation, additional sensors are required in order to detect states of maximal and minimal deformation (which translates into capacitance), increasing the cost and complexity of a DEG system. Capacitance sensors based on charge measurements are typically more complicated than standard voltage and current sensors since they are generally based on indirect measurement methods [58]. In addition, the orders of magnitude of the voltage (kV) and capacitance (nF) involved in typical DEG applications, as well as the parasitic leakage that exists in the material simultaneously with the resistance of its electrodes in series, further complicate the design of DEG capacitance sensors [116].

Indeed, methods have already been designed to provided sensing capabilities to DEs [87, 149], usually consisting of inserting an oscillating signal and evaluating gain and phase shift due to the capacitive behaviour. Depending on the situation, assumptions can be made, such as neglecting the leakage current through the elastomer, which still represents the expected behaviour for high-frequency signals, or neglecting the electrode resistance, suitable for low-frequency signals [87]. Such sensing capabilities have already been expanded to create sensor-less DEA applications, where the DE works both as an actuator and a sensor, commonly known as self-sensing DEAs [41, 42, 52, 54, 55, 118, 121]. Gisby *et al.* [42] used a current controlled source to generate a slew rate controlled PWM signal together with synchronised sampling frequency so that there was control over which phase in a PWM cycle data was sampled from. Using interpolation techniques, the method calculates the series resistance, which is later used to obtain the voltage through the DEG membrane only, and infer the capacitance of the DE. The method was later evolved [41] and, through a regression window, data points are represented in a 4D hyper-plane having as axes time, voltage across the DEG, charge, and the current in the equivalent series resistor (that compensates the electrodes) and the capacitance can then be estimated by one of the coefficients of the hyperplane. The approach presents good results, but the specificity of the PWM signal it requires, as well as the high sampling rate, in the order of tens of kHz make implementation complicated and hardware dependent. Hoffstadt *et al.* [52] used a superimposed high frequency sensing signal on top of the low frequency actuation signal. The proposed method required the

current and voltage information, as well as information regarding phase and amplitude since it consisted of a frequency domain approach, which implied extra processing steps.

An approach using similar models to the ones used in [52], but developing a self-sensing method for DEAs in the time domain, was made in [119], which did not require the phase and amplitude calculations and consisted of simple regression operations. Considering the electric model as shown in Figure 5.1, the following model of the system dynamics can be obtained;

$$\frac{d}{dt}q(t) = -\frac{1}{CR}q(t) + \frac{1}{R}v(t) \tag{5.1}$$

$$i(t) = -\frac{1}{CR}q(t) + \frac{1}{R}v(t), \tag{5.2}$$

where C is the DE capacitive element, R is the DE series resistive element, i is the curent that flows through the system, v is the voltage, measured as indicated in Figure 5.1, and $q(t)$ is the charge stored in the capacitive element. Using forward Euler rule, the following Linear-in-Parameters relation was obtained,

$$V_k - V_{k-1} = Ri_k + \left(\frac{T_s}{C} - R\right)i_{k-1}, \tag{5.3}$$

where V_k is the k^{th} voltage sample, i_k is the k^{th} current sample and T_s is the sampling interval. A Recursive Least Squares (RLS) regression algorithm can then be used to obtain the values of the capacitance, C and the series resistance, R, for small enough time step. This has been shown to provide less noise and better accuracy than the Least Minimum Squares (LMS) [119]. A further evolution of this approach was shown in [118], considering a pre-warped Tustin discretisation instead of the forward Euler rule, which extended the results obtained with low sampling rate and will be detailed further later in this chapter.

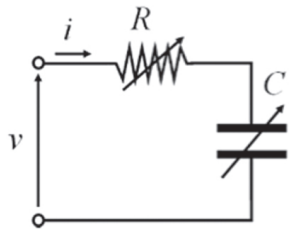

Figure 5.1: DE electric model consisting of a variable capacitor and a variable resistor in series, which accounts for the electrodes' resistance. Reproduced from [120].

Other notable methods of self-sensing for DEAs were proposed in [54] and [55]. The first extended the model used in [52] for the time domain in an Autoregressive - moving - average model with exogenous inputs model (ARMAX), a type of model for times series regression,

using a 5^{th} order filter and a Recursive Extended Least Squares (RELS) regression method, obtaining better dynamic response at the price of increased complexity, compared to the RLS method described. Hoffstadt *et al.* [55], later proposed a new self-sensing approach based on an Extended Kalman filter, which required no excitation signal to be superimposed in the actuation signal for the DEA while obtaining good dynamic response and accuracy. On the other hand, it requires refined hardware for both sensing accuracy and a fast sampling rate (tested using 20kHz sampling rate). These approaches provided good results, but they were implemented using expensive and sophisticated hardware for sampling and live data processing. Additionally, the techniques proposed require extra computing steps that, for cheaper computing hardware, might jeopardise the live implementation of the algorithms.

The combination of self-sensing and DEGs has already been demonstrated in [95], where the self-sensing method described in [41] was implemented together with a SPC system. Since, typically, a DEG has phases when it is disconnected from the priming device (here, a SPC), the circuit was assembled as illustrated in Figure 5.2, using a sensing signal input connected to the low voltage terminal of one DEG, and using a two DEG in parallel arrangement, in order to allow the current & voltage to change during open circuit conditions. Using a SPC, the main goal for this project was to develop a way to verify the DEG stretch level and avoid failure modes. Although an important proof of concept, we are not aware of any following studies that develop this technique further. Further, the paper lacks practical information regarding e.g. the voltage levels used on the sensing signal, as well as the energetic cost of implementing the self-sensing.

In this chapter, we will present a novel approach for self-sensing of DEGs, as well as an algorithm that can be implemented in a microcontroller to automatically control the charge and discharge of a DEG, according to its maximum and minimum deformation states. In Section 5.2, we introduce the self-sensing requirements and strategies. In Section 5.2.1 we present the general hardware requirements for the proposed method, as well as an improved energy harvesting cycle that can be easily adapted for the self-sensing method we developed, which is detailed in section 5.2.2. In Section 5.3, we detail how we use the self-sensed signal to infer the maxima and minima when the DEG should be charged or discharged, proposing a charge management algorithm. In Section 5.4, we report the results obtained by a first investigation using numerical methods, which quantifies the impact on the energy outcome of the implemented method. In section 5.5, we report how the charge management scheme can be implemented in practice, reporting the results obtained in an experimental investigation.

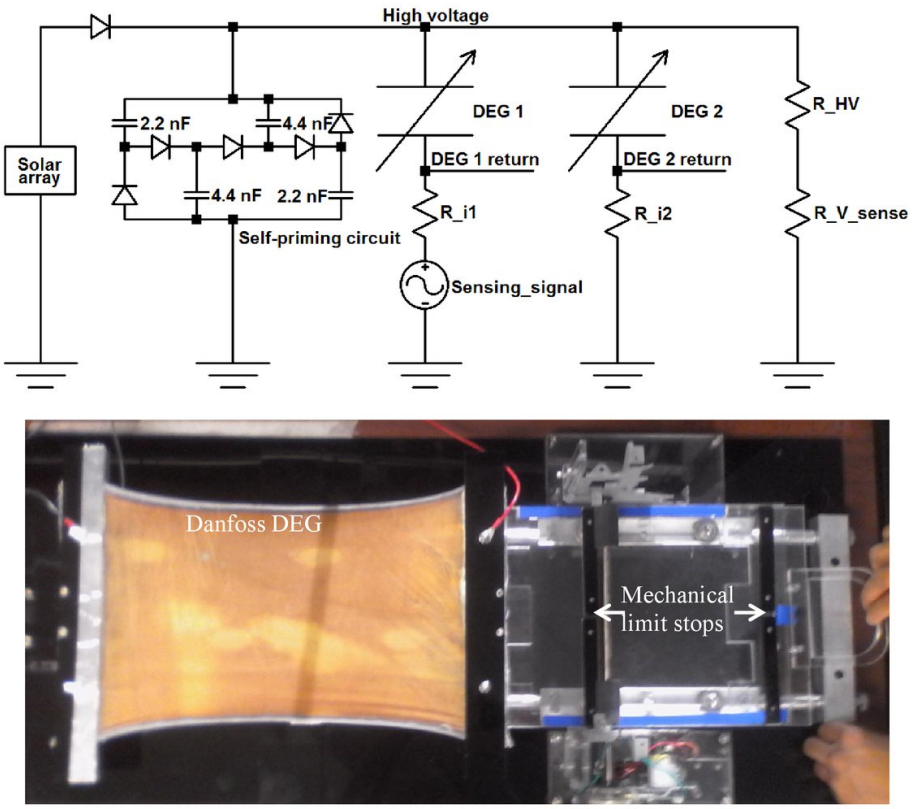

Figure 5.2: Self-sensing DEG scheme proposed in [95]. R_i1 and R_i2 are resistors used to measure current, while R_HV and R_V_sense represent a voltage divider, such that the system can be monitored when subjected to high voltage. Reproduced from [95].

5.2 Self-sensing

5.2.1 DEG cycle and hardware

As highlighted in [95], DEGs are integrated into a more complex circuit topology then DEAs, which normally are directly connected to a power supply; due to the need for charge and discharge in every cycle, DEGs typically cycle through at least three circuit conditions:

1. the *charging phase*, when the DEG is connected to a higher potential (e.g., a power supply) and current flows into it,

2. *open-circuit*,

3. the *discharging phase*, when the DEG is connected to a lower potential (e.g., a capacitor) and current flows from it.

During the charging phase, the methods cited above for DEA self-sensing can be implemented in a straightforward manner, since the DEG can be directly connected to a power supply. The design proposed in [95] could also be directly implemented using two DEGs connected in parallel, while connecting a sensing signal to the low voltage terminal of one of the DEGs. Instead, we look for a more general method, not requiring permanent stimulation, and seek to simplify the system by avoiding the necessity to use two DEGs.

In order to develop our method, we first defined the DEG circuit, and the energy harvesting cycle to be used. In contrast with the layout proposed by [95], we chose a classic circuit topology for experimental work using DEGs, with two switches that allow the DEG to be connected to a power supply (S1) or to a load (S2) where it can discharge, as shown in Figure 5.3.

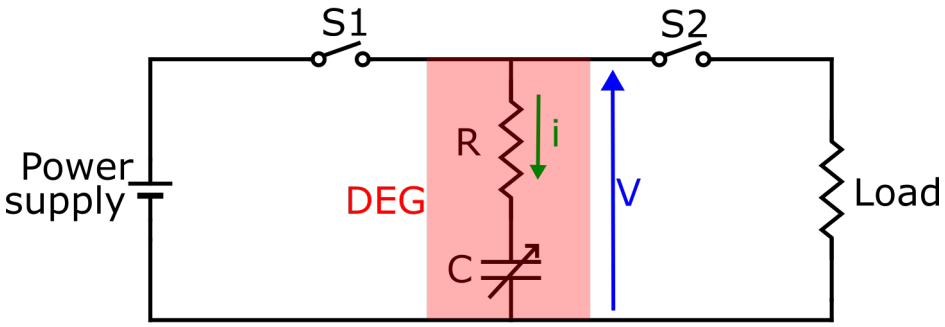

Figure 5.3: Simplified DEG circuit: S1 allows the DEG to charge under constant voltage, while S2 discharges the DEG through a constant load. DEG is modelled as a capacitor, C, and resistor, R, in series, as in Figure 5.1, an acceptable model that provided good results in [118]. DEG voltage V and current i are measured to implement the self-sensing.

We then chose a cycle as described in Figure 5.4 that consists of a variation of the classic constant charge cycle [47], in which we use a partial discharge and keep the voltage constant during the stretch phase, according to the following phases:

1. stretch the DEG under constant voltage (S1 closed, S2 open): charges flow to it as its capacitance increases,
2. allow the DEG to relax in open-circuit condition (S1 open, S2 open), keeping the charge level constant,

3. discharge (partially) the DEG (S1 open, S2 closed) until the charge reaches the same level as the start of the stretch phase.

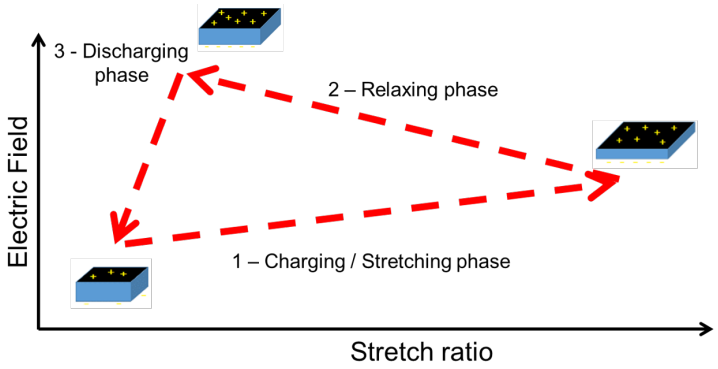

Figure 5.4: Schematic illustration of the three phases of the DEG cycle.

This cycle presents the theoretical advantage of avoiding the high current peak during the charge phase that some traditional charging cycles use [47, 130], which increases the losses due to the electrode resistance (since resistive losses scale according to the square of the current), as well as recycling the charges from one cycle into the next.

5.2.2 Self-sensing algorithm

This adapted cycle, additionally, allows us to directly charge the DEG during its stretch phase, while the DEG is directly connected to the power supply as in most of the self-sensing techniques described previously. We split the self-sensing method in a different approach for each of the cycle phases, in order to provide the best adjustment for the circuit topology.

5.2.2.1 Charging while stretching

Our aim is for a self-sensing method that can be implemented for the charging phase without the requirement of complex hardware, being able to perform at low sampling rate, that does not require expensive processing, with minimum data storage and that avoid charge calculation through current integration (which, in case of a current measurement bias might generate significant miscalculation [116]). Therefore we chose to develop the DEA self-sensing method proposed in [118]. It consists of a recursive least squares over a time domain model to obtain the capacitance, requiring only sensing of voltage and current, which are trivial to implement on our experimental setup to be described later in this chapter. Moreover, the RLS method can be implemented through simple and straightforward operations and the application of the pre-warped Tustin method for the discretisation enables the use of low sampling frequency.

We begin by modelling our DEG circuit, shown in Figure 5.3, rewriting eq. (5.1) and eq. (5.2) as

$$V = Ri + q/C, \tag{5.4}$$

$$\frac{d}{dt}q = i, \tag{5.5}$$

where V is the measured voltage as indicated in Figure 5.3, R the series resistance of the model, q the charge stored in the DEG, C the DEG capacitance and i the current through the DEG, which is also measured. To avoid needing to integrate to obtain the charge, as cited above, we consider that between samples, the capacitance, C, and the resistance, R, remain constant, an assumption which is considered appropriate by [41, 54]. Thus, it enables us to write

$$\frac{d}{dt}V = R\frac{d}{dt}i + \frac{1}{C}i. \tag{5.6}$$

We will use a pre-warped Tustin method [38], tuned at the sensing frequency, f_e, to approximate derivatives, such that if

$$y = \frac{d}{dt}x, \tag{5.7}$$

we approximate in a digital scenario by

$$y_k \approx -y_{k-1} + \frac{1}{K_T}(x_k - x_{k-1}) \tag{5.8}$$

with

$$K_\mathrm{T} = \tan(\pi f_e/f_S)/2\pi f_e, \tag{5.9}$$

where f_S is the sampling frequency.

Applying eq. (5.8) to eq. (5.6), we obtain the difference equation:

$$V_k - V_{k-1} = R(i_k - i_{k-1}) + \frac{K_\mathrm{T}}{C}(i_k + i_{k-1}), \tag{5.10}$$

where the subscripts k refer to the k^{th} sample element.

From eq. (5.10), we take the inputs as discrete voltage change

$$Y_k = V_k - V_{k-1}, \tag{5.11}$$

and

$$\varphi_k = \begin{bmatrix} i_k + i_{k-1} & i_k - i_{k-1} \end{bmatrix}^T, \tag{5.12}$$

and consider the states given by θ_k as

$$\theta_k = \begin{bmatrix} \frac{K_T}{C_k} & R_k \end{bmatrix}^T. \tag{5.13}$$

The RLS algorithm is implemented as follows [120]:

$$\hat{\theta}_k = \hat{\theta}_{k-1} + H_k(Y_k - \varphi_k^T \hat{\theta}_{k-1}) \tag{5.14}$$

$$H_k = \frac{P_{k-1}\varphi_k}{1 + \varphi_k^T P_{k-1}\varphi_k} \tag{5.15}$$

$$P_k = \frac{1}{\mu}\left(P_{k-1} - \frac{P_{k-1}\varphi_k\varphi_k^T P_{k-1}}{1 + \varphi_k^T P_{k-1}\varphi_k}\right). \tag{5.16}$$

$\hat{\theta}_k$ is the estimate of θ_k, P_k and H_k are respectively a covariance matrix and an observer gain matrix (P_k can be initialised as an identity matrix and H_k calculated from there), and μ is a forgetting factor, which should be chosen in the interval $0 < \mu \leqslant 1$, with $\mu = 1$ being used for θ constant. Smaller μ provides faster convergence but also reduces the filtering power of the algorithm.

5.2.2.2 Open circuit while relaxing

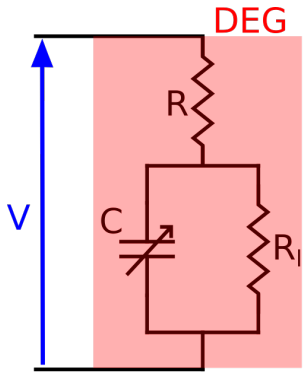

Figure 5.5: DEG model considered during the relaxing phase. It considers the leaking resistance, R_l parallel to the capacitance, C. Due to open circuit condition, no current flows through the series resistor R during this phase.

In the relaxing phase, we have open-circuit condition, meaning there is no current flowing in or out of the DEG since we do not hold a permanent excitation scheme as [95]. Thus, we consider that the DEG charge loss occurs only due to the leakage through the membrane with resistance R_l, which is now considered as shown in Figure 5.5, enabling us to estimate the capacitance by

$$C_k = V_k^{-1} C_{k-1} V_{k-1} \exp\left(-\frac{t_k - t_{k-1}}{K_{\text{decay}}}\right), \tag{5.17}$$

where t_k is the sampled time, and $K_{\text{decay}} = R_1 C$ is assumed constant since, as the capacitance of the DEG decreases, the leakage resistance of the membrane increases at the same rate [117]. This assumption allows us to measure (and retain) the values of R_1 and C from any deformation state (e.g. before the system is initiated) to calculate K_{decay}. Alternatively, charging the DEG and letting it discharge in an open circuit condition while keeping the DEG at constant stretch level (consequently $C_k = C_{k-1}$), provides data for V_k and t_k in a similar condition so that K_{decay} can be estimated.

5.2.2.3 Discharging

For the discharge phase, as it consists of a short interval compared to the cycle period and the change in DEG deformation is small, we assume that the capacitance remains constant, thus

$$C_k = C_{k-1}. \tag{5.18}$$

5.2.2.4 Self-sensing verification

In accordance with the states of the switches S1 and S2, we estimate the capacitance of the DEG using eq. (5.10), eq. (5.17),and eq. (5.18). As a first concept test of this novel combined self-sensor and DEG, we implemented it in a simulation scenario. The simulation considered a silicone 4-layered cone DEG, and used the model described in [116]. The model consisted of an annular DEG which is pushed out of plane in a truncated right-angled cone geometry. It assumes the hoop strain to be the same for the whole membrane as a simplifying hypothesis. To emulate real-world implementation issues, we included noise disturbance at a realistic level for measurements from the hardware available in the intelligent Material Systems Lab (iMSL) at Saarland University: an additive noise amplitude of 4V for voltage, and 4μA for current. Self-sensing parameters implemented are shown in table 5.1. The inferred capacitance in the simulated scenario showed good agreement between true and self-sensed capacitances, as shown in Figure 5.6. To further improve the capacitance estimation accuracy, comb filters can be used to eliminate noise and harmonics around the self-sensing signal frequency.

It is important to note that the higher the amplitude and frequency of the sensing signal, the higher the induced current, and therefore the higher the signal-to-noise ratio, providing better and more reliable values. On the other hand, this also suggests more energy consumed by the self-sensor; a design compromise that must be considered since energy harvesting is the main goal. We point out that, since DEs behave mostly as capacitors, the dissipated power should be comparably small with respect to the instantaneous power, as it is mostly reactive [121].

Table 5.1: Self-sensing simulation parameters

μ	0.98
sampling frequency f_S	10kHz
sensing signal frequency f_e	200Hz
sensing signal amplitude	30V
mechanical deformation period	1s
maximum cycle capacitance	893pF
minimum cycle capacitance	498pF

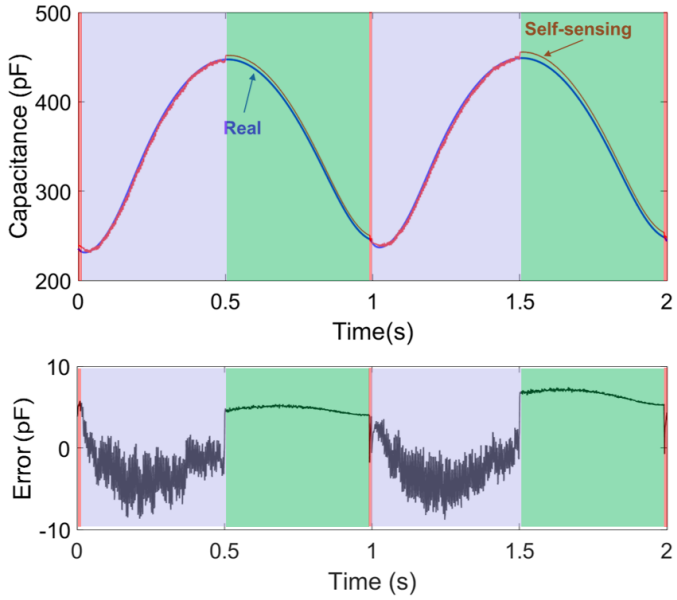

Figure 5.6: (a) Capacitance and (b) error (difference between target and estimated capacitance) produced by the self-sensing method during a simulated DEG cycle.

5.3 Charge management

As mentioned in section 5.1, in order to obtain the maximum performance from a DEG, we need to have the charging process completed before the relaxing phase, and discharging completed before the DEG starts stretching again. In order to do so, we can extend the use of self-sensing not only for stretch level monitoring but also to also identify these critical points in the cycle, which correspond to local maxima and minima in the capacitance signal.

This peak detection method uses a robust sliding-mode differentiator [131] to obtain the first and second derivatives of the capacitance signal from the self-sensor. In order to obtain

more robust estimation, we used a 5th order differentiator, which, compared to lower orders, provided good results for the first and second derivatives we intend to use. The differentiator is implemented through the set of equations

$$
\begin{aligned}
\dot{z}_0 &= -\lambda_k L^{1/(k+1)} z_0 - C^{k/(k+1)}(z_0 - C) + z_1, \\
&\vdots \\
\dot{z}_j &= -\lambda_{k-j} L^{1/(k-j+1)} z_j - \dot{z}_{j-1}{}^{(k-j)/(k-j+1)}(z_j - \dot{z}_{j-1}) + z_{j+1}, \\
&\vdots \\
\dot{z}_k &= -\lambda_0 L(z_k - \dot{z}_{k-1}),
\end{aligned}
\tag{5.19}
$$

where $\dot{z}_j$ is the jth order derivative estimator, L is the Lipschitz constant [131], $\lambda_j > 0$ are control parameters, and k is the highest order derivative we want to compute; here $k = 5$. A trapezoidal integration of those derivatives is used as input to the following step, since z is needed to calculate $\dot{z}$. Thus, our differentiator has seven parameters to be tuned ($\lambda_0, \lambda_1, \ldots, \lambda_5$ and L), chosen in order to provide the necessary balance between noise (too high) and delay (too low) in the calculated derivatives. Values of λ_i, suggested in [131], that provided satisfactory results are shown in table 5.2 and L can be chosen as a function of the expected mechanical excitation cycle period T, e.g. $L = 200T$.

Table 5.2: Control parameters for the simulation performed

λ_0	1.5
λ_1	5
λ_2	8
λ_3	12
λ_4	18
λ_5	150
L	200
$x\%$	2%
x_{ff}	10^-6

Since noise might still exist, we additionally filter the derivative signals of interest (here, first and second) using a first order low pass filter, setting its cut-off frequency based on the expected bandwidth of the mechanical excitation of the dielectric elastomer. For the present case, 10Hz was set as cut-off frequency, for 1Hz mechanical excitation and 10kHz sampling rate.

To find a local maximum capacitance, we seek states which satisfy the following four conditions:

1. $\text{sign}(\dot{C}_k) \neq \text{sign}(\dot{C}_{k-1})$,
2. $C_k < C_{k-1}$,
3. $\langle \ddot{C} \rangle_N < 0$,
4. $C_k > (1 + x\%) C_{\min} (1 + x_{\text{ff}})^m$,

where $\dot{C}_k$ is a calculated value of the capacitance's first derivative, $\langle \ddot{C} \rangle_N$ is the average of the last N values of the second derivative, $C_{\min}$ is the capacitance value of the last point that was considered a minimum, x_{ff} is a forgetting factor, m the number of samples since $C_{\min}$ was recorded, and x is a coefficient to guarantee that a peak should be at least $x\%$ higher than the previous minimum. Condition 1 provides the basis for a maximum detection since it represents the change of sign of the first derivative. Conditions 2 and 3 seek to guarantee that the capacitance is decreasing (after it reaches a maximum). Condition 4 aims to add robustness and avoid noise or small perturbations, since we not only have noise issues, but charge/discharge of the material might provide small variations in capacitance due to the electrostatic pressure from the charges, rather than the external forcing of the DEG across a cycle that we wish to identify, thus the use of the coefficient x in the condition. In order to account for a change of circumstances where the cycle amplitude is reduced, we apply a forgetting factor, x_{ff}, that multiplies and corrects $C_{\min}$ at each step of the controller, progressively reducing it and making peak detection more likely. To detect a local minimum, the conditions 1–4 above are inverted accordingly.

5.4 Simulation test

In order to validate the new proposed Self-Sensing with Peak Detection (SSPD) method, we tested it in simulation, using the same procedure and models from section 5.2.2.4. This permits to evaluate the robustness of the method in realistic operating conditions, providing first regarding the filtering level that might be required in practice. The simulation used a sensing signal of 30V amplitude and 200Hz frequency, superimposed onto an input voltage of 2kV. The simulated sampling time was 10kHz, achievable with common data acquisition devices, such as the ones present the Intelligent Material Systems Lab at Saarland University that were used to develop the self-sensing method we adapted [118]. The RLS forgetting coefficient was set to $\mu = 0.98$. The differentiator parameters can be found in table 5.2.

The SSPD was successfully able to sense the displacement, detect the maxima and minima and promote charging/discharging when we simulated irregular DEG displacements, superimposing different frequencies and amplitudes, as shown in 5.7. This demonstrates its potential to be implemented in systems where the amplitude and frequency of DEG excitation are unknown.

Moreover, in order to analyse the bandwidth of the SSPD, it was also tested with varying excitation frequencies, as shown in 5.8. As frequency increases, a reduction in the accuracy of the detection is shown. Such errors are a consequence of the filtering techniques, which promote delay in the sensing signal.

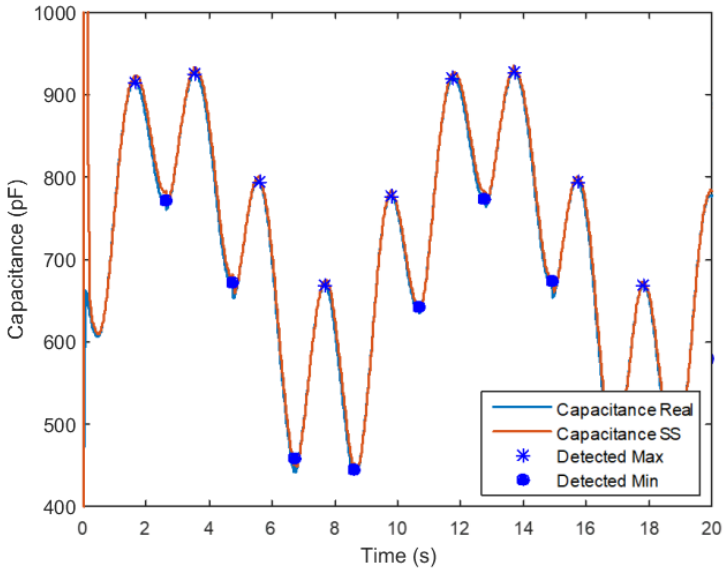

Figure 5.7: Capacitance (pF) as a function of time, together with the results obtained through the Self-sensing with Peak Detection method, when a DEG subjected to a random excitation signal.

Parameters such as x, x_{ff}, L, $\lambda_0, \lambda_1, \ldots, \lambda_5$, forgetting and further filtering methods can be tuned in an application-dependent way. Nonetheless, with manual tuning, we were able to identify parameters that guaranteed fair robustness and reliability as shown above.

As illustrated in 5.9, the error in the peak detection increases as the frequency increases, due to the filtering delay (as explained above), but it also shows how error might increase as frequency reduces. The explanation for such cases is that slower variation in capacitance means smaller absolute values in the first and second derivatives that are used by the SSPD. As the noise level is kept constant (since it is a hardware intrinsic characteristic), higher noise-to-signal ratio leads to an early peak detection, as the zero-crossing in the first derivative happens earlier due to the noise.

In order to quantify and compare the efficacy of the SSPD method, we also simulated the same cycle for stable sinusoidal excitation but with a programmed charge and discharge, to be aligned with the peaks; the ideal scenario that gives the best performance. We then compared this ideal

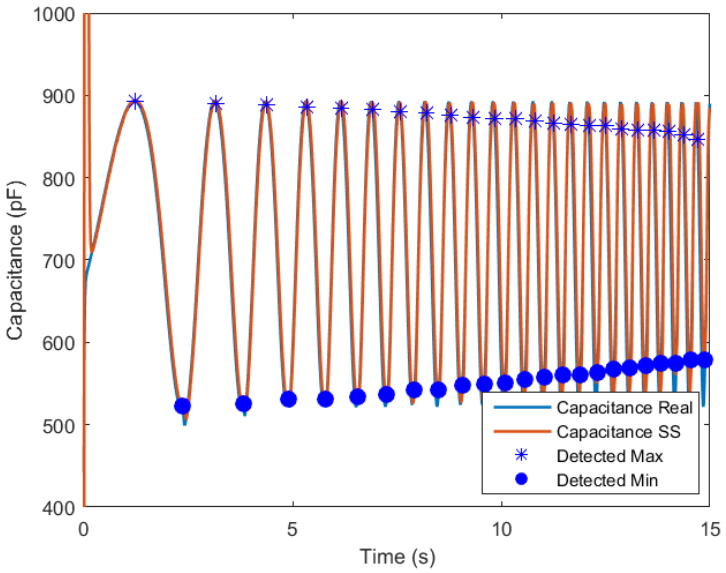

Figure 5.8: Capacitance (pF) as a function of time and the results obtained through the peak detection algorithm and self-sensing when a DEG subjected to excitation frequencies from 0.1Hz to 3Hz.

scheme with the SSPD method for a range of different input (forcing) frequencies. When we compare the energy harvesting performance, as shown in 5.10, we see the price of the inaccuracy for higher frequency: delayed peak detection reduces the useful capacitance swing in the cycle, thus reducing the energy harvested. Further, since we spend energy on the self-sensing process, a lower frequency also reduces the final amount of energy harvested. Nevertheless, the proposed method allows us to autonomously run and repeat the desired cycle independent of quantitative knowledge of external excitation and without the need of further sensors.

5.5 Experimental validation

5.5.1 Cycle verification

We implemented self-sensing with peak detection method in hardware, through the experimental setup shown in Figure 5.11. The DEG membrane is made of 3M VHB 4905, and MG Chemicals 846 Conductive Grease, which, subjected to 4×4 pre-stretch, is stuck over a laser cut ring of acrylic with an internal diameter of 53mm, and assembled on a chamber, as shown in Figure 5.13, connected to a syringe. As a way of increasing the conductivity between the contacts and the DEG, as well as providing a clean contact (no grease) outside the chamber, the top and bottom parts of the chamber received copper tape contacts that lead from its internal parts to the outside, and we also used two rings of 0.2 mm thick conductive rubber (000 397 043, J-Flex, UK),

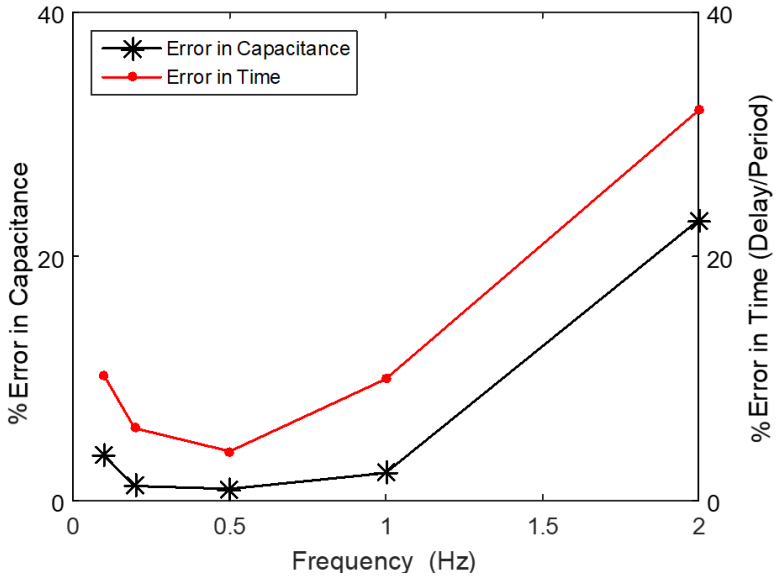

Figure 5.9: Errors in the peak detection algorithm for different frequencies.

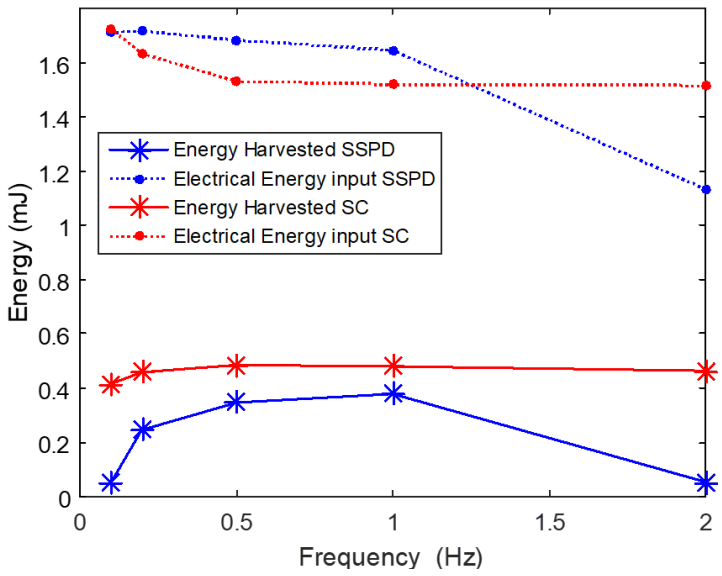

Figure 5.10: Energy input and harvested comparing the peak detection algorithm (SSPD) with a Scheduled Charge/Discharge (SC) for a known sinusoidal deformation for different frequencies.

see Figure 5.13, which not only increase the contact surface between the soft DEG and the rigid PLA print/copper tape, but also avoid stress concentration points due to print imperfections and folds in the copper tape.

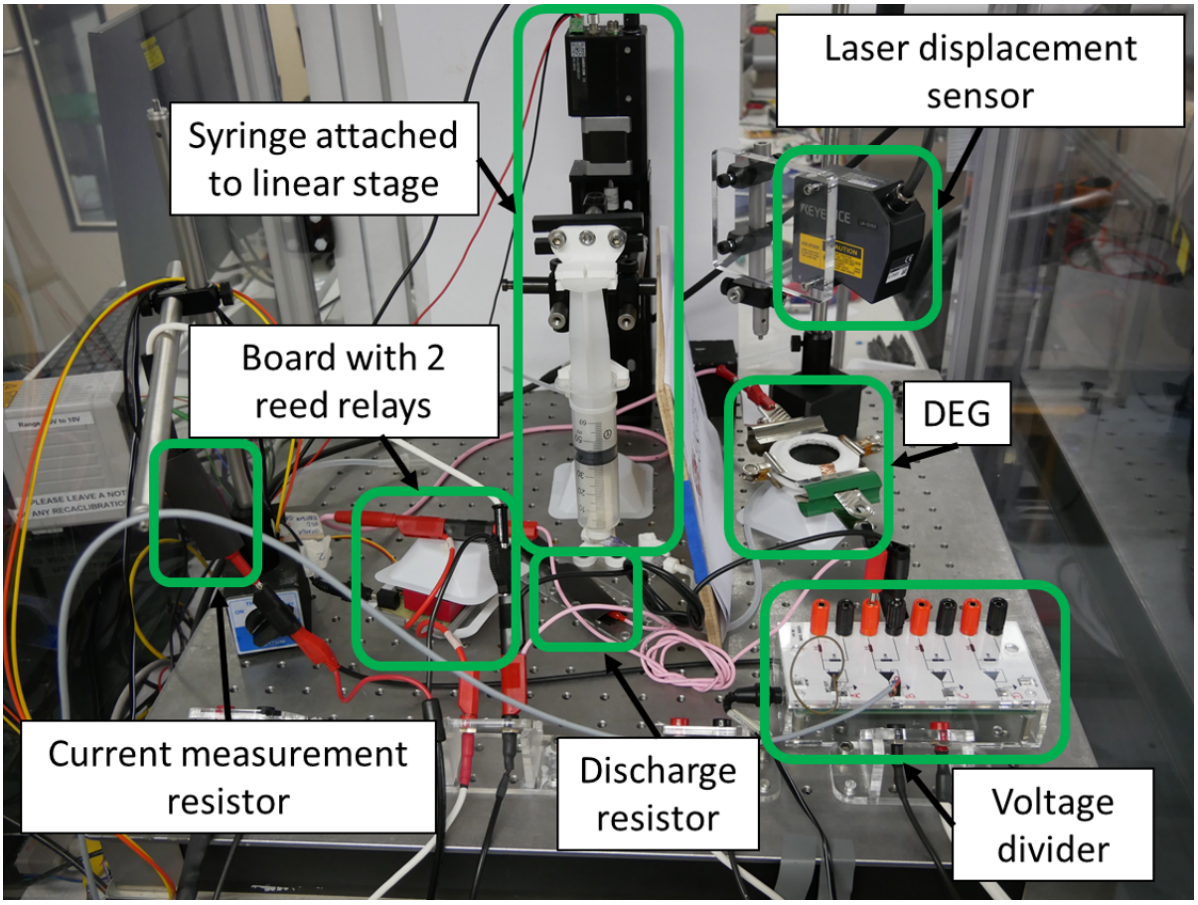

Figure 5.11: Test setup with components arranged over a 60cm x 60cm breadboard inside a enclosure for high voltage protection.

A National Instruments data acquisition device (DAQ) USB-6343 was used to buffer the voltage output signal that is fed into a high voltage amplifier UltraVolt 5HVA24-BP1, produced by Advanced Energy Industries, and the signal for opening and closing the Coto Technology 5501-05-1 reed relays (switches S1 and S2 from Figure 5.3). Since the relays are activated by 12V input, we use 2N3904 Bipolar (BJT) Single Transistors that can be activated with the 5V digital signal provided by the DAQ. The current was measured using a resistor connected between the DEG's low voltage terminal and ground. DEG voltage was obtained through a 5GΩ impedance voltage divider, as in Chapter 4. To inflate the DEG, the syringe was actuated using a motorised linear stage Zaber X-LSQ150-E01. The deformation on the tip of the inflated DEG was obtained through a laser displacement sensor LK-G152, produced by Keyence.

Although the traditional constant charge cycle, as proposed in [47], herein denominated "traditional", can be implemented through a previously scheduled charge/discharge, the cycle proposed above, herein called "adapted", requires the discharge switch to be open when the voltage drops below the desired level. For such control, a STM32 NUCLEO-F401RE development board was utilised to control the switches, receiving the signals that could be scheduled from the DAQ and coordinating the discharge switch to avoid full discharge.

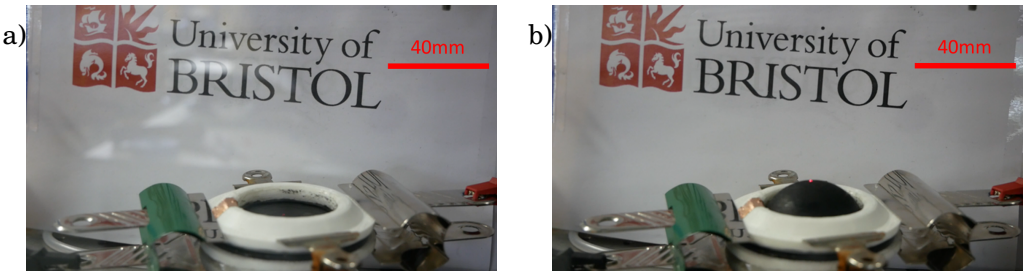

Figure 5.12: DEG in flat (a) and inflated (b) state.

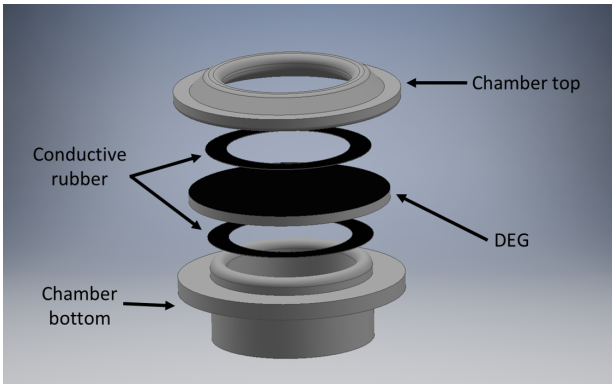

Figure 5.13: Detail of the inflatable DEG chamber components.

Figure 5.14a shows a comparison of the voltage versus time curves for the experiments performed. We can use the data obtained from the traditional cycle to estimate the capacitance of the DEG during its charging and discharging phases. Choosing a point from the start of the discharge, we know that after a time interval equal to the time constant of a RC circuit, the voltage decreases by 63.2%. Considering the DEG series resistance to be orders of magnitude smaller than the 10MΩ resistor used as discharge load, from the points illustrated in Figure 5.15, we have a time constant of 18ms, thus approximating the discharge capacitance, $C_{\text{discharge}}$, to 1.8nF. Knowing the final capacitance, we can estimate the capacitance at the start of the relaxing phase, C_{charge}. We know there is leakage through the voltage divider that measures the voltage, V, across the DEG, but, aware of its impedance ($R_L = 5G\Omega$), we can estimate how much charge

leaked. By the end of the relaxing phase, we have stored in the DEG a charge

$$Q_{\text{discharge}} = C_{\text{discharge}} V_{\text{discharge}}. \tag{5.20}$$

We can estimate the total charge that was stored in the DEG by the start of the relaxing phase, by summing $Q_{\text{discharge}}$ to the charge leaked, given by

$$Q_{\text{leak}} = \int_{t_{\text{start relaxing}}}^{t_{\text{discharge}}} \frac{V}{R_L} dt. \tag{5.21}$$

Finally, the capacitance at the beginning of the relaxing phase, right after the DEG was charged, can be found by

$$C_{\text{charge}} = (Q_{\text{discharge}} + Q_{\text{leak}})/V_{\text{charge}}. \tag{5.22}$$

We can extend the capacitance reconstruction process described above for all the points during the discharge phase, which yields the capacitance versus displacement data shown in Figure 5.15b.

Due to the deformation applied, seeking to avoid the stress of the sample and premature break, the capacitance change estimated is 41%, which, given that only 50% of the energy input for this kind of cycle is stored in the DEG [144], is not enough to compensate the implicit charging losses. In line with this prediction, Figure 5.14b shows that for both the cycles more energy is used as input than they are able to output. Nonetheless, we are able to see that the adapted cycle still outperforms the traditional one, having a reduced energy deficit as the outcome. A complete comparison of the cycles was performed through simulations in [155], which considers a higher capacitance swing able to produce a positive energy outcome and reports an overall better performance of the adapted cycle. While the hardware implementation is not capable of generating energy, it is still suitable for testing the SSPD method, as we describe below.

5.5.2 Self-sensing Peak Detection

To evaluate the feasibility of the proposed automatic charge management method proposed here, we used the test setup detailed in section 5.2.1. The algorithm was coded in the STM32 NUCLEO-F401RE development board (code can be found in appendix B) and we logged the data for current, voltage and the signal sent to the relays during the experiment, as well as the height of the tip of the inflated DEG through the DAQ. For the reported implementation, a sensing signal of 100V peak-to-peak amplitude, and 50Hz sinusoidal oscillation was superimposed over a 1.2kV bias voltage. The parameters used in the SSPD method implementation can be found in table 5.3.

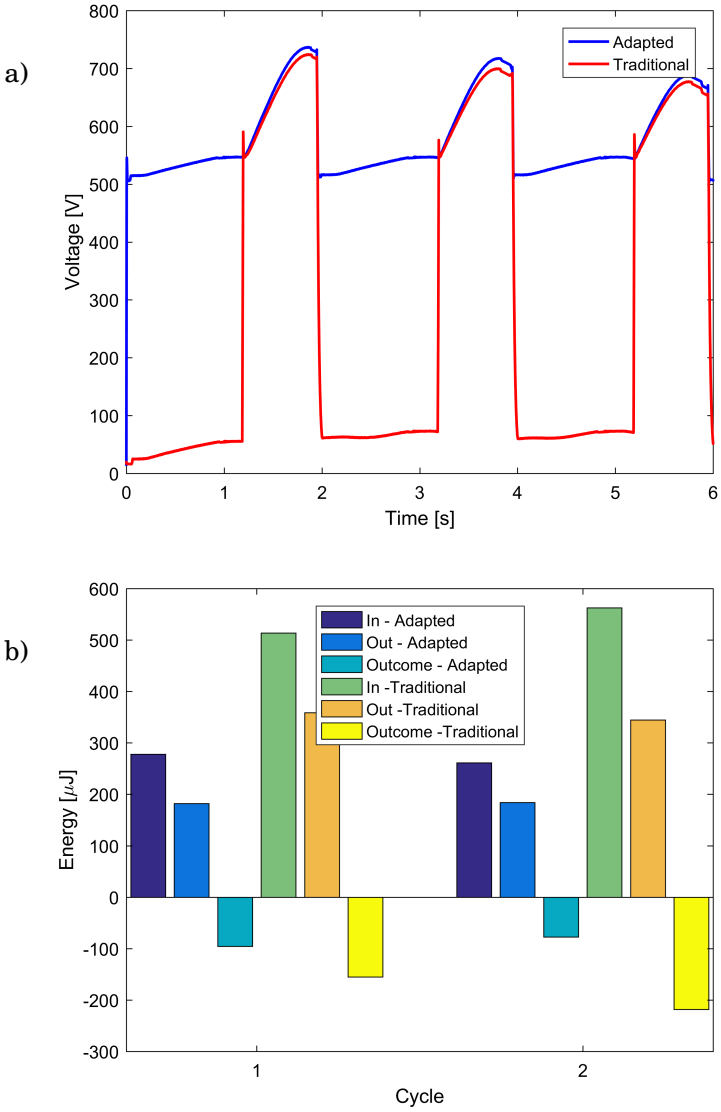

Figure 5.14: Voltage as a function of time for each of the cycles (a). Energy balance for each of the cycles in two of the cycles (b).

Figure 5.16 illustrates the first difficulty in the implementation of the method: although the DAQ was able to log the signals accurately, noise-free and in order of kHz, it does not perform computations internally, only transmits data to the computer. On the other hand, the microcontroller has a sampling frequency $f_S \approx 650 - 700$Hz (an Arduino Uno was tested and performed at 150Hz maximum) and had the interference of high amplitude noise, thus making a more challenging scenario to the implementation than previously tested. As an additional measure, to avoid the effects of the high amplitude noise in the capacitance value calculated, we implemented in the code a condition that the capacitance could not vary more than 5% at

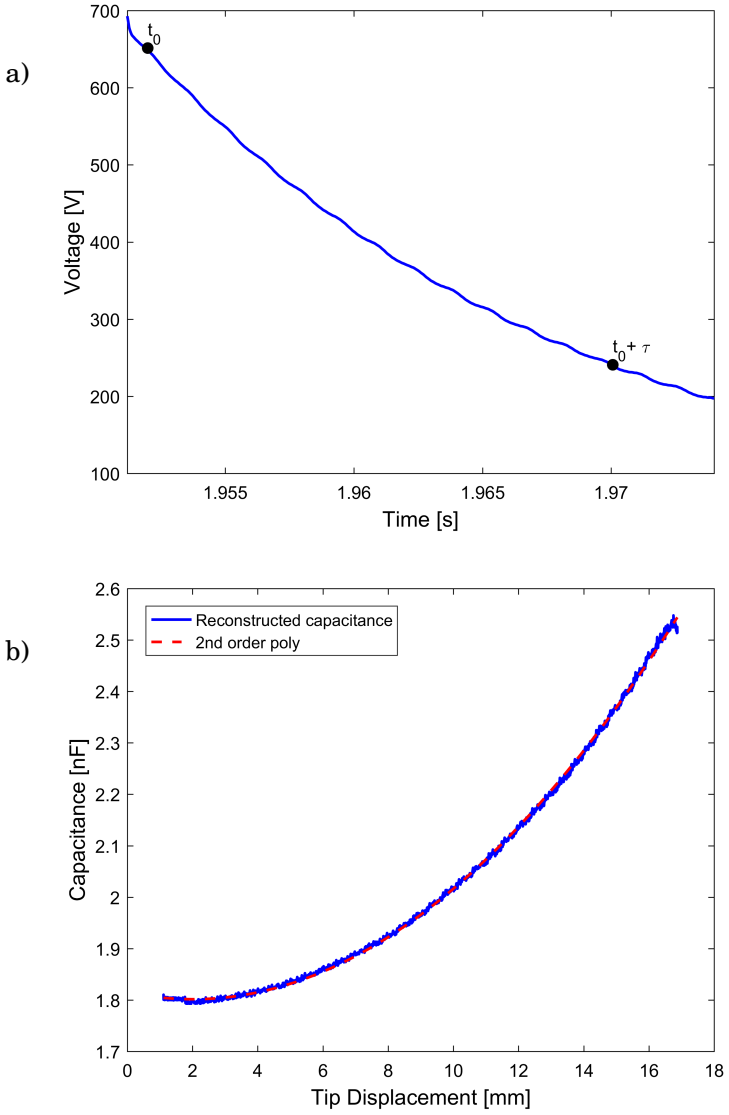

Figure 5.15: Detail of the discharging phase of the traditional cycle and the points used to calculate the capacitance during the discharge phase (a) and the capacitance reconstructed as a function of DEG tip height (b)

each iteration (in the implementation reported ≈ 0.1nF in 1.5ns). This condition avoided spikes in the capacitance signal due to noise, since only the latter would be able to induce the self-sensing algorithm to indicate a capacitance variation in the order of 66.6nF/s (obtained from 0.1nF/0.0015s), far more than the values found for the derivative of the capacitance, shown in Figure 4.14b.

Table 5.3: Control parameters for the experimental implementation

μ	0.95
K_{delay}	7.8s
λ_0	1.5
λ_1	5
λ_2	8
λ_3	12
λ_4	18
λ_5	150
L	0.0005
$x\%$	10%
x_{ff}	1.5×10^{-4}

Nonetheless, the SSPD scheme was implemented successfully, as shown in Figures 5.17, 5.18, and 5.19. Figure 5.17 demonstrates how the criteria of comparison with the previous minimum/maximum (criteria 4 on p. 113) was implemented: to find a maximum, the capacitance (blue line) at a given time should be $x\%$ (10%) higher than the corrected value of the last minimum (orange line), which is updated every time a new minimum is found, and to find a minimum, lower than the corrected value of the last maximum (yellow line), which is updated every time a new maximum is found. The stored last maximum (yellow line)/minimum (orange line) values shown in 5.17, correspond to the values of the capacitance during the detection, corrected each algorithm iteration ($\approx$ 1.5ms for the present implementation) by the factor x_{ff}. For faster sampling, lower values of the forgetting factor x_{ff} are required, since the algorithm will iterate faster. Similarly, x can be tuned by application: if high amplitudes are expected, or there is a need to avoid low amplitude cycles, x should be tuned higher. We also did not explore the use of the second derivative of the capacitance signal in the experiment reported, since this is a robustness feature to avoid false peak detection; due to the regular characteristic of the oscillations used, this did not occur. Figure 5.18 shows that we had a clear detection of the minimums (0.9ms advanced in average), implementing the discharge during the expected time, while the charging phase lasted longer than expected due to the delay in the inferred capacitance signal in relation to the deformation of the DEG; maximums were detected with an average delay of 0.28s.

In order to evaluate the accuracy of the capacitance values obtained by the SSPD method, we fitted a (second-order) polynomial to the data of the capacitance as a function of the height of the inflated DEG tip shown in Figure 5.15b. Using as input to this function the logged values for the DEG tip height from the experiment, we obtained the DEG capacitance values shown

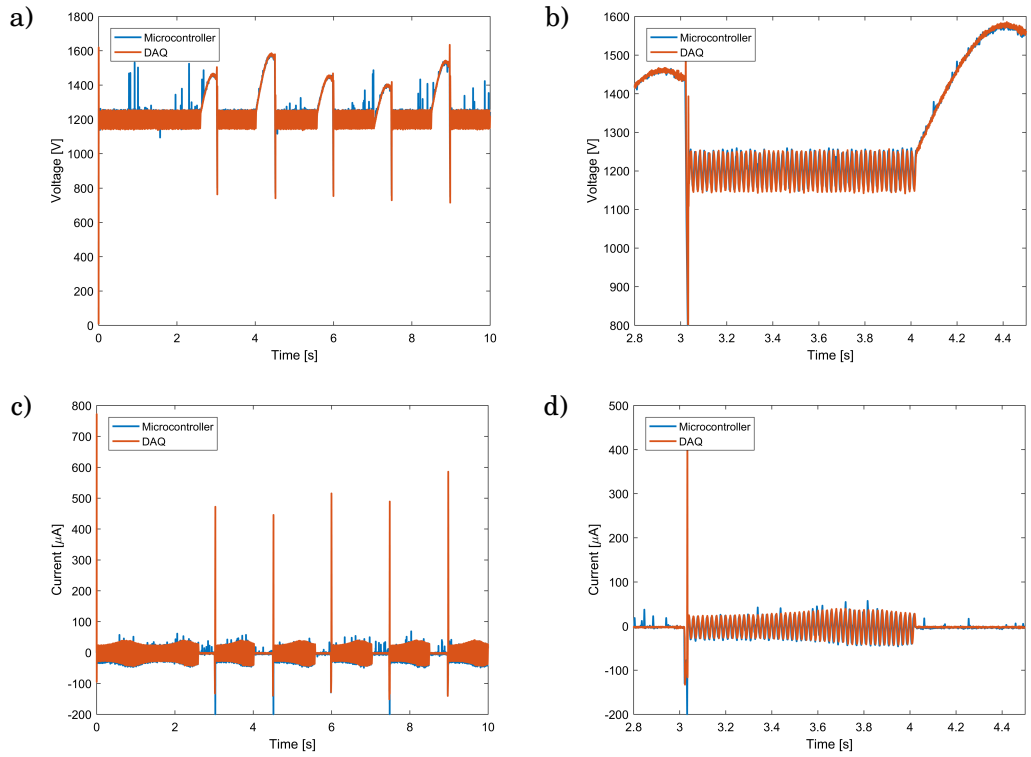

Figure 5.16: Voltage (a), detail of the voltage curve (b), electrical current (c), and detail of the electrical current (d) during the experiment duration as logged by the DAQ (orange) and read by the microcontroller (blue).

in the purple curve in Figure 5.17. Comparing these capacitance values with those obtained through the self-sensing scheme, the self-sensed capacitance signal showed a delay during its rising phase mainly, which is likely to be a combination of the filters used (moving average of the values within a window size of $\approx 1.2 f_S/f_e$ and $\mu = 0.95$), a lower sampling rate compared to the self-sensing implementations used as benchmark (usually in the order of kHz [55, 95, 121] and anti-noise factors implemented.

Among the advantages of the proposed model method to infer capacitance during the relaxing phase, against the setup compared with the approach used in [95], is the fact we do not require excitation, and its consequent energy losses, during the relaxing phase. In addition, our capacitance calculations in the relaxing phase depend only on the voltage signal, which tends to have a higher signal-to-noise ratio, reducing the exposure of the capacitance value obtained to noise. That results in a smoother signal than during charging, as shown in Figure 5.19, where we notice that the derivative of the capacitance signal has much lower noise when negative (capacitance signal decreasing) than when it is positive (capacitance signal increasing).

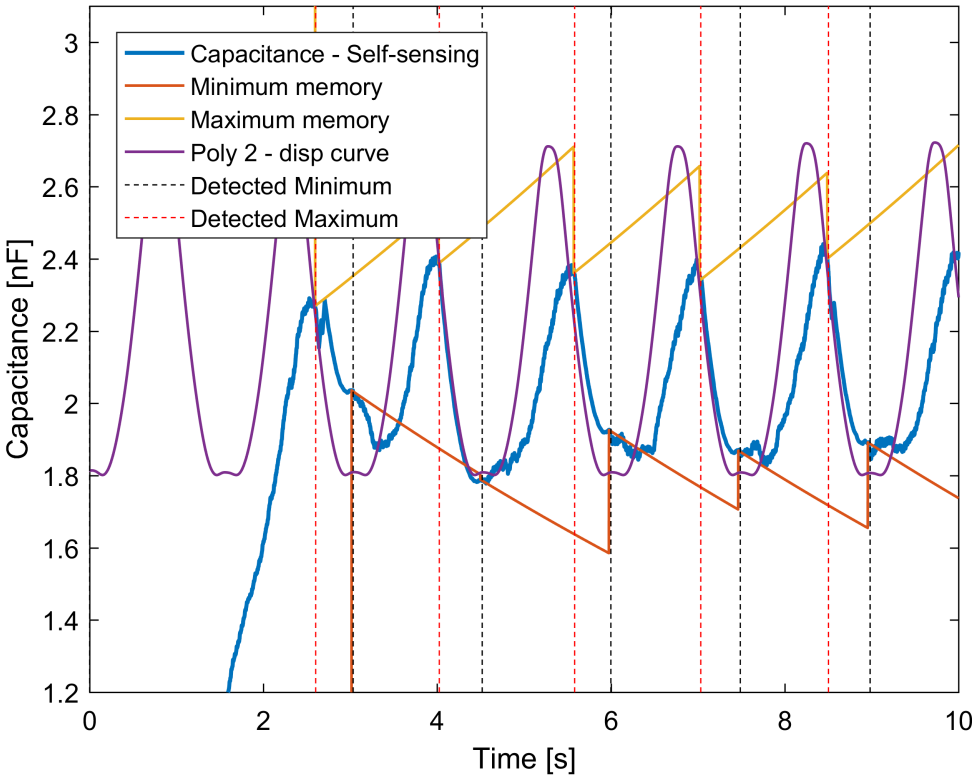

Figure 5.17: SSPD implementation outcome: capacitance signal inferred (blue), memory signal from last maximum (yellow) and minimum (red) corrected by forgetting factor, expected capacitance profile from the polynomial fit obtained from Figure 5.15b, dashed lines mark detection of maximum (red) and minimum (black).

Another relevant point to consider is that the self-sensed capacitance curve matches well the expected capacitance given by the interpolated data during the DEG's relaxing phase, although it does not always reach the minimum value. This could be due to the assumption that the exponential charge decay during the relaxing phase has constant K_{decay}, since it should depend on the membrane leaking characteristic, considering the reduction in capacitance, C, is compensated by the inversely proportional increase in membrane leakage resistance, R_l, keeping $K_{\text{decay}} = R_l C$ constant. This hypothesis does not hold true for the experimental setup we have, since the major leak source is the resistive voltage divider used to measure the voltage that has constant impedance, not compensating the varying C in the $R_l C$ term. Nonetheless, the capacitance calculated during the relaxing phase does track most of the expected capacitance curve. To account for the charge leakage through the voltage divider, K_{decay} can be easily tuned by keeping the DEG stretch constant, allowing the DEG to discharge and chose the value of K_{decay} such that the inferred capacitance results in a constant value (matching the fact the DEG is stationary).

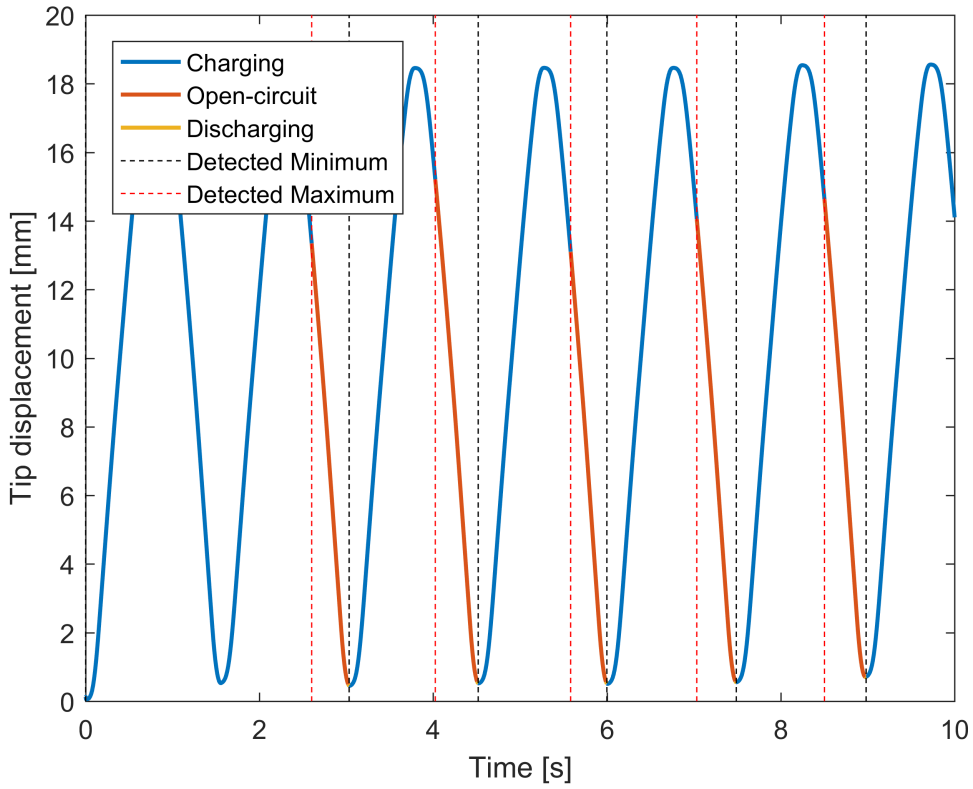

Figure 5.18: SSPD implementation outcome: capacitance derivative obtained through the differentiator, dashed lines mark detection of maximum (red) and minimum (black).

Note that the value obtained for K_{decay}, 7.8s, matches the order magnitude if we consider the voltage divider impedance (5GΩ) and the DEG capacitance (2nF): approximately 10s.

We also conducted experiments where the DEG was deformed in an irregular way, different from the periodic deformations shown previously. Example results are shown in Figure 5.20; our SSPD developed algorithm was able to detect successfully the peaks and coordinate independently the charging/discharging phases as required, showing the above-cited capacitance error and delay for peak detection during fast cycles.

5.6 Conclusion

This chapter reports the development of a self-sensing technique for DEGs which can be implemented using simple hardware. It also demonstrates experimentally that the cycle chosen for the self-sensing method to be implemented has equivalent performance to other traditional cycles in the literature. The final goal of developing and implementing a novel method to automate the

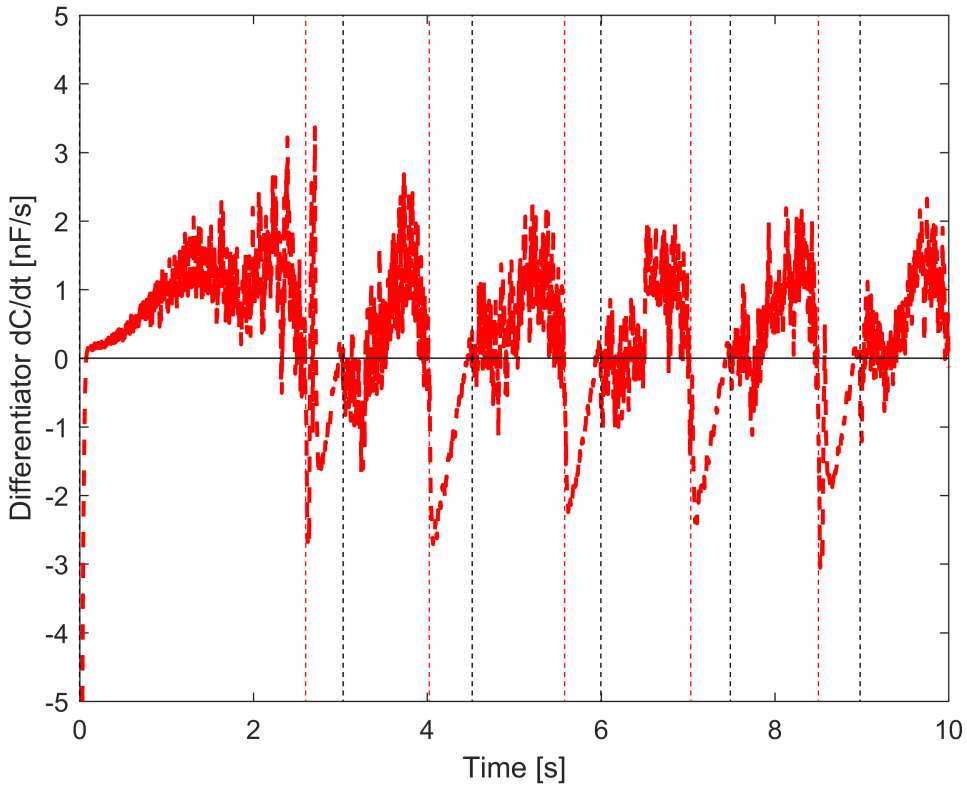

Figure 5.19: SSPD implementation outcome: DEG tip displacement and the correspondent phase of the DEG cycle as colour coded, dashed lines mark detection of maximum (red) and minimum (black).

energy harvesting process in DEGs through the use of self-sensing techniques was achieved. Both self-sensing and the charge management scheme were successfully tested through simulations and demonstrated to be feasible experimentally.

Regarding the self-sensing scheme proposed, it could incorporate some variations, such as the layout change proposed by McKay *et al.* [95], using a DC high voltage signal for charging while using a second source to provide the oscillating signal connected to the DEG low voltage terminal and a capacitor in parallel, which could give flexibility to use an active sensing method such as the one used during the stretching/charging phase during relaxing phase, e.g. for tuning of K_{decay} in an autonomous way after a certain number of cycles.

For higher capacitance swing (capacitance variation in a single cycle), if the hypothesis used for K_{decay} does not hold (which is bound to be investigated in future work) but an empirical relation between K_{decay} and C_k can be found, eq. (5.17) can be modified accordingly in the algorithm and

the method should work with no further disturbance. Further investigation on this assumption and how to best address this possible issue should be scope of future work.

Regarding the energetic aspect, since most of the power used in the self-sensing method is reactive, since the capacitor-like nature of the DEG governs most of the dynamics, the sensing signal does consume some power, mostly due to the power dissipation that occurs in the resistive elements of the circuitry when the sensing signal is implemented. One way to reduce this would be to reduce the sensing signal amplitude. However, this would reduce the magnitude of the current signal, and in turn reduce the signal-to-noise ratio, requiring more reliable and less noisy current reading. Alternatively, we could reduce the sensing frequency, and the same effect would be expected from the current signal, but it is important to highlight that, depending on its voltage magnitude and the material used, we could generate electrostatic actuation on the DE, as highlighted in Chapter 2, an undesired effect for the proposed application.

Despite being designed and implemented for a specific three stage cycle, the SSPD method could be easily adapted to other cycles. If one intended to implement the traditional constant charge cycle [47], the power supply DC signal could be adjusted so that the sensing signal was kept on during the whole stretching phase, with the charging by high voltage occurring only by the end of it. For example, high voltage charging could be marked to start when the capacitance derivative signal goes close to zero and stop after it becomes negative. The cycle scheme presented by [130], which uses a capacitor in parallel with the DEG would only require the straightforward change of the equation for the discharging phase so that it incorporates the parallel capacitor in the model.

The method proposed presents several parameters, that could affect its performance; but optimally tuning them was beyond the scope of this work. The tuning of such parameters, as well as the correct choice of filtering level, presents great potential for improvement of the performance demonstrated in the experimental application shown. Another point of potential improvement regards the implementation with a low-cost and low-specification microcontroller: better hardware could provide a faster sampling rate and less noise, which could allow the use of a lower amplitude in the sensing signal (reducing the energy consumption), and reduce the delay while increasing the capacitance calculation accuracy.

In spite of the room for improvement regarding the results presented, we have demonstrated a method through which a DEG can be controlled autonomously, providing adequate timing for the phase changes in the energy harvesting cycle while using simple computational hardware, showing its flexibility and robustness. It provides a low-cost solution for charge management for applications such as buoys [99], that might require the system to be simple and compact. The method proposed could also be used as an enabler of cycles such as the constant electric field

[47] that could yield the highest energy output per cycle, but require an active control of charges. These could be estimated based on the DEG voltage and capacitance level. In addition, the SSPD method provides a way to infer the deformation level of the DEG and provide safer operation, monitoring the likelihood of failure modes such as the rupture in case of high stretch levels, or dielectric breakdown in case the electric field rises above a safety threshold.

a)

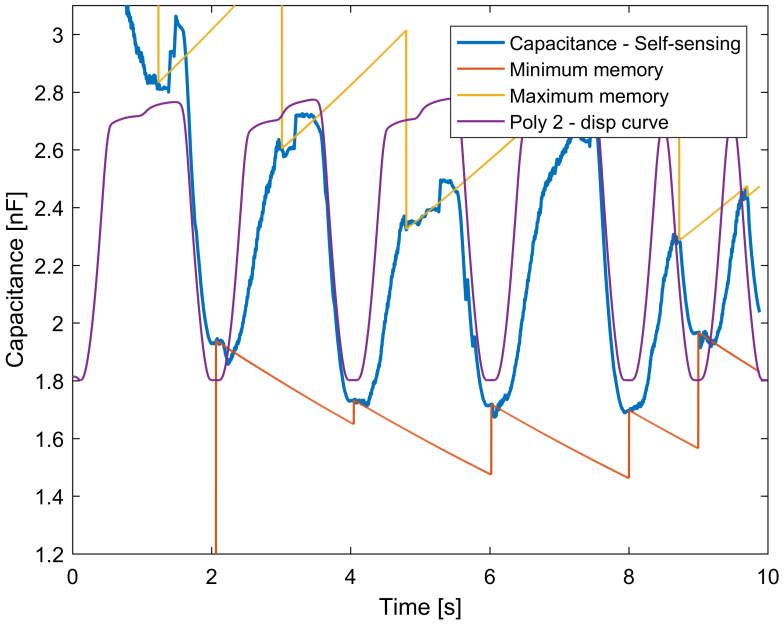

b)

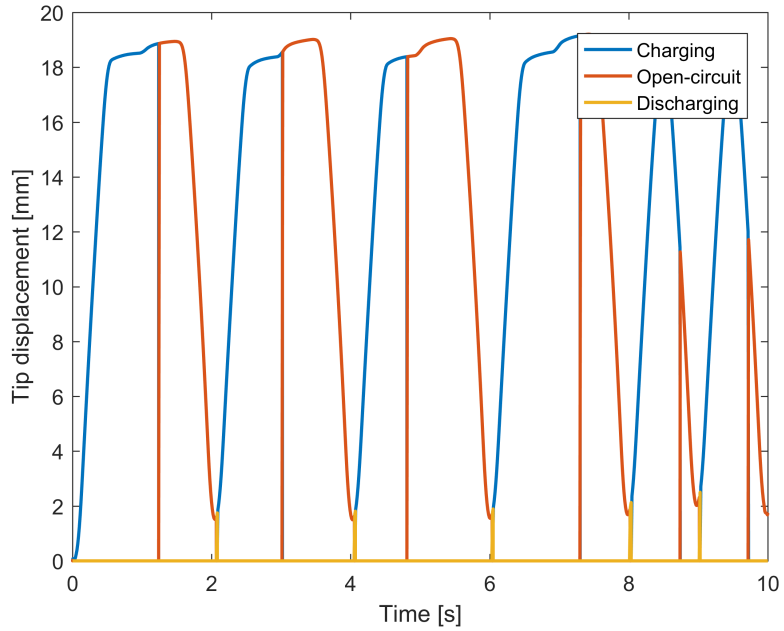

Figure 5.20: SSPD test on non regularly deformed DEG:capacitance signal inferred (blue), memory signal from last maximum (yellow) and minimum (red) corrected by forgetting factor, and expected capacitance profile from the polynomial fit obtained from Figure 5.15b (a); DEG tip displacement and the correspondent phase of the DEG cycle as colour coded (b).

CHAPTER 6

CONCLUSION

Covering a broad range of themes in the previous chapters, this thesis promotes the idea of smart Dielectric Elastomer Generators (DEGs) by exploring their multimodal capabilities. This chapter summarises and highlights the key findings, and suggests areas for future work in this theme.

6.1 Summary

In this thesis, we observed that when DEGs are charged, they exhibit some degree of actuator-like behaviour, varying according to the material stiffness and the electrostatic forces on the membrane. This behaviour might lead to undesired material deformation and result in viscoelastic losses. In contrast, by combining DEGs' actuator-like behaviour with SPCs, we a self-stabilising behaviour. Such behaviour can be explored in a beneficial way to prevent an SPC-DEG system from increasing its voltage indefinitely and suffering from dielectric breakdown or electromechanical instability. Finally, we were able to integrate the sensor mode into DEGs, which allowed not only deformation state monitoring but also promoted automatic charge management without the use of extra sensors.

Chapter 1 presented the concept of Dielectric Elastomers (DEs), explained in general terms how their behaviour can be mathematically described, introduced the motivation to investigate DEGs, as well as detailing some possible applications of DEGs.

Chapter 2 described the "actuator-like behaviour" of DEGs, which has not been previously investigated in the literature. The processes of charging and discharging were studied for a cycle and different modes of charging compared. It was concluded that the charging and discharging of

DEGs are processes that might yield significant losses and affect the overall system performance. It was further observed that limiting the current, promoting slower charging, can reduce these losses, both electrical and viscoelastic, the later due to the actuator-like effect.

Chapter 3 introduced the concept of the Self-Priming Circuit (SPC) and how it is integrated into DEG systems. New mathematical models were derived to describe their electric behaviour and we propose rules to optimise their design, based on the analytical model, that agree with those previously suggested by design rules in the literature. The concept of Integrated Self-Priming Circuit (ISPC) was also introduced, and a novel model for their dynamic derived. The proposed model was then validated against experimental results, showing good performance.

Chapter 4 analysed SPC-DEG systems in more depth, a pioneering approach also considering the implications from the electromechanical coupling, and that in some conditions, due to the actuator-like effect described in Chapter 2, the maximum and minimum values on a DEG cycle are not fixed. This led to the prediction of a self-stabilising behaviour of these systems, which could be exploited to passively avoid the constant rise in voltage in SPC-DEG systems and their consequent failure through dielectric breakdown. We proposed a simulation-based method to predict the occurrence of the self-stabilisation, as well as how it could be used as a design characteristic and explored to avoid failure modes. Through experiments, we analysed the actuator-like effect in an SPC-DEG system, as well as the self-stabilising behaviour. We quantify the energy conversion efficiency of the device and propose a straightforward method to predict the maximum voltage the system would achieve through self-stabilisation, based only on data obtained when its voltage is relatively low.

Chapter 5 presents a novel method to integrate sensing capabilities into DEGs. This method was verified to work in a simulation environment. We developed an algorithm to detect maxima and minima in the capacitance signals obtained through self-sensing. Finally, it was demonstrated that the proposed method works for coordinating charging and discharging according to a DEG harvesting cycle chosen in experimental conditions. The method was shown to provide additional robustness to the DEG, enabling it to perform in high noise and low sampling rate conditions.

6.2 Future work

Regarding future work, two main themes arise from this thesis: self-stabilising behaviour and charge management through self-sensing DEGs. The exploration of the self-stabilising behaviour in this thesis consisted of a proof of its existence and a brief characterisation, predicted numerically in a model DEG system, and also seen experimentally. However, its existence and use in DEG systems more generally would certainly be beneficial in case of using a continuous energy extraction method, which should affect the system as the charge leakage from the tests

reported in Chapter 4. Requiring fine estimations of the mechanical loads involved, such a system would allow the device to self-prime from a low voltage input up to the desired voltage level and then self-regulate without the need of further embedded dedicated electronics.

Regarding the work presented on self-sensing for DEGs, this could be developed in several lines. First, a methodology to optimally tune the parameters is required, which could be done through a fine-tuned model and the use of optimisation algorithms. Secondly, based on the noise level of the application scenario, a study of the best filtering techniques would be also beneficial, since the self-sensing method requires a smooth signal but the charge management performance can be heavily penalised if there is too much delay in the signal. Again, it would be clearly application dependent, requiring a clear specification of the hardware capabilities. Also, different cycles could be implemented through the technique developed. One could, for example, infer, based on the voltage and capacitance signal, the electric field and use the signal to obtain higher energy extraction per cycle, while avoiding dielectric breakdown and electromagnetic instability, if those were reliably characterised.

The actuator-like behaviour and the self-stabilisation behaviour in SPC-DEG systems reported and analysed in this thesis are highly dependent on the electromechanical coupling characteristics of the dielectric material. As the development of new DEG materials aims at improving the electromechanical coupling (e.g., increasing the relative dielectric permittivity), these phenomena could become more evident in future devices designed in the future, such that the analysis here reported provide guidelines on how to better exploit these behaviours.

The topics here presented provide important insights regarding the application of DEGs in real-world scenarios, providing tools to design self-contained energy harvesting systems, not only based on dielectric elastomer generators, but that could be extended to other capacitive energy harvesting devices.

APPENDIX A — ISPC MODEL INCLUDING LOSSES

Code used in the simulations for the ISPC including an equivalent leaking element in parallel to the system.

```
%% Numeric simulation values
dt = 1e-4; % [s] Time step for plotting and transition time calculation. Eg. Voltage C1 series == Voltave C2 parallel
Tol = 20; % [V] Tolerance for transition time calculation
T = 1.01; % [s] Oscilattion period
Cycles = 10; % [-] Number of cycles to simulate
Rn = 3.1e9; % [Ohm] Parallel resistance to the i-SPC
Bmaxn = 2.14; % [-] Ratio between maximum and minimum capacitance over a cycle for the biggest element of the iSPC
% V0n = 97.635; % [V] Initial priming voltage
V0n = 147; % [V] Initial priming voltage
nn = 1; % [-] Order of the circuit
C0n =1.4e-09; % [F] Minimum capacitance the biggest element of the iSPC reaches on a cycle

%% iSPC System definition

% Declaring variables used
syms C1(t) C2(t) V(t) R B(t) C0 Bmax f n N0 V0 t1 t2 t3 t4

N0 = n/(n+1); % [-] Variable to simplify the equation in subsequent calculations

% Functions defining capacitance change over time for the iSPC
B = (Bmax-1)*(0.5*cos(2*pi*f*t))+0.5*(Bmax+1);
C1 = C0*B;
C2 = C0*(1+Bmax)-C1;
```

```
25
%% Phase 0-1
27 t01 = [0:dt:T/2]; % Time array for calculations over the Phase 0-1

29 eq1 = (0 == (N0^-1*C1*diff(V,t)+V*diff(N0^-1*C1,t))+V/R); % Diff eq for C1 controlling in
       its parallel config
   eq2 = (0 == (C2*diff(V,t)+V*(diff(C2,t)))); % Diff eq for voltage in C2 in its series
       config
31

33 V01eq = vpa(dsolve(eq1,V(0) == N0*V0)); % Voltage for C1 and system in its parallel
       config
   VC2_01eq = vpa(dsolve(eq2,V(0) == V0)); % Voltage for C2 in its series config
35

37 %Assining numeric values for the equations obtained
   param = {C0       f      R      Bmax    V0    n};
39 val =   {C0n     1/T     Rn     Bmaxn   V0n   nn};
   V01n = subs(V01eq,param,val);
41 VC2_01n = subs(VC2_01eq,param,val);

43
   % Finding the transition time numerically
45 idx_t1= find((abs(double(subs(V01n,t,t01))-double(subs(VC2_01n,t,t01))))<Tol); % Find the
       index points close to t1 (difference smaller than Tol)
   while isempty(idx_t1) %Increase tolerance if the points no point were found in the
       previous step
47     Tol2=Tol*2;
       idx_t1= find((abs(double(subs(V01n,t,t01))-double(subs(VC2_01n,t,t01))))<Tol2);
49 end
   t1n = t01(round(mean(idx_t1))) % Average index values of points around t1 and round (to
       guerantee an integer) to determine t1
51 Vt1n = double(subs(V01n,t,t1n)) % Calculate the voltage at the transition to the next
       phase

53 % Plot the curve for the phase desired
   fplot(V01n,[0 t1n],'r--')
55 hold on

57

59 %% Phase 1-2
   t12 = [t1n:dt:T/2]; %Time array for calculations over the Phase 1-2
61

63 eq3 = (0 == (C1/N0+N0*C2)*diff(V,t)+V*(diff(C1/N0,t)+diff(N0*C2,t)+1/(R))); %Diff eq for
```

```
    C1 in its parallel config charging C2 in its series config

syms Vt1; % Transition voltage from previous phase and current for transition calculation
V12eq = vpa(dsolve(eq3,V(t1n) == Vt1)); %Voltage for current phase
i2_12=vpa(-(V12eq*diff(C2,t)+C2*diff(V12eq,t))*N0); %Current flowing to C2 in current
    phase

%Assining numeric values for the equations obtained
param = {C0      f      R      Bmax   V0   n     Vt1      pi};
val =   {C0n     1/T    Rn     Bmaxn  V0n  nn    Vt1n     3.1415};
V12n = subs(V12eq,param,val);
i2_12n = subs(i2_12,param,val);

i2_12n_double = real(double(subs(i2_12n,t, t12))); % Numeric solution for current flowing
     to C2 in current phase)

% Finding the transition time numerically
idx_t2 = find(i2_12n_double(end/2:end)>0)+round(length(i2_12n_double)/2); % Find index of
     time when current stops flowing to C2
t2n = t12(idx_t2(1)-1) % Obtain transition time by the index before the 1st index
    obtained above
Vt2n = double(subs(V12n,t,t2n)) % Calculate the voltage at the transition to the next
    phase

% Plot the curve for the phase desired
figure(Voltage);
V12_double = double(subs(V12n,t,[t1n:dt:t2n]));
plot([t1n:dt:t2n],V12_double,'r--');


%% Phase 2-3

% Split time array in 2 to avoid the discontinuity in the solution
t22 = [t2n:dt:T/2]; % Time array for calculations over the Phase 2-3 before half the
    cycle period
t23f = [T/2:dt:T]; % Time array for calculations over the Phase 2-3 after half the cycle
    period

eq4 = (0 == (C1/N0)*diff(V,t)+V*diff(C1/N0,t)+V/R); %Diff eq for C1 in its parallel
    config governing system voltage
eq5 = (0 == (C2*diff(V,t)+V*(diff(C2,t)))); %Diff eq for voltage in C2

% Split voltage eq array in 2 to avoid the discontinuity in the solution
syms Vt2 Vt22; %Vt22 being the voltage then time = T/2
V22eq = vpa(dsolve(eq4,V(t2n) == Vt2)); %Voltage of the system before time = T/2
V23eq = (dsolve(eq4,V(T/2) == Vt22)); %Voltage of the system after time = T/2
VC2_23eq = vpa(dsolve(eq5,V(t2n) == Vt2*N0)); %Voltage in C2 during current phase
```

```
%Assining numeric values for the equation obtained referring to voltage before time = T/2
param = {C0       f      R      Bmax   n     Vt2      pi};
val =   {C0n      1/T    Rn     Bmaxn  nn    Vt2n     3.14159};
V22n = subs(V22eq,param,val);

Vt22n = double(subs(V22n,t,T/2)); % Determining system voltage when time = T/2

%Assining numeric values for the equation obtained referring to voltage before time = T/2

param = {C0       f      R      Bmax   n     Vt2     Vt22      pi};
val =   {C0n      1/T    Rn     Bmaxn  nn    Vt2n     Vt22n     3.142};
V23n = vpa(subs(V23eq,param,val));
VC2_23n = subs(VC2_23eq,param,val);

% Finding the transition time numerically
idx_t3= find((abs(double(subs(V23n,t,t23f))-double(subs(VC2_23n,t,t23f))))<Tol); % Find
    the index points close to t3 (difference smaller than Tol)
t3n = t23f(round(mean(idx_t3)))% Average index values of points around t1 and round (to
    guerantee an integer) to determine t3
Vt3n = double(subs(V23n,t,t3n)) % Calculate the voltage at the transition to the next
    phase

% Plot the curve for the phase desired
figure(Voltage);
fplot(V22n,[t2n T/2],'r--');
fplot(V23n,[T/2 t3n],'r--');



%% Phase 3-4
t34 = [t3n:dt:T]; %Time array for calculations over the Phase 3-4

eq6 = (0 == N0^-1*(C2*diff(V,t)+V*diff(C2,t))+V/R); % Diff eq for C2 controlling in its
    parallel config
eq7 = (0 == (C1*diff(V,t)+V*(diff(C1,t)))); % Diff eq for voltage in C1 in its series
    config


syms Vt3;
V34eq = vpa(dsolve(eq6,V(t3n) == Vt3)); % Voltage for C2 and system in its parallel
    config
VC1_34eq = vpa(dsolve(eq7,V(t3n) == Vt3/N0)); % Voltage for C1 in its series config

%Assining numeric values for the equations obtained
param = {C0       f      R      Bmax   V0    n     Vt3      pi};
val =   {C0n      1/T    Rn     Bmaxn  V0n   nn    Vt3n     3.1415};
```

```
143
V34n = subs(V34eq,param,val);
145 VC1_34n = subs(VC1_34eq,param,val);

147 % Finding the transition time numerically
idx_t4= find((abs(double(subs(V34n,t,t34))-double(subs(VC1_34n,t,t34))))<Tol); % Find the
     index points close to t4 (difference smaller than Tol)
149 while isempty(idx_t4) %Increase tolerance if the points no point were found in the
    previous step
    Tol2=Tol*2;
151     idx_t4= find((abs(double(subs(V34n,t,t34))-double(subs(VC1_34n,t,t34))))<Tol2);
end
153 t4n = t34(round(mean(idx_t4))) % Average index values of points around t1 and round (to
    guerantee an integer) to determine t4
Vt4n = double(subs(V34n,t,t4n)) % Calculate the voltage at the transition to the next
    phase
155
% Plot the curve for the phase desired
157 figure(Voltage);
fplot(V34n,[t3n t4n],'r--');
159



161
%% Phase 4-5
163 t45 = [t4n:dt:T]; %Time array for calculations over the Phase 45

165 eq8 = (0 == (C2/N0+N0*C1)*diff(V,t)+V*(diff(C2/N0,t)+diff(N0*C1,t))+V/(R)); %Diff eq for
    C2 in its parallel config charging C1 in its series config

167 syms Vt4 ; % Transition voltage from previous phase and current for transition
    calculation
V45eq = vpa(dsolve(eq8,V(t4n) == Vt4)); %Voltage for current phase
169 i1_45=vpa(-(V45eq*diff(C1,t)+C1*diff(V45eq,t))*N0); %Current flowing to C1 in current
    phase

171 %Assining numeric values for the equations obtained
param = {C0      f     R     Bmax   V0   n    Vt4     pi};
173 val =   {C0n    1/T   Rn    Bmaxn  V0n  nn   Vt4n    3.1415};
V45n = subs(V45eq,param,val);
175 i1_45n = subs(i1_45,param,val);

177 i1_45n_double = double(subs(i1_45n,t, t45)); % Numeric solution for current flowing to C1
     in current phase

179 % Finding the transition time numerically
idx_t5 = find(i1_45n_double(end/2:end)>0)+round(length(i1_45n_double)/2); % Find index of
     time when current stops flowing to C1
```

```
t5n = t45(idx_t5(1)-1) % Obtain transition time by the index before the 1st index
    obtained above
Vt5n = double(subs(V45n,t,t5n)) % Calculate the voltage at the transition to the next
    phase

% Plot the curve for the phase desired
figure(Voltage);
V45_double = double(subs(V45n,t,[t4n:dt:t5n]));
plot([t4n:dt:t5n],V45_double,'r--');


%% Next cycles
count = 2; % Number of half cycles past
while (count<2*Cycles)
    tic
    %% Equivalent to phase 2-3

    %Assining numeric values for the equation obtained referring to voltage before time =
     T/2
    param = {C0       f      R      Bmax    n     Vt2      pi};
    val =   {C0n     1/T     Rn     Bmaxn   nn    Vt5n     3.14159};
    V22n = subs(V22eq,param,val);

    Vt22n = double(subs(V22n,t,T/2)) % Determining system voltage when time = T/2


    %Assining numeric values for the equation obtained referring to voltage before time =
     T/2
    param = {C0       f      R      Bmax    n     Vt2     Vt22      pi};
    val =   {C0n     1/T     Rn     Bmaxn   nn    Vt5n     Vt22n     3.142};
    V23n = vpa(subs(V23eq,param,val));
    VC2_23n = subs(VC2_23eq,param,val);

    % Finding the transition time numerically
    idx_t3= find((abs(double(subs(V23n,t,t23f))-double(subs(VC2_23n,t,t23f))))<Tol); %
    Find the index points close to t3 (difference smaller than Tol)
    while isempty(idx_t3) %Increase tolerance if the points no point were found in the
    previous step
        Tol2=Tol*2;
        idx_t3= find((abs(double(subs(V23n,t,t23f))-double(subs(VC2_23n,t,t23f))))<Tol2);
    end
    t3n = t23f(round(mean(idx_t3)))% Average index values of points around t1 and round (
    to guerantee an integer) to determine t3
    Vt3n = double(subs(V23n,t,t3n)) % Calculate the voltage at the transition to the next
     phase

    % Plot the curve for the phase desired
```

```
figure(Voltage);
V22_double = double(subs(V22n,t,[t2n:dt:T/2]));
plot([t5n:dt:T]+(count-2)*T/2,V22_double,'r--');
V23_double = double(subs(V23n,t,[T/2:dt:t3n]));
plot([0:dt:t3n-T/2]+count*T/2,V23_double,'r--');



%% Equivalent to phase 3-4


%Assining numeric values for the equations obtained
param = {C0      f      R      Bmax   V0   n     Vt3     pi};
val =   {C0n     1/T    Rn     Bmaxn  V0n  nn    Vt3n    3.1415};
V34n = subs(V34eq,param,val);
VC1_34n = subs(VC1_34eq,param,val);

% Finding the transition time numerically
idx_t4= find((abs(double(subs(V34n,t,t34))-double(subs(VC1_34n,t,t34))))<Tol); % Find
 the index points close to t4 (difference smaller than Tol)
while isempty(idx_t4) %Increase tolerance if the points no point were found in the
previous step
    Tol2=Tol*2;
    idx_t4= find((abs(double(subs(V34n,t,t34))-double(subs(VC1_34n,t,t34))))<Tol2);
end
t4n = t34(round(mean(idx_t4))) % Average index values of points around t1 and round (
to guerantee an integer) to determine t4
Vt4n = double(subs(V34n,t,t4n)) % Calculate the voltage at the transition to the next
 phase

% Plot the curve for the phase desired
figure(Voltage);
V34_double = double(subs(V34n,t,[t3n:dt:t4n]));
plot([t3n-T/2:dt:t4n-T/2]+count*T/2,V34_double,'r--');

%% Equivalent to phase 4-5

%Assining numeric values for the equations obtained
param = {C0      f      R      Bmax   V0   n     Vt4     pi};
val =   {C0n     1/T    Rn     Bmaxn  V0n  nn    Vt4n    3.1415};
V45n = subs(V45eq,param,val);
i1_45n = subs(i1_45,param,val);

i1_45n_double = double(subs(i1_45n,t, t45)); % Numeric solution for current flowing
to C1 in current phase

% Finding the transition time numerically
```

```
    idx_t5 = find(i1_45n_double(end/2:end)>0)+round(length(i1_45n_double)/2); % Find
    index of time when current stops flowing to C1
    t5n = t45(idx_t5(1)-1) % Obtain transition time by the index before the 1st index
    obtained above
    Vt5n = double(subs(V45n,t,t5n)) % Calculate the voltage at the transition to the next
     phase

    % Plot the curve for the phase desired
    figure(Voltage);
    V45_double = double(subs(V45n,t,[t4n:dt:t5n]));
    plot([t4n-T/2:dt:t5n-T/2]+count*T/2,V45_double,'r--');

    count = count+1;

end

hold off

gcf;
ylabel('Voltage (V)','FontSize',16,'Fontname','Timesnewroman');
xlabel('Time (s)','FontSize',16,'Fontname','Timesnewroman');
xlim([0 t5n+(count-2)*T/2]);
```

APPENDIX B

APPENDIX B — CODE USED IN THE MICROCONTROLLER FOR CHARGE MANAGEMENT

Code implemented in the STM32 NUCLEO-F401RE development board to control charge and discharge switches during a dielectric elastomer generator cycle as described in section section 5.2.1

```

#include <BasicLinearAlgebra.h>
#include <math.h>
#include <Filters.h>

// All the functions in BasicLinearAlgebra are wrapped up inside the namespace BLA, so
    specify that we're using it like so:
using namespace BLA;


// Declare variables


//float BufferC[20] = {0.5, 0, 0, 0, 0, 0, 0, 0, 0, 0, 0, 0, 0, 0, 0, 0, 0, 0, 0, 0};
//float BufferCdot[20] = {0, 0, 0, 0, 0, 0, 0, 0, 0, 0, 0, 0, 0, 0, 0, 0, 0, 0, 0, 0};
//float BufferCdotdot[20] = {0, 0, 0, 0, 0, 0, 0, 0, 0, 0, 0, 0, 0, 0, 0, 0, 0, 0, 0, 0};
float BufferC[200];
float BufferCf[200];
float BufferCdot[200];
float BufferCdotdot[200];

char t_temp[10];
char V_temp[10];
```

```
char I_temp[10];
char C_temp[10];
char msg[20];

float fe = 50;
float filterFrequency = 90;
FilterOnePole lowpassFilter( LOWPASS, filterFrequency );
FilterOnePole lowpassFilter2( LOWPASS, 10 );

float epsilon = 10 ^ -5;
float imin = .05;
float V;
float V_old = 0;
float I;
float I_old = 0;
float R;
float C;
float Rs;
float C0 = .5; //[nF]

float mu = .95;
float RlC = 7.8;
float q_old = 0;
float y;

float K_comb;
float Kt;
int Kc;
float Ts;
float Cf_old = C0;
float Cf;
//int j;



float z_dot[6] = {1, 1, 1, 1, 1, 1};
float z[6] = {C0, 1, 1, 1, 1, 1};



#define N 200
//float NC;
float NCdot;
float NCdotdot;
float LC;
float LCdot;
float LCdotdot;
```

```
float LP[2] = {C0 * 9, C0 * .5};
72
74
76 float pc = 10;
float X0 = -1;
78 float X = X0;
float Aux = 0;
80
82 float t0 = 0;
float t;
84 float t_new;
float t_old = 0;
86
int s = 1;
88 int s_old = 1;
int swt_c;
90 int swt_d;
92
float Start = 0;
94 float Start_old = 0;
96 BLA::Matrix<2, 2> P_new = {1, 0, 0, 1};
BLA::Matrix<2, 2> P_old = {1, 0, 0, 1};
98 BLA::Matrix<2, 1> theta_new = {1, 1};
BLA::Matrix<2, 1> theta_old = {1, .01};
100 BLA::Matrix<2, 1> Fi = {1, 1};
102 BLA::Matrix<2, 1> M21;
BLA::Matrix<1, 2> M12;
104 BLA::Matrix<2, 2> M22;
BLA::Matrix<1, 1> M11;
106 BLA::Matrix<1, 1> M11_2;
108 //pins
const int Ipin = A5;
110 const int Vpin = A4;
const int enabler = 2;
112 const int PinMax = 4;
const int PinMin = 3;
114
116
```

```
118
120
void setup() {
122   // put your setup code here, to run once:
   //Set initial state to zero
124   int state = 0;
   BufferC[0] = .5;
126   swt_c = 1;
   swt_d = 0;
128   digitalWrite(PinMin, HIGH);
   digitalWrite(PinMax, LOW);
130
132
134
   //Initialise serial comms
136   Serial.begin(2000000);
   digitalWrite(13, LOW);
138
   pinMode(Vpin, INPUT);
140   pinMode(Ipin, INPUT);
   pinMode(PinMax, OUTPUT);
142   pinMode(PinMin, OUTPUT);
   pinMode(enabler, INPUT);
144   pinMode(LED_BUILTIN, OUTPUT);
146
   digitalWrite(PinMin, LOW);
148   digitalWrite(PinMax, LOW);
}
150
void loop() {
152
   swt_c = 1;
154   swt_d = 0;
   digitalWrite(LED_BUILTIN, LOW);
156
   while (digitalRead(enabler) == HIGH) {
158
     selfsensing();
160
     differentiator();
162     //     differentiator2();
     peakdetection();
164     if (V < .9) {
```

```
      swt_c = 1;
      swt_d = 0;
    }

    //send serial message
    Serial.print(t, 4); //2
    Serial.print(":");
    Serial.print(V, 4);
    Serial.print(":");
    Serial.print(I, 4);
    Serial.print(":");
    Serial.print(Cf, 4);
    Serial.print(":");
    Serial.print(z_dot[0], 4);
    Serial.print(":");
    Serial.print(LP[1], 4);
    Serial.print(":");
    Serial.print(LP[0], 4);
    Serial.println(":");
//        Serial.print(swt_c,4);
//        Serial.print(":");
//        Serial.print(swt_d,4);
//        Serial.println(":");


    digitalWrite(LED_BUILTIN, HIGH);
  }
  t0 = 0;
  t = 0;
  digitalWrite(PinMin, LOW);
  digitalWrite(PinMax, LOW);
  LP[0] = C0 * 9;
  LP[1] = C0 *.5;
}


void selfsensing() {

  if (t0 == 0) {
    t0 = micros() / 1000000.;
    //      Serial.println(t0);
  }
  //    Serial.println(t0);
  t = micros() / 1000000.;
  //    Serial.println(t);
  t = t - t0;
  Ts = t - t_old;
```

```
212   //     Serial.print(t); //1
      //     Serial.print(":");
214   Kt = tan(3.1415926 * fe * Ts) / (2 * 3.1415926 * fe);
      K_comb = round(1. / (Ts * fe));
216   Kc = K_comb;


218


220   V = analogRead(Vpin) * 3.3 / 1024.; //   [kV]
//    if (V > .500) {
222 //     V = lowpassFilter.input( V );
//      //     if (abs(V - V_old) > .1 * V_old) {
224 //      //       V = analogRead(Vpin) * 3.3 / 1024.;
//      //     }
226 //    }


228


230   I = ((analogRead(Ipin) * 3.3) / 1024. - 1.65) * 255.9;
      if (I > 200) {
232     I = 200;
      }
234   if (I < -200) {
        I = -200;
236   }

238   if ((swt_c == 1) &&(s_old!=2)) {
        s = 1;
240     digitalWrite(PinMin, HIGH);
        digitalWrite(PinMax, LOW);
242     //     Serial.println("Charging");
      }
244   if ((swt_d == 1) &&(s_old!=1)) {
        s = 3;
246     digitalWrite(PinMin, LOW);
        digitalWrite(PinMax, HIGH);
248     //     Serial.println("Discharging");
      }
250   if ((swt_c == 0) && (swt_d == 0)&&(s_old!=3)) {
        s = 2;
252     digitalWrite(PinMin, LOW);
        digitalWrite(PinMax, LOW);
254     //     Serial.println("Open circuit");
      }
256

      // reset initial condition and variables depending on change of switch
258   t_new = t;
```

```
260   if ((s == 1 || s == 3) && (s_old == 2)) { //Start Charging/Discharging
        t_new = t_old;
262   }

264   if ((s == 2) && (s_old != 2)) { //Start Open-circuit
        t_new = t;
266   }

268   // run RLS
      if (s == 1) {       //charging
270

272     // compute regressors for RLS
        //       I = lowpassFilter.input( I );
274     y = V - V_old;
        Fi(0, 0) = I + I_old;
276     Fi(1, 0) = I - I_old;

278     //     if ((abs(I) <= imin) && (abs(I_old) <= imin)) { //if current for two samples is
         smaller than imin
        M11 = (((~Fi * P_old) * Fi) + 1.);
280     P_new =  (P_old - ( P_old * Fi * (~Fi) * P_old) / M11(0)); //calculate Pk
        P_new = P_new * (1 / mu);
282     M11 = ~Fi * theta_old;
        M11_2 = ~Fi * P_old * Fi;
284     theta_new = theta_old + (P_old * Fi) * ((y - M11(0, 0)) / (1. + M11_2(0, 0))); //
        calculate theta (C and R indirectly)
      }
286   else {


288
        P_new = P_old;
290     if (s == 3) { //discharging
          theta_new = theta_old;
292       C = BufferC[0];
        }
294     else {       //open-circuit

296       Rs = theta_old(1, 0);
          if ((s == 2) && (s_old != 2)) { //Start Open-circuit
298       }
          else {
300         C = q_old / (V) * exp(-(Ts) / RlC);
          }
302       theta_new = {Kt / C, Rs};
        }
```

```
304   }

306   // compute resistance and capacitance
      C = Kt / max(epsilon, theta_new(0, 0));
308
      if (C > 1.05 * BufferCf[0] ) {
310     C = 1.05 * BufferCf[0];
      }
312   if (C < .95 * BufferCf[0] ) {
        C = .95 * BufferCf[0];
314   }
      Rs = theta_new(1);
316   theta_new(0) = Kt / C;


318
      // Comb filter
320   Kc = round(1.2*Kc + 1);

322   if (Kc > N - 1) {
        Kc = N;
324   }


326


328   for (int j = 0; j <= N - 2; j++) {

330     BufferC[N - 1 - j] = BufferC[N - 2 - j];
        BufferCf[N - 1 - j] = BufferCf[N - 2 - j];
332   }
      BufferC[0] = C;
334
      Cf = average(BufferC, Kc);
336
      BufferCf[0] = Cf;
338   theta_new(0) = Kt / Cf;


340



342
      // update variables
344   q_old = C * V;
      t_old = t;
346
      V_old = V;
348   I_old = I;
      theta_old = theta_new;
350   P_old = P_new;
```

```
  s_old = s;
352
354
356 }
358
360 void differentiator() {
362
  float lambda[6];
364  float L = .0005;
  lambda[0] = 1.5;
366  lambda[1] = 5;
  lambda[2] = 8;
368  lambda[3] = 12;
  lambda[4] = 18;
370  lambda[5] = 150;
  int k = 5;
372
  z_dot[0] = -lambda[k] * pow(L, (1. / (k + 1.))) * pow((abs(z[0] - Cf)), ((k) / (k + 1.)
    )) * sign(z[0] - Cf) + z[1];
374  for (int i = 1; i <= k - 1; i++) { // i = 1, 2, 3, 4
    z_dot[i] = -lambda[k - i] * pow(L, (1. / (k + 1. - i))) * pow((abs(z[i] - z_dot[i -
    1])), ((k - i) / (k + 1. - i))) * sign(z[i] - z_dot[i - 1]) + z[i + 1];
376  }
  int i = k; //i = 5
378  z_dot[k] = -lambda[k - i] * L * sign(z[i] - z_dot[i - 1]);

380  for (int i = 0; i <= k; i++) {
    z[i] = z[i] + z_dot[i] * (Ts);
382  }

384

386  return;
}
388

390
void peakdetection() {
392
  int n = round(.085 / Ts);
394
  for (int j = 0; j <= N - 2; j++) {
```

```
396
    BufferCdot[N - 1 - j] = BufferCdot[N - 2 - j];
398    BufferCdotdot[N - 1 - j] = BufferCdotdot[N - 1 - j];
  }
400  BufferCdot[0] = z_dot[0];
  BufferCdotdot[0] = z_dot[1];
402

404  //  NC = average(BufferC, N);
  //  NCdot = average(BufferCdot, N);
406  //  NCdotdot = average(BufferCdotdot, N);

408  float LC = BufferCf[n];
  float NC = BufferCf[0];
410  LCdot = BufferCdot[n];
  NCdot = BufferCdot[0];
412  //   LCdotdot = BufferCdotdot[19];
  //  NCdotdot = BufferCdotdot[0];.
414  NCdotdot = average(BufferCdotdot, Kc);

416

  float forget_f = .00015;
418  LP[0] = LP[0] * (1 + forget_f);
  LP[1] = LP[1] * (1 - forget_f);
420

  if (t > .1) {
422


424    //MIN
    //    if ((NC > LC) && (LCdot * NCdot < 0) && (NCdotdot > 0) && (NC < (1 - pc / 100)*
    LP[0])) {
426    if ((NC > LC) && (LCdot * NCdot < 0) && (NC < (1 - pc / 100)*LP[0]) ) {
      Aux = -1;
428

      if (Aux != X) {
430        X = Aux;
        LP[1] = NC;
432        swt_d = 1;
        swt_c = 0;
434      }
    }
436



438


440    //MAX
```

```
442     //     if ((LC > NC) && (LCdot * NCdot < 0) && (NCdotdot < 0) && (NC > (1 + pc / 100)*
        LP[1])) {

444     if ((LC > NC) && (LCdot * NCdot < 0) && (NC > (1 + pc / 100)*LP[1])) {
          Aux = 1;
446
          if ( Aux != X) {
448         X = Aux;
            LP[0] = NC;
450         swt_d = 0;
            swt_c = 0;
452       }
        }
454   }
      else {
456     swt_d = 0;
        swt_c = 1;
458   }

460 }


462


464
    float sign(float number) {
466   return (number / abs(number));
    }
468
    float average (float *array, int len)  // assuming array is int.
470 {
      float sum = 0 ;  // sum will be larger than an item, long for safety.
472   for (int i = 0 ; i < len ; i++) {
        sum += array [i] ;
474   }
      return  (sum) / len ;  // average will be fractional, so float may be appropriate.
476 }
```

BIBLIOGRAPHY

[1] *CTsystems - About us*.
http://www.ct-systems.ch/.
[Online; accessed 19-August-2018].

[2] *ElastiSense: Robust Industrial Sensors with Electro-Active Polymer tech*.
https://www.elastisense.com/.
[Online; accessed 19-August-2018].

[3] *Parker FlexSense Evaluation Kits | Parker Quick Coupling Division*.
http://solutions.parker.com/FlexSenseKit.
[Online; accessed 19-August-2018].

[4] *Silicon sheets harvest electricity from ocean waves - Bosch Media Service*.
https://www.bosch-presse.de/pressportal/de/en/silicon-sheets-harvest-electricity-from-ocean-waves-42267.html.
[Online; accessed 19-August-2018].

[5] *StretchSense*.
www.stretchsense.com.
[Online; accessed 19-August-2018].

[6] *Technical Data Sheet 846 Carbon Conductive Grease*.
www.mgchemicals.com/downloads/tds/tds-846.pdf.
[Online; accessed 9-November-2018].

[7] P. ALSTONE, D. GERSHENSON, AND D. M. KAMMEN, *Decentralized energy systems for clean electricity access*, Nature Climate Change, 5 (2015), pp. 305–314.

[8] A. BABARIT, B. GENDRON, J. SINGH, C. MÉLIS, AND P. JEAN, *Hydro-Elastic Modelling of an Electro-Active Wave Energy Converter*, in Volume 9: Odd M. Faltinsen Honoring Symposium on Marine Hydrodynamics, ASME, 6 2013, p. V009T12A033.

[9] J. A. BAROUDI, V. DINAVAHI, AND A. M. KNIGHT, *A review of power converter topologies for wind generators*, Renewable Energy, 32 (2007), pp. 2369–2385.

[10] C. BAUMEISTER AND L. KILIAN, *Forty Years of Oil Price Fluctuations: Why the Price of Oil May Still Surprise Us*, Journal of Economic Perspectives, 30 (2016), pp. 139–160.

[11] S. P. BEEBY, M. J. TUDOR, AND N. M. WHITE, *Energy harvesting vibration sources for microsystems applications*, Measurement Science and Technology, 17 (2006), pp. R175–R195.

[12] P. G. BINH, D. N. C. NAM, AND K. K. AHN, *Design and Modeling of an Innovative Wave Energy Converter Using Dielectric Electro-active Polymers Generator*, International Journal of Precision Engineering and Manufacturing, 16 (2015), pp. 1833–1843.

[13] E. BORTOT, M. GEI, AND G. DEBOTTON, *Optimal energy harvesting cycles for load-driven dielectric elastomer generators under equibiaxial deformation*, Meccanica, 50 (2015), pp. 2751–2766.

[14] A. E. BOWERS, J. M. ROSSITER, P. J. WALTERS, AND I. A. IEROPOULOS, *Dielectric elastomer pump for artificial organisms*, vol. 7976, International Society for Optics and Photonics, 3 2011, p. 797629.

[15] J.-B. CAO, S.-J. E, Z. GUO, Z. GAO, AND H.-P. LUO, *Electromechanical conversion efficiency for dielectric elastomer generator in different energy harvesting cycles*, AIP Advances, 7 (2017), p. 115117.

[16] F. CARPI, S. BAUER, AND D. DE ROSSI, *Stretching dielectric elastomer performance*, Science (New York, N.Y.), 330 (2010), pp. 1759–61.

[17] F. CARPI, G. FREDIANI, AND D. DE ROSSI, *Opportunities of hydrostatically coupled dielectric elastomer actuators for haptic interfaces*, vol. 7976, International Society for Optics and Photonics, 3 2011, p. 797618.

[18] F. CARPI, G. FREDIANI, S. TURCO, AND D. DE ROSSI, *Bioinspired Tunable Lens with Muscle-Like Electroactive Elastomers*, Advanced Functional Materials, 21 (2011), pp. 4152–4158.

[19] F. CARPI, D. D. ROSSI, R. KORNBLUH, R. PELRINE, AND P. SOMMER-LARSEN, *Dielectric elastomers as electromechanical transducers fundamentals, materials, devices, models and applications of an emerging electroactive polymer technology*, Elsevier, Amsterdam, Netherlands, 2008.

[20] C. CHIANG FOO, S. Q. CAI, S. JIN ADRIAN KOH, S. BAUER, Z. G. SUO, C. C. FOO, S. Q. CAI, S. J. A. KOH, S. BAUER, AND Z. G. SUO, *Model of dissipative dielectric elastomers*, Journal of Applied Physics, 111 (2012).

[21] S. CHIBA, M. WAKI, K. FUJITA, K. MASUDA, AND T. IKOMA, *Simple and Robust Direct Drive Wave Power Generation System Using Dielectric Elastomers*, Journal of Materials Science and Engineering B, 7 (2017), pp. 39–47.

[22] S. CHIBA, M. WAKI, R. KORNBLUH, AND R. PELNINE, *Innovative power generators for energy harvesting using electroactive polymer artificial muscles*, Electroactive Polymer Actuators and Devices (Eapad) 2008, 6927 (2008).

[23] S. CHIBA, M. WAKI, R. KORNBLUH, AND R. PELRINE, *Innovative wave power generation system using electroactive polymer artificial muscles*, in OCEANS 2009-EUROPE, IEEE, 5 2009, pp. 1–3.

[24] S. CHIBA, M. WAKI, T. WADA, Y. HIRAKAWA, K. MASUDA, AND T. IKOMA, *Consistent ocean wave energy harvesting using electroactive polymer (dielectric elastomer) artificial muscle generators*, Applied Energy, 104 (2013), pp. 497–502.

[25] H. CHOI, S. LEE, K. JUNG, J. KOO, S. LEE, R. CHOI, J. JEON, AND J. NAM, *Tactile display as a braille display for the visually disabled*, in 2004 IEEE/RSJ International Conference on Intelligent Robots and Systems (IROS) (IEEE Cat. No.04CH37566), vol. 2, IEEE, pp. 1985–1990.

[26] C. CHRISTIANSON, N. N. GOLDBERG, D. D. DEHEYN, S. CAI, AND M. T. TOLLEY, *Translucent soft robots driven by frameless fluid electrode dielectric elastomer actuators*, Science Robotics, 3 (2018), p. eaat1893.

[27] C. CHRISTIANSON, N. N. GOLDBERG, AND M. T. TOLLEY, *Elastomeric diaphragm pump driven by fluid electrode dielectric elastomer actuators (FEDEAs)*, in Electroactive Polymer Actuators and Devices (EAPAD) XX, Y. Bar-Cohen, ed., vol. 10594, SPIE, 3 2018, p. 21.

[28] A. T. CONN AND J. ROSSITER, *Antagonistic dielectric elastomer actuator for biologically-inspired robotics*, vol. 7976, International Society for Optics and Photonics, 3 2011, p. 79761Z.

[29] A. T. CONN AND J. ROSSITER, *Towards holonomic electro-elastomer actuators with six degrees of freedom*, Smart Materials and Structures, 21 (2012), p. 035012.

[30] K. A. COOK-CHENNAULT, N. THAMBI, AND A. M. SASTRY, *Powering MEMS portable devices‚Äîa review of non-regenerative and regenerative power supply systems with special emphasis on piezoelectric energy harvesting systems*, Smart Materials and Structures, 17 (2008), p. 043001.

[31] A. CORNOGOLUB, P.-J. COTTINET, AND L. PETIT, *Hybrid energy harvesting systems, using piezoelectric elements and dielectric polymers*, Smart Materials and Structures, 25 (2016), p. 095048.

[32] E. DIMOPOULOS, I. TRINTIS, AND S. MUNK-NIELSEN, *Energy Harvesting Cycles of Dielectric ElectroActive Polymer Generators*, 38th Annual Conference on Ieee Industrial Electronics Society (Iecon 2012), (2012), pp. 374–381.

[33] B. DREW, A. R. PLUMMER, AND M. N. SAHINKAYA, *A review of wave energy converter technology*, Proceedings of the Institution of Mechanical Engineers, Part A: Journal of Power and Energy, 223 (2009), pp. 887–902.

[34] M. DUDUTA, R. J. WOOD, AND D. R. CLARKE, *Multilayer Dielectric Elastomers for Fast, Programmable Actuation without Prestretch*, Advanced Materials, 28 (2016), pp. 8058–8063.

[35] O. EDENHOFER, R. PICHS-MADRUGA, Y. SOKONA, K. SEYBOTH, P. MATSCHOSS, S. KADNER, T. ZWICKEL, P. EICKEMEIER, G. HANSEN, S. SCHLOMER, AND C. VON STECHOW, eds., *Renewable Energy Sources and Climate Change Mitigation*, Cambridge University Press, Cambridge, 2011.

[36] P. FAN AND H. CHEN, *Performance investigation of a dissipative dielectric elastomer generator by the damping model*, Applied Physics A, 124 (2018), p. 148.

[37] P. FAN, H. CHEN, B. LI, AND Y. WANG, *Performance investigation on dissipative dielectric elastomer generators with a triangular energy harvesting scheme*, EPL (Europhysics Letters), 120 (2017), p. 47007.

[38] G. F. FRANKLIN, J. D. POWELL, AND M. L. WORKMAN, *Digital control of dynamic systems*, Addison-Wesley, 1998.

[39] A. N. GENT, *A New Constitutive Relation for Rubber*, Rubber Chemistry and Technology, 69 (1996), pp. 59–61.

[40] M. GIOUSOUF AND G. KOVACS, *Dielectric elastomer actuators used for pneumatic valve technology*, Smart Materials and Structures, 22 (2013), p. 104010.

[41] T. A. GISBY, B. M. O'BRIEN, I. A. ANDERSON, B. M. OBRIEN, I. A. ANDERSON, B. M. O'BRIEN, AND I. A. ANDERSON, *Self sensing feedback for dielectric elastomer actuators*, Applied Physics Letters, 102 (2013), p. 193703.

[42] T. A. GISBY, B. M. O'BRIEN, S. Q. XIE, E. P. CALIUS, AND I. A. ANDERSON, *Closed loop control of dielectric elastomer actuators*, vol. 7976, International Society for Optics and Photonics, 3 2011, p. 797620.

[43] N. C. GOULBOURNE, M. I. FRECKER, AND E. MOCKENSTURM, *Electro-elastic modeling of a dielectric elastomer diaphragm for a prosthetic blood pump*, vol. 5385, International Society for Optics and Photonics, 7 2004, p. 122.

[44] C. GRAF, M. AUST, J. MAAS, AND D. SCHAPELER, *Simulation Model for Electro Active Polymer Generators*, Proceedings of the 2010 Ieee International Conference on Solid Dielectrics (Icsd 2010), (2010).

[45] C. GRAF, J. HITZBLECK, T. FELLER, K. CLAUBERG, J. WAGNER, J. KRAUSE, AND J. MAAS, *Dielectric elastomer-based energy harvesting: Material, generator design, and optimization*, Journal of Intelligent Material Systems and Structures, 25 (2014), pp. 951–966.

[46] C. GRAF, T. HOFFSTADT, AND J. MAAS, *Optimization of the Charging Process for Dielectric Elastomer Generators*, Proceedings of the Asme Conference on Smart Materials, Adaptive Structures and Intelligent Systems, Vol 2, (2012), pp. 909–918.

[47] C. GRAF, J. MAAS, AND D. SCHAPELER, *Energy Harvesting Cycles based on Electro Active Polymers*, Electroactive Polymer Actuators and Devices (EAPAD) 2010, 7642 (2010).

[48] ——, *Optimized Energy Harvesting based on Electro Active Polymers*, Proceedings of the 2010 Ieee International Conference on Solid Dielectrics (ICSD 2010), (2010).

[49] S. J. HIERMAIER, *Structures under crash and impact : continuum mechanics, discretization and experimental characterization*, Springer, 2008.

[50] M. HILL, G. RIZZELLO, AND S. SEELECKE, *Development and experimental characterization of a pneumatic valve actuated by a dielectric elastomer membrane*, Smart Materials and Structures, 26 (2017), p. 085023.

[51] T. HOFFSTADT, C. GRAF, AND J. MAAS, *Optimization of the energy harvesting control for dielectric elastomer generators*, Smart Materials and Structures, 22 (2013).

[52] T. HOFFSTADT, M. GRIESE, AND J. MAAS, *Online identification algorithms for integrated dielectric electroactive polymer sensors and self-sensing concepts*, Smart Materials and Structures, 23 (2014), p. 104007.

[53] T. HOFFSTADT, R. HEINZE, T. WAHL, F. KAMEIER, AND J. MAAS, *DEAP-based energy harvesting using vortex-induced vibrations*, Proc. SPIE, 9056 (2014), p. 90561E.

[54] T. HOFFSTADT AND J. MAAS, *Self-sensing Algorithms for Dielectric Elastomer Multilayer Stack-Transducers*, IFAC-PapersOnLine, 49 (2016), pp. 373–379.

[55] ——, *Model-based self-sensing algorithm for dielectric elastomer transducers based on an extended Kalman filter*, Mechatronics, 50 (2018), pp. 248–258.

[56] J. HUANG, S. SHIAN, Z. SUO, AND D. R. CLARKE, *Maximizing the energy density of dielectric elastomer generators using equi-biaxial loading*, Advanced Functional Materials, 23 (2013), pp. 5056–5061.

[57] J. S. HUANG, S. SHIAN, Z. G. SUO, AND D. R. CLARKE, *Dielectric Elastomer Generator with Equi-biaxial Mechanical Loading for Energy Harvesting*, Electroactive Polymer Actuators and Devices (Eapad) 2013, 8687 (2013).

[58] S. HUANG, R. GREEN, A. PLASKOWSKI, AND M. BECK, *A high frequency stray-immune capacitance transducer based on the charge transfer principle*, IEEE Transactions on Instrumentation and Measurement, 37 (1988), pp. 368–373.

[59] T. IKEGAME AND K. TAKAGI, *Charging efficiency of a passively switched flyback converter for dielectric elastomer generator*, in Electroactive Polymer Actuators and Devices (EAPAD) XX, Y. Bar-Cohen, ed., vol. 10594, SPIE, 3 2018, p. 78.

[60] T. IKEGAME, K. TAKAGI, T. ITO, H. KOJIMA, AND H. YOSHIKAWA, *Energy harvesting by dielectric elastomer generator and self-priming circuit: verification by radio transmission*, vol. 10163, International Society for Optics and Photonics, 4 2017, p. 1016331.

[61] P. ILLENBERGER, K. TAKAGI, H. KOJIMA, U. K. MADAWALA, AND I. A. ANDERSON, *A Mathematical Model for Self-Priming Circuits: Getting the Most from a Dielectric Elastomer Generator*, IEEE Transactions on Power Electronics, 32 (2017), pp. 6904–6912.

[62] P. K. ILLENBERGER, K. E. WILSON, E.-F. M. HENKE, U. K. MADAWALA, AND I. A. ANDERSON, *A mathematical model for an integrated self priming dielectric elastomer generator*, vol. 10163, International Society for Optics and Photonics, 4 2017, p. 101630H.

[63] P. K. ILLENBERGER, P. ZANINI, S. ROSSET, U. K. MADAWALA, AND I. A. ANDERSON, *An integrated self priming circuit with electret charge source*, in Electroactive Polymer Actuators and Devices (EAPAD) XX, Y. Bar-Cohen, ed., vol. 10594, SPIE, 3 2018, p. 81.

[64] C. J AND B. R, *Future Marine Energy: Results of the Marine Energy Challenge : Cost Competitiveness and Growth of Wave and Tidal Stream Energy*, London, United Kingdom, 2006.

[65] P. JEAN, A. WATTEZ, G. ARDOISE, C. MELIS, R. VAN KESSEL, A. FOURMON, E. BARRABINO, J. HEEMSKERK, AND J. P. QUEAU, *Standing wave tube electro active polymer wave energy converter*, 8340 (2012), p. 83400C.

[66] C. JEAN-MISTRAL, S. BASROUR, AND J.-J. CHAILLOUT, *Dielectric polymer: scavenging energy from human motion*, Proc. SPIE, 6927 (2008), pp. 692716–692716.

[67] C. JEAN-MISTRAL, S. BASROUR, AND J. J. CHAILLOUT, *Modelling of dielectric polymers for energy scavenging applications*, Smart Materials & Structures, 19 (2010).

[68] C. JEAN-MISTRAL, T. V. CONG, AND A. SYLVESTRE, *Advances for dielectric elastomer generators: Replacement of high voltage supply by electret*, Applied Physics Letters, 101 (2012).

[69] H.-E. KIIL, M. BENSLIMANE, Y. BAR-COHEN, H.-E. KIIL, T. WALLMERSPERGER, AND M. BENSLIMANE, *Scalable industrial manufacturing of DEAP*, Proc. SPIE, 7287 (2009), p. 72870R.

[70] J. A. KILNER, *Functional materials for sustainable energy applications*, Woodhead Pub, 2012.

[71] H. S. KIM, J. H. J. J.-H. KIM, AND J. H. J. J.-H. KIM, *A review of piezoelectric energy harvesting based on vibration*, International Journal of Precision Engineering and Manufacturing, 12 (2011), pp. 1129–1141.

[72] G. KOFOD, *Dielectric Elastomer Actuators*, PhD thesis, The Technical University of Denmark, 2001.

[73] G. KOFOD AND P. SOMMER-LARSEN, *Silicone dielectric elastomer actuators: Finite-elasticity model of actuation*, Sensors and Actuators A: Physical, 122 (2005), pp. 273–283.

[74] G. KOFOD, P. SOMMER-LARSEN, R. KORNBLUH, AND R. PELRINE, *Actuation Response of Polyacrylate Dielectric Elastomers*, Journal of Intelligent Material Systems and Structures, 14 (2003), pp. 787–793.

[75] S. J. A. KOH, C. KEPLINGER, T. LI, S. BAUER, AND Z. SUO, *Dielectric elastomer generators: How much energy can be converted?*, IEEE/ASME Transactions on Mechatronics, 16 (2011), pp. 33–41.

[76] S. J. A. KOH, X. H. ZHAO, AND Z. G. SUO, *Maximal energy that can be converted by a dielectric elastomer generator*, Applied Physics Letters, 94 (2009).

[77] R. D. KORNBLUH, R. PELRINE, H. PRAHLAD, A. WONG-FOY, B. MCCOY, S. KIM, J. ECKERLE, AND T. LOW, *From boots to buoys: Promises and challenges of dielectric elastomer energy harvesting*, Proc. SPIE, 7976 (2011).

[78] G. KOVACS, P. LOCHMATTER, AND M. WISSLER, *An arm wrestling robot driven by dielectric elastomer actuators*, Smart Materials and Structures, 16 (2007), pp. S306–S317.

[79] C. LAGOMARSINI, C. JEAN-MISTRAL, S. MONFRAY, AND A. SYLVESTRE, *New approach to improve the energy density of hybrid electret-dielectric elastomer generators*, Proc. SPIE, 10163 (2017), p. 101632C.

[80] C. LAGOMARSINI, G. LOMBARDI, C. JEAN-MISTRAL, AND A. SYLVESTRE, *Alternatives to external polarization source for dielectric elastomers generators: electrets versus piezoelectric materials*, in 7th International conference on Electromechanically Active Polymer (EAP) transducers and artificial muscles (EUROEAP2017), 2017.

[81] G. J. LIN, M. CHEN, AND D. C. SONG, *Research of Micro-power generator based on the Dielectric Electro Active Polymer*, Iceet: 2009 International Conference on Energy and Environment Technology, Vol 1, Proceedings, (2009), pp. 782–786.

[82] G. J. LIN AND K. S. WANG, *A Novel Wind Power Micro-Generator Research on Dielectric Electro Active Polymer*, Advanced Materials Research, 1039 (2014), pp. 415–426.

[83] G. J. LIN, X. B. ZHANG, AND D. C. SONG, *Wind Power Micro-Generator Using Dielectric Electric Active Polymer*, Advanced Materials Research, 328-330 (2011), pp. 1491–1494.

[84] H. C. LO, T. MCKAY, B. M. O'BRIEN, E. CALIUS, AND I. ANDERSON, *Circuit Design Considerations for Regulating Energy Generated by Dielectric Elastomer Generators*, Proc. SPIE, 7976 (2011), pp. 79760C–79760C–8.

[85] P. LOTZ, M. MATYSEK, AND H. F. SCHLAAK, *Peristaltic pump made of dielectric elastomer actuators*, vol. 7287, International Society for Optics and Photonics, 3 2009, p. 72872D.

[86] J. MAAS AND C. GRAF, *Dielectric elastomers for hydro power harvesting*, Smart Materials and Structures, 21 (2012).

[87] J. MAAS, M. GRIESE, AND T. HOFFSTADT, *Integrated Sensor Concepts for Dielectric Elastomer Actuators*, in Volume 2: Mechanics and Behavior of Active Materials; Structural Health Monitoring; Bioinspired Smart Materials and Systems; Energy Harvesting, ASME, 9 2013, p. V002T02A019.

[88] A. MASOUMZADEH, E. NEKOUEI, T. ALPCAN, AND D. CHATTOPADHYAY, *Impact of Optimal Storage Allocation on Price Volatility in Energy-Only Electricity Markets*, IEEE Transactions on Power Systems, 33 (2018), pp. 1903–1914.

[89] K. MASUDA, T. IKOMA, K. NAKATSUGAWA, M. WAKI, AND S. CHIBA, *A Real Sea Test of Wave Powered Generation Buoys Using Dielectric Elastomers*, in Volume 7: Ocean Space Utilization; Ocean Renewable Energy, ASME, 7 2012, p. 587.

[90] D. MCCOUL, C. MURRAY, D. DI CARLO, AND Q. B. PEI, *Dielectric elastomer actuators for active microfluidic control*, Electroactive Polymer Actuators and Devices (Eapad) 2013, 8687 (2013).

[91] D. MCCOUL AND Q. PEI, *Tubular dielectric elastomer actuator for active fluidic control*, Smart Materials and Structures, 24 (2015), p. 105016.

[92] T. MCKAY, B. O'BRIEN, E. CALIUS, AND I. ANDERSON, *An integrated, self-priming dielectric elastomer generator*, Applied Physics Letters, 97 (2010).

[93] T. MCKAY, B. O,ÄôBRIEN, E. CALIUS, AND I. ANDERSON, *Self-priming dielectric elastomer generators*, Smart Materials and Structures, 19 (2010), p. 055025.

[94] T. G. MCKAY, *Soft, Low Complexity Dielectric Elastomer Generators*, PhD thesis, The University of Auckland, 2010.

[95] T. G. MCKAY, T. A. GISBY, AND I. A. ANDERSON, *Artificial muscles harvesting sensational power using self-sensing*, Electroactive Polymer Actuators and Devices (Eapad) 2014, 9056 (2014), p. 905603.

[96] T. G. MCKAY, B. M. O'BRIEN, E. P. CALIUS, AND I. ANDERSON, *Self-Priming dielectric Elastomer Generator Design*, Proc. SPIE, 8340 (2012), pp. 83401Y–83401Y–9.

[97] T. G. MCKAY, B. M. O'BRIEN, E. P. CALIUS, AND I. A. ANDERSON, *Soft generators using dielectric elastomers*, Applied Physics Letters, 98 (2011).

[98] T. G. MCKAY, D. K. SHIN, S. PERCY, C. KNIGHT, S. MCGARRY, AND I. A. ANDERSON, *Artificial Muscles on Heat*, Proc. SPIE, 9056 (2014).

[99] MIKIO WAKI, SEIKI A. CHIBA, Z. SONG, S. ZHU, AND K. OHYAMA, *Experimental Investigation on the Power Generation Performance of Dielectric Elastomer Wave Power Generator Mounted on a Square Type Floating Body*, Journal of Materials Science and Engineering B, 7 (2017).

[100] G. MORETTI, M. FONTANA, AND R. VERTECHY, *Modeling of a Heaving Buoy Wave Energy Converter With Stacked Dielectric Elastomer Generator*, in Volume 1: Development and Characterization of Multifunctional Materials; Modeling, Simulation and Control of Adaptive Systems; Structural Health Monitoring; Keynote Presentation, ASME, 9 2014, p. V001T03A020.

[101] ——, *Model-based design and optimization of a dielectric elastomer power take-off for oscillating wave surge energy converters*, Meccanica, 50 (2015), pp. 2797–2813.

[102] ——, *Parallelogram-shaped dielectric elastomer generators: Analytical model and experimental validation*, Journal of Intelligent Material Systems and Structures, 26 (2015), pp. 740–751.

[103] G. MORETTI, D. FOREHAND, R. VERTECHY, M. FONTANA, AND D. INGRAM, *Modeling of an Oscillating Wave Surge Converter With Dielectric Elastomer Power Take-Off*, in Volume 9A: Ocean Renewable Energy, ASME, 6 2014, p. V09AT09A034.

[104] G. MORETTI, G. P. R. PAPINI, M. RIGHI, D. FOREHAND, D. INGRAM, R. VERTECHY, AND M. FONTANA, *Resonant wave energy harvester based on dielectric elastomer generator*, Smart Materials and Structures, 27 (2018), p. 035015.

[105] B. M. O'BRIEN, E. P. CALIUS, T. INAMURA, S. Q. XIE, AND I. A. ANDERSON, *Dielectric elastomer switches for smart artificial muscles*, Applied Physics A: Materials Science and Processing, 100 (2010), pp. 385–389.

[106] R. W. OGDEN, *Large Deformation Isotropic Elasticity - On the Correlation of Theory and Experiment for Incompressible Rubberlike Solids*, Proceedings of the Royal Society A: Mathematical, Physical and Engineering Sciences, 326 (1972), pp. 565–584.

[107] ——, *Non-linear elastic deformations*, Ellis Horwood series in mathematics and its applications, E. Horwood ; Halsted Press, Chichester New York, 1984.

[108] R. PELRINE, R. KORNBLUH, J. ECKERLE, P. JEUCK, S. J. OH, Q. B. PEI, AND S. STANFORD, *Dielectric elastomers: Generator mode fundamentals and applications*, Proc. SPIE, 4329 (2001), pp. 148–156.

[109] R. PELRINE, R. KORNBLUH, AND G. KOFOD, *High-strain actuator materials based on dielectric elastomers*, Advanced Materials, 12 (2000), pp. 1223–1225.

[110] R. PELRINE, R. KORNBLUH, Q. B. PEI, AND J. JOSEPH, *High-speed electrically actuated elastomers with strain greater than 100%*, Science, 287 (2000), pp. 836–839.

[111] J.-S. PLANTE, *Dielectric elastomer actuators for binary robotics and mechatronics*, PhD thesis, Massachusetts Institute of Technology, 2006.

[112] J.-S. PLANTE, L. M. DEVITA, AND S. DUBOWSKY, *A road to practical dielectric elastomer actuators based robotics and mechatronics: discrete actuation*, vol. 6524, International Society for Optics and Photonics, 4 2007, p. 652406.

[113] P. PODDER, D. MALLICK, AND S. ROY, *Bandwidth widening in nonlinear electromagnetic vibrational generator by combined effect of bistability and stretching*, Journal of Physics: Conference Series, 557 (2014), p. 012039.

[114] M. RAGHEB, *Control of Wind Turbines*. `http://mragheb.com/NPRE475WindPowerSystems/ControlofWindTurbines.pdf`. [Online; accessed 19-August-2018].

[115] C. D. RICHARDS, M. J. ANDERSON, D. F. BAHR, AND R. F. RICHARDS, *Efficiency of energy conversion for devices containing a piezoelectric component*, Journal of Micromechanics and Microengineering, 14 (2004), pp. 717–721.

[116] G. RIZZELLO, *Modeling, Control and Self-Sensing of Dielectric Elastomer Actuators*, PhD thesis, Politecnico di Bari, 2016.

[117] G. RIZZELLO, M. HODGINS, D. NASO, A. YORK, AND S. SEELECKE, *Modeling of the effects of the electrical dynamics on the electromechanical response of a DEAP circular actuator with a mass-spring load*, Smart Materials and Structures, 24 (2015).

[118] G. RIZZELLO, M. HODGINS, S. SEELECKE, AND D. NASO, *Self-sensing at low sampling-to-signal frequency ratio: An improved algorithm for dielectric elastomer actuators*, in 2016 12th IEEE/ASME International Conference on Mechatronic and Embedded Systems and Applications (MESA), no. August, 2016, pp. 1–6.

[119] G. RIZZELLO, D. NASO, A. YORK, AND S. SEELECKE, *Self-sensing in dielectric electroactive polymer actuator using linear-in-parametes online estimation*, in 2015 IEEE International Conference on Mechatronics (ICM), IEEE, 3 2015, pp. 300–306.

[120] ——, *Closed loop control of dielectric elastomer actuators based on self-sensing displacement feedback*, Smart Materials and Structures, 25 (2016), p. 035034.

[121] ——, *A Self-Sensing Approach for Dielectric Elastomer Actuators Based on Online Estimation Algorithms*, IEEE/ASME Transactions on Mechatronics, 22 (2017), pp. 728–738.

[122] S. ROSSET AND H. R. SHEA, *Flexible and stretchable electrodes for dielectric elastomer actuators*, Applied Physics a-Materials Science & Processing, 110 (2013), pp. 281–307.

[123] ——, *Towards fast, reliable, and manufacturable DEAs: miniaturized motor and Rupert the rolling robot*, Electroactive Polymer Actuators and Devices (Eapad) 2015, 9430 (2015).

[124] J. ROSSITER, P. WALTERS, AND B. STOIMENOV, *Printing 3D dielectric elastomer actuators for soft robotics*, vol. 7287, International Society for Optics and Photonics, 3 2009, p. 72870H.

[125] S. ROUNDY, *On the Effectiveness of Vibration-based Energy Harvesting*, Journal of Intelligent Material Systems and Structures, 16 (2005), pp. 809–823.

[126] S. ROUNDY, P. K. WRIGHT, AND J. M. RABAEY, *Energy Scavenging for Wireless Sensor Networks*, Springer US, Boston, MA, 2004.

[127] B. SCHERBER, M. GRAUER, A. KOLLNBERGER, AND A. KÖLLNBERGER, *Electroactive polymers for gaining sea power*, Electroactive Polymer Actuators and Devices (Eapad) 2013, 8687 (2013), p. 86870K.

[128] S. SHIAN, K. BERTOLDI, AND D. R. CLARKE, *Dielectric Elastomer Based "Grippers" for Soft Robotics*, Advanced Materials, 27 (2015), pp. 6814–6819.

[129] S. SHIAN, R. M. DIEBOLD, AND D. R. CLARKE, *Tunable lenses using transparent dielectric elastomer actuators*, Optics Express, 21 (2013), p. 8669.

[130] S. SHIAN, J. HUANG, S. ZHU, AND D. R. CLARKE, *Optimizing the Electrical Energy Conversion Cycle of Dielectric Elastomer Generators*, Advanced Materials, 26 (2014), pp. 6617–6621.

[131] Y. SHTESSEL, C. EDWARDS, L. FRIDMAN, AND A. LEVANT, *Sliding mode control and observation*, Birkhäuser Basel, New York, USA, 2014.

[132] L. SODERLUND, J.-T. ERIKSSON, J. SALONEN, H. VIHRIALA, AND R. PERALA, *A permanent-magnet generator for wind power applications*, IEEE Transactions on Magnetics, 32 (1996), pp. 2389–2392.

[133] S. SON AND N. C. GOULBOURNE, *Pulsatile dielectric elastomer membrane sensors*, Proceedings of SPIE, 7287 (2009), pp. 72870K–72870K–12.

[134] Z. G. SUO, *Theory of Dielectric Elastomers*, Acta Mechanica Solida Sinica, 23 (2010), pp. 549–578.

[135] D. TEPEL, C. GRAF, AND J. MAAS, *Modeling of mechanical properties of stack actuators based on Electroactive polymers*, Electroactive Polymer Actuators and Devices (Eapad) 2013, 8687 (2013).

[136] L. A. TOTH AND A. A. GOLDENBERG, *Control system design for a dielectric elastomer actuator: the sensory subsystem*, Proc. SPIE, 4695 (2002), pp. 323–334.

[137] R. VAN KESSEL, B. CZECH, P. BAUER, AND J. A. FERREIRA, *Optimizing the Dielectric Elastomer Energy Harvesting Cycles*, Iecon 2010 - 36th Annual Conference on Ieee Industrial Electronics Society, (2010).

[138] R. VERTECHY AND M. FONTANA, *Dielectric Elastomers for Wave Energy Harvesting*, SPIE Newsroom, (2015), pp. 148–156.

[139] R. VERTECHY, M. FONTANA, G. P. R. PAPINI, D. FOREHAND, G. P. ROSATI PAPINI, AND D. FOREHAND, *In-Tank Tests of a Dielectric Elastomer Generator for Wave Energy Harvesting*, Electroactive Polymer Actuators and Devices (EAPAD) 2014, 9056 (2014), p. 90561G.

[140] R. VERTECHY, M. FONTANA, G. P. ROSATI PAPINI, M. BERGAMASCO, G. P. R. PAPINI, AND M. BERGAMASCO, *Oscillating-water-column wave-energy-converter based on dielectric elastomer generator*, Electroactive Polymer Actuators and Devices (Eapad) 2013, 8687 (2013), p. 86870I.

[141] R. VERTECHY, G. P. P. ROSATI, AND M. FONTANA, *Reduced Model and Application of Inflating Circular Diaphragm Dielectric Elastomer Generators for Wave Energy Harvesting*, Journal of Vibration and Acoustics-Transactions of the ASME, 137 (2015).

[142] T. VU-CONG, C. JEAN-MISTRAL, AND A. SYLVESTRE, *Electrets substituting external bias voltage in dielectric elastomer generators: application to human motion*, Smart Materials and Structures, 22 (2013).

[143] C. WALKER AND I. ANDERSON, *From land to water: bringing dielectric elastomer sensing to the underwater realm*, vol. 9798, International Society for Optics and Photonics, 4 2016, p. 97982B.

[144] H. M. WANG, C. S. WANG, AND T. Y. YUAN, *On the energy conversion and efficiency of a dielectric electroactive polymer generator*, Applied Physics Letters, 101 (2012).

[145] Y. WANG, Z. LI, L. QIN, G. CADDY, C. H. YAP, AND J. ZHU, *Dielectric Elastomer Fluid Pump of High Pressure and Large Volume Via Synergistic Snap-Through*, Journal of Applied Mechanics, 85 (2018), p. 101003.

[146] A. WESTLAKE, J. BUMBY, AND E. SPOONER, *Damping the power-angle oscillations of a permanent-magnet synchronous generator with particular reference to wind turbine applications*, IEE Proceedings - Electric Power Applications, 143 (1996), p. 269.

[147] M. WISSLER AND E. MAZZA, *Modeling and simulation of dielectric elastomer actuators*, Smart Materials & Structures, 14 (2005), pp. 1396–1402.

[148] ——, *Mechanical behavior of an acrylic elastomer used in dielectric elastomer actuators*, Sensors and Actuators A: Physical, 134 (2007), pp. 494–504.

[149] D. XU, A. TAIRYCH, AND I. A. ANDERSON, *Stretch not flex: programmable rubber keyboard*, Smart Materials and Structures, 25 (2016), p. 015012.

[150] O. H. YEOH, *Some Forms of the Strain Energy Function for Rubber*, Rubber Chemistry and Technology, 66 (1993), pp. 754–771.

[151] X. YUAN AND Y. LI, *Control of variable pitch and variable speed direct-drive wind turbines in weak grid systems with active power balance*, IET Renewable Power Generation, 8 (2014), pp. 119–131.

[152] P. ZANINI, G. RIZZELLO, S. SEELECKE, M. HOMER, AND J. ROSSITER, *Self-sensing for robust automatic charge management of dielectric elastomer generators*, in Electroactive Polymer Actuators and Devices (EAPAD) XX, Y. Bar-Cohen, ed., vol. 10594, SPIE, 3 2018, p. 52.

[153] P. ZANINI, J. ROSSITER, AND M. HOMER, *Modelling the effect of actuator-like behavior in dielectric elastomer generators*, Applied Physics Letters, 107 (2015).

[154] ——, *Modeling self-priming circuits for dielectric elastomer generators towards optimum voltage boost*, Proc. SPIE, 9798 (2016), p. 97980W.

[155] ——, *Frequency-domain trade-offs for dielectric elastomer generators*, Proc. SPIE, 10163 (2017), p. 101631C.

[156] ——, *Self-stabilizing dielectric elastomer generators*, Smart Materials and Structures, 26 (2017), p. 35037.